Transport in concrete with new CO2 reduced cements - Reactive Transport Model for Durability Estimations

Addassi, Mouadh

Publication date:
2018

Document Version
Publisher's PDF, also known as Version of record

Citation (APA):
Addassi, M. (2018). Transport in concrete with new CO2 reduced cements - Reactive Transport Model for Durability Estimations. Technical University of Denmark, Department of Civil Engineering. B Y G D T U. Rapport, No. 393

Transport in concrete with new CO_2 reduced cements

- Reactive Transport Model for Durability Estimations

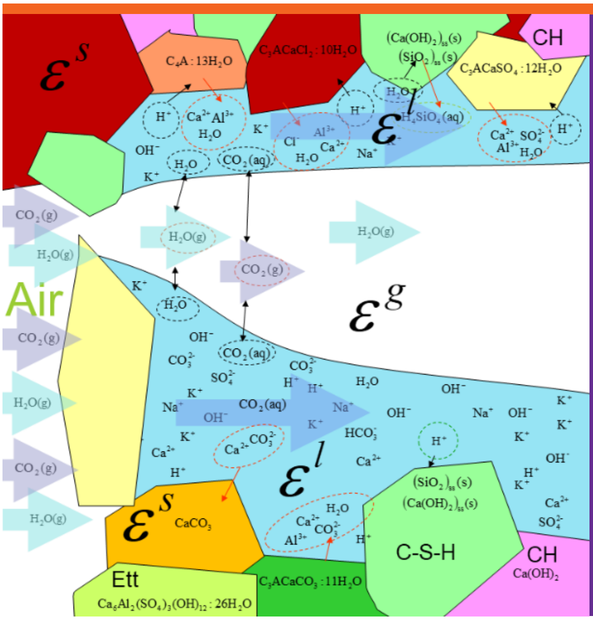

Mouadh Addassi

PhD Thesis

Department of Civil Engineering
2018

DTU Civil Engineering Report 393

DTU Civil Engineering
Department of Civil Engineering

Transport in concrete with new CO_2-reduced cements

- Reactive Transport Model for Durability Estimations

Mouadh Addassi

Ph.D. Thesis

Department of Civil Engineering
Technical University of Denmark

2018

Supervisors:

Professor Björn Johannesson, Linnaeus University, Sweden
Professor Ida Lykke Fabricius, DTU Byg, Denmark
Professor Henrik Stang, DTU Byg, Denmark

Assesment Committee:

Dr. Veronique Baroghel-Bouny, IFSTTAR, Group leader, France
Dr. Yoshifumi Hosokawa, Taiheiyo Cement Corporation, R&D Center, Japan
Professor Assaf-Avraham Klar, DTU Byg, Denmark

Transport in concrete with new CO_2-reduced cements
-Reactive Transport Model for Durability Estimations

Printed by DTU-Tryk
Department of Civil Engineering
Technical University of Denmark
ISBN: 9788778774897

Preface

This thesis is submitted as a partial fulfillment of the requirements for the Danish PhD degree at the Technical University of Denmark. The PhD project is aiming at understanding durability related moisture and gas transport properties for new CO_2-reduced cement-binders. The study is a part of an innovation consortium about green transition of cement and concrete production in Denmark. The thesis consists of two parts. Part I introduces the background, motivation, aim and scope of the study and summarizes the major research findings. Part II is a collection of three papers treating important topics related to the undertaken research.

Preface to published version

The thesis was defended at a public defense on Thursday the 5^{th} of Julay 2018. Official opponents were Professor Assaf-Avraham Klar, Technical University of Denmark, Research group leader Dr. Veronique Baroghel-Bouny, IFSTTAR and Dr. Yoshifumi Hosokawa, Taiheiyo Cement Corporation, R&D Center. Compared to the the original submitted version of the thesis, very minor editorial corrections have been made.

Kongens Lyngby, July 09, 2018

Mouadh Addassi

Acknowledgements

I owe my thanks to the Danish Innovation Fond (Innovations Fonden) for the financial support to this work as a part of the ”Green transition of cement and concrete production” (Grøn Beton II) project (grant no. 1382-00054B). Without their financial support and the contribution from the project partners this research would not have been possible. Thanks to INGENIØR CAND POLYT ERIKHEGENHOFTS LEGAT for supporting my visit to the Department of Mathematical and Statistical Sciences at the University of Colorado Denver. Thanks to the Department for Civil Engineering at the Danish Technical University for the awarded travel grant included in the PhD Paper of the year 2016 award.

There is a long list of people who have either directly or indirectly made this work possible for whom I am grateful.

First and foremost, I would like to express my deepest thanks and gratitude to my supervisor professor Björn Johannesson. Without his assistance, patience, and unlimited support all the way through, this thesis would truly not have been possible. Further, I would like to thanks my academic coordinators, professor Ida Lykke Fabricius, professor Henrik Stang and assistant professor Alexander Michel for their support during the project.

I am truly grateful to all my colleagues at the Geotechnical section at DTU Byg for a wonderful work environment. Special thanks to my fellow PhD colleagues Leonardo Meireles, Tobias Orlander, Konstantina Katika, Asmus Skar, Stine Madsen, Tulika Bose and Einar Storebøfor creating an enjoyable working atmosphere.

Sincere thanks to Professor Lynn Schreyer for her kind hospitality and for an amazing learning experience during my research stay at the Dept. of Mathematical and Statistical Sciences at the University of Colorado Denver.

Further, thanks to the staff at the Division of Building Materials at Lund University, especially professor Lars Wadsö for a wonderful collaboration experience.

Finally, I would like to thank my family and friends, the list of whom is too long to mention, for their encouragement and unconditional support.

Abstract

Concrete is the most used building material in the world due to its cheap price and desired properties such as strength, workability and durability. Concrete is a composite material obtained by mixing cement, water, aggregates and small amounts of chemical additives. Following the mixing, a (fast) chemical process called hydration is initiated in which the different cement clinkers react with water and form different hydration products, such as calcium-silicate-hydrate (C-S-H), ettringite and monosulfate. The hydration process can continue slowly over the lifetime of concrete structures and is influenced by the so-called service environment, which is the environment surrounding the concrete. In aggressive service environments, for instance, in the case of marine exposure, the altering of hydrated cement can lead to the end of its service life. Most of the altering processes are related to moisture and gas transport within the pores of the concrete.

This thesis was part of a project aiming to provide the basis for a green conversion of cement and concrete production in Denmark. The thesis contributes to a better understanding of long-term consequences of implementing new CO_2-reduced cement in concrete through experimental investigations and reactive mass transport modeling. CO_2-reduced cement refer to binder-systems where amounts of the Portland cement is replaced with supplementary cementitious materials such as calcined clay and limestone filler, in order to decrease the CO_2 emission from the production of concrete. Three major areas of focus related to moisture and gas transport in cement-based systems were covered.

First focus area was the explanation of vapor transport through a partially saturated capillary pore. In unsaturated porous materials, the presence of trapped fluid in a capillary pore increase the overall rate of vapor transport rather than blocking it. This is simply due to the fact that the trapped liquid can be considered as a bridge shortening of the apparent distance the vapor needs to travel through the pore system. A simple approach was proposed describing the process with a single equation using the gradient of the chemical potential as the driving force for diffusion, in this case, equal to the

gradient of the relative humidity. The model was established without the use of fitting parameters. The proposed method was compared with, experimental results for isothermal vapor transport through a partially saturated cylindrically symmetric capillary tube of variable cross-sectional area, with excellent agreement. The study concluded that the enhancement of vapor transport in the presence of trapped pore liquid can be modeled using the geometry and the relative humidity at the gas-liquid interface. It is nearly impossible to directly apply this model to cement-based materials since it is not possible to accurately describe the geometry and boundary conditions at each gas-liquid interface, due to the complex microstructure of the pores of hydrated cement. However, the study provided insight into one important pore-scale vapor transport mechanism in unsaturated systems. Furthermore, the study also demonstrated the conceptual advantage of using the chemical potential in modeling vapor transport at the pore-scale.

Secondly, liquid water and water vapor transport properties relevant to concrete durability modeling were investigated. Moisture properties of ten different CO_2-reduced cement-based binder-systems containing supplementary cementitious material in the form of fly ash, calcined clay, burnt shale and gray micro-filler, where investigated using four different experiments being, (i) sorption tests (moisture fixation), (ii) cup tests in two different relative humidity intervals, (iii) drying tests, and, (iv) capillary suction tests. An inverse approach was developed for determining a separate description of the effective diffusion in the liquid phase and in the vapor phase as a function of the saturation degree, relevant for the proposed continuum moisture transport model adopted. The inverse approach in all essential parts uses the measured mass change over time, as obtained from all the experimental investigations, to inversely obtain the effective diffusion parameters. Due to the use of multiple diffusion experiments both in absorption and desorption, covering different relative humidity intervals, the moisture properties obtained with the proposed inverse analyses method provide a good description valid for a wide range of cases of the moisture transport for the ten different binder-systems. The proposed method does not explicitly account for the effect of pore structural change over time, but it provides a good description of moisture properties at the conditions the samples were tested at. Accurate models for moisture transport is crucial for more involved durability models also including ionic and gas transport features.

Thirdly, a multi-phase reactive mass transport framework for durability estimation of cement-based materials was developed. The goal was to include the gas phase alongside the implemented liquid phase and solid phase developed in earlier works. The addition of the gas phase into an earlier developed framework includes the description of gaseous transport in the

air-filled space and chemical gas-liquid interaction. The governing system of equations includes a modified version of the Poisson-Nernst-Planck system of equations including gaseous transport in the air-filled space, ionic transport in the liquid phase, electro-migration of ionic species, two-phase moisture transport consisting of water vapor and liquid water, and sorption. A stringent model for mass transport also including for gaseous constitutes contributes to a better understanding of the true mechanisms responsible for the altering of hydrated cement-based materials in unsaturated conditions as well as in cyclic drying-wetting conditions. Furthermore, the inclusion of gaseous constituents into the framework enhances the model's accuracy and enables the investigation of combined effects of different degradation processes acting simultaneously, for example, carbonation and chloride ingress. Different numerical examples are included demonstrating applications of the above mentioned added futures.

Resumé

Beton er det mest anvendte byggemateriale i verden på grund af dets billige pris og egenskaber, så som, styrke, funktionalitet og holdbarhed. Beton er et kompositmateriale opnået ved blanding af cement, vand, aggregater og små mængder kemiske additiver. Efter blanding indledes en forholdsvis hurtig kemisk proces, kaldet hydrering, hvor de forskellige cementklinkere reagerer med vand og danner forskellige hydrerings produkter, såsom calcium silikat hydrat (C-S-H), ettringit og monosulfat. Hydreringsprocessen kan fortsætte langsomt henover betonkonstruktionens levetid og påvirkes af det såkaldte servicemiljø, som er omgivelserne omkring betonen. I aggressive servicemiljøer, f.eks. i tilfælde af marin brug, kan nedbrydning af hydreret cement føre til endt levetid for konstruktionen. De fleste af nedbrydningsprocesser er relateret til fugt- og gastransport gennem betonens porer.

Denne afhandling var en del af et projekt som har til formål at danne grundlag for en grøn omstilling af cement og betonproduktion i Danmark. Afhandlingen bidrager til en bedre forståelse af de langsigtede konsekvenser af implementeringen af nye CO_2-reduceret cement (cement bindesystemer, hvor en andel af Portlandcement erstattes med supplerende cementmaterialer såsom brændt ler og kalkstenspulver, for at reducere CO_2 emissionen fra produktion af Portland cement) i beton gennem eksperimentelle undersøgelser og reaktive massetransportmodellering. Følgende tre fokus områder inden for fugt og gas transport i cementbaserede systemer blev dækket.

Første fokusområde handler om forklaringen af damptransport gennem en delvist mættet kapillærpore. I umættede porøse materialer, vil tilstedeværelsen af fanget væske i en kapillærpore, accelerere den samlede damptransporthastighed frem for at blokere den. Dette skyldes at den fangede væske kan betragtes som en broforkortelse af den tilsyneladende afstand, som dampen skal rejse i poresystemet. En simpel tilgang blev foreslået for at beskrive processen med en enkelt ligning ved anvendelse af gradienten af det kemiske potentiale som drivkraft for diffusion, som i dette tilfælde er lig med gradienten af den relative fugtighed. En model blev etableret uden brug af justeringsparametre. Den foreslåede metode blev sammenlignet med eksperimentelle

rimentelle resultater for isotermisk damptransport gennem et delvist mættet symmetrisk cylindrisk kapillærrør med variabelt tværsnitsareal, og resultatet var fremragende. Undersøgelsen konkluderede, at forøgelsen af damptransport ved fremkomst af fanget porevæske kan modelleres ved anvendelse af geometrien og den relative luftfugtighed ved gas-væske-grænsefladen. Det er næsten umuligt at anvende denne model direkte på cementbaserede materialer, da det ikke er muligt præcist at beskrive geometrien og randbetingelserne ved hver gas-væske-grænseflade på grund af den komplekse mikro-strukturer af porerne af hydratiseret cement. Undersøgelsen gav dog indsigt i en vigtig pore-skala damptransportmekanisme i umættede systemer. Desuden viste undersøgelsen også den konceptuelle fordel ved at anvende det kemiske potentiale i modellering af damptransport på poreskalaen.

Andet fokusområde handler om undersøgelsen af transportegenskaber af vanddamp og flydende vand, der er relevant for betonholdbarheds modellering. Fugtegenskaber af ti forskellige CO_2-reducerede cementbaserede bindersystemer indeholdende supplerende cementmateriale i form af flyveaske, brændt ler, brændt skifer og kalksten pulver, som blev undersøgt ved anvendelse af fire forskellige eksperimenter, som er (i) sorptionstest (fugtfiksering), (ii) koppeprøver i to forskellige relative fugtighedsintervaller, (iii) tørprøvninger, og (iv) kapillærsugningstest. En fremgangsmåde blev udviklet til inverse analyser til bestemmelse af en separat beskrivelse af den effektive diffusion i flydende fase og i dampfasen som funktion af mætningsgraden, der er relevant for den foreslåede kontinuerte fugttransportmodel. Den inverse modulerings tilgang anvender masseændringen over tid, som opnået fra alle forsøgsundersøgelser for at opnå de effektive diffusionsparametre. På grund af brugen af flere diffusionsforsøg, både ved absorption og desorption, der dækker forskellige relative fugtighedsintervaller, giver de fugtighedsegenskaber, der opnås ved den foreslåede inverse analysemetode, en god beskrivelse, der gælder for en lang række af tilfælde af fugttransporten for de ti forskellige bindersystemer. Den foreslåede metode beskriver ikke eksplicit virkningen af porestrukturændringer over tid, men den giver en god beskrivelse af fugtegenskaber under de betingelser, som prøverne blev testet i. Nøjagtige modeller til fugttransport er afgørende for mere avancerede holdbarhedsmodeller, hvor ion- og gastransport også er inkluderet.

Tredje fokusområde handler om udvikling af en flerfaset reaktiv massetransports modelramme for holdbarhedsvurdering af cementbaserede materialer. Målet var at inkludere gasfasen sammen med den flydende fase og den faste fase, som blev udviklet og implementeret i tidligere projekter. Tilsætningen af gasfasen til en tidligere udviklet ramme indbefatter beskrivelsen af gastransport i det luftfyldte rum og gas-væske-interaktion. Det regulerende system af ligninger indbefatter en modificeret version af Poisson-Nernst-

Planck-systemet, herunder gastransport i det luftfyldte rum, iontransport i flydende fase, ionmigration, en tofaset fugttransport bestående af vanddamp og flydende vand og sorption hysterese. En streng model for massetransport, der også tager hensyn til gasformige stoffer, bidrager til en bedre forståelse af de sande mekanismer, der er ansvarlige for ændring af hydrerede cementbaserede materialer i umættede betingelser såvel som i cykliske tørrings-befugtnings betingelser. Desuden indbefatter inklusion af gasformige bestanddele i rammen modellernes nøjagtighed og muliggør undersøgelser af den kombinerede virkning af forskellige nedbrydningsprocesser samtidigt, som for eksempel karbonisering og kloridindtrængning. Forskellige numeriske eksempler blev benyttet for at demonstrere applikationer af de tilsatte funktioner.

١

نبذة مختصر

يعتبر الإسمنت المسلّح أو الخرسانة أو البوتون، المادّة الأكثر استعمالا في البناء في جميع أنحاء العالم، ويعود ذلك إلى انخفاض ثمنه من ناحية وإلى خاصياته من ناحية أخرى… تلك الخاصيات المتعلقة بالقوة والمقاومة والأداء الوظيفي والديمومة.

ونتحصل على الخرسانة بخلط الإسمنت والماء والمواد الرّكاميّة كالرّمل والحصى، بالإضافة إلى بعض العناصر الكيمياويّة بكميات بسيطة. تتفاعل المواد المخلوطة بسرعة مع بعضها البعض تفاعلا كيمياويا يسمى الهدرجة، حيث تتفاعل حبيبات الإسمنت مع الماء ليكونا مختلف المنتجات المهدرجة، مثل هيدرات سيليكات الكالسيوم (C-S-H) تتواصل عمليّة الهدرجة ببطء خلال مدة بقاء الخرسانة، وتتأثر بما يسمّى بيئة الخدمة، وهي البيئة المحيطة بالخرسانة. قد توصف بيئة الخدمة بالعنيفة، إذا ما كان المحيط شديد التأثير على الإسمنت المهدرج وعامل إهلاك وتحطيم له، مثال ذلك الاستعمالات البحرية الواقعة تحت تأثير الرّطوبة والغازات المتسربة عبر مسام الخرسانة. تعتبر هذه الرسالة جزء من مشروع يهدف إلى خلق البديل النّظيف (الأخضر) لصناعة الإسمنت والخرسانة في الدنمارك. تسهم الرّسالة في تيسير فهم الآثار بعيدة الآجال المترتبة على إنتاج أنواع الإسمنت الجديدة مخفضة منسوب ثاني أكسيد الكربون، حيث يعوض جزء من إسمنت بورتلاند، بمواد أخرى مثل الطين المحمى الناضج ومسحوق الحجر الجيري، من أجل تخفيض منسوب ثاني أوكسيد الكربون في الخرسانة وذلك عن طريق التجارب المخبرية والحسابات الرقمية. لقد ركزت الرّسالة على المجالات الثلاثة التالية المتعلقة بتنقل الرطوبة والغاز في الأنظمة ذات القاعدة الإسمنتيّة!…

- المجال الأوّل أو منطقة التركيز الأولى، تتعلّق بشرح نقل البخار عبر فتحات شعيرية دقيقة مشبعة جزئيا. فإذ عدم الإشباع في المواد المثقوبة يعطي إمكانية وجود السوائل في تلك الثّقوب. وجود تلك السوائل يجعل تنقل البخار خلالها أسرع حيث تعتبر السّوائل بمثابة الجسر المساهم في اختصار المسافة التي سوف يقطعها البخار عبر الفتحات الشّعيرية الدقيقة. تمكنا من تفسير وشرح هذه العملية باستخدام معادلة واحدة تعتمد على استعمال نسبة التغير في العملية الكيمياوية المنتجة للطاقة الحرارية المذيبة، وهي في هذه الحالة مساوية للتغير في درجة الرّطوبة النّسبية. لقد وقعت مقارنة هذه الطريقة المقترحة بالنتائج التجريبيّة لنقل البخار عبر الأجسام المتناظرة شبه الدائرية، المشبعة جزئيا، فكانت النّتائج جد طيبة. نستخلص من الدراسة أنه بالإمكان حساب نسبة تسريع نقل البخار بواسطة السوائل المحجوزة في الثقب الشعيريّة الدّقيقة باستعمال الأشكال الهندسيّة ورطوبة الهواء النسبيّة في الحدّ بين الغاز والسائل. يرى من شبه المستحيل استعمال هذه الطريقة بصفة دقيقة ومباشرة على المواد ذات القاعدة الإسمنتية، التي لا يمكن ضبط أشكالها الهندسية ولا حدود تماس الغاز والسائل فيها، وذلك بسبب التعقيد الناجم عن الطبيعة المجهريّة الدّقيقة للإسمنت المرطب. لقد شرحت هذه

الدّراسة جوانب مهمة لنقل البخار عبر المسامّ غير المشّبعة. بالإضافة إلى ذلك، فإنّ الدراسة أظهرت مزيّة استعمال الطاقة الكمياويّة للمواد في حساب تنقل البخار عبر المسامّ الشّعيريّة.

المجال الثاني الحري بالاهتمام هو دراسة خاصيات تنقل الماء في حالتيه الغازيّة والسائلة وحساب تأثيرها على خاصّية الديمومة في الخرسانة. تم التركيز على عشر خلطات للإسمنت المخفض من ثاّني أوكسيد الكربون والمحتوية على نسب من رماد الوقود والطين المحمى والحجارة الحامية الضاغطة ومسحوق الحجر الجيري. تمت دراسة خاصيات تنقل الماء في حالتيه الغازيّة والسائلة للخلطات العشر عن طريق أربع تجارب مخبريّة ركّزت علي حساب سرعة امتصاص الرّطوبة وبسطها عبر الثقب الشّعيرية الدّقيقة. طورت طريقة تحليل معكوسة وذلك من أجل التحصل على وصف مستقلّ للانتتشار الفعّال ذي الجدوى للماء في الحالتين السائلة والغازيّة في علاقة بدرجة التشبع. تعتمد تقنية التحليل المعكوسة على مجموعة التغيرات التي رصدت بالتجارب المخبرية عبر الزمن، من أجل تحديد عوامل الانتشار الأكثر فاعليّة. نظرا للاعتماد على الكثير من التجارب المخبرية لتنقل الماء في حالتيه السائلة والغازيّة سواء كان بطريقة الامتصاص أو بالدّفع والانتشار، لتغطية مختلف خاصيّات الرّطوبة للعشر خلطات، يمكن وصف نتاج طريقة التحليل المعكوسة المعتمدة بالدّقيقة. لا تشرح هذه الطريّقة ببساطة التحوّلات والتغيّرات في الثقب الشّعيرية الدّقيقة عبر الزمن، ولكنّها تعطي وصفا دقيقا لخاصيات الرّطوبة ضمن الشروط والظروف التي تمت فيها التجارب المخبريّة. تظلّ طرائق حسابات دقيقة وصحيحة لنقل الرطوبة أساسا مهما تعتمد عليه أساليب تقّييم المتانة والديمومة المتّقدمة الآخذة بالاعتبار حالة المادّة في حالتّها الشاردة في حال (ion) أو الغازيّة.

وأما المجال الثالث فيتعلق بضبط وتطوير مراحل نقل المادّة التفاعلي وذلك من أجل تقدير ديمومة المواد الإسمنتيّة. ويكمن الهدف في دمج المرحلة الغازية في برنامج حساب رقمي مع المرحلة السائلة والصلبة، التي تم تطويرها واعتمادها في مشاريع سابقة. إضافة المرحلة الغازيّة لما سبق تطويره يتطلب وصف نقل الغاز في المجال المليء بالهواء والتفاعل بين الغاز والسّائل. يحتوي النّظام الأصلي للمعادلة الأساسية لبرنامج الحساب الرقمي على نسخة منقّحة لنظام (Poisson-Nernst-Planck))، تشمل وصف نقل الغاز في المجال المليء بالهواء ونقل الشّوارد (ion) في مرحلتها السائلة وتنقّل الشّوارد وحركتها ونقل الرّطوبة في مرحلتيها البخاريّة (الغازيّة) أو السائلة والامتصاص المنفعل. تم تصميم نموذج منضبط صارم لنقل المادة يهتمّ كذلك بالمواد الغازيّة المساهمة في فهمٍ أوضح للآليات الصحيحة، ذات المسؤولية في التغييرات الحادثة على المواد الإسمنتيّة. بالإضافة إلى ذلك فإنّ إدراج المكونات الغازيّة في هذا الإطار يحسن دقة برنامج الحساب الرقمي ويمكن من دراسة التأثير المشترك لآليات التآكلات المتزامنة، مثل التفحم وتسرب الكلور. أمثلة رقميّة مختلفة وقع استعمالها لبيان تطبيقات الوظائف المضافة لبرنامج الحساب الرقمي.

Contents

Part I

Introduction and Summary

Chapter 1

Introduction

1.1 Background

This thesis is a part of an innovation consortium called “Green Transition of Cement and Concrete Production”. The goal of the consortium is to motivate and prepare for a green transition of cement and concrete production in Denmark. The role of this thesis is creating a better understanding of durability related mechanisms of green concrete. The thesis includes the study of new CO_2-reduced binder-systems, containing combinations of limestone filler, fly ash, calcined clay, and burnt shale.

According to a review report on cement production (CEMBUREAU, 2017) the cement production almost doubled in a ten year period from about 2.2 billion tons produced in 2004 to approximately 4.2 billion tons in 2014. In the same 10 year period, the world population grew about 12% (UnitedNations, 2015). With a world population of about 7 billion in 2014, the cement production corresponds to about 0.6 ton of cement per capita, making cement the most manufactured product in the world and concrete the second most used material on earth only exceeded by water (Scrivener et al., 2016). The increase in cement production is expected to continue as the world’s population continue to increase, especially in low-income countries in Africa and Asia where 65% of the urban population still lives in slums (WorldBank, 2016).

The manufacturing processes of Portland cement result in the release of CO_2-gas from two sources:

(i) The calcination of limestone, a process where limestone react under high temperature to produce free lime (CaO) and CO_2-gas.

(ii) Energy demand and fuel consumption, as the manufacturing process,

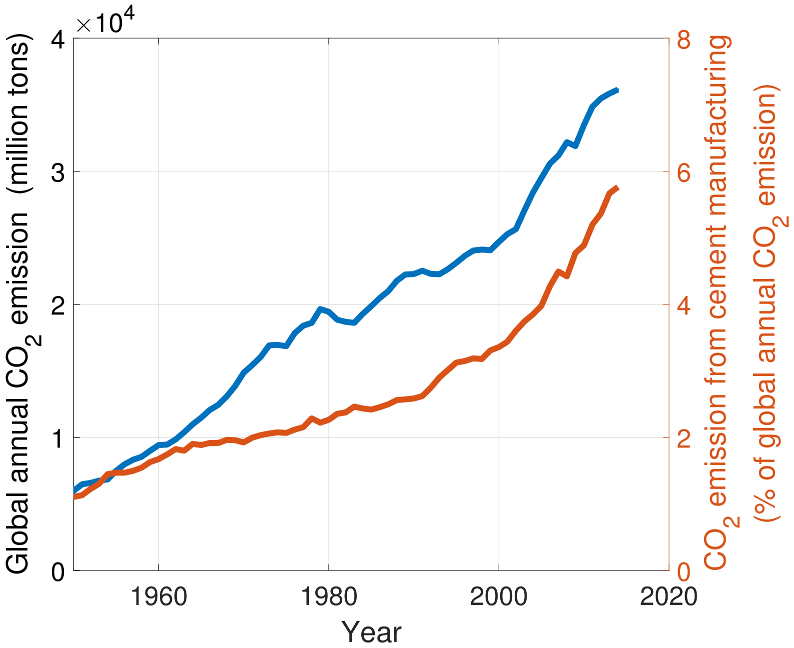

***Figure 1.1**: Total CO_2 emission from fossil fuel consumption and percentage of cement production emissions as part of the total worldwide emissions (Data from (Tom Boden, 2017)).*

involve the burning of raw materials at high temperatures, up to about 1500 °C.

It is estimated that about 0.8-1.0 ton of CO_2 is released per ton of Portland cement clinker produced, e.g., see (Oss and Padovani, 2002; Van Den Heede and De Belie, 2012). Figure 1.1 show the development of the global annual CO_2 emission from fossil-fuel consumtion, gas flaring and cement manufacture together with the percentage of the cement manufacturing contribution. The percentage of CO_2 emission from cement almost doubled from the year 2000 to 2014 going from about 3% to about 6%. This rapid increase is proportional to the increased cement production in the same period. This is despite the fact that the cement industry has had the focus on energy efficiency since the 1970's. This increased focus led to a significant increase in the efficiency of cement production plants, and increased focus on CO_2 emission in particular since 1999 (Scrivener et al., 2016). However, the efficient production methods have not been implemented worldwide. According to a report on potential, economically viable solutions for a low-CO_2, cement-based materials industry (Scrivener et al., 2016), the technology in the modern dry cement manufacturing plant have already reached a high level of energy efficiency and further improvement has been proved difficult. Of course, upgrading older plants and using alternative fuel is an obvious step to reduce the CO_2 emission. Cement clinker substitution and more efficient use of cement and concrete have been pointed out by (Scrivener et al., 2016) as the two main areas of focus for the next decades towards the reduction CO_2 emission from cement and concrete production.

Clinker substitution refers to the use of blended cements where parts of the Portland cement clinker is replaced with other materials. The term CO_2-reduced cement and the term cement-based binder-system are often used to denote some form of a blended cement. The replacement materials used for clinker substitution are either naturally occurring materials or waste and byproducts which in the presence of Portland cement can have cement-like properties. Some replacement materials need to be processed before use. For example, clay minerals need to be calcined. Replacement materials are commonly referred to as Supplementary Cementitious Materials (SCMs). Examples of SCMs, are limestone filler (crushed limestone powder), slag (a byproduct from steel production), fly ash (a byproduct in coal combustion plants), and silica fume (a byproduct of silicon production). The first use of SCM's can be dated to the Romans, who used a mixture of lime cement, which is burned limestone, and volcanic ash to join the stones in their buildings 5000 years ago (Malinowski and Frifelt, 1993). The mixing of lime cement with volcanic ash improved the lime cement durability and was the secret behind the survival of historical building like the Pantheon in Rome built in 125 AD.

As a part of the effort to reduce the CO_2 emission, significant amount of research in recent years is focusing on new combination of SCMs, e.g., see (Antoni, 2013; Fernandez Lopez, 2009), and to better understand the physical properties of blended cements, e.g., see (Moser et al., 2010; Lothenbach et al., 2011; De Weerdt et al., 2011; Meshgin and Xi, 2012; Scrivener et al., 2015; Saeidpour and Wadsö, 2015). The durability aspects introduced by the increased use of SCM's is of most importance. The presence of SCM's introduce major changes in the chemistry and microstructure of the final hydrated cement product (Lothenbach et al., 2011). These changes have an effect on the durability performance of concrete structures.

Concrete structures are in general very durable and can be expected to last for hundreds of years. However, in aggressive and potentially aggressive environments the concrete can deteriorate over time eventually leading to damages in the structure. For reinforced concrete structures, corrosion is the major degradation mechanism (Tuutti, 1982; Ahmad, 2003). Corrosion occurs as consequence of mass transport of moisture, ions and gases in the concrete cover.

Reactive transport models, e.g., (Samson and Marchand, 1999; Baroghel-Bouny et al., 2009; Hosokawa et al., 2011; Campos et al., 2016) can be used as a useful tool for a better understanding of the degradation mechanisms of reinforced concrete structures exposed to different service conditions.

This thesis contributes, among other things, to the improvement of a reactive transport framework model presented in (Jensen et al., 2014). A step towards a better understanding of some of the transport mechanisms related to moisture and gas transport in cement-based materials are taken. For example, a contribution to an improved description of mass transport in unsaturated systems and in changing environments, e.g., drying-wetting conditions have been obtained. The long-term durability of concrete structures needs, in general, a good model for its verification.

Summary

(i) The increasingly high demand for concrete products has led to a dramatic increase in Portland cement production which has resulted in that the portion of the total worldwide CO_2 emissions due to cement manufacturing has increased.

(ii) The process of Portland cement manufacturing is harmful to the environment. About one ton of CO_2 is released for each ton of Portland cement produced.

(iii) The use of clinker substitution to form new CO_2-reduced cement binders is one of the more effective paths towards a greener cement and concrete industry.

(iv) The long-term durability effect of using new CO_2-reduced cements is a major concern that needs to be studied.

1.2 Aim and scope

The overall aim of this project was to improve the understanding of the long-term consequences on durability by implementing new CO_2-reduced cements. Here, continuum-based numerical models for moisture and gas transport in porous media were established and integrated into the numerical framework for reactive transport modeling presented in (Jensen et al., 2014). The extended modeling framework developed can be used to estimate the long-term durability of concrete structures including new CO_2-reduced cements exposed to natural climate variations such as cyclic drying-wetting conditions, de-icing salt exposures and submerged marine conditions.

The main research objectives were:

(i) To understand important pore-scale vapor transport mechanism in unsaturated systems.

(ii) To experimentally investigate important moisture transport properties of ten different CO_2-reduced cement-based binder-systems.

(iii) To develop a method for determining a separate description of the effective diffusion in the liquid phase and in the vapor phase, accounting for sorption, that is, to develop a coupled two-phase transport model.

(iv) To describe and implement the gaseous transport in the air-filled space of the cement-based materials.

(v) To implement the chemical gas-liquid interaction into the existing multiphase reactive mass transport framework for durability estimation of cement-based materials presented in (Jensen, 2014).

(vi) To verify and demonstrate applications of the developed transport models.

1.3 Outline of the thesis

This thesis is divided into two main parts, an introduction and summary of the core topics of the thesis and three appended papers.

The background and relevant fundamentals of cement-based materials are presented in Chapter 1 and 2. Chapter 3 covers important properties of SCMs. Chapter 4 and 5 includes topics more directly related to reactive mass transport methods. A summary and the main conclusions of this PhD project are presented in Chapter 6. Table 1.1 provide an overview of the organization of the content in this thesis.

Table 1.1: *Organization of the thesis.*

Chapter	*Subject*	*Paper*
1	Introduction	
2	Fundamentals of cement-based materials	
3	Cement replacement materials	Paper II
4	Moisture transport	
	Vapor transport in unsaturated conditions	Paper I
	Moisture transport properties of CO_2-reduced cements	Paper II
5	Hybrid mixture theory	
	Reactive transport model including gas phase	Paper III
6	Research findings and conclusions	
A	Appendix	
Appended Papers		

Chapter 2

Fundamentals of cement-based materials

In this chapter some of the basic fundamentals of cement-based materials are covered in order to provide basic understating of the reactive nature of the material and how it can affect the long-term durability of concrete structures. The experienced concrete specialist might find most of the information in this chapter trivial.

A brief introduction section is followed by a short description of the manufacturing processes of Portland cement and their impact on the environment. The chapter also covers chemical and physical aspects of the hydration processes of Portland cement as well as a short introduction to the microstructure of hydrated cement and the durability of concrete structures.

2.1 Introduction

Although most of the research related to cement and concrete cannot be dated to more than 200 years ago (Johannesson, 2012). The increased focus on the use of byproducts and other natural latent hydraulic materials, such as calcined clay, in cement, is relatively recent within the past decades. The art of using cement and even the art of using latent hydraulic materials in lime-based materials is very old and can be traced back to ancient civilizations, such as Assyrians, Babylonians, Egyptians, and Greeks.

The most simple form of cement is pure lime, which is calcium oxide (CaO) also called burned lime. Pure lime is produced by roasting of limestone ($CaCO_3(s)$) at about 1000 °C. This chemical process is called calcination

$$\mathrm{CaCO_3(s)} \rightarrow \mathrm{CaO(s)} + \mathrm{CO_2(g)} \tag{2.1}$$

The calcination process results in the release of CO_2-gas from the chemical reaction (2.1) as well as from the heating process. About half the weight of the original limestone is transformed into CO_2-gas in the process. When pure lime is grind into fine powder and mixed with water, a slurry called slaked lime ($Ca(OH)_2$) is produced

$$\mathrm{CaO(s) + H_2O(l) \rightarrow Ca(OH)_2(s)} \tag{2.2}$$

As the slaked lime slurry starts to dry, it reacts with CO_2-gas from the atmosphere resulting in artificial hardened lime.

$$\mathrm{Ca(OH)_2(s) + CO_2(g) \rightarrow CaCO_3(s) + H_2O(l)} \tag{2.3}$$

This form of cement was typically used to join stones or bricks together in the ancient times. The main drawback of pure lime is that the hardened cement has poor strength and durability performance, especially in wet environments where the hardening reaction (2.3) can be slowed down or even reversed. It should be remarked that lime is not a hydraulic cement, that is, it does not react with water to form a hardening product. In the ancient times, lime cement was used together with volcanic ash. Volcanic ash is a latent hydraulic cement which by itself does not react with water. The relatively high pH of a lime slurry mixed with volcanic ash triggers the volcanic ash to react with water and forms a solid product with many similarities with modern hardened cement.

2.2 Portland cement

Portland cement is the most commonly used form of cement today. The name Portland cement was first patented about 200 years ago by the Englishman Joseph Aspdin. The overall idea behind Portland cement production is to burn a mixture of limestone and clay at a very high temperature then grind the resulting mixture into a fine powder of cement. An overview of the processes involved in the manufacturing of Portland cement is illustrated in Figure 2.1. The first step in the manufacturing process is the collection of raw materials containing calcium and silica. Cement manufacturing plants are often located nearby limestone or chalk quarries. Clay, sand and shale are examples of raw materials containing silica which are readily available. Prior to burning, the raw materials are crushed and grind into fine powder to optimize the burning process. The raw materials are mixed to obtain a weight percentage of about 70% limestone, $CaCO_3$, 20% quartz sand, SiO_2, and 10% clay rich in alumina and iron oxides. Other materials such as fly ash

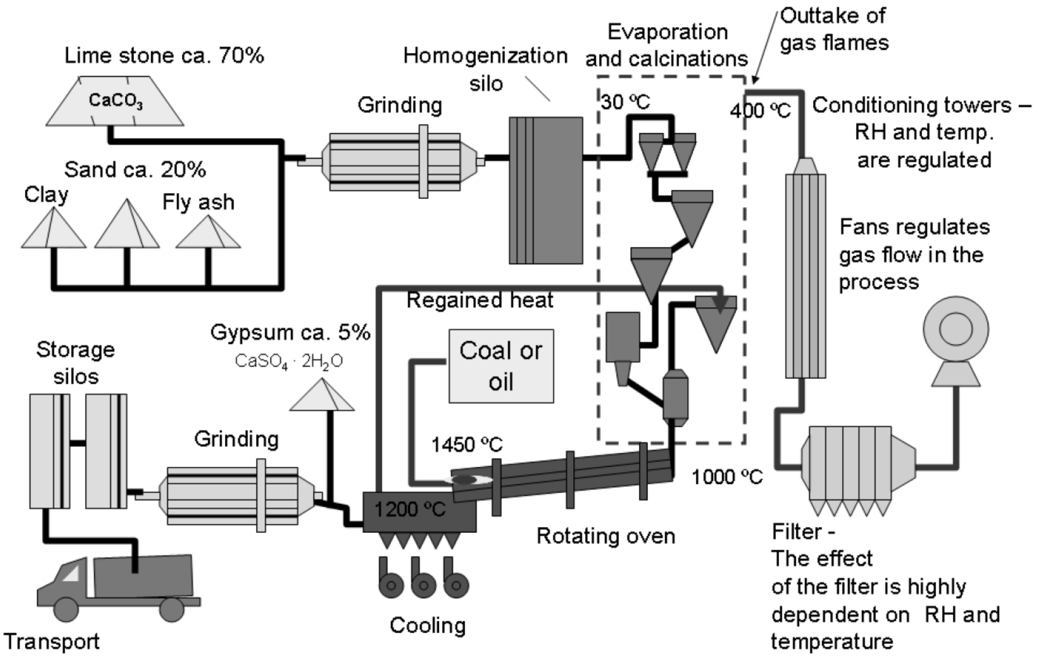

***Figure 2.1**: Simplified schematic flow chart of the dry process of manufacturing of Portland cement (after (Johannesson, 2012)).*

can be used to reach the correct chemical composition of the raw material. The mixed raw material is burned at different temperatures, first in the calcination chambers reaching a maximum temperature of about 1000 °C, then in the rotary kiln where the maximum temperature is about 1500 °C. The two main reactions in the calcination chambers are the calcination of limestone and the decomposition of clay minerals (Clay→ 'Meta' clay + H_2O (g)). In the rotary kiln the calcined raw materials react at very high temperatures forming the Portland cement clinkers, where the most important reactions are between SiO_2 and the free lime CaO. The final steps of the production are the cooling process followed by the grinding of the cement clinkers into fine cement power. The main clinker phases of the cement powder are listed in Table 2.1. The belite and alite phases are formed in the rotary kiln at high temperatures, and the aluminate and ferrite phases are formed during the cooling process, as illustrated in Figure 2.2. A small amount of gypsum is usually added to the cement in order to regulate the setting time of the aluminate phase. An example of a typical weight percentage of the different oxide phases in a cement type I is provided in Table 2.1.

Table 2.1*: The main Portland cement clinkers and a typical weight percentage of cement types I according to (Mindess et al., 2003).*

Clinker phase	Oxide composition	Oxide notation	weight percent
Alite	$3CaO{\cdot}SiO_2$	C_3S	55
Belite	$2CaO{\cdot}SiO_2$	C_2S	18
Aluminate	$3CaO{\cdot}Al_2O_3$	C_3A	10
Ferrite	$4CaO{\cdot}Al_2O_3{\cdot}Fe_2O_3$	C_4AF	8
Gypsum	$2(CaSO_4{\cdot}2H_2O)$	$C\overline{S}H_2$	6
Impurities			3

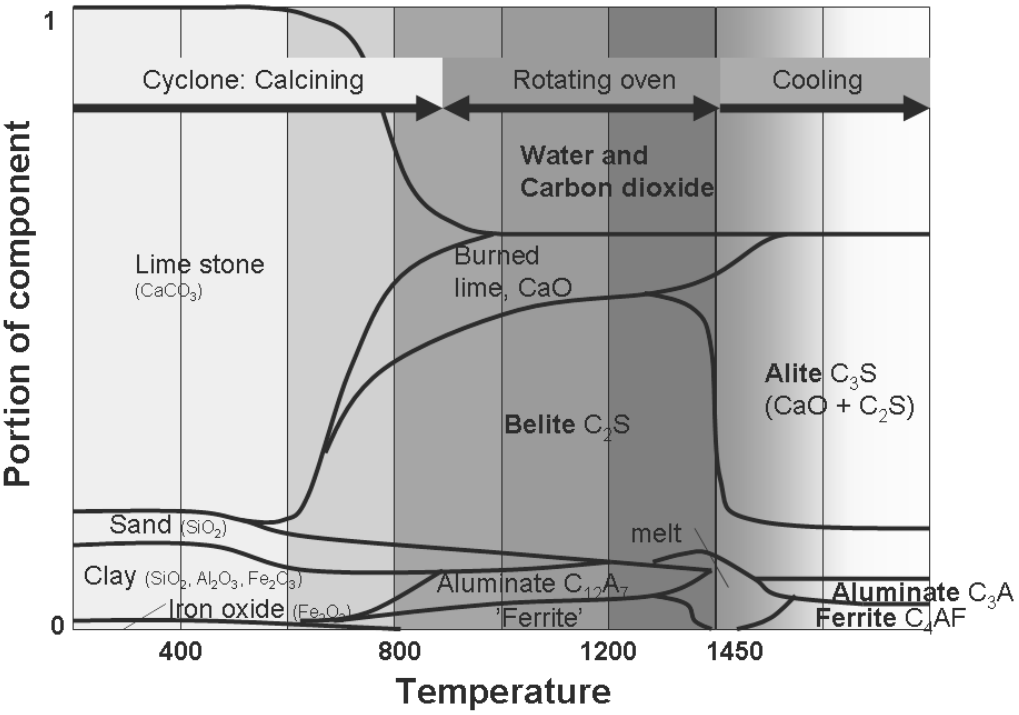

Figure 2.2*: A schematic illustration of the clinker phase formations during Portland cement manufacturing process (after (Johannesson, 2012)).*

2.3 Hydration processes

In order to understand and apply reactive transport models to estimate the durability of concrete, it is crucial to have some understanding of the reaction mechanism forming the cement hydration products as well as a general idea about the microstructure of hardened cement.

The term hydrate is used in chemistry to indicate that a substance contains water. Consequently, anhydrous substance contains no water. Portland cement in its powder form is anhydrous, but when it is mixed with water, the hydration process of the cement clinkers starts to form the so-called hydration products. The hydration process of cement is an inorganic chemical reaction where water reacts with the cement mineral phases of dry cement powder over time creating a solid product. The hydration process of Portland cement is very complex since water reacts with all the different cement minerals, e.g., C_3S, C_2S, C_3A, C_4AF and $C\overline{S}H_2$, at the same time but with different reaction rates forming a mixture of different hydration products. The hydration process of cement consists of two main stages, a setting stage and a hardening stage. The hydration during the setting or stiffening stage starts from the time the cement and water are mixed together and continues to react for a few hours depending on the surrounding environment and the cement properties. During the setting stage, the fresh past slowly gets stiffer without a significant strength development. The setting stage is followed by a hardening stage where most of the strength development occurs. The hydration processes during the hardening stage get slower with time. After about a week of hardening, the hydration reaches a semi-steady state condition in which the hydration process slowly can continue for many years. The changes occurring to the hydration products at the semi-steady state condition are the main focus related to the type of durability model developed in this thesis.

Main products of cement hydration

Hydrated Portland cement mainly consists of calcium silicate hydrate gel (C-S-H gel), portlandite, ettringite and a family of hydrated calcium aluminate hydrate often denoted AFm, (Balonis, 2010). A short description of the chemistry and structure of the main hydration products is covered in this section. More detailed description of the chemical reactions of each cement mineral is available in, e.g., (Taylor, 1997; Mindess et al., 2003; Johannesson, 2012).

During the setting stage, the first and fastest hydration reaction occurs between the water, gypsym ($C\overline{S}H_2$) and alumina from either the aluminate phase, C_3A or the ferrite phase, C_4AF . These reactions lead to the formation of a crystalline trigonal needle-shaped phase called ettringite, C_6AH_{32}. Using the short oxide notation from Table 2.1, the reaction with the aluminiate phase can be expressed as

$$C_3A+3C\overline{S}H_2+26H\rightarrow C_6A\overline{S}_3H_{32} \tag{2.4}$$

Here H is a short notation for H_2O. The reaction above is responsible for the early stage heat release. The ettringite formation is considerably fast since the dissolution of alumina and gypsum happens very fast at the start of the hydration process. The dissolution of alumina and gypsum can be written as

$$\mathrm{C_3A{+}C\overline{S} + 6H \rightarrow 4Ca^{2+} + 2Al^{3+} + 12OH^{-} + SO_4^{2-}} \tag{2.5}$$

where $\mathrm{C\overline{S} = CaSO_4}$. The dissolution reaction creates a solution with a very high pH, that is, a high concentration of $\mathrm{OH^-}$ ions. When all the available gypsum is consumed, part of the ettringite phases become unstable and react with the remaining $\mathrm{C_3A}$ phase to form a crystalline structure family named AFm. AFm is short notation for a family of calcium aluminate hydrate phases with a general formula of $\mathrm{[Ca_2(Al,Fe)(OH)_6]{\cdot}X{\cdot}xH_2O}$, where X is an ion and x is the number of water molecules (Balonis, 2010). Example of AFm phases are monosulfoaluminate ($\mathrm{SO_4 - AFm}$) and monocarboaluminate ($\mathrm{CO_3 - AFm}$). If nitrate and nitrite are present, e.g., from chemical admixtures, then nitrate and nitrite AFm can be formed. The function of the added gypsum in the cement is to curb the fast reaction between alumina phases and water. The formation of AFm phases from ettringite can be reversed in the presence of sulfate, leading to delayed etteringite formation.

The reaction between the ferrite phase, water and gypsum can be expressed as

$$\mathrm{C_4AF{+}3C\overline{S}H_2{+}30H{\rightarrow}\ C_6(A,F)\overline{S}_3H_{32} + (A,F)H_3{+}CH} \tag{2.6}$$

where (A,F) indicates that Fe ions, when present, can replace Al ions. The reaction between water and gypsum with the ferrite phase is considerably slower than the one with the aluminate phase and does not result in the same amount of heat release. The term AFt (aluminate-ferrite-trisubstituted) is often used to refer to the family of ettringite phases. Reaction (2.6) also includes the formation of calcium hydroxide, CH, also called portlandite.

Portlandite is a crystalline phase structured in layer of octahedral shapes. CH is mainly formed together with calcium-silicate-hydrate, C-S-H, as a hydration product primarily from the alite phase, $\mathrm{C_3S}$, and to a lesser extent, the belite phase, $\mathrm{C_2S}$. CH and C-S-H are considered the two main hydration products of Portland cement. The hydration reaction between alite or belite and water is not well defined mainly because the amount of bound water by the C-S-H is not stoichiometrically fixed. The relation between calcium silicate and water in C-S-H varies depending on different conditions. The hydration reaction of $\mathrm{C_3S}$ can be simplified as follows

$$\mathrm{C_3S}{+}(y+z)\mathrm{H} \rightarrow \mathrm{C}_x\mathrm{SH}_y{+}z\mathrm{CH} \tag{2.7}$$

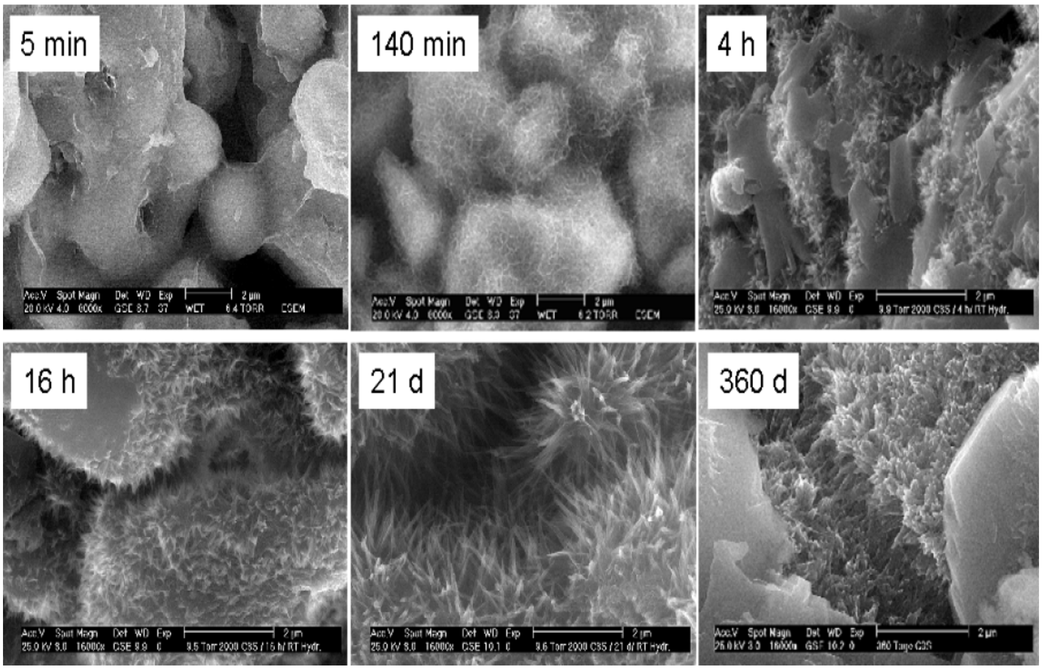

Figure 2.3: *Scanning electron microscopic images (SEM) of the hydration of C_3S after 2, 4, 24 an73 hours of hydration (after (Sato and Diallo, 2010)).*

where x, y and z can be integers or fractions. The composition of C-S-H can vary in terms of C/S ratio (Ca/Si ratio) represented by x, and H/S ratio (H_2O/Si ratio) represented by y. The hydration reaction of C_3S starts almost instantaneously after mixing the cement clinker with water with the dissolution of ions from the surface of C_3S. Similar to the dissolution reaction of alumina and gypsum (2.5), the dissolution of the surface of the cement powder grains leads to a high OH^- concentration in the solution close to the grain surface which triggers the formation of the C-S-H phase on the cement grain surface and later the formation of the CH crystalline phase occur on top of the previously formed C-S-H. Figure 2.3 shows a scanning electron microscopic images (SEM) of the hydration products of a pure C_3S phase cured at room temperature and 100% relative humidity (Sato and Diallo, 2010). It can be seen in Figure 2.3, how the formation of the fibrous C-S-H gel grew over time and became more and more amorphous like. The formation of the first clear CH crystalline structure is first observed after 24 hours of hydration in this example.

More complex forms of C-S-H are reported in the literature, e.g., C-A-S-H can be formed where alumina is built into the C-S-H structure (Hong and Glasser, 1999). In the same principle manner, M-S-H gel can be formed if magnesium is present (Brew and Glasser, 2005).

A simplified hydration reaction for the belite phase can be expressed in a similar way as the alite phase

$$C_2S+(y+z)H \rightarrow C_xSH_y+zCH \tag{2.8}$$

The hydration of C_2S occurs as one of the later stages of the overall hydration process before the semi-steady state hydration is reached.

A very rough approximate order of hydration of the main clinker phases is $C_3A > C_3S > C_4AF > C_2S$. The chemical reaction, as well as the exact reaction rates of the individual cement clinker phases in a Portland cement, are to this day still not fully understood, e.g., see (Luc et al., 2018). Thermodynamical databases for cement hydration reactions are under constant development, e.g., CEMDATA07 (Möschner et al., 2008, 2009; Schmidt et al., 2008; Lothenbach and Winnefeld, 2006; Lothenbach et al., 2008) and CEMDATA14 (Lothenbach et al., 2012; Kulik, 2011; Dilnesa et al., 2011, 2012, 2014).

An important factor affecting the reaction rate of cement clinker phases is the fineness of the cement powder. The product description of cement often includes the fineness of the cement in terms of the specific surface area, and the clinker phase composition or the oxide composition. The oxide composition can be determined experimentally, e.g., using X-ray diffraction (Redler, 1991). The clinker composition is calculated from the experimentally determined oxide composition using the Bogue equation.

Cement admixtures

Admixtures are used in cement in order to adjust the properties of the fresh or/and hardened cement. Clinker replacement with SCMs is also considered as a form of admixture since the replacing materials will change the properties of the fresh and/or the hardened blended cement. Admixtures can be categorized in according to their functionality, for example:

(i) Air-entraining admixtures are used to create small stable air bubbles in the mixing process. When water in the pore system of cement freezes and transform to ice it expands in volume by approximately 9% (Litvan, 1972), which can lead to cracks in the hardened cement-based material. The air bubbles introduced by the air-entraining admixture act as a pressure absorbent in the hardened cement or concrete during freeze/thaw conditions.

(ii) Water-reducing admixtures are used in order to obtain satisfying workability and setting times for concretes with low water to binder ratios.

Lowering the water content in concrete is often desired since it results in higher strength and lower permeability.

(iii) Retarding/accelerating admixtures are used to either slow down or accelerate the setting time and the early hydration of the main cement clinker compound C_3S.

Admixtures can be categorized into two major groups:

(i) Chemical admixtures are synthesized surface active chemical agents designed to improve a specific property, e.g., the fluidity of the concrete and/or create air bubbles in the hardened product. For example, a chemical superplasticizer, called Glenium sky 631, was used to adjust the fluidity in the mix design of mortar in the CO_2-reduced cement investigated in Paper II.

(ii) Mineral admixtures:

  (a) Latently hydraulic, meaning that they contain reactive substances that can react in the presence of the cement clinker phases. Examples of latently hydraulic minerals included in this study are fly ash, calcined clay and burnt shale.

  (b) Non-hydraulic filler materials such as limestone filler.

The role of mineral admixtures as cement-replacing admixtures is of importance to this study. Section 3 addresses some of the properties of pozzolanic materials with the focus on the cement-replacing materials.

2.4 Pore structure of hydrated cement

The microstructure of hydrated cement-based materials is very complex. Some understanding of the microstructure of hydrated cement-based materials is of vital importance when describing the mass transport since many properties can, at some level, be related to the microstructure. The altering of microstructure due to the use of replacement materials have a significant effect on moisture transport properties, e.g., (Saeidpour and Wadsö, 2015, 2016), changed permeability and its effects on chloride ingress, e.g., (Thomas and Bamforth, 1999; Maes et al., 2012) and carbonation resistance, e.g., (Van Den Heede and De Belie, 2014; Mo et al., 2016; Shi et al., 2016).

The development of the microstructure starts from the time cement is mixed with water and continues to develop during the early and late hydration stage. The resulting microstructure consists of a heterogeneous mixture

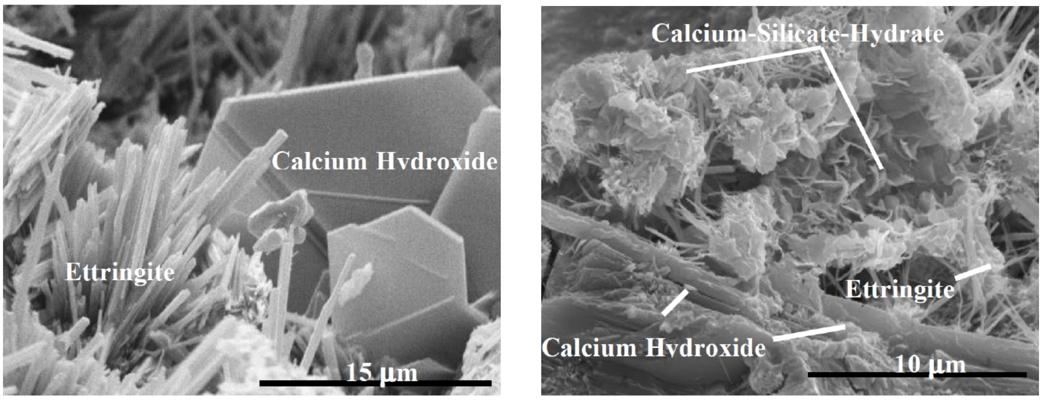

Figure 2.4: *SEM of hardened cement paste at earlier age where large voids are available for the growth (left) and after 7 days where the space is more limited (right) (after (Stutzman, 2000)) .*

of the multiple components representing different hydration products as well as unhydrated materials. The volume and shape development of hydrated products over time results in a more packed and complex microstructure, e.g., see Figure 2.4.

The level of complexity in the microstructure increases even further when cement-replacing materials are used. This is partly due to different reaction rates and degrees of hydration of the different replacing materials and that porous portlandite structure formed from the Portland cement reactions transforms into C-S-H in the presence of pozzolans. Another factor is the increased amount of unhydrated and unreacted materials of various shapes and sizes having a filling effect which affects the microstructure. Figure 3.1 illustrate schematically how the microstructure develops in a cement-pozzolan system as a result of different reactivity and reaction rates as well as unreacted pozzolan particles. Many of the illustrated mechanisms in Figure 3.1 are still under debate.

The type of pores and the connectivity between the pores are of most importance to mass transport properties of the material. The pores in a hydrated cement vary in type and size with the smallest pores in the nanoscale, in between the hydrated grans, and the largest pores up to few millimeters, often caused by entrapped air voids during mixing (Kosmatka et al., 2002). The pores within cement and concrete are often classified into two major types according to their size and the way they have been formed, that is capillary pores and gel pores (Powers and Brownyard, 1947; Mindess et al., 2003). Capillary pores are the larger pores initially filled with water or air and gel pores are present in the inner or outer layers of the formed cement gel. Gel pores have a much smaller pore size but can occupy significant volume (Jennings, 2008). There is no clear distinction in the literature between the size limit between capillary and gel pores. The characteristics of the two pore types are related to their properties and how they are formed. According to (Jennings, 2008) most of the mass transport processes affecting the durability occurs in the capillary pores. This was one of the main reason why a special study was performed in this thesis with the aim to increase the understanding of some of the mechanisms of vapor transport at the capillary pore scale, see Paper I.

2.5 Concrete durability

The innovation of steel reinforcement of concrete is what made concrete the most used building material. Today the demands on concrete durability assessment are very high as reinforced concrete structures are exposed to a vast variety of aggressive environments, e.g., marine, acidic liquids and gases, nuclear radiation and cyclic conditions of various kinds. The exposure of concrete to aggressive environments can lead to the failure of concrete before the expected lifetime. A detailed description of cement degradation processes can be found in, e.g., (Taylor, 1997; Johannesson, 2012; Alexander et al., 2013). The degradation processes associated with long-term durability estimations are the ones occurring after the main initial cement hydration stages. The long-term degradation processes are a result of mass transport of ions and gases through the concrete pore structure and the chemical changes they introduce by reaction with the hydrated cement. This is the reason why reactive transport models are essential tools for concrete durability estimations. Examples of the most important long-term degradation process associated with concrete durability are chloride penetration and carbonation.

Chapter 3

Cement replacement materials

Various applications of replacing Portland cement with different pozzolans have been widely investigated, e.g., see (Mehta, 1981; Massazza, 1993; Lothenbach et al., 2011; Ramezanianpour, 2014a). Pozzolanic materials are used as a substitution to Portland cement in order to reduce the CO_2 emission and reduce the cost. Other applications exist, e.g., improve the permeability and reduce the early stage heat evaluation. It is well known that the use of pozzolans also introduces challenges, for example, reducing the early age strength. Here some of the general properties of pozzolanic materials are covered with the main focus on fly ash, calcined clay, burnt shale and limestone filler. These materials are the cement-replacing materials used in the 10 different binders-systems investigated experimentally in this study (Paper II).

3.1 Pozzolans

A pozzolan is a latent hydraulic material with no or very little cementitious properties in its self but can in the presence of calcium hydroxide solution trigger a pozzolanic reaction. Fly ash, calcined clay, burnt shale and limestone filler can be classified as pozzolans. In general, pozzolanic material can be categorized into two major groups, which are:

(i) Natural pozzolan: Materials rich in silica and alumina such as volcanic ash.

(ii) Artificial pozzolan: Artificial pozzolans are either materials that need treatment to get pozzolanic properties or waste products with pozzolanic properties. Calcined clay, burnt shale, and fly ash are examples of artificial pozzolans.

***Table 3.1**: The oxide composition of included SCMs and the K1 cement clinker measured by XRF (Geiker et al., 2017).*

	Fly-ash	Calcined clay	Limestone filler	Burnt Shale	K1 clinker
CaO	0.82	4.48	44.03	30.13	65.39
SiO_2	62.51	55.04	12.7	34.24	20.17
Al_2O_3	16.64	19.92	3.57	8.25	5.52
Fe_2O_3	9.38	5.53	1.85	4.81	3.97
SO_3	0.37	0.38	0.44	5.56	1.55
MgO	2.95	1.81	0.60	5.59	0.80
TiO_2	2.82	2.16	0.58	4.38	0.54
Na_2O	1.95	1.12	0.23	0.11	0.21
TiO_2	0.93	0.9	0.24	0.48	0.28
P_2O_5	0.15	0.53	0.20	0.15	0.26
Cr_2O_3	0.02	0.02	0.01	0.02	0.01
Cl	0.03	0	0.21	0.29	0.03
LOI	2.39	3.20	35	4.55	0.24
Total (%)	100.96	95.09	99.66	98.56	98.97

A pozzolanic reaction is a reaction between the pozzolanic material and the calcium hydroxide solution. The reaction forms cement-like hydration products. The reactivity of pozzolanic materials is usually related to the amount of glassy amorphous material present in the pozzolan. The chemical composition of pozzolanic materials can vary a lot depending on their origin. The oxide compositions of the pozzolanic materials used in this study are given in Table 3.1, which also includes data for one of the used cement clinkers in this thesis, that is, an ordinary rapidly hardening cement clinker.

Pozzolanic reactions are in general slower than the Portland cement hydration. The use of pozzolans often results in changed properties, e.g., slow early age strength development which often is compensated by a higher long-term strength. The resulting hydration products of pozzolan-cement mixtures are in many ways similar to Portland cement hydration products. Hydration products like C-S-H, ettringite and monosulfoaluminate are produced in a pozzolanic reaction. The hydration process of pozzolan-cement mixtures is however very complex partly due to the difference in reactivity and in reaction rates between different pozzolans and its interaction with the pure Portland cement. Figure 3.1 illustrates the complexity of the hydration mechanisms and interaction between (a) pozzolan and C_3S clinker phase and

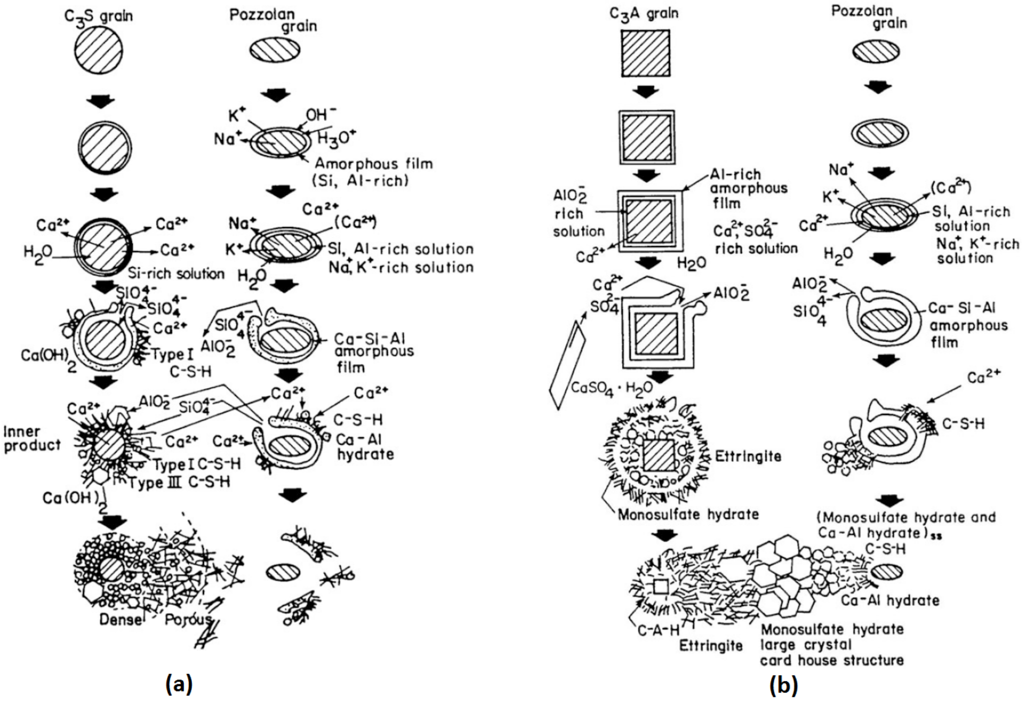

(a) (b)

Figure 3.1: *Schematic illustration of the hydration mechanisms of pozzolans with (a) C_3S and (b) C_3A (after (Takemoto and Uchikawa, 1980)).*

(b) a pozzolan and C_3A clinker phase.

The physical properties of a pozzolan, e.g., fineness, specific surface area, density and the shape of particles, vary widely which affects the reactivity of pozzolans and, therefore, the properties of fresh and hardened concrete are affected. Pozzolan's physical properties can both have positive and negative effects on the properties of fresh and hardened concrete, e.g., consistency, workability and setting time. For example, the workability of fresh concrete is often improved if the used pozzolans particles are round and smooth in shape, e.g., fly ash particles (Ramezanianpour, 2014a). In contrast, the effects on workability are negative if the pozzolans particles shape is irregular and rough, e.g., calcined clay which often require the use of chemical admixtures for improved workability.

The durability of cement-pozzolan systems, as for any binder-system, depends on the chemical and physical properties of the system as well as the service environment. In general, it is believed that especially when higher replacement rates are used, the durability at early age suffers mainly due to higher permeability at this stage. The slow pozzolanic reaction, together with the amount of un-reacted pozzolan has a negative effect on the permeability. A high initial permeability means that, for example, ions from seawater splash zones can penetrate the concrete cover easier which means that the chloride, sulfate and carbonation resistance is weakened at early ages for this case. The later age durability of pozzolan-cement systems are in most cases reported being improved. Longer curing time allows the pozzolanic reactions to progress leading to decrease in the porosity and the permeability of the system (Ramezanianpour, 2014a).

3.2 Fly ash

Fly ash is the name of the dust collected in electro-static filter in the process of coal combustion. The first use of fly ash in blended Portland cement was reported in 1937 (Davis et al., 1937). About 33% of the world production of fly ash was utilized in 1992, about 50% of it was used in cement and concrete (Manz, 1997). The total production of fly ash worldwide today is around 900 Mt/year and yet only about 1/3 is utilized (Scrivener et al., 2016).

Fly ash particles are characterized by a spherical shape and range in particle size from about 1μm to 150 μm depending on the source, with an average size about 10-15μm (Ramezanianpour, 2014b). The specific surface area also varies a lot depending on the source, from about 100 m^2/kg up to 1500 m^2/kg (Ramezanianpour, 2014b). The chemical composition and quality of fly ash also varies depending on the source. In general, the major oxide components of fly ash are SiO_2, Al_2O_3, Fe_2O_3 and CaO. Fly ash is classified as siliceous fly ash or low-calcium fly ash if the content of CaO is less than 10% and reactive SiO_2 and Al_2O_3 are the two main components. Siliceous fly ash has pozzolanic properties meaning it requires the presence of $Ca(OH)_2$ to hydrate and form strength-developing products. Fly ash with CaO content higher than 10% have both pozzolanic properties and hydraulic properties. This type of fly ash is called calcareous fly ash or high-calcium fly ash.

The use of fly ash is, in general, reported having positive long-term effect on the durability of reinforced concrete. In Denmark, cement products containing about 20wt% siliceous fly ash are often used in concrete constructions in aggressive environments (Geiker et al., 2017). The long-term durability of concrete containing siliceous fly ash was used in seven out of the ten binder-systems investigated in Paper II of this thesis. The oxide composition of the fly ash used is shown in Table 3.1.

3.3 Calcined clay-rich minerals

The availability of good quality fly ash is becoming a limiting factor in several locations, e.g., in Denmark, where the goal is to close all coal combustion plants by 2030 as a part of the green transaction. This is one of the reasons why the use of calcined clay-rich minerals as a replacement material is of interest due to their unlimited availability as the most abundant type of mineral on earth. The activation of clay-rich minerals requires heat treatment at a temperature around 600-800 °C. The CO_2 impact of the calcination process is lower than the impact of Portland cement production, thus it is beneficial for the environment to use calcined clay minerals as a cement replacement material. The use of calcined clay for cement replacement has been in use for a long time in some countries such as India and Brazil (Scrivener, 2014).

The calcination treatment breaks down the layered structure of clay or shale resulting in a more reactive pozzolanic material. The calcination process occurs under controlled conditions, which allow the properties of the treated minerals to be optimized to some extent. The physical and chemical properties of calcined clay or shale strongly depend on the origin, but some properties can be adjusted during the treatment process. In general, the oxide components of calcined clay-rich minerals are dominated by SiO_2 as the major component followed by Al_2O_3 for pure clay, or CaO for some types of shale as the one used in this study. The chemical properties and the reactivity of calcined clay are commonly reported to be higher than the reactivity of fly ash, e.g, see (Ferreiro et al., 2017). The particle size of calcined clay-rich minerals is often about one order of magnitude smaller than that of fly ash, while the surface area often is one order of magnitude higher (Ramezanianpour, 2014b).

3.4 Limestone filler

Most of the produced Portland cement contains small amounts of limestone up to about 5 wt%. The use of limestone filler in combination with other SCMs, e.g., calcined clay or shale and cement clinker can be of great benefit and is considered one of the most promising mixture combination of SCMs (Scrivener, 2014). When limestone filler is combined with SCMs with high alumina content, the calcium carbonate from the grind limestone filler can react with the alumina phases and calcium hydroxide from the cement clinker to form calcium aluminate carbonate hydrates, which has so-called filling properties making the material denser (Scrivener, 2014).

Summary

It is evident that the use of pozzolans in cement binder-systems adds another level of complexity to the chemical and physical properties of concrete. Despite extensive research, the action of the pozzolans used in Portland cement is yet not fully understood. For each new combination of SCMs general trends can be predicted from previous research results, however, the specific properties still need to be further investigated using specific experiments and numerical investigations. As a part of this PhD study, moisture transport properties of nine new pozzolanic binder-systems and a reference-binder were investigated in Paper II. The binder composition of eight of these binder-systems has a clinker replacement of 35 wt% and one has a replacement level of 40 wt%. The materials tested included combinations of fly ash, limestone filler, calcined clay and burnt shale. See Table 2 in Paper II for the detailed binder compositions.

Chapter 4

Moisture transport

The moisture state of unsaturated porous materials, e.g, cement-based materials, is rarely in equilibrium due to internal moisture transport processes and variation in the surrounding conditions. Moisture transport in concrete plays an important role in multi-species transport in concrete, especially during drying and wetting conditions. It is crucial to have good knowledge of the physical processes behind moisture transport and how they are coupled to multi-species transport and chemical interaction in cement-based systems in order to evaluate if new binder-systems can perform good in the long time perspective, that is, more than 100 years.

One way to gain more knowledge about moisture transport properties in general and in cement and concrete in particular is to establish physically based numerical models which are tuned against a number of different laboratory controlled experimental results. If such models can be successfully verified by short-term experiments, the models can be used to better predict the performance of different concrete mixtures during its expected lifetime.

Moisture transport properties of ten CO_2-reduced binder-systems, included in this thesis, where established through experimental investigations and inverse numerical modeling as detailed in Paper II. This chapter contains more detail to some of the experimental investigations which were omitted in Paper II in order to focus more on the developed inverse analyses method. Here also a brief description of relevant moisture transport properties in saturated and unsaturated conditions is provided. More detailed description of moisture transport properties can be found in, e.g., (Johannesson, 2012; Jennings et al., 2002; Baroghel-Bouny, 2007b,a).

4.1 Saturated conditions

Mass balance conditions are the basis for all moisture transport models in porous media, such as concrete. In the type of continuum flow model adopted in this thesis, three main mass transport processes are of importance for the mass balance in saturated systems, that is, (i) liquid water transport, driven by capillary suction due to surface tension, (ii) diffusion of ions in the liquid phase, driven by the ionic concentration gradient, and (iii) migration of ions in the liquid phase, driven by the electrical field. The transport of liquid water is commonly governed by different forms of Darcy's law where the pressure gradient is used as driving potential, or as in this work, the volume fraction. The correctness of using a modified Darcy law where the volume fraction of liquid water in a porous material is the driving potential for flow is derived in (Bennethum and Cushman, 2002a, 1996). The diffusion of ions in the liquid phase is commonly described by some form of Fick's law where the concentration gradient is the driving potential. The migration of ions in the liquid phase due to the electrical field is commonly described using the Nernst-Planck equation. In the reactive transport model described in Paper III and in Chapter 5 of this introduction, the ionic diffusion and electro-migration of ions are governed using a modified version of the Poisson-Nernst-Planck (PNP) system of equations.

4.2 Unsaturated conditions

In unsaturated conditions, the mass balance and transport mechanisms are more complex than the saturated case and can not be described by mass transport in a single-phase. Mass transport processes of the water vapor and other gases in the air filled space (gas phase) needs to be considered, in addition to mass transport processes within the liquid water phase.

In concrete, the transport processes of gaseous species in the gas phase are mainly driven by diffusion due to pressure or concentration gradients. The diffusion of gases in the air filled space of the concrete can be described in a similar manner as for ionic diffusion in the liquid phase as detailed in Paper III. The chemical interaction between the liquid and gas phase can also be accounted for in the model presented in Paper III.

Water vapor transport behavior needs special attention, since it occurs both through the air filled pores and the partly saturated pores in the presence of a relative humidity gradient on both sides of trapped liquid water meniscus in the pore system, see Figure 4.1. In fact, it is concluded from experiments that water vapor transport trough partly saturated pores is faster

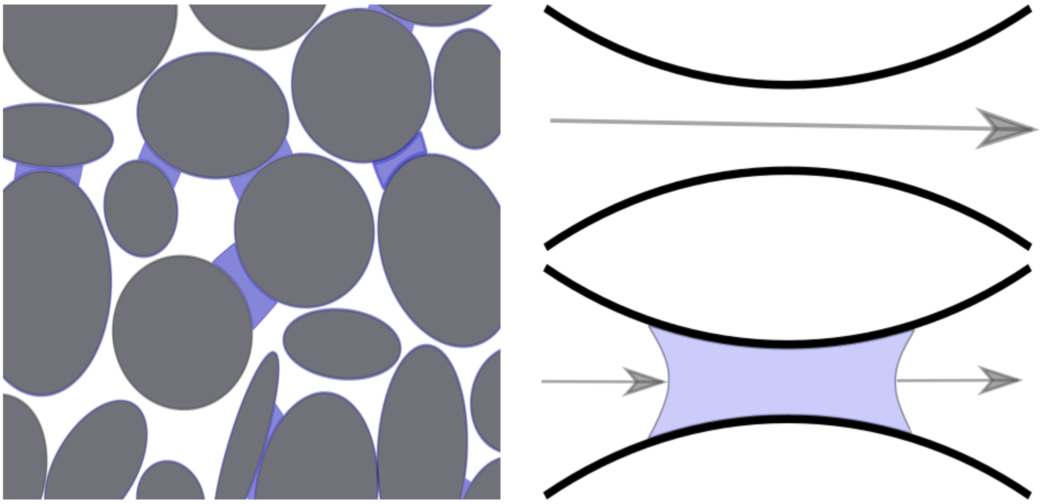

Figure 4.1: *Simplified illustration of partly saturated pore system showing trapped liquid in the meniscus between the grains (right), together with an illustration of the path of water vapor transport with and without trapped liquid (left).*

compared to water vapor transport through air-filled pores. This is because water vapor condensate on the one side of the liquid meniscus and immediately evaporate on the other side, thus the liquid in the meniscus shortens the distance of transport for water vapor, as illustrated in Figure 4.1. The interaction between liquid water and water vapor transport in terms of enhanced transport in unsaturated capillary pores was previously described in (Shahraeeni and Or, 2010, 2012) using a very complex model including a detailed description of surface tension and contact angle as well as many other parameters including fitting parameters. The development and validation of a conceptually simple model explaining water vapor transport mechanisms at the pore scale is the subject of Paper I. The developed model provides a simple but accurate description of vapor in unsaturated capillary pores only using the geometry and the relative humidity at the vapor-liquid interfaces. Paper I also demonstrates the general advantages of using the chemical potential (or relative humidity) as the driving potential when modeling vapor flow.

Due to the complexity of the microstructure of cement-based materials, it is not possible to determine the exact geometry and the relative humidity variations at the pore scale. In stead, a theoretically sound coupled two-phase smeared continuum description of the liquid water and water vapor transport by (Johannesson and Nyman, 2010) was adopted. In this two-phase continuum model, presented in Paper II, the knowledge from the enhancement effect on vapor diffusion, discussed in Paper I, was used to motivate the non-intuitive choice of constituting an increase of the vapor diffusion parameter with increased water content. The moisture transport model requires a description of the sorption isotherms as well as a separate description of the effective diffusion of the liquid water phase and the water vapor phase as detailed in Paper II.

4.3 CO_2-reduced binder-systems

Important moisture transport properties of CO_2-reduced binder-systems where established through a number of experimental investigations and inverse numerical modeling as explained in Paper II. The experiments were designed to measure all the material constants and moisture transport parameters needed for the reactive mass transport durability model described in Chapter 5 and Paper III.

As detailed in Paper II, it is not always possible to measure the needed moisture transport properties directly. The problem is that the moisture transport and sorption processes are always coupled and non-linear. With the complexity of the microstructure of concrete there is no way to decouple the transport process from the sorption process during an experiment. The sorption process itself is simpler and can quite well be isolated in an experiment, see Paper II.

The compositions of the CO_2-reduced binder-systems is to be found in Table 2 of Paper II. The following sections in this chapter contain a brief description of the main experimental moisture fixation and moisture transport investigations together with additional data not included in Paper II.

Sorption measurements

As stated earlier, the vapor sorption process itself can quite well be isolated in an experiment. Here, a Dynamic Vapor Sorption instrument (DVS) was used to measure the drying and wetting boundary sorption isotherms of the included ten binder-systems of Paper II. Figure 4.2 shows a schematic illustration of the set up for a DVS instrument. The DVS instrument mixes dry and saturated vapor at desired proportions using very accurate flow regulators and in this manner, a given relative humidity is generated. A slow flow of the mixed dry air and saturated vapor passes a symmetrical balance system with very high accuracy.

After a 90 days curing period, saturated powders of the cement paste samples were used for the measurement where a drying program was followed

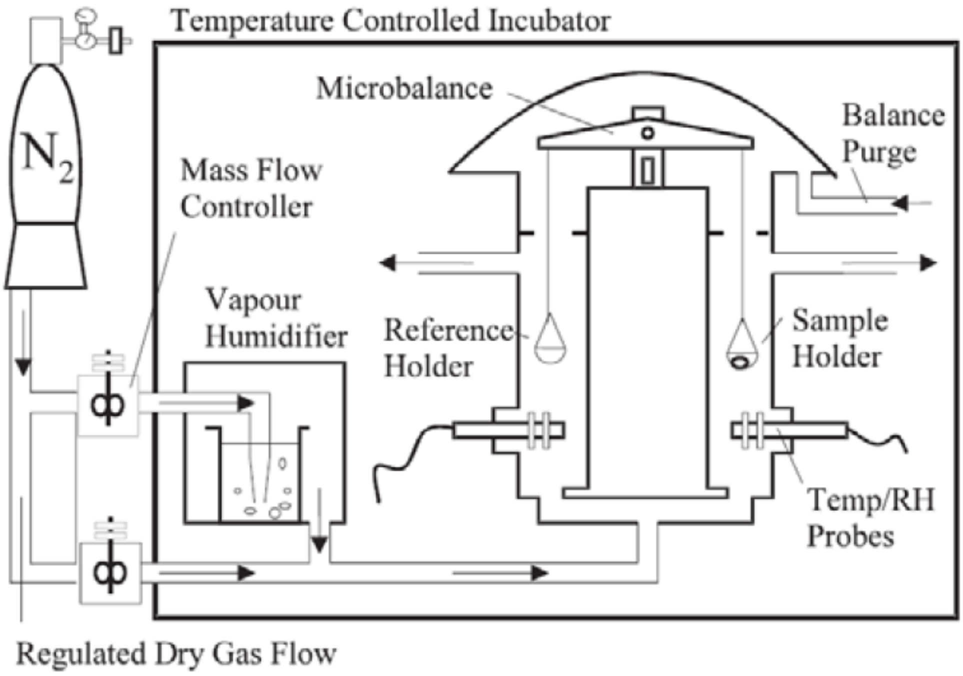

***Figure 4.2**: Schematic illustration of the DVS instrument (after (Johannesson, 2012)).*

by a wetting program, see Appendix A.1 for a detailed description of the program cycles. The DVS runs automatically in the sense that the instrument proceeds to the next step once a certain criterion for equilibrium, specified by the user, is reached. The main output results from the measurements are the drying and wetting boundary sorption isotherms which are presented in Paper II. More detailed experimental results of the DVS measurements including the preset relative humidity program cycle and the corresponding transient sample response is presented in Appendix A.1.

Cup-measurements

Disc-shaped mortar samples are exposed to two different relative humidity (RH) conditions in a standard cup test, one RH inside the cup and another RH in the salt box acting as the surrounding environment. An illustration of the cup test setup is given in Figure 4.3.

In general, the main purpose of a standard cup-measurement is to find the steady-state flow of moisture through a sample with two different constant RH conditions on each sides of the sample. From a series of weight

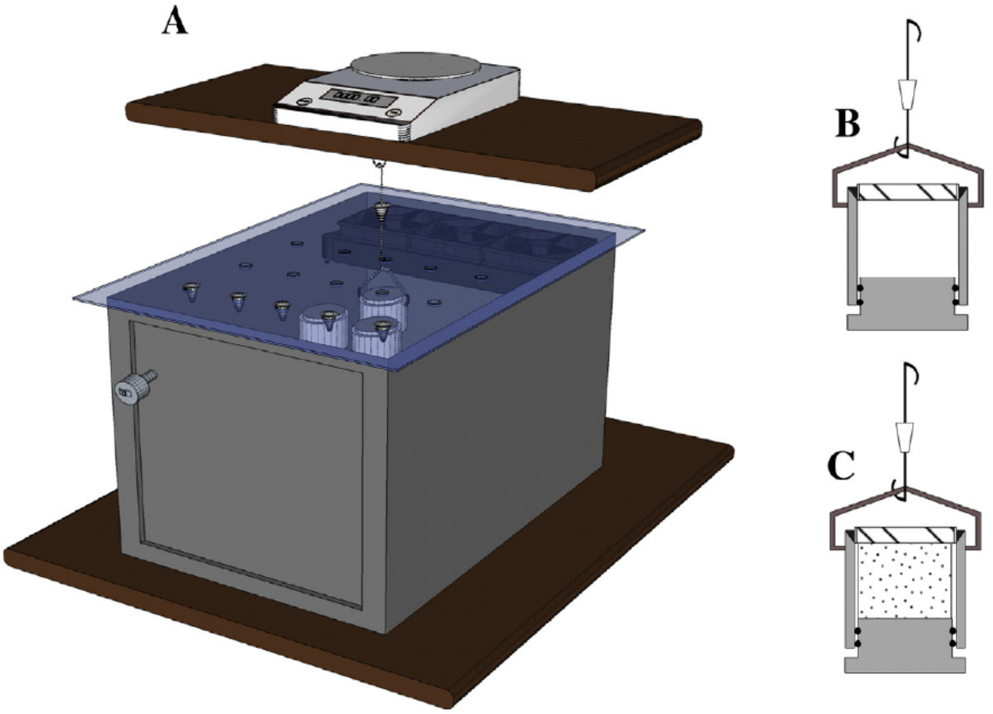

***Figure 4.3**: Illustration of the cup method setup (after (Saeidpour and Wadsö, 2016). B) an empty cup container with sample and C) a cup with a relativity humidity condition generated by a salt solution with a sample in place.*

measurements of the cup the apparent diffusion coefficient can be calculated, e.g, see (Saeidpour and Wadsö, 2016). The apparent diffusion coefficient describes the combined coupled liquid water and water vapor transport using a single averaged diffusion coefficient for the selected RH interval in the cup test. However, as the difference of the RH conditions on the two sides of the sample typically needs to be quite large to induce a significant steady-state moisture flow through the sample, it is questionable if it is adequate to use the steady-state result to evaluate the moisture transport coefficient. This is due to the fact that the moisture transport coefficient is extremely non-linear with respect to the moisture content and the large RH intervals between the inside and outside of the cup are therefore not optimal. It was therefore proposed in this work to use a two-phase moisture transport model to simulate the whole process from the time of exposure of the sample in the cup to the established equilibrium (with equilibrium it is here meant that a constant flow through the sample is established). In this fitting simulation procedure,

***Table 4.1**: The fitted apparent diffusion coefficients for one-phase moisture flow calculated according to the method described in (Saeidpour and Wadsö, 2016).*

Binder name	75-85% RH $1 \cdot 10^{-6}$	Standard div. $1 \cdot 10^{-7}$	85-95% RH $1 \cdot 10^{-6}$	Standard div. $1 \cdot 10^{-7}$
R1	0.15	0.09	0.20	0.08
B1	0.16	0.13	0.20	0.01
B2	0.14	0.05	0.18	0.12
B3	0.15	0.03	0.17	0.03
B4	0.15	0.05	0.17	0.04
B5	0.15	0.02	0.17	0.08
B6	0.53	0.17	0.73	0.16
B7	0.08	0.06	0.10	0.03
B8	0.10	0.05	0.11	0.04
B9	0.09	0.03	0.11	0.05

the sorption isotherm for the material in question is needed as input and is taken from the DVS measurement results mentioned earlier. Further, the vapor diffusion coefficient and the liquid water moisture coefficient was assigned a certain shape regarding its variation with saturation degree (using, for example, a polynomial) which was optimized in the sense that the shape of the diffusion parameters giving the best match to the measured data was used. The described approach is detailed in Paper II.

Nevertheless, it is convenient here to include calculated averaged apparent diffusion coefficients, using Fick's law as described in (Saeidpour and Wadsö, 2016), as a measure of how the moisture transport properties of the ten different binders roughly compare. Table 4.1 lists the calculated averaged apparent diffusion coefficient and standard deviation of all ten binder-systems in the two tested RH intervals, that is 75-85% and 85-95%. This can be considered as a complement to the more detail analyses of the difference between the binder-systems presented in Paper II.

Capillary suction measurements

The standard cup-measurement is not directly applicable for measure the moisture transport behavior at very high moisture contents. For this reason, the cup-measurements were complemented by a set of capillary suction measurements for the evaluation of the moisture transport properties at high

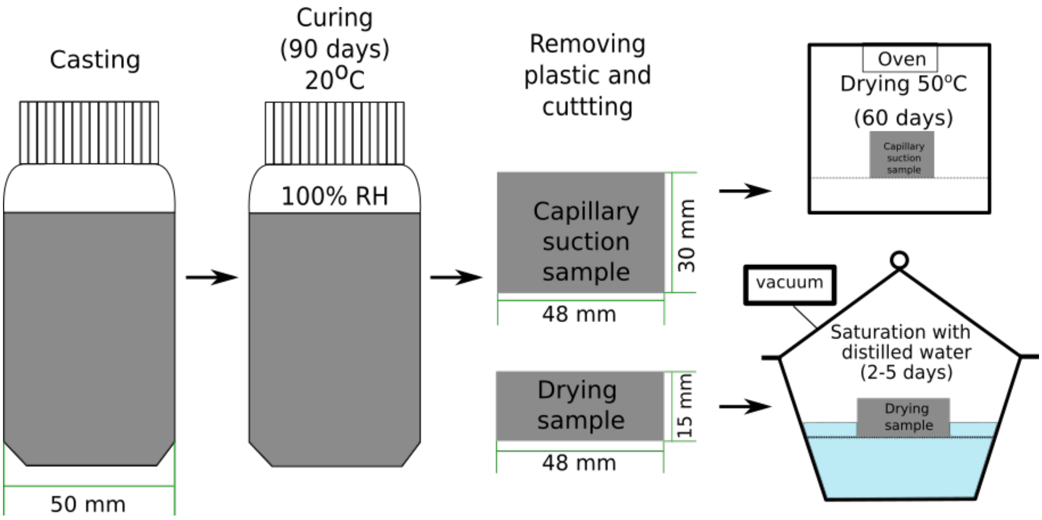

***Figure 4.4**: Schematic illustration of sample preparation of the drying and capillary suction samples.*

relative humidities. The capillary suction measurements were performed on pre-dried samples as illustrated in Figure 4.4. The initial mass and the length of the samples is listed in Table A.1. The mass change of the samples during the drying process was mentored until a steady weight was reached. The development of the mass change during the drying period is given in Appendix A.2. This mass loss during the drying period can be used as an additional indicator of how the different binder-systems compare to each other in terms of, for example, permeability.

The capillary suction was measured by placing the samples at a free water surface and continuously measure the weight gain of the sample using an external balance. The measured total mass gain of the sample is compared with the same type of fitting simulation performed on the cup-measurement results, but now with the emphasis on the dependence of the moisture transport coefficient on the saturation degree in the high saturation degree range not accessible in a normal cup measurement setup. The simulated moisture penetration profiles is integrated in order to get the calculated total mass gain which is compared with the measured result as detailed in Paper II.

Drying experiments

The philosophy of evaluate the drying experiment is much the same as evaluating the capillary suction experiment. The samples are pre-conditioned using vacuum saturation to assure a saturation degree very close to 1. Optimization simulations are used to fit the shape of the liquid water moisture transport coefficient and its dependence on the saturation degree until a satisfying agreement between the model result and experimental result is obtained. For this evaluation, the measured drying boundary sorption curves are also used. The initial mass and length of the samples in the drying experiment are listed in Table A.1. The sample mass, the change of mass, the relative humidity of the ambient drying climate and the sample length were used as input in the numerical optimization simulation. The result is the calculated diffusion parameters for liquid water and water vapor giving the best fit to the measured weight loss of samples during drying.

Chapter 5

Reactive transport model

This chapter provides an introduction to the theoretical background of the durability multi-phase reactive transport model presented in Paper III. The chapter presents a description of mass transport equations and chemical equilibrium suitable for modeling of cement based materials.

5.1 Hybrid mixture theory

In Hybrid Mixture Theory (HMT) the balance principles are postulated for constituents building up the phases, the phases themselves and the whole mixture (Hassanizadeh and Gray, 1980; Bennethum and Cushman, 1996; Bennethum et al., 1996; Johannesson, 2010). The volume fractions of the phases are used to describe the balance principles of the constituents and the phases. In general HMT models the following balance principles are considered:

(i) Mass balance equations for the constituents, phases and the whole mixture.

(ii) Momentum equation for the constituents, phases and the whole mixture in which the electroquasistatic coupling, due to the presence of ionic constituents, is included.

(iii) Angular momentum for the constituents, phases and the whole mixture in which the electroquasistatic coupling is included.

(iv) Energy balance for the constituents, phases and the whole mixture in which the electroquasistatic coupling is included.

(v) Entropy 'balance' for the constituents, phases and the whole mixture.

Exchange or coupling terms are postulated in the balance equations for the constituents and phases in order to model the interactions between them, e.g., the chemical reaction between phase boundaries (Ristinmaa et al., 2011). The Truesdell's third metaphysical principle is used which states that the balance principles of the constituents need to sum up to the phase balance equations and the summation of the phase equations should result in the classical postulates regarding the balance principles for the mixture as a whole (Bowen, 1976). In HMT the Truesdell's third metaphysical principle results in that there are some strong restrictions on the introduced coupling terms in the balance equations.

The Maxwell's balance principles are used in generalized HMT approaches to account for charged species in a phase and charged phase surfaces. A slightly simplified quasi-static approach is normally used for applications related to porous materials. Maxwell's quasistatic balance principles are:

(i) Gauss' law for the constituents, phases and the whole mixture.

(ii) Faraday's law for the constituents, phases and the whole mixture.

(iii) Ampre's law for the constituents, phases and the whole mixture.

The Gauss', Faraday's and Ampre's law for the constituents and phases includes electroquaistatic couplings between constituents and phases. The Truesdell's third metaphysical principle results in restrictions on these coupling terms.

In mixture theories for electroquasistatic cases conservation of electric charge is commonly used, e.g., (Bennethum and Cushman, 2002a,b). Conservation of charge is a combination of taking the divergence of Ampres' law and the time derivative of Gauss' law and summing the results, that is, conservation of charge is already taken into account in Maxwell's balance principles for mixtures.

A central step in obtaining models using HMT is to evaluate the Clausius-Duhems inequality, to obtain thermodynamically correct constitutive relations, e.g., generalized Fick's laws and Darcy type of laws (Hassanizadeh, 1986). By combining the entropy 'balance' and the energy balance and summing over all constituents and phases a special type of Clausius-Duhems inequality is obtained. In many application, properties such as mass balance and charge balance are enforced in the Clausius-Duhems inequality using Lagrange multipliers (Liu, 1972). Different terms in the inequality are typically used to define and identify properties such as, the entropy, the chemical potentials and stresses in terms of the Helmholtz free energy of the whole mixture or for the phases besides the identification of the meaning of the Lagrange multipliers themselves.

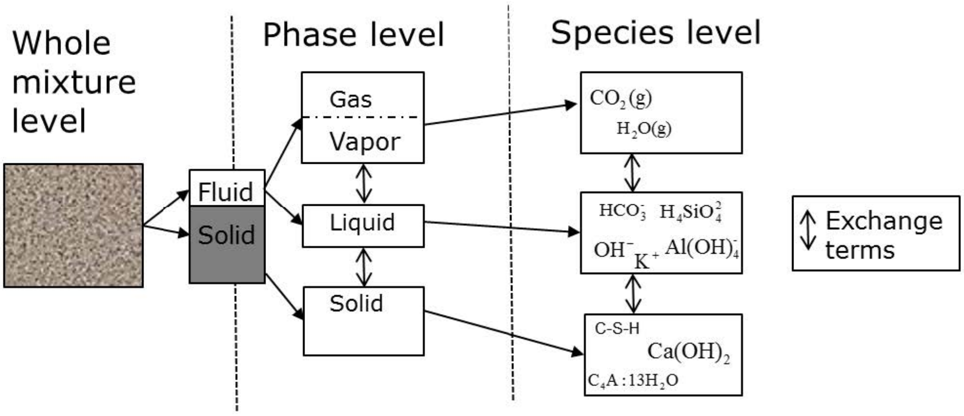

Figure 5.1*: Schematic illustration of the representation of concrete with the different levels of the HMT with examples of chemical interactions among constituents in the phases and in between the phases.*

Usually, the results from the above type of analyses are divided into equilibrium conditions and nonequilibrium conditions. It is common to make linearizations to obtain constitutive equations, such as the generalized Fourier and Fick's laws for the heat flux and mass diffusion which obey the Clausius-Duhems inequality.

Lagrange multipliers are commonly used in mixture theory to define, for example, the chemical potentials of the constituents. In the case of electroquasistatic HMT novel type of Lagrange multipliers has been analyzed by enforcing Gauss' law, Faraday's law, conservation of charge, charge neutrality and the mass balance equations for the constituents to obtain thermodynamically consistent generalized models for reactive mass transport in porous media including for ionic constituents (Bennethum and Cushman, 2002a,b).

Figure 5.1 shows an illustration of the concept of HMT used as a base to develop the coupled mass transport equations in this study. A simplified version of the general governed equations obtained from the electroquasistatic HMT approach is used in this thesis to build a model for a reactive two-phase flow model tailor-made for cement-based materials. The two transporting phases considered are the liquid water phase including dissolved charged and neutral ionic species and the air phase which includes gases, such as, CO_2 and water vapor, see Paper III. The solid phases and its constituents are considered as one rigid mixture and are only part of the model due to its chemical interaction with the constituents present in the liquid water phase.

The chemical reactions are included in the HMT through kinetic source/sink terms in the mass balance equations for the constituents. In the model considered in this thesis, the mass transport equations and the chemical reactions are split into two coupled models using an operate split approach (Jensen et al., 2014). The transport equation is solved by a finite element approach following (Paz-García et al., 2011; Johannesson, 2010), and the chemical part and its equilibrium conditions are solved with the program PHREEQC (Parkhurst, 1995; Parkhurst and Appelo, 1999).

5.2 Mass transport

Governing system of transport equations

The transport equations in this chapter is based on a simplified application of HMT (Johannesson, 2010). The transport equations are coupled to the chemical reactions between the dissolved ionic constituents in the liquid water, the reactions between ionic constituents in the liquid water with the solid phases and reactions between gaseous species in the air filled space of the porosity with constituents dissolved in the liquid phase. The governing system of equations includes a modified version of the Poisson-Nernst-Planck (PNP) system of equations including ionic diffusion and migration in the liquid phase, water vapor and liquid water transport with sorption. The transport of gas constituents in the air filled space of the porosity is modeled with equations similar to those for the ionic constituents in the liquid phase.

The transport of ions in the liquid phase and gases in the air filled space of the porosity are highly dependent on the total porosity of the system, ε_p. The sum of the porosity and the solid phase volume fraction ε^s is restricted by the following

$$\varepsilon_p + \varepsilon^s = 1. \tag{5.1}$$

The saturation degree or the volume fraction of the liquid phase relative to the pore space, ε^l (the superscript l denote the liquid phase), and the volume fraction of the gas phase ε^g (the superscript g denote the gas phase) being the non-water filled pore space

$$\varepsilon^g = \varepsilon_p - \varepsilon^l. \tag{5.2}$$

The liquid water transport is expressed using a generalized version of Darcy's law derived in (Bennethum and Cushman, 2002a), here the liquid volume fraction is used as the driving potential for the liquid flow for incompressible fluids in the porous material. The liquid water transport is expressed as

$$\rho_w \frac{\partial \varepsilon^l}{\partial t} = \nabla \cdot \left(D_{\varepsilon^l} \nabla \varepsilon^l \right) + \hat{m}_l \tag{5.3}$$

where ρ_w is the water density, $D_{\varepsilon^l} = D_{\varepsilon^l}(\varepsilon^l)$ is the diffusion coefficient for the liquid phase which is a function of the liquid volume fraction ε^l and $\hat{m}_l$ is the mass exchange between the liquid water phase and the water vapor phase due to sorption.

The equation for the water vapor is expressed in terms of the relative humidity ϕ_v in the following manner

$$\rho_{vs}(\varepsilon_p - \varepsilon^l)\frac{\partial \phi_v}{\partial t} - \rho_{vs}\phi_v\frac{\partial \varepsilon^l}{\partial t} = \nabla \cdot (D_\phi \nabla \phi_v) + \hat{m}_v \tag{5.4}$$

$$\hat{m}_l = -\hat{m}_v = R(\varepsilon^{l,eq}(\phi_v) - \varepsilon^l) \tag{5.5}$$

where ρ_{vs} is the vapor saturation density, $D_\phi = D_\phi(\varepsilon^l)$ is the diffusion coefficient for the vapor phase which is a function of the volume fraction of the liquid water, $\hat{m}_v$ is the mass exchange of vapor phase, R is the rate constant for mass exchange between liquid and vapor and $\varepsilon^{l,eq}$ is the sorption hysteresis function. In a general case where sorption hysteresis is accounted for, the function $\varepsilon^{l,eq}$ is given by the upper (drying) boundary sorption curve, the lower (wetting) boundary sorption curve or scanning curves between the lower and upper boundary curves. The function $\varepsilon^{l,eq}$ is history dependent and can be formulated in different ways, e.g., see (Frandsen and Svensson, 2007; Johannesson and Nyman, 2010; Johannesson and Janz, 2009).

The transport of gaseous species j in the domain occupied by the gas phase ε^g is described by

$$(\varepsilon_p - \varepsilon^l)\frac{\partial c_j^g}{\partial t} - c_j^g\frac{\partial \varepsilon^l}{\partial t} = \nabla \cdot \left(D_j^g(\varepsilon_p - \varepsilon^l)\nabla c_j^g - D_j^g c_j^g \nabla \varepsilon^l\right) + q_j^g; \quad j = 1, 2.., M \tag{5.6}$$

where c_j^g is the concentration of gas species j in the phase and is defined as a density fraction of the total density of the gas phase ρ^g, D_j^g is diffusion coefficient for gas j, q_j^g is the mass exchange term for gases chemical interactions and M denotes the number of gas species building up the gas phase.

The form of the PNP equation derived within HMT (Bennethum and Cushman, 2002a,b) and applied in (Johannesson, 2010) is as follows

$$\begin{aligned} \varepsilon^l\frac{\partial c_i^l}{\partial t} + c_i^l\frac{\partial \varepsilon^l}{\partial t} &= \nabla \cdot \left(D_i^l \varepsilon^l \nabla c_i^l + D_i^l c_i^l \nabla \varepsilon^l - A_i^l z_i \varepsilon^l c_i^l \nabla \Phi\right) + \\ &\quad \mathbf{v}^{l,s} \cdot \varepsilon^l \nabla c_i^l + \mathbf{v}^{l,s} \cdot c_i^l \nabla \varepsilon^l + q_i^l; \quad i = 1, 2.., N \end{aligned} \tag{5.7}$$

where D_i^l is the effective diffusion coefficient of species i in liquid phase, A_i^l is the ionic mobility of species i in liquid phase, z_i is the valance of species i, Φ is the electrical potential, $\mathbf{v}^{l,s}$ is the liquid velocity relative to the solid, q_i^l is the mass exchange term for chemical interactions between the species and N is the total number of constituent in the liquid phase. The equation (5.7) states that the mass concentration of each constituent in the liquid phase over time is dependent on the liquid volume fraction and is equal to the diffusion driven transport, expressed by the first term on the right-hand side, the motion of the liquid phase relative to the solid phase is expressed in the second and third term on the right-hand side, and the mass exchange between the constituents due to chemical interaction is expressed by the last term. The equation (5.7) needs a relation for the electrical potential in order to contain a closed system of equations. The relation is based on Gauss' law and represents the Poisson part of the equation which have the following form

$$\xi_d \xi_0 \nabla^2 \Phi = F \sum_{i=1}^{N} c_i^l z_i \tag{5.8}$$

where ξ_d is the relative dielectricity coefficient, ξ_0 is the dielectricity coefficient of vacuum and F is the Faraday's constant and z_i is valance for the ion i.

The chemical reactions and the moisture sorption of the reactive transport model presented are very much dependent on the temperature (Philip and Vries, 1957; Fillmore, 2004; Lothenbach et al., 2008; Wu et al., 2014). The standard heat equation can be used as a approximation to calculate the temperature profiles of the porous material at different time levels. For the case of transport mechanisms in concrete this approximation is reasonable, however, for cases where the reactions in the material are strongly exothermic and/or endothermic, the heat involved in the reactions needs to be incorporated into the equation determining the temperature. The heat equation is

$$c_p \rho \frac{\partial T}{\partial t} = \nabla \cdot (\lambda \nabla T) \tag{5.9}$$

where c_p the specific heat capacity and λ is the thermal heat conductivity and ρ is the density. It should be remarked that the temperature profiles changes rapidly in the material due to natural variations in the surrounding temperature. Typically a time step of an hour or so needs to be used to be able to follow the temperature variations in the material due to changes at the boundary. This fact makes the model numerically heavy compared to isothermal cases of reactive transport where considerably larger time steps can be used.

Weak formulation of the transport equations

The weak form of the coupled differential equations of the model is obtained by dividing the problem in a spatial domain and a time domain using a weight function $\mathbf{w}(\mathbf{x})$ for the spatial domain and a weight function $W(t)$ for the time domain (Zienkiewicz et al., 2005). The terms of the equations are multiplied by the two weight functions and integrated over the spatial and time domains. The Green-Gauss theorem is used on the mass transport terms in order to separate the boundary flow conditions from the volume properties in a standard way. A time increment is used in the integration, starting with t_1 and ending with t_2 . The weak formulation for the liquid water transport (5.3) with the primary unknown ε^l is

$$\begin{aligned}\int_{t_1}^{t_2} W \oint\limits_V \mathbf{w}\rho_w \frac{\partial \varepsilon^l}{\partial t} dV dt &= -\int_{t_1}^{t_2} W \int_V (\nabla \mathbf{w})^{\mathrm{T}} \left(D_{\varepsilon^l} \nabla \varepsilon^l\right) dV dt \\ &+ \int_{t_1}^{t_2} W \oint\limits_V \mathbf{w} R(\varepsilon^{l,eq}(\phi_v) - \varepsilon^l) dV dt \\ &+ \int_{t_1}^{t_2} W \oint\limits_S \mathbf{w}\mathbf{j}^l \mathbf{n} dS dt\end{aligned} \tag{5.10}$$

where $\mathbf{j}^l$ is the flow of the liquid water phase at the boundary surface dS and $\mathbf{n}$ is the out-drawn normal to the same boundary surface.

The weak form of the vapor transport equation (5.4) with the relative humidity ϕ_v as the primary unknown variable is given, as

$$\begin{aligned}\int_{t_1}^{t_2} W \oint\limits_V \mathbf{w}\rho_{vs}(\varepsilon_p - \varepsilon^l) \frac{\partial \phi_v}{\partial t} dV dt &= \int_{t_1}^{t_2} W \oint\limits_V \mathbf{w}\rho_{vs}\phi_v \frac{\partial \varepsilon^l}{\partial t} dV dt \\ &- \int_{t_1}^{t_2} W \int_V (\nabla \mathbf{w})^{\mathrm{T}} \left(D_{\phi} \nabla \phi_v\right) dV dt \\ &- \int_{t_1}^{t_2} W \oint\limits_V \mathbf{w} R(\varepsilon^{l,eq}(\phi_v) - \varepsilon^l) dV dt \\ & \int_{t_1}^{t_2} W \oint\limits_S \mathbf{w}\mathbf{j}^{\phi} \mathbf{n} dS dt\end{aligned} \tag{5.11}$$

where $\mathbf{j}^l$ is the flow of the water vapor phase at the boundary surface dS.

The partial concentrations c_j^g of the gaseous species, $j = 1, ..., M$, according to equation (5.6), are given by the following weak form of the gas transport equation

$$\begin{aligned}
\int_{t_1}^{t_2} W \int_V \mathbf{w}(\varepsilon_p - \varepsilon^l)\,\frac{\partial c_j^g}{\partial t} dV dt = {} & \int_{t_1}^{t_2} W \int_V \mathbf{w} c_j^g \frac{\partial \varepsilon^l}{\partial t} dV dt \\
& - \int_{t_1}^{t_2} W \int_V (\nabla \mathbf{w})^{\mathrm{T}} \left(D_j^g (\varepsilon_p - \varepsilon^l) \nabla c_j^g - D_j^g c_j^g \nabla \varepsilon^l \right) dV dt \\
& + \int_{t_1}^{t_2} W \oint_V \mathbf{w} q_j^g dV dt + \int_{t_1}^{t_2} W \oint_S \mathbf{w} \mathbf{j}_j^g \mathbf{n} dS dt
\end{aligned} \tag{5.12}$$

where $\mathbf{j}_j^g$ is the flow of the j:th gaseous specie at the boundary surface dS.

The concentrations c_i^l of the ionic and non-ionic species, $i = 1, ..., N$, according to equation (5.7), in the liquid water phase, are given by the following weak form

$$\begin{aligned}
\int_{t_1}^{t_2} W \oint_V \mathbf{w} \varepsilon^l \frac{\partial c_i^l}{\partial t} dV dt = {} & - \int_{t_1}^{t_2} W \oint_V \mathbf{w} c_i^l \frac{\partial \varepsilon^l}{\partial t} dV dt \\
& - \int_{t_1}^{t_2} W \int_V (\nabla \mathbf{w})^{\mathrm{T}} \left(D_i^l \varepsilon^l \nabla c_i^l + D_i^l c_i^l \nabla \varepsilon^l \right) dV dt \\
& + \int_{t_1}^{t_2} W \int_V (\nabla \mathbf{w})^{\mathrm{T}} \left(A_i^l z_i \varepsilon^l c_i^l \nabla \Phi \right) dV dt \\
& + \int_{t_1}^{t_2} W \oint_V \mathbf{w} \left(\mathbf{v}^{l,s} \cdot \varepsilon^l \right) \nabla c_i^l dV dt \\
& + \int_{t_1}^{t_2} W \oint_V \mathbf{w} \left(\mathbf{v}^{l,s} \cdot c_i^l \right) \nabla \varepsilon^l dV dt \\
& + \int_{t_1}^{t_2} W \oint_V \mathbf{w} q_i^l dV dt + \int_{t_1}^{t_2} W \oint_S \mathbf{w} \mathbf{j}_j^l \mathbf{n} dS dt
\end{aligned} \tag{5.13}$$

The weak form of the Poisson equation (5.8) for the electrical potential is given by

$$\int_V (\nabla \mathbf{w})^{\mathrm{T}} \xi_d \xi_0 \nabla \Phi dV = - \oint_V w F \sum_{i=1}^{N} c_i^l z_i dV + \oint_S \mathbf{w} \mathbf{j}^{\Phi} \mathbf{n} dS \tag{5.14}$$

where $\mathbf{j}^{\Phi}$ is the electric displacement at the boundary surface dS. The weak form of the standard heat equation (5.9) is the following expression

$$\int_{t_1}^{t_2} W \oint_V \mathbf{w} c_p \rho \frac{\partial T}{\partial t} dV dt = - \int_{t_1}^{t_2} W \int_V (\nabla \mathbf{w})^{\mathrm{T}} \lambda \nabla T dV dt + \oint_S \mathbf{w} \mathbf{j}^T \mathbf{n} dS \quad (5.15)$$

where $\mathbf{j}^T$ is the heat flux at the boundary surface dS. In the next section it is shown how the coupled weak formulations can be approximated using shape functions both in the time domain and in the spatial domain.

Finite element formulation of the transport equations

The unknown state variables ε^l, ϕ_v and c_j^g are approximated with the shape function $\mathbf{N}(\mathbf{x})$, that is

$$\varepsilon^l = \mathbf{N}\mathbf{a}^l; \quad \phi_v = \mathbf{N}\mathbf{a}^\phi; \quad c_j^g = \mathbf{N}\mathbf{a}_j^g \quad (5.16)$$

where $\mathbf{a}^l$, $\mathbf{a}^\phi$ and $\mathbf{a}_j^g$ are the vectors containing the approximated values of the state variables at the selected nodal points.

In the same manner as described above the state variables c_i^l, Φ and T and the weight function $\mathbf{w}$ are approximated as

$$c_i^l = \mathbf{N}\mathbf{a}_i^l; \quad \Phi = \mathbf{N}\mathbf{a}^\Phi; \quad T = \mathbf{N}\mathbf{a}^T; \quad \mathbf{w} = \mathbf{c}^{\mathrm{T}}\mathbf{N}^{\mathrm{T}} \quad (5.17)$$

where $\mathbf{c}$ is an arbitrary matrix.

The gradients of the included state variables of the model is approximated as

$$\nabla\varepsilon^l = \mathbf{B}\mathbf{a}^l; \quad \nabla\phi_v = \mathbf{B}\mathbf{a}^\phi; \quad \nabla c_j^g = \mathbf{B}\mathbf{a}_j^g \quad (5.18)$$

and

$$\nabla c_i^l = \mathbf{B}\mathbf{a}_i^l; \quad \nabla\Phi = \mathbf{B}\mathbf{a}^\Phi; \quad \nabla T = \mathbf{B}\mathbf{a}^T; \quad \nabla\mathbf{w} = \mathbf{c}^{\mathrm{T}}\mathbf{B}^{\mathrm{T}} \quad (5.19)$$

where $\mathbf{B}$ is the gradient of the shape function $\mathbf{N}$, that is, $\mathbf{B} = \nabla\mathbf{N}$.

The approximations for ε^l and its gradient according to (5.16) and (5.18) is inserted into the weak form of the liquid water transport equation (5.10) to obtain the following finite element formulation

$$\begin{aligned} \int_{t_1}^{t_2} W \int_V \mathbf{c}^{\mathrm{T}}\mathbf{N}^{\mathrm{T}}\rho_w \mathbf{N}\dot{\mathbf{a}}^l dV dt &= - \int_{t_1}^{t_2} W \int_V \mathbf{c}^{\mathrm{T}}\mathbf{B}^{\mathrm{T}} D_{\varepsilon^l} \mathbf{B}\mathbf{a}^l dV dt \\ &+ \int_{t_1}^{t_2} W \oint_S \mathbf{c}^{\mathrm{T}}\mathbf{N}^{\mathrm{T}}\mathbf{j}^l \mathbf{n} dS \\ &+ \int_{t_1}^{t_2} W \int_V \mathbf{c}^{\mathrm{T}}\mathbf{N}^{\mathrm{T}} R(\mathbf{N}\mathbf{a}^{l,eq} - \mathbf{N}\mathbf{a}^l) dV dt \end{aligned} \quad (5.20)$$

where $\dot{\mathbf{a}}^l$ is the spatial time derivative of the corresponding nodal values and $\varepsilon^{l,eq}(\phi_v) = \mathbf{N}\mathbf{a}^{l,eq}$ where $\mathbf{a}^{l,eq}$ is the equilibrium values of the nodal points in terms of sorption which are calculated based on the nodal values of $\mathbf{a}^\phi$ according to the shape of the sorption isotherm. The weight function in (5.10) is approximated using (5.17) and (5.19). For further reference the terms of (5.20) will be denoted by the following local stiffness and damping matrices

$$\mathbf{C}^l = \int_V \mathbf{N}^{\mathrm{T}} \rho_w \mathbf{N} dV; \quad \mathbf{K} = \int_V \mathbf{B}^{\mathrm{T}} D_{\varepsilon^l} \mathbf{B} dV \tag{5.21}$$

and

$$\mathbf{R}^{eq}_\varepsilon = \int_V \mathbf{N}^{\mathrm{T}} R \frac{\tilde{a}^{l,eq}}{\tilde{a}^l} \mathbf{N} dV; \quad \mathbf{R}^l = \int_V \mathbf{N}^{\mathrm{T}} R \mathbf{N} dV \tag{5.22}$$

where $\tilde{a}^{l,eq}$ and $\tilde{a}^l$ are lumped values of the corresponding nodal values of an element of the equilibrium value of the liquid water content and the liquid water fraction.

To obtain the finite element formulation of the weak form of the vapor transport equation an aproximations of both ϕ_v and ε^l together with the weight function $\mathbf{w}$ are needed using the shape function and its corresponding gradients, to obtain the following finite element formulation

$$\begin{aligned}\int_{t_1}^{t_2} W \int_V \mathbf{c}^{\mathrm{T}} \mathbf{N}^{\mathrm{T}} \rho_{vs} (\varepsilon_p - \varepsilon^l)\, \mathbf{N} \dot{\mathbf{a}}^\phi dV dt = \qquad & \\ \int_{t_1}^{t_2} W \int_V \mathbf{c}^{\mathrm{T}} \mathbf{N}^{\mathrm{T}} \rho_{vs} \phi_v \mathbf{N} \dot{\mathbf{a}}^l dV dt & \\ - \int_{t_1}^{t_2} W \int_V \mathbf{c}^{\mathrm{T}} \mathbf{B}^{\mathrm{T}} D_\phi \mathbf{B} \mathbf{a}^\phi dV dt & \\ + \int_{t_1}^{t_2} W \oint_S \mathbf{c}^{\mathrm{T}} \mathbf{N}^{\mathrm{T}} \mathbf{j}^\phi \mathbf{n} dS & \\ - \int_{t_1}^{t_2} W \int_V \mathbf{c}^{\mathrm{T}} \mathbf{N}^{\mathrm{T}} R (\mathbf{N}\mathbf{a}^{l,eq} - \mathbf{N}\mathbf{a}^l) dV dt &\end{aligned} \tag{5.23}$$

where the following will be used in (5.24) besides the conditions shown in (5.22),

$$\mathbf{C}^\phi = \int_V \mathbf{N}^{\mathrm{T}} \rho_{vs} (\varepsilon_p - \varepsilon^l) \mathbf{N} dV; \quad \mathbf{M}^\phi = - \int_V \mathbf{N}^{\mathrm{T}} \rho_{vs} \phi_v \mathbf{N} dV \tag{5.24}$$

and

$$\mathbf{K}^\phi = \int_V \mathbf{B}^{\mathrm{T}} D_\phi \mathbf{B} dV \tag{5.25}$$

In the same principle manner as above the finite element formulation of the weak form of the gas transport equation (5.12) becomes

$$\begin{aligned}\int_{t_1}^{t_2} W \int_V \mathbf{c}^{\mathrm{T}}\mathbf{N}^{\mathrm{T}}(\varepsilon_p - \varepsilon^l)\,\mathbf{N}\dot{\mathbf{a}}_j^g dV dt = &\\ &\int_{t_1}^{t_2} W \int_V \mathbf{c}^{\mathrm{T}}\mathbf{N}^{\mathrm{T}} c_j^g \mathbf{N}\dot{\mathbf{a}}^l dV dt\\ &- \int_{t_1}^{t_2} W \int_V \mathbf{c}^{\mathrm{T}}\mathbf{B}^{\mathrm{T}}\left(D_j^g(\varepsilon_p - \varepsilon^l)\mathbf{B}\mathbf{a}_j^g - D_j^g c_j^g \mathbf{B}\mathbf{a}^l\right)\\ &+ \int_{t_1}^{t_2} W \oint_S \mathbf{c}^{\mathrm{T}}\mathbf{N}^{\mathrm{T}}\mathbf{j}_j^g \mathbf{n} dS\end{aligned} \tag{5.26}$$

where the following notations will be used

$$\mathbf{C}_j^g = \int_V \mathbf{N}^{\mathrm{T}}(\varepsilon_p - \varepsilon^l)\mathbf{N} dV; \quad \mathbf{W}_j^g = -\int_V \mathbf{N}^{\mathrm{T}} c_j^g \mathbf{N} dV \tag{5.27}$$

and

$$\mathbf{K}_j^g = \int_V \mathbf{B}^{\mathrm{T}} D_j^g(\varepsilon_p - \varepsilon^l)\mathbf{B} dV; \quad \mathbf{P}_j^g = \int_V \mathbf{B}^{\mathrm{T}} D_j^g c_j^g \mathbf{B} dV \tag{5.28}$$

The finite element equation for the weak form of the PNP equations (5.13) are

$$\begin{aligned}\int_{t_1}^{t_2} W \int_V \mathbf{c}^{\mathrm{T}}\mathbf{N}^{\mathrm{T}}\,\varepsilon^l \mathbf{N}\dot{\mathbf{a}}_i^l dV dt = &\\ &- \int_{t_1}^{t_2} W \int_V \mathbf{c}^{\mathrm{T}}\mathbf{N}^{\mathrm{T}} c_i^l \mathbf{N}\dot{\mathbf{a}}^l dV dt\\ &+ \int_{t_1}^{t_2} W \int_V \mathbf{c}^{\mathrm{T}}\mathbf{B}^{\mathrm{T}}(D_i^l \varepsilon^l \mathbf{B}\mathbf{a}_i^l + D_i^l c_i^l \mathbf{B}\mathbf{a}^l - A_i^l z_i \varepsilon^l c_i^l \mathbf{B}\mathbf{a}^{\Phi} dV dt)\\ &+ \int_{t_1}^{t_2} W \oint_S \mathbf{c}^{\mathrm{T}}\mathbf{N}^{\mathrm{T}}\mathbf{j}_i^l \mathbf{n} dS dt\\ &+ \int_{t_1}^{t_2} W \int_V \mathbf{c}^{\mathrm{T}}\mathbf{N}^{\mathrm{T}}\mathbf{v}^{l,s}\cdot \varepsilon^l \mathbf{B}\mathbf{a}_i^l dV dt\\ &+ \int_{t_1}^{t_2} W \int_V \mathbf{c}^{\mathrm{T}}\mathbf{N}^{\mathrm{T}}\mathbf{v}^{l,s}\cdot c_i^l \mathbf{B}\mathbf{a}^l dV dt\end{aligned} \tag{5.29}$$

where the following short notations will be used in (5.30)

$$\mathbf{C}_i^l = \int_V \mathbf{N}^{\mathrm{T}}\varepsilon^l \mathbf{N} dV; \quad \mathbf{W}_i^l = \int_V \mathbf{N}^{\mathrm{T}} c_i^l \mathbf{N} dV; \tag{5.30}$$

and

$$\mathbf{K}_i^l = \int_V \mathbf{B}^{\mathrm{T}} D_i^l \varepsilon^l \mathbf{B} dV; \;\; \mathbf{P}_i^l = \int_V \mathbf{B}^{\mathrm{T}} D_i^l c_i^l \mathbf{B} dV; \;\; \mathbf{V}_i^l = \int_V \mathbf{B}^{\mathrm{T}} A_i^l z_i \varepsilon^l c_i^l \mathbf{B} dV \tag{5.31}$$

$$\tilde{\mathbf{K}}_i^l = \int_V \mathbf{N}^{\mathrm{T}} \mathbf{v}^{l,s} \varepsilon^l \mathbf{B} dV; \;\; \tilde{\mathbf{P}}_i^l = \int_V \mathbf{N}^{\mathrm{T}} \mathbf{v}^{l,s} c_i^l \mathbf{B} dV \tag{5.32}$$

The finite element version of the weak formulation of the Poisson equation (5.14) is

$$\int_V \mathbf{c}^{\mathrm{T}} \mathbf{B}^{\mathrm{T}} \xi_d \xi_0 \mathbf{B} \mathbf{a}^{\Phi} dV = \sum_{i=1}^{N} \int_V \mathbf{c}^{\mathrm{T}} \mathbf{N}^{\mathrm{T}} F z_i \mathbf{N} \mathbf{a}_i^l dV + \oint_S w \mathbf{j}^{\Phi} \mathbf{n} dS \tag{5.33}$$

where the following will be used

$$\mathbf{K}^{\Phi} = \int_V \mathbf{c}^{\mathrm{T}} \mathbf{B}^{\mathrm{T}} \xi_d \xi_0 \mathbf{B} dV; \;\; \mathbf{E}_i^l = \int_V \mathbf{N}^{\mathrm{T}} F z_i \mathbf{N} dV \tag{5.34}$$

The finite element version of the weak formulation of the standard heat equation (5.15) is

$$\int_V \mathbf{c}^{\mathrm{T}} \mathbf{N}^{\mathrm{T}} c_p \rho \mathbf{N} \dot{\mathbf{a}}^T dV = \int_V \mathbf{c}^{\mathrm{T}} \mathbf{B}^{\mathrm{T}} \lambda \mathbf{B} \mathbf{a}^T dV + \oint_S w \mathbf{j}^T \mathbf{n} dS \tag{5.35}$$

For later references the following short notations will be used for the damping and conduction matrices in the finite element formulated heat equation

$$\mathbf{C}^T = \int_V \mathbf{c}^{\mathrm{T}} \mathbf{N}^{\mathrm{T}} c_p \rho \mathbf{N} dV; \;\; \mathbf{K}^T = \int_V \mathbf{N}^{\mathrm{T}} \lambda \mathbf{N} dV \tag{5.36}$$

Solution of the coupled system of transport equations

The global equation to be solved in the coupled system including all states variables of the model, is

$$\int_{t_1}^{t_2} W \left[\mathbf{C} \dot{\mathbf{a}} + \mathbf{K} \mathbf{a} - \mathbf{f} \right] dt \tag{5.37}$$

where **C** and **K** is the global damping matrix and the stiffness matrix for the whole coupled transport problem, respectively, and **a** containing all state variables ε^l, ϕ_v, c_j^g, c_i^l, Φ and T at the nodal points. The weight function in the time domain $W(t)$ is related to the time integration parameter Θ, as

$$\Theta = \frac{\int_0^{\triangle t} W \tau dt}{\triangle t \int_0^{\triangle t} W dt} \tag{5.38}$$

where $0 \leq \tau \leq \triangle t$ is the time integration domain for a time step which results in the interval $0 \leq \Theta \leq 1$ for the time integration parameter. Different choices of $W(t)$ results in different time stepping schemes, for example, $\Theta = 0$ is a truly explicit scheme and $\Theta = 1$ is a truely implicit scheme.

The assumption for the spatial time derivative $\dot{\mathbf{a}}$ is the linear assumption given as

$$\dot{\mathbf{a}} = \frac{(\mathbf{a}_{n+1} - \mathbf{a}_n)}{\triangle t} \tag{5.39}$$

The coupled system of transport equations will be solved for the unknown nodal vector $\mathbf{a}_{n+1}$ at the new time step level, as

$$\mathbf{C}\frac{(\mathbf{a}_{n+1} - \mathbf{a}_n)}{\triangle t} + \mathbf{K}\left(\mathbf{a}_n + \Theta\left(\mathbf{a}_{n+1} - \mathbf{a}_n\right)\right) + \mathbf{f}_n + \Theta\left(\mathbf{f}_{n+1} - \mathbf{f}_n\right) = \mathbf{0} \tag{5.40}$$

where nodal values of the previous known time step level is denoted by $\mathbf{a}_n$ and where $\mathbf{a}$ is approximated in the time domain as: $\mathbf{a} = \mathbf{a}_n + \Theta\left(\mathbf{a}_{n+1} - \mathbf{a}_n\right)$.

Using the proposed set up of the problem the global damping matrix $\mathbf{C}$ becomes

$$\text{Ca=}\begin{bmatrix}
\mathbf{C}_1^l & 0 & 0 & 0 & 0 & 0 & 0 & 0 & 0 & 0 & \mathbf{W}_1^l & 0 \\
0 & \mathbf{C}_2^l & 0 & 0 & 0 & 0 & 0 & 0 & 0 & 0 & \mathbf{W}_2^l & 0 \\
0 & 0 & \ddots & 0 & 0 & 0 & 0 & 0 & 0 & 0 & \vdots & 0 \\
0 & 0 & 0 & \mathbf{C}_N^l & 0 & 0 & 0 & 0 & 0 & 0 & \mathbf{W}_N^l & 0 \\
0 & 0 & 0 & 0 & \mathbf{C}_1^g & 0 & 0 & 0 & 0 & 0 & \mathbf{W}_1^g & 0 \\
0 & 0 & 0 & 0 & 0 & \mathbf{C}_2^g & 0 & 0 & 0 & 0 & \mathbf{W}_2^g & 0 \\
0 & 0 & 0 & 0 & 0 & 0 & \ddots & 0 & 0 & 0 & \vdots & 0 \\
0 & 0 & 0 & 0 & 0 & 0 & 0 & \mathbf{C}_M^g & 0 & 0 & \mathbf{W}_M^g & 0 \\
0 & 0 & 0 & 0 & 0 & 0 & 0 & 0 & \mathbf{C}^T & 0 & 0 & 0 \\
0 & 0 & 0 & 0 & 0 & 0 & 0 & 0 & 0 & 0 & 0 & 0 \\
0 & 0 & 0 & 0 & 0 & 0 & 0 & 0 & 0 & 0 & \mathbf{C}^l & 0 \\
0 & 0 & 0 & 0 & 0 & 0 & 0 & 0 & 0 & 0 & \mathbf{M}^\phi & \mathbf{C}^\phi
\end{bmatrix}
\begin{bmatrix}
\dot{\mathbf{a}}_1^l \\ \dot{\mathbf{a}}_2^l \\ \vdots \\ \dot{\mathbf{a}}_N^l \\ \dot{\mathbf{a}}_1^g \\ \dot{\mathbf{a}}_2^g \\ \vdots \\ \dot{\mathbf{a}}_M^g \\ \dot{\mathbf{a}}^T \\ \dot{\mathbf{a}}^\Phi \\ \dot{\mathbf{a}}^l \\ \dot{\mathbf{a}}^\phi
\end{bmatrix} \tag{5.41}$$

and the global stiffness $\mathbf{K}$ is

$$\mathbf{Ka} = \begin{bmatrix} \mathbf{K}_1^l + \tilde{\mathbf{K}}_1^l & 0 & 0 & 0 & 0 & 0 & 0 & 0 & 0 & \mathbf{V}_1^l & \mathbf{P}_1^l + \tilde{\mathbf{P}}_1^l & 0 \\ 0 & \mathbf{K}_2^l + \tilde{\mathbf{K}}_2^l & 0 & 0 & 0 & 0 & 0 & 0 & 0 & \mathbf{V}_2^l & \mathbf{P}_2^l + \tilde{\mathbf{P}}_2^l & 0 \\ 0 & 0 & \ddots & 0 & 0 & 0 & 0 & 0 & 0 & \vdots & \vdots & 0 \\ 0 & 0 & 0 & \mathbf{K}_N^l + \tilde{\mathbf{K}}_N^l & 0 & 0 & 0 & 0 & 0 & \mathbf{V}_N^l & \mathbf{P}_N^l + \tilde{\mathbf{P}}_N^l & 0 \\ 0 & 0 & 0 & 0 & \mathbf{K}_1^g & 0 & 0 & 0 & 0 & 0 & \mathbf{P}_1^g & 0 \\ 0 & 0 & 0 & 0 & 0 & \mathbf{K}_2^g & 0 & 0 & 0 & 0 & \mathbf{P}_2^g & 0 \\ 0 & 0 & 0 & 0 & 0 & 0 & \ddots & 0 & 0 & 0 & \vdots & 0 \\ 0 & 0 & 0 & 0 & 0 & 0 & 0 & \mathbf{K}_M^g & 0 & 0 & \mathbf{P}_m^g & 0 \\ 0 & 0 & 0 & 0 & 0 & 0 & 0 & 0 & \mathbf{K}^T & 0 & 0 & 0 \\ \mathbf{E}_1^l & \mathbf{E}_2^l & \cdots & \mathbf{E}_N^l & 0 & 0 & 0 & 0 & 0 & \mathbf{K}^\Phi & 0 & 0 \\ 0 & 0 & 0 & 0 & 0 & 0 & 0 & 0 & 0 & 0 & \mathbf{K}^l + \mathbf{R}^l & -\mathbf{R}_\varepsilon^{eq} \\ 0 & 0 & 0 & 0 & 0 & 0 & 0 & 0 & 0 & 0 & -\mathbf{R}^l & \mathbf{K}^\phi + \mathbf{R}_\varepsilon{}^{eq} \end{bmatrix} \begin{bmatrix} \mathbf{a}_1^l \\ \mathbf{a}_2^l \\ \vdots \\ \mathbf{a}_N^l \\ \mathbf{a}_1^g \\ \mathbf{a}_2^g \\ \vdots \\ \mathbf{a}_M^g \\ \mathbf{a}^T \\ \mathbf{a}^\Phi \\ \mathbf{a}^l \\ \mathbf{a}^\phi \end{bmatrix} \tag{5.42}$$

Due to the non-linearity of $\mathbf{C}$ and $\mathbf{K}$, a modified Newton-Raphson scheme is used in the iterations within the time step calculations. The scheme is modified in the sense that an approximate tangential stiffness is calculated in which the non-linearity in $\mathbf{C}$ is ignored. Further, the tangential stiffness is only occasionally updated within the time step calculations without jeopardizing the successful search for minimization of the residual.

5.3 Chemical equilibrium

This section deals with the formal format of chemical reactions and chemical equilibrium conditions. In Paper III chemical equilibrium are considered for reactions among ionic species in the liquid phase, the equilibrium between ionic constituent and the solid cement hydrate phases, and between gaseous constituents in the air filled space of the porosity and the dissolved constituents of the liquid phase.

The term in the form of the entropy inequality including chemical reaction rates q_a of the constituents and the chemical potentials μ_a of the reacting constituents of a mixture in a single phase, is

$$-\sum_{a=1}^{\Re} q_a \mu_a \geq 0 \tag{5.43}$$

When working with chemical reaction schemes it is convenient to arrange the equation (5.43) using all the chemical reaction rates of constituents q_a and all the chemical potentials μ_a into two column vectors, that is

$$-\mathbf{q} \cdot \boldsymbol{\mu} \geq 0 \tag{5.44}$$

The following choice of constitutive equation is used for the chemical reaction rate vector $\mathbf{q}$

$$\mathbf{q} = \mathbf{V}\mathbf{j} \tag{5.45}$$

where $\mathbf{j}$ is the rate of the specific reactions considered and $\mathbf{V}$ is the stoichiometric mass matrix for the $\Re$ number of constituents and m number of reactions. The size of the matrix $\mathbf{V}$ is the number of constituents times the number of chemical reactions considered.

The chemical reactions $\mathbf{q}$ can alternatively be written with indexes, as

$$q_i = \sum_{j=1}^{m} V_{ij} j_j \tag{5.46}$$

The stoichiometric mass matrix is normalized so that the reactions are considered to proceed from left to right meaning that the constituents being consumed in the reaction are assigned with a negative value and those produced (on the right-hand side of the reaction scheme) are considered positive (Blomberg and Koukkari, 2011). Furthermore, the specific reactions considered are normalized so that the sum of the fractions of the mass densities of the left and right-hand side of the reaction is -1 on the left-hand side and 1 at the right-hand side, that is

$$\sum_{i=1}^{q_i} V_{ij} = -1; \quad \sum_{i=d_i+1}^{\Re} V_{ij} = 1; \quad \sum_{i=1}^{\Re} V_{ij} = 0 \tag{5.47}$$

where d_i denotes the number of constituents involved in left-hand side of reaction j. It also follows directly that the sum of all the rows of the matrix $\mathbf{V}$ is zero meaning that the mass is conserved in each of the reactions included in the model.

The individual reaction mass rates are arranged in the vector $\mathbf{j}$ and the whole system is constituted by using the chemical potential vector $\boldsymbol{\mu}$, the stoichiometric mass matrix $\mathbf{V}$ and the constant chemical reaction rate matrix $\mathbf{L}$, as

$$\mathbf{j} = \mathbf{L}\mathbf{V}^{\mathrm{T}}\boldsymbol{\mu} \tag{5.48}$$

Due to the normalization and arrangement of the stoichiometric mass matrix $\mathbf{V}$ into the left-hand and right-hand side of the reaction, the reaction rates are basically determined by the difference of the mass-weighted average of the chemical potentials of the right and left-hand side of the reactions considered. Under the condition that $\mathbf{L}$ includes off-diagonal terms, the chemical reaction rate of a specific reaction is coupled to the rate of another reaction (Paz-García et al., 2013).

By combining (5.48) and (5.45) the gain or loss of mass of each constituent considered can be formulated, as

$$\mathbf{q} = \mathbf{V}\mathbf{L}\mathbf{V}^{\mathrm{T}}\boldsymbol{\mu} \tag{5.49}$$

Now returning to our main task, namely, to check that our chemical constitution is thermodynamically correct. By using (5.49) and (5.44) one obtain the following inequality

$$-\left(\mathbf{V}\mathbf{L}\mathbf{V}^{\mathrm{T}}\boldsymbol{\mu}\right) \cdot \boldsymbol{\mu} \geq 0 \tag{5.50}$$

And it is immediately concluded that the required condition of the inequality is fulfilled as long as the term $\mathbf{V}\mathbf{L}\mathbf{V}^{\mathrm{T}}$ is negative semi-definite.

In chemical reaction schemes, it is for most cases more convenient to work with stoichiometric relations in the individual reactions included in the model rather than working with the mass density changes involved in the different reactions (Blomberg and Koukkari, 2011; Bethke, 1996). For this reason consider (5.49) written in terms of mole quantities rather than in mass quantities, that is

$$\widetilde{\mathbf{q}}^{aq} = \mathbf{V}^{*}\mathbf{L}^{*}\mathbf{V}^{*\mathrm{T}}\widetilde{\boldsymbol{\mu}}^{aq} \tag{5.51}$$

By analyzing the connections between mass density quantities and the mole density quantities, one obtains the following relations between the properties

$$V_{ij}^{*} = \frac{a_j V_{ij}}{M_i}; \quad j_j^{*} = \frac{j_j}{a_j}; \quad L_{jm}^{*} = \frac{L_{jm}}{a_j a_m} \tag{5.52}$$

where M_i is the molar mass of the constituent i. The properties a_j are coefficients given by

$$a_j = -\sum_{i=1}^{q_i} V_{ij}^{*} M_i = \sum_{i=q_i+1}^{\Re} V_{ij}^{*} M_i \tag{5.53}$$

At chemical equillibrium for the aqueous species is expressed in mole properties rather than in mass concentration and becomes

$$\mathbf{V}^{*\mathrm{T}}\widetilde{\boldsymbol{\mu}}^{aq} = \mathbf{0} \tag{5.54}$$

Each row of the above equation system represent a condition for a specific reaction. Once the chemical potentials of the individual constituents have been constituted, with a proper definition of the reference potentials, the solubility equations of the individual reactions of the system studied will be obtained.

Example of the stoichiometric matrix

In combined models for transport and chemical equilibrium, it is important to be able to convert mol quantities to mass concentration quantities in relation to the progress of reactions. Chemical reactions are best described by mole quantities as the atomic elements participating in the reaction then automatically are conserved in the progress of the reaction driven from left to right or vice verse. However, transport equations are based on mass balances rather than mole balance and therefore the conversion of the two are of importance when combined chemical action and transport is of interest.

As an example consider the following reaction scheme, with reaction $j = 1$, as

$$\mathrm{A{+}B} \leftrightarrow \mathrm{AB} \tag{5.55}$$

and reaction $j = 2$,

$$\mathrm{2B{+}C} \leftrightarrow \mathrm{B_2C} \tag{5.56}$$

and reaction $j = 3$,

$$\mathrm{4A{+}2B{+}C} \leftrightarrow \mathrm{AB} + \mathrm{A_3BC} \tag{5.57}$$

The stoichiometric mole reaction matrix $\mathbf{V}^*$ for the 6 considered component of the three reaction can be established directly, as

$$\mathbf{V}^* = \begin{bmatrix} -1 & 0 & -4 \\ -1 & -2 & -2 \\ 0 & -1 & -1 \\ 1 & 0 & 1 \\ 0 & 1 & 0 \\ 0 & 0 & 1 \end{bmatrix} \quad ; \quad \mathbf{L}^* = \begin{bmatrix} 1 & 0 & 0 \\ 0 & 1 & 0 \\ 0 & 0 & 1 \end{bmatrix} \tag{5.58}$$

where the rate constants $\mathbf{L}^*$ are also given as an example. Let the molar masses of the constituents be: $M_A = 1$,$M_B = 2$, $M_C = 4$,$M_{AB} = 3$, $M_{B_2C} = 8$ and $M_{A_3BC} = 9$. With the reaction scheme given by (5.55), (5.56) and (5.57) the normalization coefficients becomes: $a_1 = 3$, $a_2 = 8$ and $a_3 = 12$. From the above it is concluded that the mole quantities of the stoichiometric matrix and the rate constant matrix, in the studied example, becomes

$$\mathbf{V} = \begin{bmatrix} -\frac{1}{3} & 0 & -\frac{4}{12} \\ -\frac{2}{3} & -\frac{1}{2} & -\frac{4}{12} \\ 0 & -\frac{1}{2} & -\frac{4}{12} \\ 1 & 0 & \frac{3}{12} \\ 0 & 1 & 0 \\ 0 & 0 & \frac{9}{12} \end{bmatrix} \; ; \quad \mathbf{L} = \begin{bmatrix} 9 & 0 & 0 \\ 0 & 64 & 0 \\ 0 & 0 & 144 \end{bmatrix} \tag{5.59}$$

The program PHREEQC uses similar types of stochiometrix matrices as discussed above for solving for chemical equilibrium (Parkhurst and Appelo, 1999). PHREEQC does not, however, use the rate constants **L** for describing kinetic conditions instead the so-called saturation rate index concept is used.

Constitution of the chemical potentials

In Paper III chemical equilibrium is considered for the ionic solution in equilibrium with solid cement hydrate phases. The included aqueous reactions in the water phase and the interaction with dissolved ions and the solid phases can be described by the same type of framework based on the constitution of the chemical potential of the individual constituent included.

The mineral equations for pure mineral dissolution/precipitation is given by classical dissolution reactions in which the activity of the mineral phase is set to a constant reference value. A solid solution phase is assumed to consist of mixed solid phases called end members. The dissolution/precipitation of the end members is assumed dependent on the individual concentration of the end members in the solid solution phase.

The chemical potentials $\widetilde{\mu}_k^{aq}$ for the species and pure minerals in an aqueous solution is the assumption

$$\widetilde{\mu}_k^{aq} = \widetilde{\mu}_k^{aq,\ominus} + RT\mathrm{ln}\mathrm{c}_k^{aq} + RTln\gamma_k^{aq} = \widetilde{\mu}_k^{aq,\ominus} + RT\mathrm{ln}\mathrm{a}_k^{aq} \tag{5.60}$$

where c_k^{aq} is the molality and γ_k^{aq} is the activity coefficients of the species k in solution and the activity is formulated as: $a_k^{aq} = c_k^{aq}\gamma_k^{aq}$. The reference state $\widetilde{\mu}_k^{\ominus,aq}$ correspondes to the standard Gibb's free energy as used in classical chemistry. The activity coefficients of the ionic water solution components is constituted by using the ionic strenght I, as

$$log_{10}\gamma_k^{aq} = A\left(z_k\right)^2\left(\frac{\sqrt{I}}{1+\sqrt{I}} - 0.3\sqrt{I}\right); \quad I = \sum_{k=1}^{N} c_k^{aq}\left(z_k\right)^2; \tag{5.61}$$

where A is a constant. and z_k is the valance of a dissolved ionic species k in the aqueous solution.

Pure minerals in contact with the solution are independent of its concentration and are constituted solely by its standard state. That is,

$$\widetilde{\mu}_k^{aq} = \widetilde{\mu}_m^{aq,\ominus} \tag{5.62}$$

The precipitation and dissolution of solid solution end-members are dependent on the mole fraction of the end member related to the total moles of the solid solution assemblage χ_{ss}^{aq} and is constituted as

$$\widetilde{\mu}_{ss}^{aq} = \widetilde{\mu}_{ss}^{aq,\ominus} + \ln\chi_{ss}^{aq} + \ln\lambda_{ss}^{aq} = \widetilde{\mu}_{ss}^{aq,\ominus} + \ln a_{ss}^{aq} \tag{5.63}$$

where the end-memeber activity is: $a_{ss}^{aq} = \chi_{ss}^{aq}\lambda_{ss}^{aq}$ and where λ_{ss}^{aq} is activity coefficients for the end members. As an example, the activity coefficients of a binary solid solution can be formulated with the Guggenheim expressions

$$\lambda_1^{aq} = \exp\left(a_0 - a_1\left(4\chi_1^{aq} - 1\right)\left(\chi_2^{aq}\right)^2\right) \tag{5.64}$$

$$\lambda_2^{aq} = \exp\left(a_0 + a_1\left(4\chi_2^{aq} - 1\right)\left(\chi_1^{aq}\right)^2\right) \tag{5.65}$$

where λ_1^{aq} and λ_2^{aq} are the activity coefficients of the binary solid solution of this example and a_0 and a_1 are non-dimensional so-called Guggenheim parameters.

Charge and atomic element balance

Chemical equilibrium systems can be solved in different ways. It is quite common that the extent of the included reactions is considered and the model solves how much all reactions of the system needs to progress from left to right or from right to left in order to obtain a global equilibrium for all reactions. This kind of method does not need any introduction of extra balance equations for the conservation of chemical elements, such as H, O and Cl, or conservation of ionic charge since the scheme for a specific reaction take this automatically into account.

The program PHREEQC works directly with the equations for the solubility products for the reactions considered in the system and, therefore, it does not follow the progress of each reaction from left to right or vice verse. For this reason, PHREEQC uses one separate equation for the charge balance of ionic solutions and one conservation equation for each chemical atomic element present in the considered reaction scheme. The numerical solution of the coupled system of solubility equations, element balance equations and the charge balance equation is complicated. This is mainly because of the wide range of numerical values of the concentrations of the dissolved species, and due to the existence of local minimums not representing a true numerical solution.

Chemical reaction systems including a gas phase

Chemical reactions between constituents in a gas phase and in a liquid phase will be schematically described in this section. In Paper III a reactive transport model valid for cement-based materials is established. The model include gas transport and gas reactions together with ionic transport coupled to moisture flow. For example, the transport of carbon dioxide gas from the atmosphere into the concrete cover and the resulting carbonation reactions, is always of interest because the process of carbonation causes the pore solution pH to drop and this increase the risk of reinforcement corrosion among other things.

The ideal condition of a gas component leads to the following assumption for the chemical potential

$$\widetilde{\mu}_j^g = \widetilde{\mu}_j^{g,\ominus} + RT\ln c_j^g \tag{5.66}$$

The ideal gas law is

$$p_j^g = RTc_j^g \tag{5.67}$$

At constant temperature one have

$$\widetilde{\mu}_j^g = \widetilde{\mu}_j^{g,\ominus} + \ln p_j^g \tag{5.68}$$

The reference chemical potential $\widetilde{\mu}_j^{g,\ominus}$ is in this setting the same as the Henry's law constant K_j^p for a gas species j in the air filled gas mixture in equilibrium with the aqueous species participating in the gas specific dissolution reaction involving the component j, that is

$$\widetilde{\mu}_j^{g,\ominus} = K_j^p \tag{5.69}$$

The equilibrium condition for the partial gases in the gas mixture phase in equilibrium with the aqueous species is

$$\mathbf{V}_g^{*\mathrm{T}}\widetilde{\boldsymbol{\mu}}^{aq} - \widetilde{\boldsymbol{\mu}}^g = \mathbf{0} \tag{5.70}$$

where $\mathbf{V}_g^{*\mathrm{T}}$ is the right-hand side stoichiometric coefficients matrix for the aqueous species participating in all the included partial gas constituents of the gas mixture. The matrix $\mathbf{V}_g^{*\mathrm{T}}$ is the right-hand side of the stoichiometric coefficients of the reaction and the gas component reacting with the aqueous species are left alone on the left-hand side of the reaction in this case.

The partial pressures $\mathbf{p}^g$ of the gas phase becomes

$$\mathbf{p}^g = \mathbf{K}^p \mathbf{V}_g^{*\mathrm{T}} \widetilde{\boldsymbol{\mu}}^{aq} \tag{5.71}$$

where $\mathbf{K}^p$ is a diagonal matrix including the inverse values of the Henry's law constants K_j^p for the different gas dissolution reactions included in the model.

The PHREEQC program has the option of specifying a constant total pressure p. In this case the following restriction will be added to the system of equations

$$\mathbf{p}^g \cdot \mathbf{n}_u^g - p = 0 \tag{5.72}$$

where the unity vector $\mathbf{n}_u^g$ have the same dimension as the partial pressure vector $\mathbf{p}^g$.

Surface complexation models

The charged nature of the C-S-H surface in terms of silanol sites makes the detailed chemical description of cement-based materials complicated (Paz-García et al., 2011). However, programs such as PHREEQC have a feature for calculating the chemical equilibrium for solid phases exhibit surface charge and hence surface complexations. The surface complexation feature in PHREEQC has been used by concrete researchers in attempts to improve the chemical description of cement-based systems. Some important effects such as alkali binding and interaction of chloride ions and C-S-H is difficult to explain without considering the charged silanol sites of the C-S-H surface and, hence, the use of surface complexation models. The numerical stability of surface complexation models for cement-based material is, however, a severe problem. One of the major problems is that the thickness of the calculated ionic double layers often is concluded to occupy a larger volume than the volume of water present in the system to hold these double-layer ions and the calculation therefore collapses. In Paper III the solid solution model is used in favor of the complexation model when describing the dissolution/-precipitation behavior of the C-S-H due to its more simple and numerically stable form.

Chapter 6

Research finding and conclusions

The overall objective of this thesis is to improve the understanding of long-term durability aspects of new CO_2-reduced cements with special focus on moisture and gas transport processes. The research findings are presented in detail in the three appended papers in Part II. This chapter provides the main summaries and conclusions of the research findings of this study and how they relate to the overall objectives of the thesis. The chapter also includes a discussion about the current stage of the durability model framework and the challenges and limitations that need to be addressed in future studies.

6.1 Summary of research

This PhD project contributes to an improved understanding of important mechanisms present in moisture and gas transport, relevant to the modeling of multi-phase reactive transport of cement-based materials. The durability modeling developed in this study is based on the prior development of a multi-phase reactive transport framework for concrete durability estimation presented in (Jensen et al., 2014) (will be referred to as MRT framework in the following). This thesis encompasses three major parts covered in detail in the appended papers.

Paper I is about both enhancing and simplifying the understanding of important vapor transport mechanisms in unsaturated systems at the pore-scale. A conceptually simple model was constructed to model vapor transport at the pore-scale, using the chemical potential as the driving potential. A one-dimensional Fick-Jacobs equation is the governing equation in the model. The model only requires the geometry of the pore and the area-averaged relative humidity at the gas-liquid interfaces. Other quantities, such as temperature, contact angle, surface tension are all taken into account in the model through the initial relative humidity at the gas-liquid interfaces. The model was used to successfully match experimental results of vapor diffusion through dry and partly filled cylindrically symmetric pores (Silverman, 1999) without the use of any fitting parameters. The only other known model used to capture this experiment is much more complicated incorporating among other things the surface tension and contact angle as well as fitting parameters (Shahraeeni and Or, 2010, 2012). The model developed in Paper I explains the physics of how the saturation degree (in terms of the length of the trapped liquid in the pore meniscus) is affected by the relative humidity flux variations on both sides of the trapped liquid (rate of evaporation/condensation). The model also explains the mechanisms of how the increased degree of saturation at the pore-scale leads to enhanced vapor flow. The simplicity of the model and the use of the chemical potential as the driving potential, provides an opportunity for the developed model to act as a ground for future research aiming to explain more complex vapor flow problems in a variety of fields. For example, it can be incorporated into two or three-dimensional models with a well-defined pore structure of porous materials to improve the description of vapor transport.

The MRT framework is currently a one-dimensional model which inherently does not include the description of the pore structure dynamics stemming from multi-dimensionality. Moisture transport in the MRT model is represented by a two-phase model and sorption as detailed in paper II.

Paper II is about the development of a novel inverse analysis approach for determining the effective diffusion coefficients of the water liquid and vapor phase in a two-phase moisture transport model. These coefficients are crucial for the description of moisture transport in the MRT framework for durability estimations in unsaturated systems with cyclic boundary conditions. The coefficients, of the empirical relations for the effective diffusion functions for the two phases attaining the form of either a polynomial or a power function. It is the coefficients of these functions that are considered the parameters driving the optimization. The aforementioned inverse analyses approach aims to match the experimental results of mass change over time, from four different types of experiments by adjusting the optimization coefficients. The experimental investigations were the drying test, the two different moisture transport test using two different cup-test RH intervals and the capillary suction test. A set of effective diffusion coefficients are tested in each computational iteration step until a good match between the simulation and the experimental results is found.

Polynomial functions with high exponential coefficients were used for the liquid diffusion function to account for the steep increase in the RH range close to saturation. Motivated by the findings in Paper I about the enhanced vapor flow, the coefficients of the function modeling the vapor diffusion was chosen to increase with increasing saturation for binder-systems R1 and B1–B6. This choice is counter-intuitive but is motivated by the results presented in Paper I. Besides the fact that it gave good results in the optimization approach. However, the increasing vapor-diffusion function approach was inapplicable for the binder-systems B7-B9. Presumably, this might be due to the reduced effect of enhanced vapor transport; the latter caused by the relative absence of capillary pores. This absence is probably related to the decreased pore sizes influenced by the calcined clay used in samples B7-B9.

The moisture transport properties of the nine new binder-systems, some of which contain combinations of fly ash, calcined clay, burnt shale and gray micro-filler (limestone filler) were compared to a reference binder R1. These properties are relevant to the MRT framework that was established in Paper II. The optimized diffusion parameters for the 10 binders presented in Table 6 in Paper II, can act as a measure of the durability performance of the binder-systems in terms of moisture transport.

Paper III describes the inclusion of gaseous transport in the air-filled space (in unsaturated systems) into the MRT framework. This broadens the capabilities of the MRT framework and allows the modeling of degradation mechanisms in unsaturated conditions with cyclic behavior. One of the most important mechanisms in cement-based materials is the carbonation of the hydrated cement. Many models describing the carbonation process exists. However, the MRT framework developed in this study is general in the sense that it include many different coupled chemical actions and transport actions in which the action of carbonation is only one of them. This general approach differ from most of the existing models and frameworks which typically are designed for simpler systems. Paper III contains the description of the governing equations in the MRT framework, including the description of the gaseous transport in the in the air-filled space of the porosity as well as the reactions between gaseous constituents between the liquid phase and the gas phase. A coupled reactive transport model where the transport processes are solved using the Finite Element Method (FEM) and the chemical equilibrium program PHREEQC.

In Paper III three numerical examples are included for schematic demonstration purposes. The three examples share the same binder-system but differ in the boundary conditions resembling the surrounding environment. One of the example include an accelerated carbonation process. The accelerated carbonation example demonstrates the possibility of modeling carbonation in a detailed manner and in turn open up for a better understanding of the underlying mechanisms in terms of chemical reactions and the resulting altering of the hydrated cement. A second example simulates a case where the boundary conditions are changed to model a case of cyclic conditions of submersion in seawater and exposure to dry air. This example includes the naturally simultaneously occurring multiple degradation processes such as chloride ingress, carbonation and leaching.

The third example simulates constant submersion in seawater. This example is used as a reference for studying the difference between the constant seawater exposure and the cycle conditions studied in the second example. The altering of the cement binder-system was concluded to be faster and more dominant in the second example than compared to the constant exposure in the third example. This theoretical result is due to the detailed account to the combined effects of the different degradation processes in the model. The results of the simulations of Paper III, should be considered as examples indicating the general behavior, hence explaining some of the important fundamental mechanisms and it is therefore not claimed to be an exact description of the real behavior.

6.2 Discussion and future studies

The presented MRT durability framework for concrete is a useful simulation tool that can be used to study the performance of new cement-based binder-system under different exposure conditions. The addition of the gas phase and the improved description of moisture transport widens the field of application of the MRT framework to include unsaturated and cyclic exposure conditions. Some topics which needs further research are listed in the following:

(i) Incorporate further the effects of pore structure development during the service life simulation. Currently, the changes in porosity due to changes in the hydrated phases are approximated by the densities of the hydrated phases. The effect of the change in porosity on the tortuosity has been studied using general relations such as the Kozeny–Carman equation. However, better approximation methods are needed accounting for the changes in pore size distribution at different hydration degrees and its effect on the transport properties.

(ii) Improved the computational speed. The model development has been mainly focused on increasing the accuracy and covering as many of the aspect affecting degradation as possible. The computational speed was not prioritized in the development of the model. Making the code more efficient computationally, provides the option to extend the model to two-dimensions and possibly three-dimensions.

(iii) Introduce multi-dimensionality to the framework. The transport processes in the model framework are solved using a finite element approach that facilitates a smooth transaction from the current one-dimension to multiple dimensions. Multi-dimensionality would, among others enable the development of structural changes into the framework.

(iv) Incorporating the effect of high pressure and high temperature on the transport processes and the chemical reactions. This widens the field of application of the model, e.g., the durability of borehole cement in oil and gas wells where temperatures and pressures exceed 180°C and 1.000 bar for high-pressure high-temperature wells. The evaluation of the integrity of cement in oil and gas wells is very crucial as the cement paste isolate the well from the surrounding aggressive environment.

(v) The dependency of chemical equilibrium calculations on the selected time step-size needs further investigation. Introducing a kinetic description of the more time-sensitive reactions might help reduce the time step-size effect. This is, however, challenging as the reaction rates are not well defined for most of the reactions occurring in concrete, this is especially true for the early hydration processes.

(vi) Customize a version of the model for engineering purposes. The current model framework requires the user to be familiar with in the model framework, especially when selecting which chemical reactions and databases to be used. User-friendly versions of the framework with pre-defined chemical models representing the most critical exposure conditions for engineering proposes is desirable.

6.3 Conclusions

(i) A new conceptually simple one-dimensional model for vapor transport at the pore-scale was developed using the chemical potential (in this case equal to the relative humidity) as the driving potential. The model explains the non-intuitive mechanisms of enhanced vapor flow as a function of increased saturation degree at the pore-scale. The model was able to match experimental results of vapor diffusion through dry and partly filled cylindrically symmetric pores without the use of fitting parameters.

(ii) Moisture transport properties of nine new types of cement-based binder-systems containing pozzolanic SCMs and a reference binder were investigated experimentally. The experimental results provided a description of the moisture transport parameters needed in the developed reactive mass transport durability model.

(iii) A novel inverse method was developed to determine the effective diffusion parameters relevant for a two-phase moisture transport model of cement-based materials. The developed method is crucial because the water vapor and liquid water diffusion which can not be measured directly. The developed method was successfully used together with experimental results to establish the two-phase effective diffusion parameters of the ten studied binder-systems.

(iv) Transport of gaseous species was described and incorporated into the existing reactive mass transport framework for concrete durability estimations. The effect of gaseous transport in the air filled space of the pores and the chemical gas-liquid interaction was taken into account. The addition of the gas phase enables the durability framework to be accurately used in unsaturated and cyclic conditions.

(v) Durability estimation in terms of the altering of a cement-binder system in three different exposure conditions were carried out through numerical examples. The three numerical examples represents an accelerated carbonation condition, a cyclic drying-wetting marine-environment, and a constantly submerged marine-environment condition. The general trends observed in the simulation results were comparable with observations reported in the literature. The examples demonstrats the usefulness of adding the gas phase to the durability model, this is especially true when aiming at understanding the combined effect of multiple degradation processes.

Bibliography

Ahmad, S. (2003). Reinforcement corrosion in concrete structures, its monitoring and service life prediction - a review. *Cement and Concrete Composites*, 25:459–471.

Alexander, M., Bertron, A., and De Belie, N. (2013). *Performance of cement-based materials in aggressive aqueous environments*, volume 56. Springer.

Antoni, M. (2013). *Investigation of cement substitution by blends of calcined clays and limestone*. PhD thesis, École polytechnique Fédérale de Lausanne.

Balonis, M. (2010). *The Influence of Inorganic Chemical Accelerators and Corrosion Inhibitors on the Mineralogy of Hydrated Portland Cement Systems*. PhD thesis, Department of chemistry university of Aberdeen.

Baroghel-Bouny, V. (2007a). Water vapour sorption experiments on hardened cementitious materials. Part I: Essential tool for analysis of hygral behaviour and its relation to pore structure. *Cement and Concrete Research*, 37:414–437.

Baroghel-Bouny, V. (2007b). Water vapour sorption experiments on hardened cementitious materials. Part II: Essential tool for assessment of transport properties and for durability prediction. *Cement and Concrete Research*, 37:438–454.

Baroghel-Bouny, V., Nguyen, T., and Dangla, P. (2009). Assessment and prediction of rc structure service life by means of durability indicators and physical/chemical models. *Cement and Concrete Composites*, 31:522–534.

Bennethum, L. and Cushman, J. (1996). Multiscale, hybrid mixture theory for swelling systems–I: balance laws. *International Journal of Engineering Science*, 34:125–145.

Bennethum, L. and Cushman, J. (2002a). Multicomponent, multiphase thermodynamics of swelling porous media with electroquasistatics: I. macroscale field equations. *Transport in Porous Media*, 47:309–336.

Bennethum, L. and Cushman, J. (2002b). Multicomponent, multiphase thermodynamics of swelling porous media with electroquasistatics: II. constitutive theory. *Transport in Porous Media*, 47:337–362.

Bennethum, L., Cushman, J., and Murad, M. (1996). Clarifying mixture theory and the macroscale chemical potential for porous media. *International Journal of Engineering Science*, 34:1611–1621.

Bethke, C. (1996). *Geochemical reaction modeling: Concepts and applications*. Oxford University Press New York.

Blomberg, P. B. A. and Koukkari, P. S. (2011). A systematic method to create reaction constraints for stoichiometric matrices. *Computers & Chemical Engineering*, 35(7):1238–1250.

Bowen, R. M. (1976). Theory of mixtures. *Continuum physics*, 3.

Brew, D. and Glasser, F. (2005). Synthesis and characterisation of magnesium silicate hydrate gels. *Cement and Concrete Research*, 35(1):85–98.

Campos, A., López, C. M., and Aguado, A. (2016). Diffusion-reaction model for the internal sulfate attack in concrete. *Construction and Building Materials*, 102:531–540.

CEMBUREAU (2017). World statistical review 2004 - 2014 cement production, imports, exports, total and per capita consumption and population. Technical report, The European Cement Association.

Davis, R. E., Carlson, R. W., Kelly, J. W., and Davis, H. E. (1937). Properties of cements and concretes containing fly ash. In *Journal Proceedings*, volume 33, pages 577–612.

De Weerdt, K., Haha, M. B., Le Saout, G., Kjellsen, K. O., Justnes, H., and Lothenbach, B. (2011). Hydration mechanisms of ternary Portland cements containing limestone powder and fly ash. *Cement and Concrete Research*, 41:279–291.

Dilnesa, B., Lothenbach, B., Le Saout, G., Renaudin, G., Mesbah, A., Filinchuk, Y., Wichser, A., and Wieland, E. (2011). Iron in carbonate containing afm phases. *Cement and Concrete Research*, 41(3):311–323.

Dilnesa, B. Z., Lothenbach, B., Renaudin, G., Wichser, A., and Kulik, D. (2014). Synthesis and characterization of hydrogarnet ca3 (alxfe1- x) 2 (sio4) y (oh) 4 (3- y). *Cement and Concrete Research*, 59:96–111.

Dilnesa, B. Z., Lothenbach, B., Renaudin, G., Wichser, A., and Wieland, E. (2012). Stability of monosulfate in the presence of iron. *Journal of the American Ceramic Society*, 95(10):3305–3316.

Fernandez Lopez, R. (2009). *Calcined clayey soils as a potential replacement for cement in developing countries.* PhD thesis, STI, Lausanne.

Ferreiro, S., Herfort, D., and Damtoft, J. (2017). Effect of raw clay type, fineness, water-to-cement ratio and fly ash addition on workability and strength performance of calcined clay–limestone portland cements. *Cement and Concrete Research*, 101:1 – 12.

Fillmore, D. (2004). *Literature Review of the Effects of Radiation and Temperature on the Aging of Concrete.* United States. Department of Energy.

Frandsen, H. L. and Svensson, S. (2007). Implementation of sorption hysteresis in multi-fickian moisture transport. *Holzforschung*, 61(6):693–701.

Geiker, M. R., De Weerdt, K., Garzon, S. F., Jensen, M. M., Johannesson, B., and Michel, A. (2017). Screening of low clinker binders, compressive strength and chloride ingress. *Nordic Concrete Research*, 57:23–38.

Hassanizadeh, M. and Gray, W. G. (1980). General conservation equations for multi-phase systems: 3. constitutive theory for porous media flow. *Advances in Water Resources*, 3(1):25–40.

Hassanizadeh, S. M. (1986). Derivation of basic equations of mass transport in porous media, part 2. generalized darcy's and fick's laws. *Advances in water resources*, 9(4):207–222.

Hong, S.-Y. and Glasser, F. (1999). Alkali binding in cement pastes: Part i. the csh phase. *Cement and Concrete Research*, 29:1893–1903.

Hosokawa, Y., Yamada, K., Johannesson, B., and Nilsson, L.-O. (2011). Development of a multi-species mass transport model for concrete with account to thermodynamic phase equilibriums. *Materials and Structures*, 44:1577–1592.

Jennings, H. M. (2008). Refinements to colloid model of C-S-H in cement: CM-II. *Cement and Concrete Research*, 38:275–289.

Jennings, H. M., Thomas, J., Rothstein, D., and Chen, J. (2002). Cements as porous materials. *Handbook of Porous Solids*, pages 2971–3028.

Jensen, M., Johannesson, B., and Geiker, M. (2014). Framework for reactive mass transport: Phase change modeling of concrete by a coupled mass transport and chemical equilibrium model. *Computational Materials Science*, 92:213–223.

Jensen, M. M. (2014). *A Coupled Transport and Chemical Model for Durability Predictions of Cement Based Materials*. PhD thesis, Department of Civil Engineering Technical University of Denmark.

Johannesson, B. (2010). Development of a generalized version of the poisson-nernst-planck equations using the hybrid mixture theory: Presentation of 2d numerical examples. *Transport in Porous Media*, 85:565–592.

Johannesson, B. (2012). Introduction to concrete technology. Lecture notes (Third draft).

Johannesson, B. and Janz, M. (2009). A two-phase moisture transport model accounting for sorption hysteresis in layered porous building constructions. *Building and Environment*, 44:1285–1294.

Johannesson, B. and Nyman, U. (2010). A Numerical Approach for Non-Linear Moisture Flow in Porous Materials with Account to Sorption Hysteresis. *Transport in Porous Media*, 84:735–754.

Kosmatka, S., Kerkhoff, B., and Panarese, W. (2002). Portland, Blended, and Other Hydraulic Cements. *Design and Control of Concrete Mixtures*, pages 21–27,39–56.

Kulik, D. (2011). Improving the structural consistency of c-s-h solid solution thermodynamic models. *Cement and Concrete Research*, 41:477–495.

Litvan, G. G. (1972). Phase transitions of adsorbates: Iv, mechanism of frost action in hardened cement paste. *Journal of the American Ceramic Society*, 55(1):38–42.

Liu, I.-S. (1972). Method of lagrange multipliers for exploitation of the entropy principle. *Archive for Rational Mechanics and Analysis*, 46(2):131–148.

Lothenbach, B., Matschei, T., Möschner, G., and Glasser, F. P. (2008). Thermodynamic modelling of the effect of temperature on the hydration and porosity of portland cement. *Cement and Concrete Research*, 38:1–18.

Lothenbach, B., Pelletier-Chaignat, L., and Winnefeld, F. (2012). Stability in the system cao–al2o3–h2o. *Cement and Concrete Research*, 42(12):1621–1634.

Lothenbach, B., Scrivener, K., and Hooton, R. D. (2011). Supplementary cementitious materials. *Cement and Concrete Research*, 41:1244–1256.

Lothenbach, B. and Winnefeld, F. (2006). Thermodynamic modelling of the hydration of portland cement. *Cement and Concrete Research*, 36:209–226.

Luc, N., Andr, N., and Damien, D. (2018). Rate-limiting reaction of c3s hydration-a reply to the discussion 'a new view on the kinetics of tricalcium silicate hydration' by e. gartner. *Cement and Concrete Research*, 104:118 – 122.

Maes, M., Gruyaert, E., and De Belie, N. (2012). Resistance of concrete with blast-furnace slag against chlorides, investigated by comparing chloride profiles after migration and diffusion. *Materials and Structures*, 46:89–103.

Malinowski, R. and Frifelt, K. (1993). Prehistoric hydraulic mortar(the ubaid period 5-4000 years bc, technical properties). *Document- Swedish Council for Building Research.*

Manz, O. (1997). Worldwide production of coal ash and utilization in concrete and other products. *Fuel*, 76(8):691–696.

Massazza, F. (1993). Pozzolanic cements. *Cement and Concrete Composites*, 15(4):185 – 214. Special Issue on Composite Cements.

Mehta, P. (1981). Studies on blended portland cements containing santorin earth. *Cement and Concrete Research*, 11(4):507 – 518.

Meshgin, P. and Xi, Y. (2012). Effect of Supplementary Cementitious Materials on Properties of Concrete. *ACI Materials Journal*, 109:71–80.

Mindess, S., Young, J. F., and Darwin, D. (2003). *Concrete.* Prentice-Hall.

Mo, L., Zhang, F., Deng, M., and Panesar, D. K. (2016). Effectiveness of using CO2 pressure to enhance the carbonation of Portland cement-fly ash-MgO mortars. *Cement and Concrete Composites*, 70:78–85.

Möschner, G., Lothenbach, B., Rose, J., Ulrich, A., Figi, R., and Kretzschmar, R. (2008). Solubility of fe–ettringite ($Ca_6[Fe(OH)_6]_2(SO_4)_3 \cdot 26H_2O$). *Geochimica et Cosmochimica Acta*, 72:1–18.

Möschner, G., Lothenbach, B., Winnefeld, F., Ulrich, A., Figi, R., and Kretzschmar, R. (2009). Solid solution between al-ettringite and fe-ettringite (ca 6 [al 1- x fe x (oh) 6] 2 (so 4) 3· 26h 2 o). *Cement and Concrete Research*, 39:482–489.

Moser, R. D., Jayapalan, A. R., Garas, V. Y., and Kurtis, K. E. (2010). Assessment of binary and ternary blends of metakaolin and Class C fly ash for alkali-silica reaction mitigation in concrete. *Cement and Concrete Research*, 40:1664–1672.

Oss, H. G. and Padovani, A. C. (2002). Cement manufacture and the environment: part i: chemistry and technology. *Journal of Industrial Ecology*, 6(1):89–105.

Parkhurst, D. (1995). *User's guide to PHREEQCA computer program for speciation, reaction-path, advective-transport, and inverse geochemical calculations*. U.S. Geological Survey Water-Resources Investigations.

Parkhurst, D. and Appelo, C. (1999). *User's Guide to PHREEQC (Version 2): a Computer Program for Speciation, Batch-reaction, One-dimensional Transport, and Inverse Geochemical Calculations*. U.S. Geological Survey Water-Resources Investigations.

Paz-García, J. M., Johannesson, B., Ottosen, L. M., Ribeiro, A. B., and Rodríguez-Maroto, J. M. (2011). Modeling of electrokinetic processes by finite element integration of the nernst–planck–poisson system of equations. *Separation and Purification Technology*, 79(2):183–192.

Paz-García, J. M., Johannesson, B., Ottosen, L. M., Ribeiro, A. B., and Rodríguez-Maroto, J. M. (2013). Computing multi-species chemical equilibrium with an algorithm based on the reaction extents. *Computers & Chemical Engineering*, 58:135–143.

Philip, J. and Vries, D. D. (1957). Moisture movement in porous materials under temperature gradients. *Eos, Transactions American . . . .*

Powers, T. C. and Brownyard, T. L. (1947). Studies of the physical properties of hardened portland cement paste. In *Journal Proceedings*, volume 43, pages 549–602.

Ramezanianpour, A. A. (2014a). *Cement Replacement Materials*. Springer.

Ramezanianpour, A. A. (2014b). Fly ash. In *Cement replacement materials*, pages 47–156. Springer.

Redler, L. (1991). Quantitative x-ray diffraction analysis of high alumina cements. *Cement and concrete research*, 21(5):873–884.

Ristinmaa, M., Ottosen, N., and Johannesson, B. (2011). Mixture theory for a thermoelasto-plastic porous solid considering fluid flow and internal mass exchange. *International Journal of Engineering Science*, 49:1185–1203.

Saeidpour, M. and Wadsö, L. (2015). Moisture equilibrium of cement based materials containing slag or silica fume and exposed to repeated sorption cycles. *Cement and Concrete Research*, 69:88–95.

Saeidpour, M. and Wadsö, L. (2016). Moisture diffusion coefficients of mortars in absorption and desorption. *Cement and Concrete Research*, 83:179–187.

Samson, E. and Marchand, J. (1999). Numerical solution of the extended nernst-planck model. *Journal of Colloid and Interface Science*, 215:1 – 8.

Sato, T. and Diallo, F. (2010). Seeding effect of nano-caco3 on the hydration of tricalcium silicate. *Transportation Research Record: Journal of the Transportation Research Board*, 2141:61–67.

Schmidt, T., Lothenbach, B., Romer, M., Scrivener, K., Rentsch, D., and Figi, R. (2008). A thermodynamic and experimental study of the conditions of thaumasite formation. *Cement and Concrete Research*, 38:337–349.

Scrivener, K. (2014). Options for the future of cement. *Indian Concrete Journal*, 88(7):11–21.

Scrivener, K., John, V., and Gartner, E. (2016). Eco-efficient cements: Potential, economically viable solutions for a low co2, cement based materials industry. *UNEP (United Nations Environment Program).*

Scrivener, K. L., Lothenbach, B., De Belie, N., Gruyaert, E., Skibsted, J., Snellings, R., and Vollpracht, A. (2015). TC 238-SCM: hydration and microstructure of concrete with SCMs. *Materials and Structures*, 48:835–862.

Shahraeeni, E. and Or, D. (2010). Pore-scale analysis of evaporation and condensation dynamics in porous media. *Langmuir*, 26(17):13924–13936.

Shahraeeni, E. and Or, D. (2012). Pore scale mechanisms for enhanced vapor transport through partially saturated porous media. *Water Resources Research*, 48(5).

Shi, Z., Lothenbach, B., Geiker, M. R., Kaufmann, J., Leemann, A., Ferreiro, S., and Skibsted, J. (2016). Experimental studies and thermodynamic modeling of the carbonation of Portland cement, metakaolin and limestone mortars. *Cement and Concrete Research*, 88:60–72.

Silverman, T. S. (1999). A pore-scale experiment to evaluate enhanced vapor diffusion in porous media. Master's thesis, Univ., Socorro, N. M.

Stutzman, P. E. (2000). Scanning electron microscopy in concrete petrography. In *Materials Science of Concrete*.

Takemoto, K. and Uchikawa, H. (1980). Hydration of pozzolanic cement. In *7th International Congress on the Chemistry of Cement, Paris, France, Editions Septima*, pages 1–28.

Taylor, H. F. (1997). *Cement chemistry*. Thomas Telford.

Thomas, M. D. and Bamforth, P. B. (1999). Modelling chloride diffusion in concrete: effect of fly ash and slag. *Cement and Concrete Research*, 29:487–495.

Tom Boden, Bob Andres, G. M. (2017). Global and national annual co2 emissions from fossil-fuel burning, cement manufacture, and gas flaring: 1751-2014. Technical report, Oak Ridge National Laboratory.

Tuutti, K. (1982). Corrosion of steel in concrete. Technical report, Swedish Cement and Concrete Research Institute, Stockholm.

UnitedNations (2015). World population prospects: The 2015 revision. Technical report, Department of Economic and Social Affairs, Population Division.

Van Den Heede, P. and De Belie, N. (2012). Environmental impact and life cycle assessment (LCA) of traditional and 'green' concretes: Literature review and theoretical calculations. *Cement and Concrete Composites*, 34:431–442.

Van Den Heede, P. and De Belie, N. (2014). A service life based global warming potential for high-volume fly ash concrete exposed to carbonation. *Construction and Building Materials*, 55:183–193.

WorldBank (2016). World development indicators. Technical report, World DataBank.

Wu, M., Johannesson, B., and Geiker, M. (2014). A study of the water vapor sorption isotherms of hardened cement pastes: Possible pore structure changes at low relative humidity and the impact of temperature on isotherms. *Cement and Concrete Research*.

Zienkiewicz, O., Taylor, R., and Zhu, J. (2005). *The finite element method: its basis and fundamentals*, volume 1. Butterworth-Heinemann.

Appendix A

Appendix

-Supporting experimental data

A.1 Sorption isotherms

Below are the detailed sorption isotherm results (RH in % and moisture content (g water per g dry sample, %) calculated from the end point of each RH-step. As can be seen in the plot of each measurement, Figure A.1-A.13, the attainment of equilibrium is quite different in different RH-steps. Generally, it is seen that desorption steps are slower than the absorption and that the final drying (in dry nitrogen at 20 °C) is very slow.

Note that:

- Even if the steps do not reach equilibrium, the initial rapid change in mass is well captured, despite of the slower process.

- "Slow" does not mean that the macro-diffusion is slow, it is other processes that limit the rate of attainment of equilibrium and measuring for longer times (for example double times for all steps) does not improve the situation much.

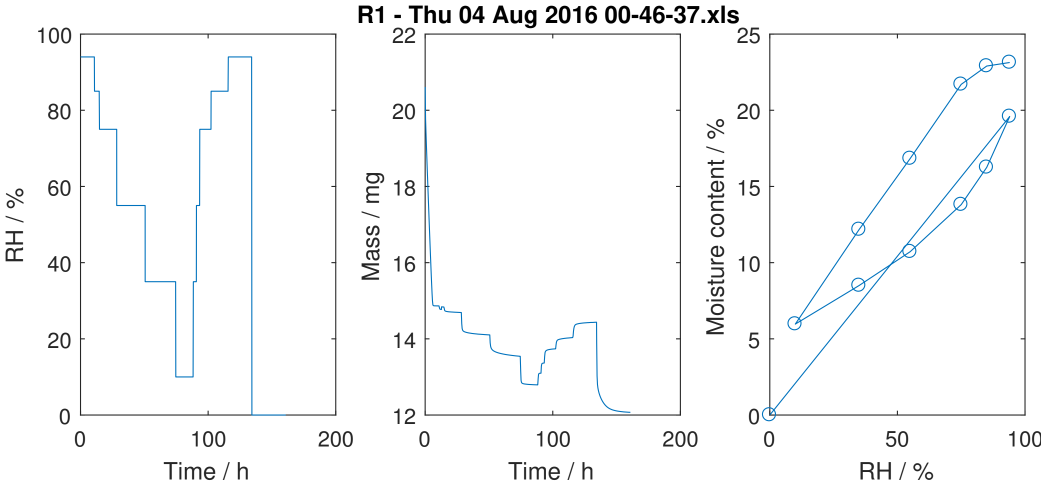

Figure A.1: DVS results for R1. The relative humidity program in % versus time in hours (right). Sample mass in mg versus time (center). Moisture content in % of g water per g dry sample versus the relative humidity % (left).

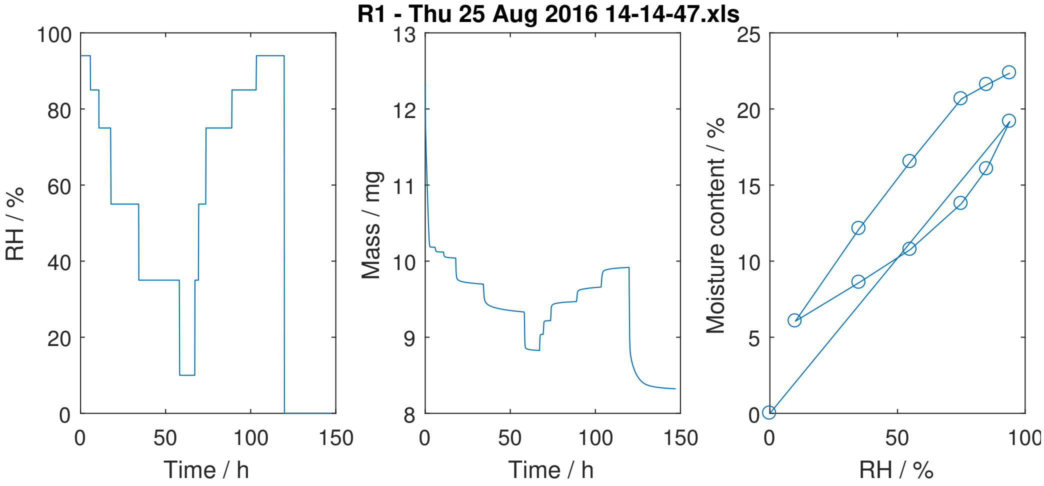

Figure A.2: DVS results for ***R1*** *repeated using a different sample. The relative humidity program in % versus time in hours (right). Sample mass in mg versus time (center). Moisture content in % of g water per g dry sample versus the relative humidity % (left).*

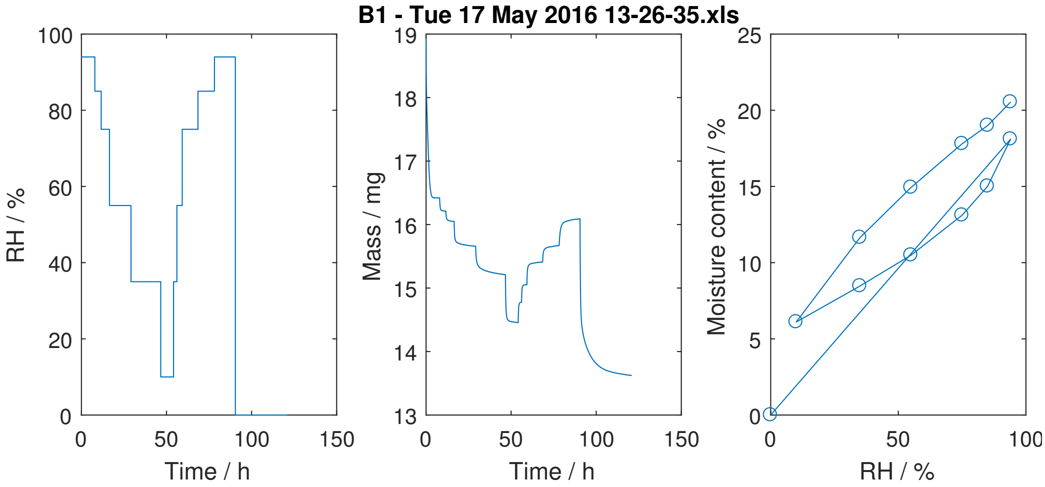

Figure A.3: *DVS results for* ***B1****. The relative humidity program in % versus time in hours (right). Sample mass in mg versus time (center). Moisture content in % of g water per g dry sample versus the relative humidity % (left).*

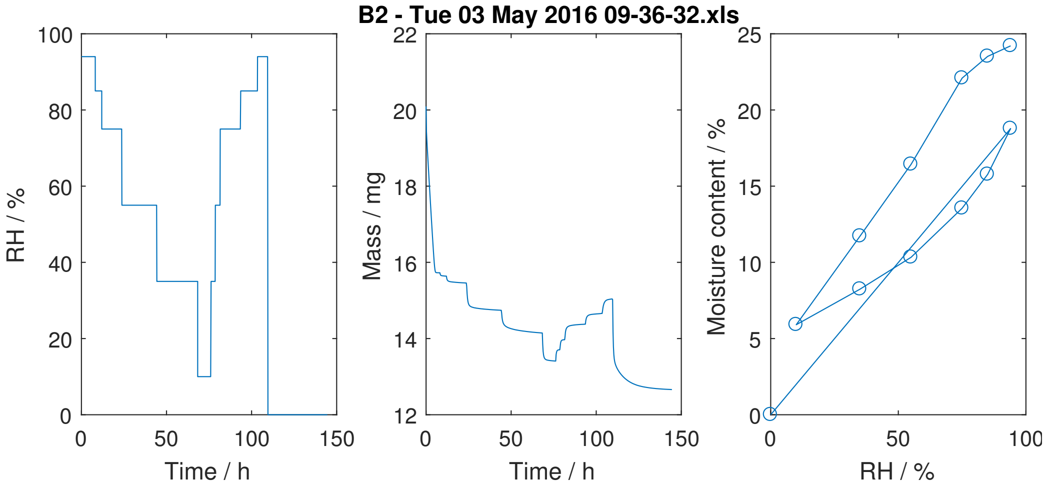

Figure A.4: *DVS results for* ***B2****. The relative humidity program in % versus time in hours (right). Sample mass in mg versus time (center). Moisture content in % of g water per g dry sample versus the relative humidity % (left).*

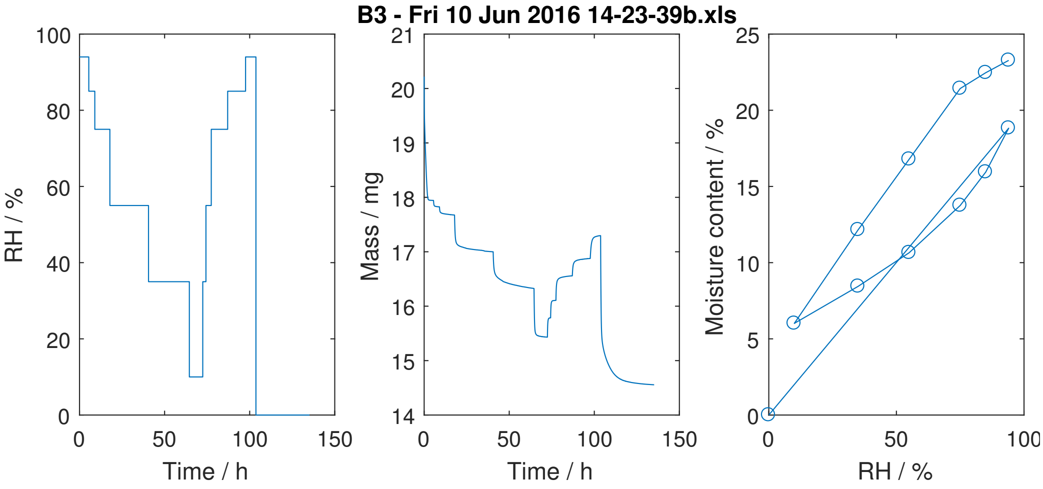

__Figure A.5__: DVS results for __B3__. The relative humidity program in % versus time in hours (right). Sample mass in mg versus time (center). Moisture content in % of g water per g dry sample versus the relative humidity % (left).

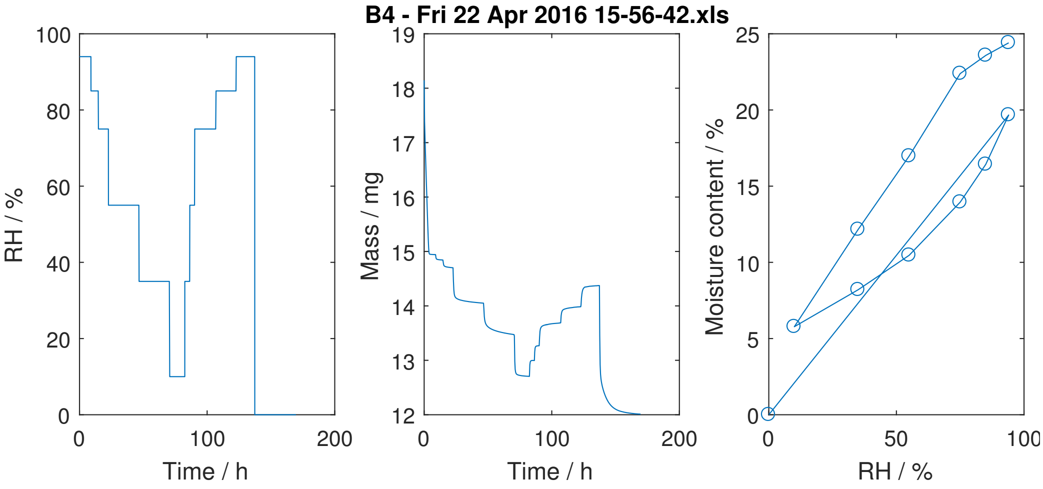

__Figure A.6__: DVS results for __B4__. The relative humidity program in % versus time in hours (right). Sample mass in mg versus time (center). Moisture content in % of g water per g dry sample versus the relative humidity % (left).

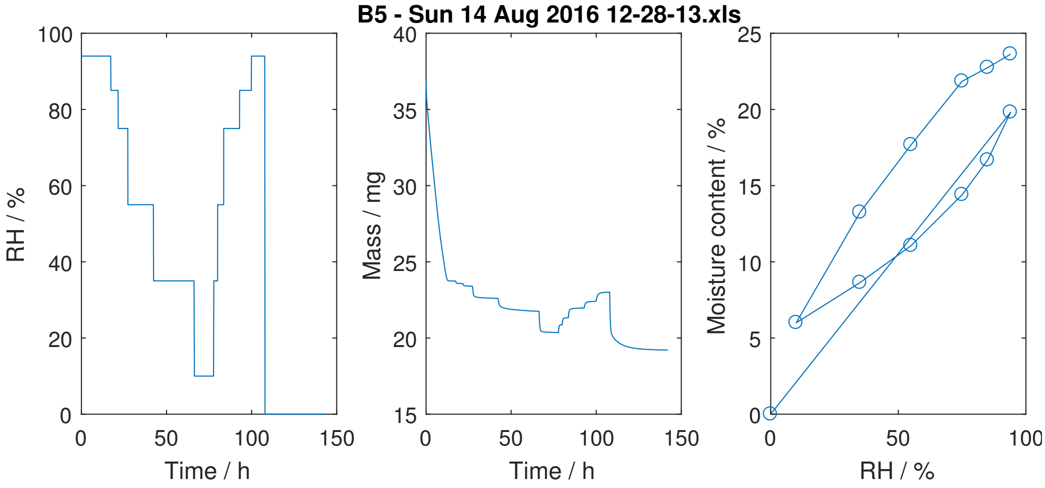

Figure A.7: *DVS results for* ***B5****. The relative humidity program in % versus time in hours (right). Sample mass in mg versus time (center). Moisture content in % of g water per g dry sample versus the relative humidity % (left).*

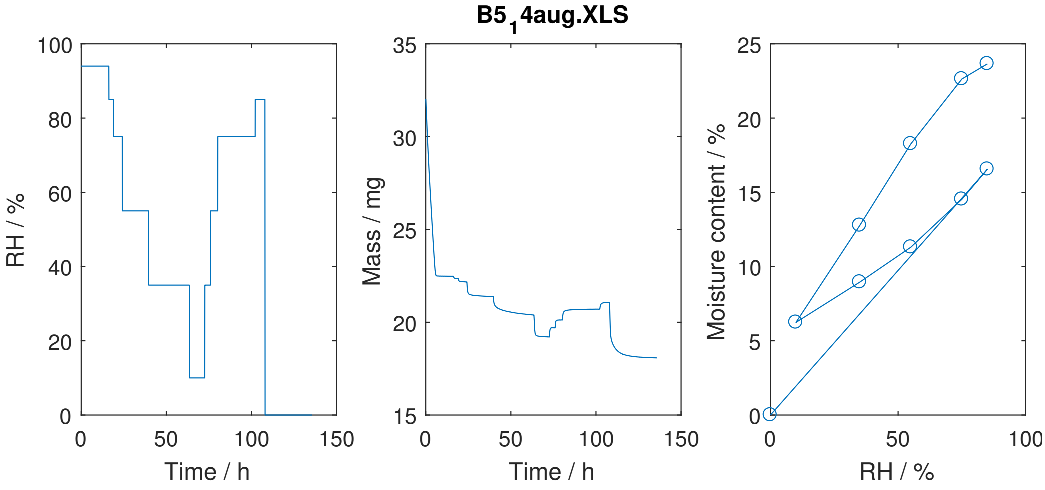

Figure A.8: *DVS results for* ***B5*** *1. repetition. The relative humidity program in % versus time in hours (right). Sample mass in mg versus time (center). Moisture content in % of g water per g dry sample versus the relative humidity % (left).*

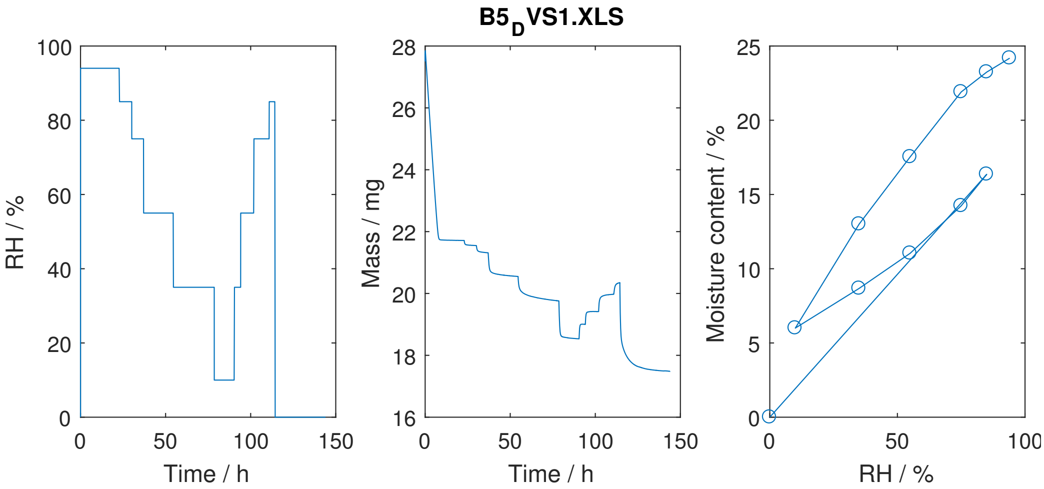

Figure A.9: *DVS results for* ***B5*** *2. repetition. The relative humidity program in % versus time in hours (right). Sample mass in mg versus time (center). Moisture content in % of g water per g dry sample versus the relative humidity % (left).*

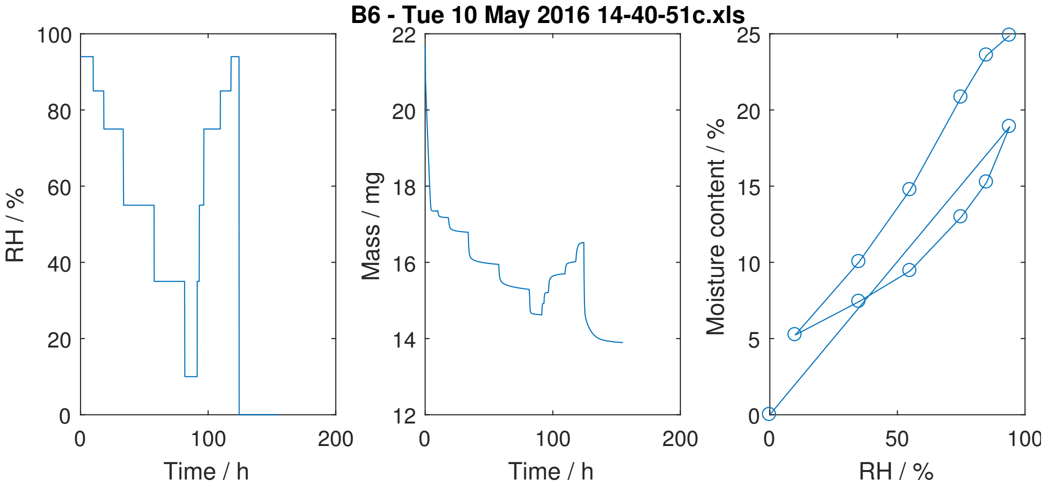

Figure A.10: *DVS results for* ***B6****. The relative humidity program in % versus time in hours (right). Sample mass in mg versus time (center). Moisture content in % of g water per g dry sample versus the relative humidity % (left).*

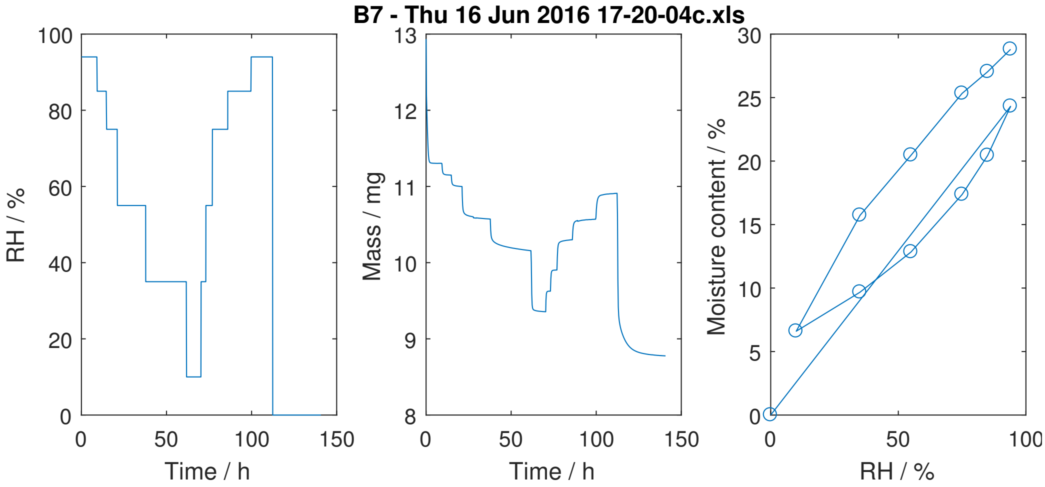

Figure A.11: *DVS results for* ***B7****. The relative humidity program in % versus time in hours (right). Sample mass in mg versus time (center). Moisture content in % of g water per g dry sample versus the relative humidity % (left).*

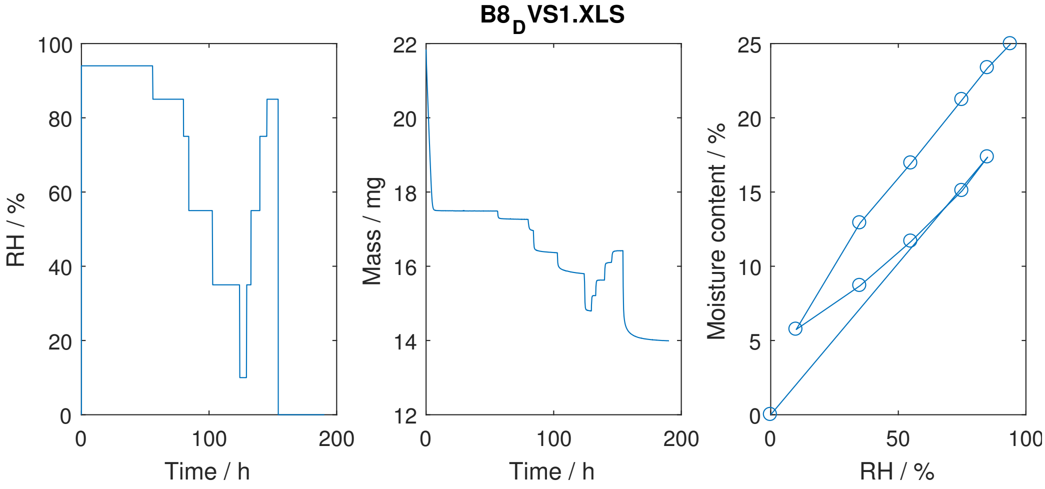

Figure A.12: *DVS results for* ***B8*** *The relative humidity program in % versus time in hours (right). Sample mass in mg versus time (center). Moisture content in % of g water per g dry sample versus the relative humidity % (left).*

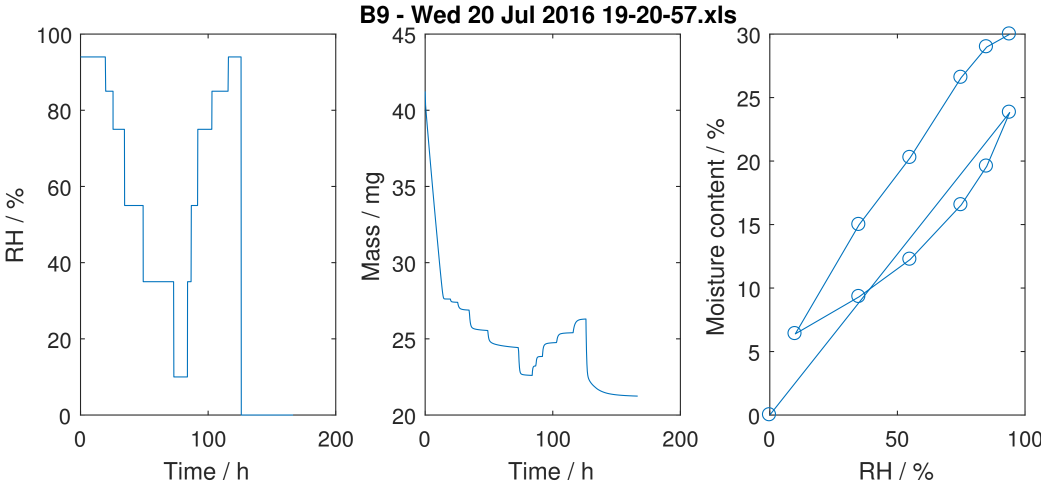

***Figure A.13**: DVS results for **B9**. The relative humidity program in % versus time in hours (right). Sample mass in mg versus time (center). Moisture content in % of g water per g dry sample versus the relative humidity % (left).*

A.2 Capillary suction test and drying test sample data

***Table A.1**: The mass and length of the samples used for capillary suction test and drying test.*

		Capillary suction samples		Drying samples	
		Mass (g)	Length (cm)	Mass (g)	Length (cm)
R1	1	192.12	31.48	-	-
	2	128.8	30.66	58.31	14.30
	3	120.9	28.83	73.47	17.87
	4	128.14	30.45	60.87	14.78
B1	1	115.28	27.33	60.86	14.76
	2	124.25	29.88	62.68	15.49
	3	122.89	29.34	58.00	14.30
B2	1	117.55	28.53	59.00	14.47
	2	123.81	29.67	47.95	14.60
	3	120.75	29.07	62.62	15.40
B3	1	125.86	30.33	60.37	14.75
	2	128.16	30.70	58.63	14.37
	3	121.12	29.57	61.18	14.88
B4	1	121.21	28.83	65.96	16.03
	2	127.83	30.47	58.85	14.38
	3	120.52	28.70	63.09	15.38
B5	1	125.55	30.10	61.88	15.15
	2	114.18	27.33	61.29	15.00
	3	122.49	29.25	61.26	14.95
B6	1	123.24	30.88	56.63	14.63
	2	121.93	30.43	58.53	14.95
	3	117.08	29.30	62.87	16.13
B7	1	105.81	25.23	64.31	15.93
	2	122.24	29.57	57.61	14.23
	3	117.27	27.98	63.64	15.58
B8	1	124.77	30.30	62.02	15.45
	2	133.36	32.27	59.18	14.60
	3	121.98	29.53	60.21	14.98
B9	1	117.21	28.72	56.05	13.97
	2	123.79	30.17	63.33	15.83
	3	118.93	28.83	60.33	15.12

A.3 Mass change during oven drying

Figures A.14-A.18 present the mass change during oven drying. The drying period was extended until the mass change of all samples has reached an equilibrium state. No significant difference in the drying rate was observed for the binder-systems B1, B2, B3 and R1, Figures A.14 and A.15. All four binders reached mass equilibrium after about 30 days of drying. The same is true for binder-system B4, Figure A.16, however, B5 continued decreasing in mass after 30 days and reached mass equilibrium after about 60 days. Binder-system B6 containing 35% limestone filler showed a more severe mass reduction which continued until after about 60 days after which mass equilibrium was reached, Figure A.17. Unfortunately, the binder-systems B7-B9 contained an experimental error as discussed in Paper II. The mass development in Figure A.18 may not represent the correct behavior of these three binder-systems.

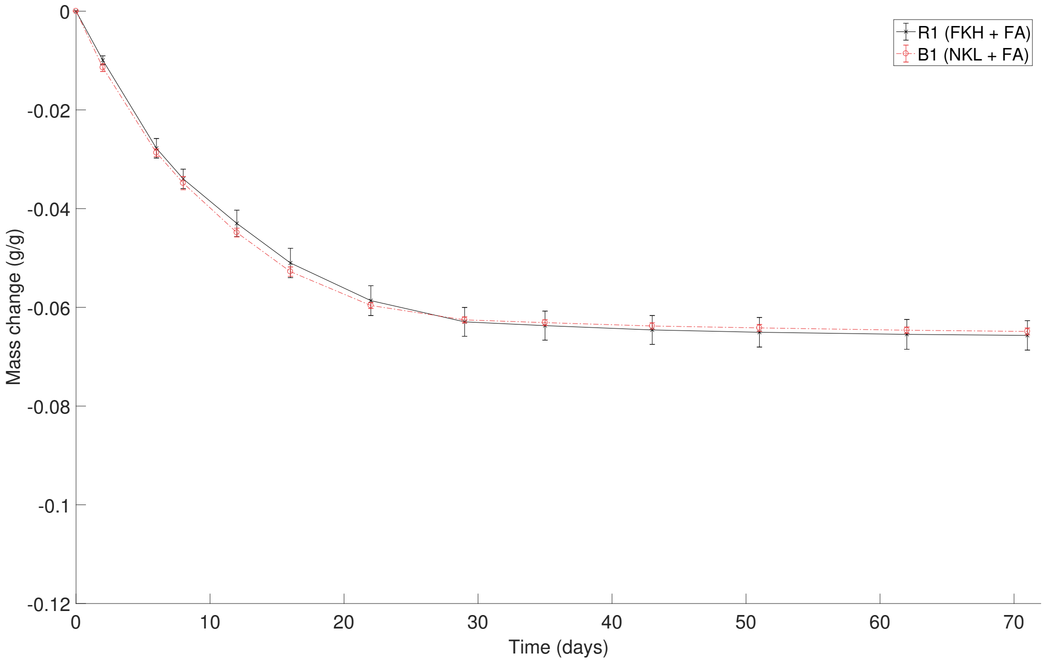

Figure A.14: *Comparing the mass change during oven drying for the K2 clinker (binder B1) and the K1 clinker (binder R1).*

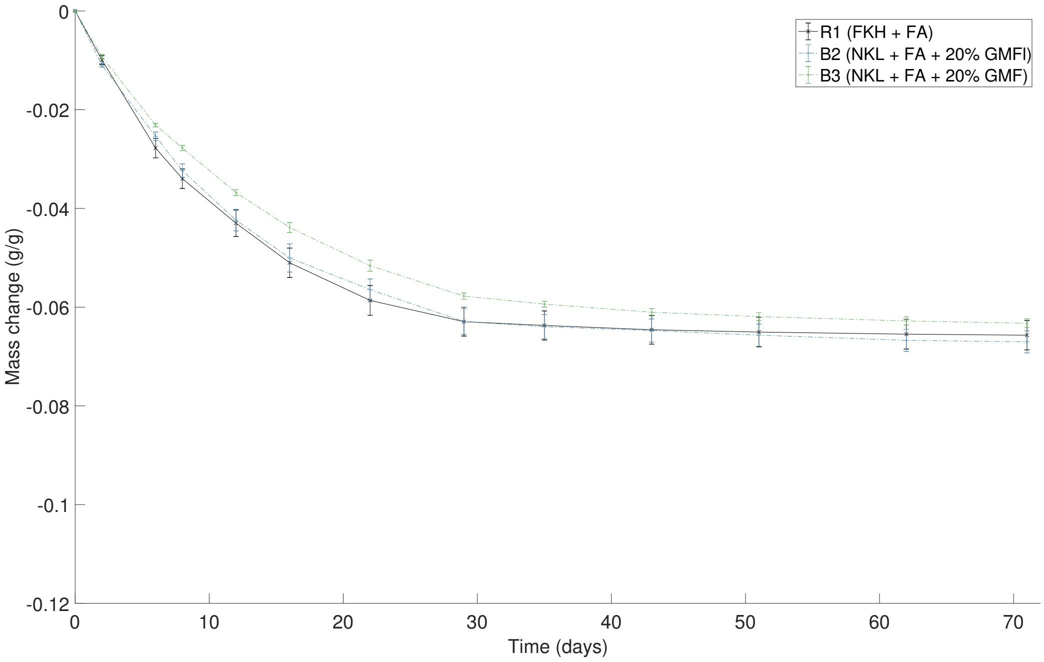

Figure A.15: *Comparing the mass change during oven drying for B2–B3 containing K2 clinker limestone filler and fly ash to the reference-binder R1.*

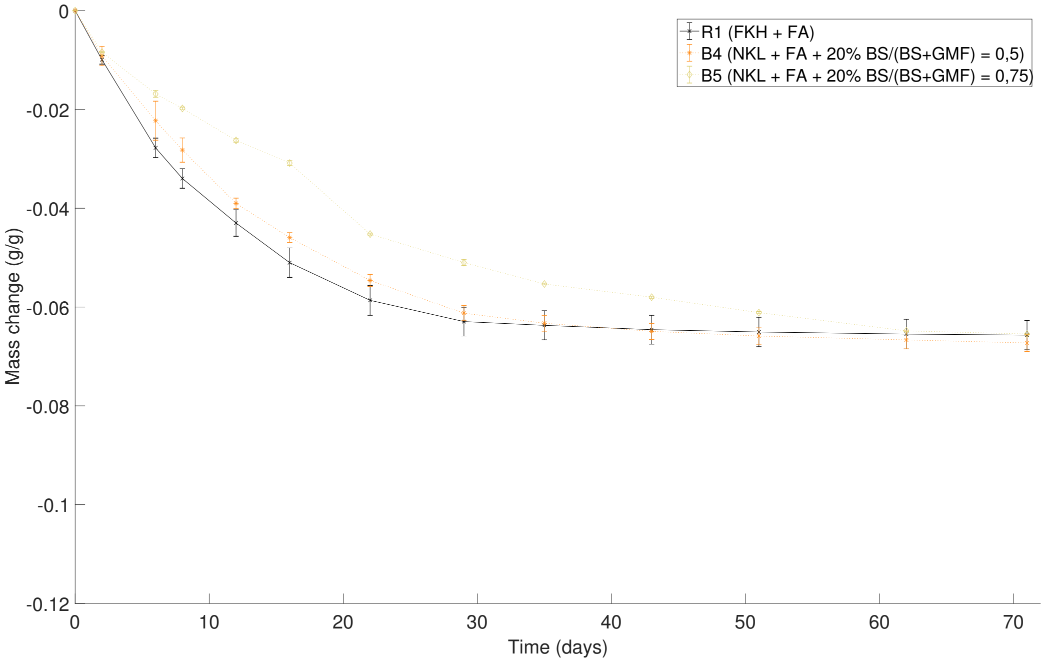

Figure A.16: *Comparing the mass change during oven drying for B4–B5 containing amounts of burnt shale and limestone filler to the reference-binder R1.*

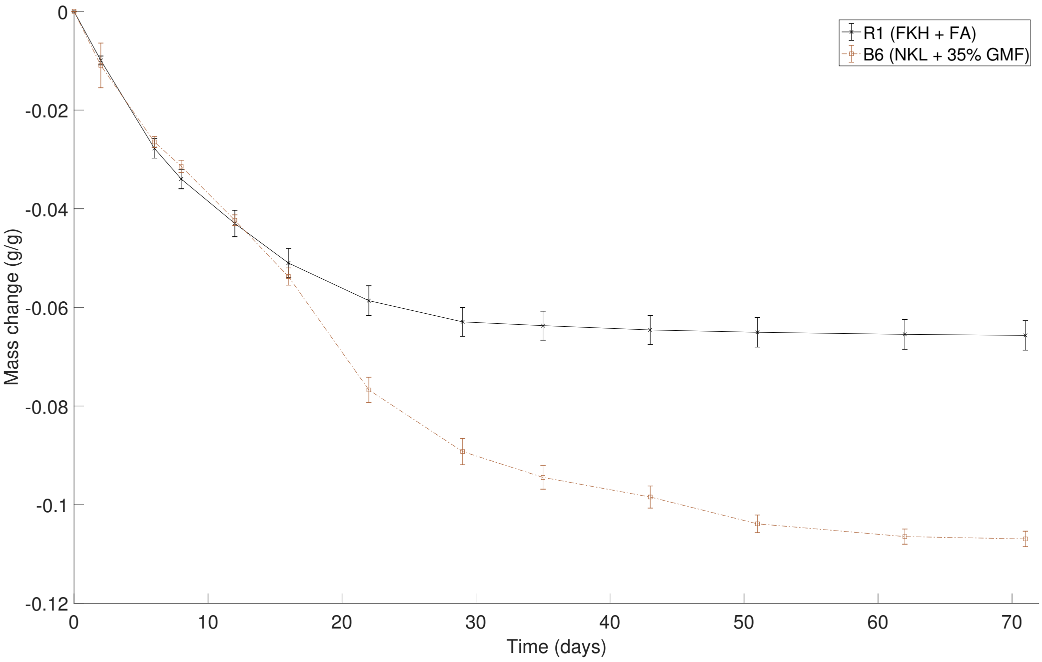

Figure A.17: *Comparing the mass change during oven drying for B6 containing K2+GMF 1 to the reference-binder R1.*

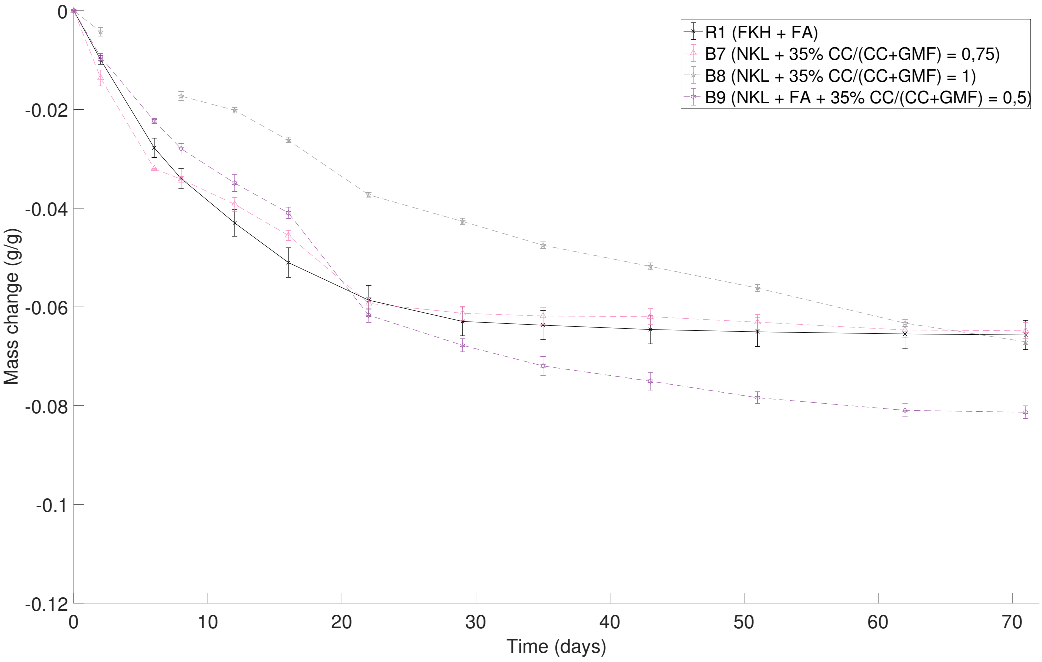

Figure A.18: *Comparing the mass change during oven drying for B7–B8 containing K2 clinker, calcined clay and limestone filler, B9 with K2 clinker, calcined clay, limestone and fly ash to the reference-binder R1.*

Part II

Appended Papers

Paper I

”Pore-scale modeling of vapor transport in partially saturated capillary tube with variable area using chemical potential”

M. Addassi & L. Schreyer & B. Johannesson & H. Lin

Published in: *Water Resources Research, 2016*

AGU PUBLICATIONS

Water Resources Research

RESEARCH ARTICLE

10.1002/2016WR019165

Key Points:

- Vapor transport through a capillary tube of variable area with liquid bridges are modeled with one equation and no fitting parameter
- Relative humidity as the dependent variable does not require modeling small temperature fluctuations, surface tension, or contact angles
- Enhancement factor depends on relative humidity boundary conditions, distance between liquid bridges, and bridge lengths

Supporting Information:

- Supporting Information S1

Correspondence to:
L. Schreyer,
Lynn.Schreyer@wsu.edu

Citation:
Addassi, M., L. Schreyer, B. Johannesson, and H. Lin (2016), Pore-scale modeling of vapor transport in partially saturated capillary tube with variable area using chemical potential, *Water Resour. Res.*, *52*, doi:10.1002/2016WR019165.

Received 5 MAY 2016
Accepted 23 AUG 2016
Accepted article online 29 AUG 2016

Pore-scale modeling of vapor transport in partially saturated capillary tube with variable area using chemical potential

Mouadh Addassi[1], Lynn Schreyer[2], Björn Johannesson[3], and Hai Lin[4]

[1]Technical University of Denmark, Lyngby, Denmark, [2]Washington State University, Pullman, Washington, USA, [3]Linnaeus University, Växjö, Sweden, [4]University of Colorado Denver, Denver, Colorado, USA

Abstract Here we illustrate the usefulness of using the chemical potential as the primary unknown by modeling isothermal vapor transport through a partially saturated cylindrically symmetric capillary tube of variable cross-sectional area using a single equation. There are no fitting parameters and the numerical solutions to the equation are compared with experimental results with excellent agreement. We demonstrate that isothermal vapor transport can be accurately modeled without modeling the details of the contact angle, microscale temperature fluctuations, or pressure fluctuations using a modification of the Fick-Jacobs equation. We thus conclude that for a single, axisymmetric pore, the enhancement factor depends upon relative humidity boundary conditions at the liquid bridge interfaces, distance between liquid bridges, and bridge lengths.

1. Introduction

Vapor transport in variably saturated soils is traditionally modeled using a system of equations including the equation representing the conservation of mass, a multiphase Darcy equation, and a version of the Philip and deVries equation [*Philip and de Vries*, 1957] for heat transfer. Typically, the continuity equations and multiphase Darcy equation are combined to form one equation with one unknown: usually moisture content or capillary pressure (which is equivalent to liquid pressure if the gas phase is assumed to be at constant pressure) [*Bear*, 1972; *Moradi et al.*, 2015]. An alternative formulation uses the matric potential—a potential that incorporates capillary potential and adsorption [*Marshall et al.*, 2006]. The term *potentials* is generalized here to include quantities that are mathematically defined as primary dependent variables. Each potential has advantages and disadvantages for quantitative analysis; for example, the capillary potential and matric potential are discontinuous at the macroscale liquid front, the capillary pressure and matric potential can vary by order of magnitudes leading to numerical instabilities, and water content in the form of saturation is not appropriate for swelling soils where 100% saturation does not give full information about water content. Use of these potentials can be difficult in more complicated situations such as three-phase flow, phase transfer due to the presence of, e.g., ice, or flow through expansive soils where swelling forces add to the myriad of other microscopic forces influencing water movement. Although other potentials have been considered (chemical potential, for example, has been used in the process of developing models mechanistically [*Cary*, 1963; *Raats*, 1975; *Bénet et al.*, 2009]), a model using alternative potentials has rarely, to these authors' knowledge, been seriously considered, perhaps because experiments are traditionally designed to measure quantities such as capillary pressure and saturation.

If we look to adjacent fields, especially building materials, we find that a wider variety of potentials are being considered for use [*Janssen*, 2014; *Arfvidsson and Claesson*, 2000; *Delgado et al.*, 2013]. While capillary pressure and moisture content are commonly used for moisture transport through concrete and wood [e.g., *Burch and Chi*, 1997], other potentials are also being explored. Examples include chemical potential [*Siau*, 1983], logarithm of capillary pressure [*Pedersen*, 1992; *van Schijndel*, 2011], relative humidity [*Bazant and Xi*, 1993; *Kunzel*, 1995; *Grasley et al.*, 2006; *Huang et al.*, 2015; *Johannesson and Nyman*, 2010], and even the Kirchhoff potential [*Arfvidsson and Claesson*, 2000]. Some of the advantages and disadvantages of these potentials are outlined by *Janssen* [2014].

Here we describe the use of the chemical potential, which for all practical purposes is equivalent to relative humidity under isothermal conditions, and demonstrate its utility by modeling an experiment designed to explain the effect of isolated liquid bridges (liquid trapped within a pore structure with gas on either side and no gas connecting path) on the *enhancement factor*. The enhancement factor is a macroscale parameter that takes into account microscale processes that cause "enhanced" diffusion and are used in macroscopic moisture transport models that incorporate heat transfer that are based on or generalizations of the model developed by Philip and de Vries [*Philip and de Vries*, 1957]. Defined as the ratio of the vapor flux in a partially saturated porous media divided by the vapor flux in "dry" (very low moisture content) porous media (based on Fick's law), it has been experimentally determined to range between 3 (at low-moisture content) and 18 (at high-moisture content) for lab and field scale experiments [*Gurr et al.*, 1952; *Taylor and Cavazza*, 1954; *Cary*, 1966; *Jackson et al.*, 1974; *Cass et al.*, 1984; *Assouline et al.*, 2013]. The incorporation of an enhancement factor is common [*Wildenschild and Roberts*, 2001; *Saito et al.*, 2006; *Sakai et al.*, 2009; *Gonzalez et al.*, 2012], although several studies have demonstrated a lack of agreement between theory and experiments [*Cahill and Parlange*, 1998; *Smits et al.*, 2011; see also *Shokri et al.*, 2009, and references therein].

The experiment we chose to simulate is conducted at the pore scale, for which most modeling approaches involve incorporating some or all of: the pressures of the liquid and gas phase, the contact angle and/or surface tension, disjoining pressure, and temperature (incorporating the latent heat of evaporation) [see, e.g., *Philip*, 1964; *Shahraeeni and Or*, 2010, 2012; *Wang and Catton*, 2001; *Gray and Miller*, 2014]. Here we conceptually explore modeling vapor transport directly using the chemical potential (relative humidity for water) as the primary unknown.

The chemical potential is a natural dependent variable because of its properties. One definition of the chemical potential is the change in Gibbs energy required to insert a mole of a species j into the system keeping temperature, number of moles of other species, and pressure fixed [*Castellan*, 1983]. The properties of the chemical potential include that (1) it is the potential for diffusive flow [*Castellan*, 1983], (2) at equilibrium the chemical potentials of one component coexisting in two phases are equal [*Castellan*, 1983], and (3) the rate of phase change is proportional to the difference in the chemical potentials [*Bennethum et al.*, 1996, 2000; *Bénet et al.*, 2009].

Here we consider vapor transport through a partially saturated cylindrically symmetric capillary tube with variable cross-sectional area at constant temperature, although the results can be generalized to nonisothermal conditions (see section 4).

In the next section we derive the governing equation, and then we compare the numerical results with experimental results under a variety of conditions. We follow this with some concluding remarks.

2. Governing Equations

Our goal is to derive the governing equation for mass transport of water vapor in terms of the relative humidity through a cylindrically symmetric pore that may be partially saturated and whose radius varies.

We first convert the diffusive equation, typically written using concentration as the dependent variable, to one in which the relative humidity is the dependent variable. Then, we introduce the upscaled version of this equation called the Fick-Jacobs equation that accounts for changes in capillary cross-sectional area.

For this derivation we make the following assumptions:

1. The gas phase has two components—water vapor g_v and dry air g_a.
2. The water vapor and dry air can each be considered as an ideal gas.
3. We assume that evaporation/condensation is dominated by diffusion, i.e., that the chemical potential of the liquid and gas phases at an interface are approximately equal. Thus, evaporation or condensation occurs only as the gaseous water molecules diffuse away from the interface causing water molecules to condense or evaporate as is appropriate to keep the thermodynamic equilibrium at the interface.
4. The mass-averaged velocity of the gas phase is negligible relative to the diffusion of the water vapor with respect to the gas phase [*Whitaker*, 1991; *Bird et al.*, 2007].
5. Within the isolated liquid phases the pressure and concentration variations are assumed negligible.
6. The water vapor in the gas phase is sufficiently dilute that the molar mass of the gas phase can be treated as constant.
7. The temperature T and gas phase pressure p^g variations are negligible.

We begin with the conservation of mass (continuity equation) and a generalized Fick's law to derive the governing equation in terms of relative humidity. Notation section provides details of the governing equation derivation, numerical validation of the governing equation, and details regarding the experimental geometry.

The conservation of mass assuming no loss or gain of mass except at the boundaries of the domain in terms of the density of component *j* of the gas phase ρ^{g_j} is given by

$$\frac{\partial \rho^{g_j}}{\partial t} = -\nabla \cdot \left(\rho^{g_j} \mathbf{v}^{g_j}\right).$$

Adding and subtracting $\nabla \cdot \left(\rho^{g_j} \mathbf{v}^{g}\right)$ and using assumption (4) we obtain

$$\frac{\partial \rho^{g_j}}{\partial t} = -\nabla \cdot \left(\rho^{g_j} \mathbf{v}^{g_j,g}\right), \tag{1}$$

where $\mathbf{v}^{g_j,g} = \mathbf{v}^{g_j} - \mathbf{v}^{g}$ is the diffusive velocity of component *j* in the gas phase and $\mathbf{v}^{g}$ is the bulk velocity of the gas phase (see notation section).

To close the system we use a generalized version of Fick's law to eliminate the diffusive velocity. Fick's law states that diffusion is proportional to either molar or mass fraction gradient, e.g., for mass fraction [*Bird et al.*, 2007]

$$\rho^{g_j} \mathbf{v}^{g_j,g} = -\rho^{g} D^{g_j} \nabla C^{g_j}, \tag{2}$$

where D^{g_j} is the diffusion coefficient for Fick's law, C^{g_j} is the mass fraction, and $\rho^{g} = \rho^{g_v} + \rho^{g_a}$. However, we will use a generalized version of Fick's law, generally reserved for diffusion of a charged species [*Castellan*, 1983]

$$\rho^{g_j} \mathbf{v}^{g_j,g} = -D_{\mu}^{g_j} \left(\frac{\rho^{g_j}}{R^{g_j} T}\right) \nabla \mu^{g_j}, \tag{3}$$

where μ^{g_j} is the mass-weighted chemical potential (see notation section), *T* is (absolute) temperature, and R^{g_j} is the specific gas constant for component *j*. As this is currently written, the units of $D_{\mu}^{g_j}$ has units of length^2 per time.

To determine the relationship between $D_{\mu}^{g_j}$ and D^{g_j} from (2), we begin with the relationship between the chemical potential of an ideal gas in a mixture μ^{g_j} and its molar fraction given by the ratio of the partial pressure p^{g_j} and total pressure of the mixture p^{g} [*Castellan*, 1983]

$$\mu^{g_j}(T,p) = \mu_{*}^{g_j}(T,p) + R^{g_j} T \ln \left(\frac{p^{g_j}}{p^{g}}\right), \tag{4}$$

where $\mu_{*}^{g_v}$ is the chemical potential of pure *j* gas at pressure *p* and temperature *T*. Assuming the water vapor and dry air can be treated as an ideal gas (Assumption (2)), we have

$$p^{g_j} = R^{g_j} T \rho^{g_j}. \tag{5}$$

If the water vapor is sufficiently dilute so that the molecular mass of the gas phase M^{g} can be treated as a constant (Assumption (6)) we have

$$\nabla \mu^{g_j} = \frac{R^{g_j} T}{C^{g_j}} \nabla C^{g_j}. \tag{6}$$

Substituting (6) into (3) to eliminate $\nabla \mu^{g_j}$ and then comparing with (2) we find that

$$D_{\mu}^{g_j} = D^{g_j}.$$

Thus for the remainder of the paper we will not distinguish between $D_{\mu}^{g_j}$ and D^{g_j}, and just use D^{g_j}. The reader however should note that these two diffusion coefficients are only the same when the mixture is dilute enough that the molar mass of the gas phase can be treated as a constant.

We next rewrite the continuity equation in terms of relative humidity, ϕ. Relative humidity is defined to be the ratio between the water vapor pressure and the water vapor pressure at saturated conditions at the same temperature

$$\phi = \frac{p^{g_v}(\rho^{g_v},T)}{p^{g_v}_{sat}(T)} = \frac{\rho^{g_v}(p^{g_v},T)}{\rho^{g_v}_{sat}(T)}, \tag{7}$$

where the second equality is a consequence of using the ideal gas law (5). Using (7) and (4) to determine the relationship between the chemical potential and the relative humidity yields

$$\mu^{g_v} = \mu_*^{g_v} + R^{g_j} T \ln(\phi) + R^{g_j} T \ln\left(\frac{p^{g_v}_{sat}(T)}{p^g}\right). \tag{8}$$

Using (8) to eliminate the chemical potential from the generalized Fick's law (3), while assuming that variations in the gas phase pressure and temperature are negligible (so that we may assume p^g, T, and $p^{g_v}_{sat}$ are constants), we obtain

$$\rho^{g_v}\mathbf{v}^{g_v,g} = -D^{g_v}\frac{\rho^{g_v}}{\phi}\nabla\phi. \tag{9}$$

Using the ideal gas law (5) twice, we also have

$$\frac{\partial\rho^{g_v}}{\partial t} = \frac{1}{R^{g_v}T}\frac{\partial p^{g_v}}{\partial t} = p^{g_v}_{sat}\frac{1}{R^{g_v}T}\frac{\partial\phi}{\partial t} = \rho^{g_v}_{sat}\frac{\partial\phi}{\partial t}. \tag{10}$$

Using (9) and (10) into the conservation of mass (2), we have the continuity equation in terms of the relative humidity

$$\begin{aligned} \rho^{g_v}_{sat}\frac{\partial\phi}{\partial t} &= D^{g_v}\nabla\cdot\left(\frac{\rho^{g_v}}{\phi}\nabla\phi\right), \\ \frac{\partial\phi}{\partial t} &= D^{g_v}\nabla\cdot(\nabla\phi), \end{aligned} \tag{11}$$

where we used (7) and we again assumed that temperature changes are negligible so that $\rho^{g_v}_{sat}$ can be treated as a constant. Equation (11) is our governing equation.

Assuming diffusion is through a cylindrically symmetric tube with variable cross-sectional area we can use a one-dimensional approximation to the diffusion equation (11). The derivation of this equation is provided in Supporting Information. Let $A(x)$ be the cross-sectional area which varies along the longitudinal direction x, and define the area-averaged relative humidity as

$$\bar{\phi}(x,t) = \frac{1}{A(x)}\int_{A(x)}\phi(x,y,z,t)\,dy\,dz. \tag{12}$$

Then the Fick-Jacobs equation [*Jacobs*, 1967; *Patlak*, 1973] can be written as

$$\frac{\partial\bar{\phi}}{\partial t} = D^{g_v}\left(\frac{\partial^2\bar{\phi}}{\partial x^2} + \frac{1}{A(x)}\frac{\partial\bar{\phi}}{\partial x}\frac{dA}{dx}\right). \tag{13}$$

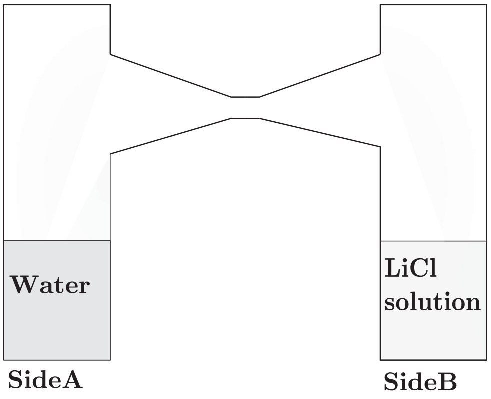

Figure 1. Experimental apparatus.

The first term on the right-hand side is the term resulting from the classical one-dimensional diffusion equation, and the second term is the modification due to changing area. This equation is the basis for further modifications, examples of which are given by *Zwanzig* [1992], where the diffusion coefficient D is modified, and *Kalinay and Percus* [2005, 2006] where the coordinate x is transformed. We numerically compared solutions of (13) with the solutions of the three-dimensional diffusion equation (11) and found the solutions to be remarkably similar (see Supporting Information).

3. Comparison With Experiments

In this section we use the transport equation in terms of relative humidity (equation (13)) to model

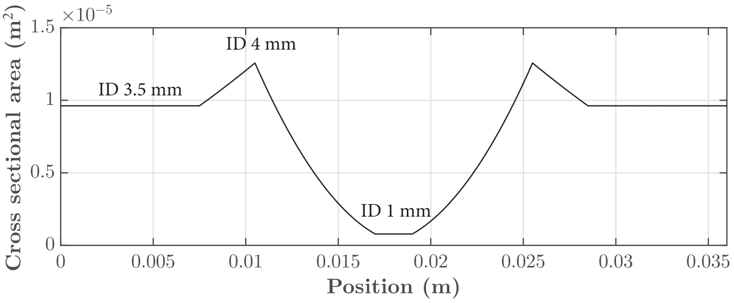

Figure 2. Cross-sectional area versus distance from base at side A.

vapor transport through a partially saturated capillary tube and compare with experimental results. Because the primary independent variable is the chemical potential (rewritten in terms of the relative humidity) which is continuous between phases at equilibrium, we do not attempt to model the air-liquid interfaces explicitly. Instead, we assume that even in the non–steady state case the vapor transport is dominated by vapor diffusion (and not evaporation or condensation) to determine how accurately we capture the physics with this simple expression. *We use no fitting parameters*.

The experimental data were obtained by experiments performed by T. S. Silverman for a MS thesis in 1999 [*Silverman*, 1999] under the supervision of John Wilson at New Mexico Institute of Mining and Technology.

3.1. Experimental Setup

The setup, given in Figure 1, consists of a glass apparatus where two liquid reservoirs are separated by a bridge that is either completely filled with an air-water vapor, or has a "liquid bridge." The reservoir on the left side (denoted as side A) is pure water and thus the boundary condition on the air-side of the liquid-air interface is 100% relative humidity. The reservoir on the right side is a saturated solution and thus the boundary condition on the right side (denoted as side B) is fixed at less than 100%, causing water to evaporate from the left side and to condense on the right side. If a liquid bridge exists, then the water transport is affected by the length of the bridge. The rate of transport is measured by taking pictures and noting the change in height of the two columns of reservoir fluids. The goal is to determine how the length of the bridge affects the movement of water vapor and to predict the vapor transport using equation (11).

The details of the geometry are given in the Supporting Information; however, here we mention that the horizontal distance between the center of the two reservoirs is 20 mm, the inner diameter of the two columns containing the reservoirs is 3.5 mm, and the maximum inner diameter for the bridge component is 4 mm which narrows to 1 mm at the center. In Figure 2, we see how the cross-sectional area varies with position, as measured from the base at side A. The cross-sectional area narrows at the center of the horizontal member, and the cross-sectional area was approximated at the 90° bends as linearly increasing between the area of the vertical members to the area of the horizontal member, neglecting the excess volume at the 90° bends.

All experiments used pure water (relative humidity of 100%) in the column at side A, while the column on the right contained a saturated LiCl solution (relative humidity at saturation of 11%) with solid LiCl crystals at the bottom to ensure brine saturation. Because the chemical potential of a component in a mixture (water with LiCl) is less than the chemical potential of the pure component (pure water), the difference in chemical potentials drives water movement (in the form of water vapor) from left to right. As can be seen from equation (8) if the gas pressure and temperature are constant, a decrease in chemical potential means the relative humidity decreases—hence we would expect the relative humidity of the air above the column containing the LiCl solution to be less than the relative humidity of pure water, and this is indeed the case.

Table 1. Water Activity for $Ca(NO_3)_2$ at 29°C

$Ca(NO_3)_2$ concentration (molarity)	1	1.5	2	2.6	3	3.5	4	4.4	5
Relative humidity	95	93	89	85	80	75	68	63	58

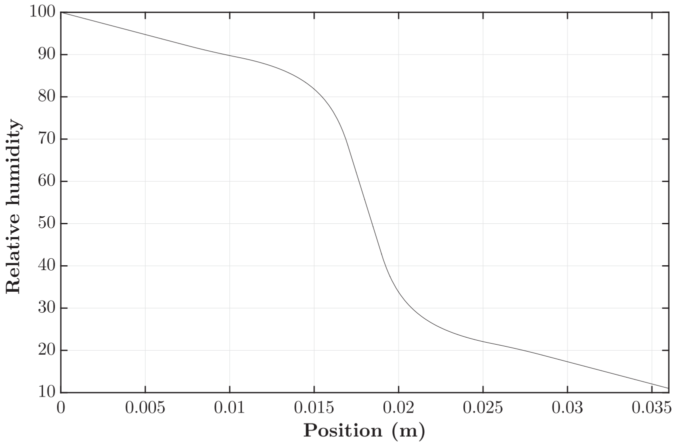

Figure 3. Numerical solution for relative humidity versus distance from base at side A with no bridge.

The relative humidity at the liquid-gas interface at side A is 100%, and the relative humidity at the liquid-gas interface at side B is held at 11% because it is saturated. If the LiCl solution were to become diluted, then the chemical potential on side B would increase and consequently the relative humidity boundary condition would increase with time. Likely, LiCl was used because of the low water chemical potential it produces when saturated and ease of access. The liquid used for the liquid bridge was a $Ca(NO_3)_2$ solution, and likely this solution was used because the relative humidity (or equivalently, chemical potential) at the solution-gas interface was between 11 and 100% for a wide range of concentrations (see Table 1).

3.2. Comparison With Data

First consider the case of no bridge. According to equation (13), the solution at steady state would be linear if the cross-sectional area was constant, but due to the varying cross-sectional area, the solution is nonlinear.

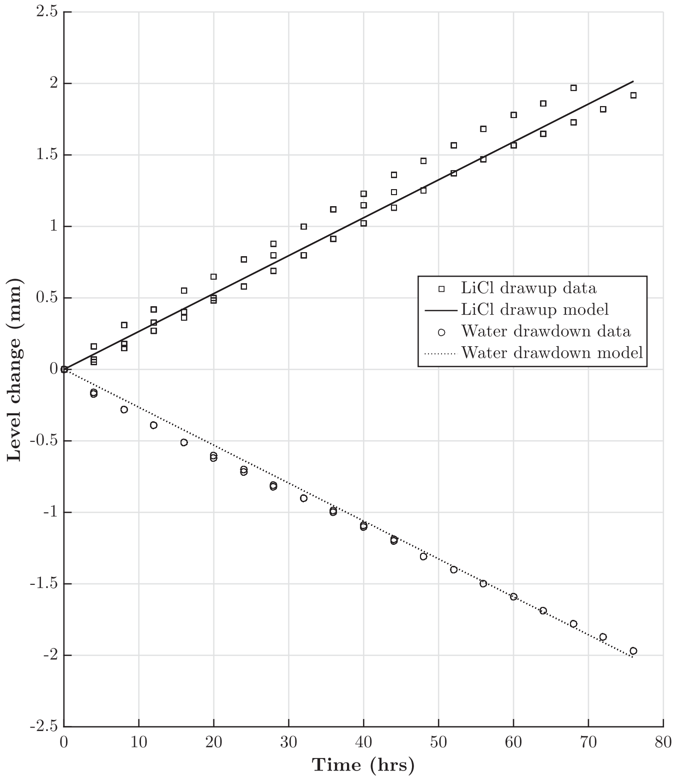

Figure 4. *Silverman* [1999] experimental data and numerical solution of drawdown at side A and drawup at side B with no bridge.

Technically, the liquid density on side A is not precisely the same as the density on side B due to the different concentrations. But this difference is second order and beyond the resolution of the experimental data. Here we used the steady state version of (13) with the following boundary conditions:

$$\frac{d^2\bar{\phi}}{dx^2}+\frac{1}{A(x)}\frac{d\bar{\phi}}{dx}\frac{dA}{dx}=0,\qquad \bar{\phi}(0)=1,\qquad \bar{\phi}(L)=0.11. \tag{14}$$

The relative humidity profile of the analytical solution is provided in Figure 3. The distance is given in meters and note that the location of the most rapid change of the relative humidity is where the cross-sectional area is most narrow.

The comparison between the experimental and analytical results is provided in Figure 4 in a chamber that was roughly at a temperature of 29°C. The line with a positive slope gives the predicted *drawup* of side B, and the negatively sloped dashed line gives the predicted *drawdown* of side A. The Silverman experimental results include the data from three runs, each lasting 80 h and each resulting with the same steady state vapor flux. The drawdown data for each of the three runs almost lie on top of each other [*Silverman*, 1999]. The numerical versus data results seem reasonable and promising.

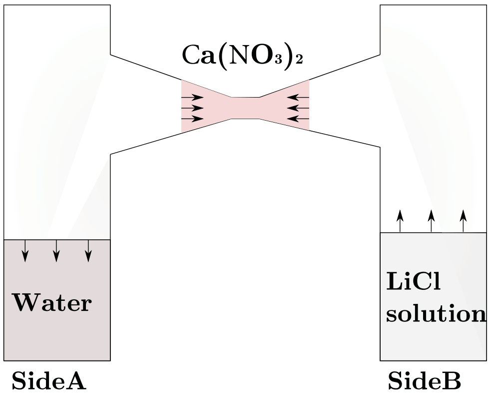

Figure 5. Experimental setup with bridge with arrows indicating direction of interfacial movement.

Next consider the case where we have an initial 9 mm bridge. A cartoon of the setup is illustrated in Figure 5. Again, the relative humidity boundary condition at side A is $\bar{\phi}=1.0$ and at side B is $\bar{\phi}=0.11$. The bridge is approximately centered at the middle of the apparatus and is initially composed of a calcium nitrate $\mathrm{Ca(NO_3)_2}$, with the quantity initially injected controlling the length of the bridge. There is inconsistency in *Silverman* [1999] regarding whether the initial concentration is 2.6 *molality* (as reported in the text) or 2.6 *molarity* (as reported in the data). This affects the boundary condition on either side of the bridge with 2.6 molality resulting in a boundary condition of 71% relative humidity and 2.6M resulting in a boundary condition of 85% relative humidity. By studying the data in *Silverman* [1999, Appendix E] (using the provided initial mass of the bridge and the provided density), and that it is stated in the thesis that “the vapor pressure of a saturated calcium nitrate solution (approximately 50%) was nearly midway between those of the two end-member” [*Silverman*, 1999] we concluded that the units must be the molality. This was further confirmed by the model. We used *molality* for all numerical experiments presented here.

The liquid pressure and concentration variation within the bridge is assumed to be negligible so that the relative humidity on either side of the bridge is assumed to be the same. However, as the experiment progresses in time there is a net change of liquid water in the bridge changing the concentration (and hence the relative humidity on either side of the bridge). The relative humidity (or activity) in equilibrium with a $\mathrm{Ca(NO_3)_2}$ solution was determined using the data provided in Table 1, where the water activity for $\mathrm{Ca(NO_3)_2}$ solutions at a variety of concentrations were determined by experiments conducted at the University of Colorado Denver Chemistry Department using a Water Activity Meter (using series 3TE AquaLab instrument). The concentration was measured in units of molarity (moles of $\mathrm{Ca(NO_3)_2}$ per liter of water), and then converted to units of molality for use in our model.

Comparing the relative humidity gradients at the experimental conditions, we found that initially the vapor transport on the right side of the bridge (side B) is considerably higher than that of the left side of the bridge (side A). Thus, we expect that the rate of condensation on the left side of the bridge is much less than the rate of evaporation on the right side of the bridge, resulting in a reduction in the length of the bridge (as noted in the experiment), a change of the bridge concentration, and a change in the relative humidity boundary conditions on either side of the bridge.

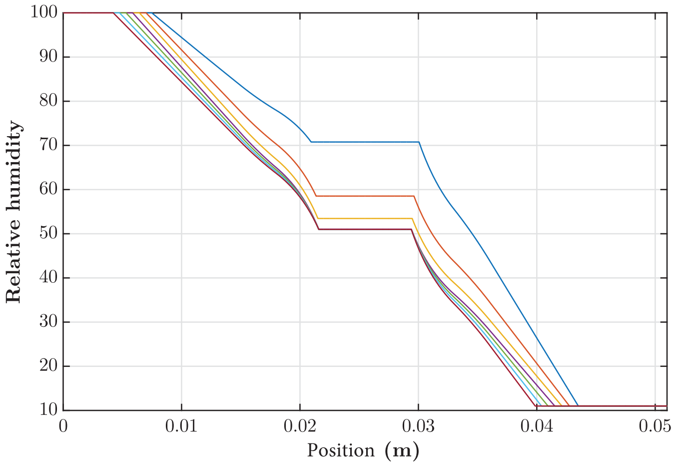

Figure 6. Numerical solution of (15)–(17) for 9.1 mm initial bridge length. The initial condition is in blue.

The numerical solution to this problem was obtained by solving the Fick-Jacobs equation (13), with an initial concentration of calcium nitrate in the bridge providing the initial relative humidity $\bar{\phi}_0$ at either side of the bridge

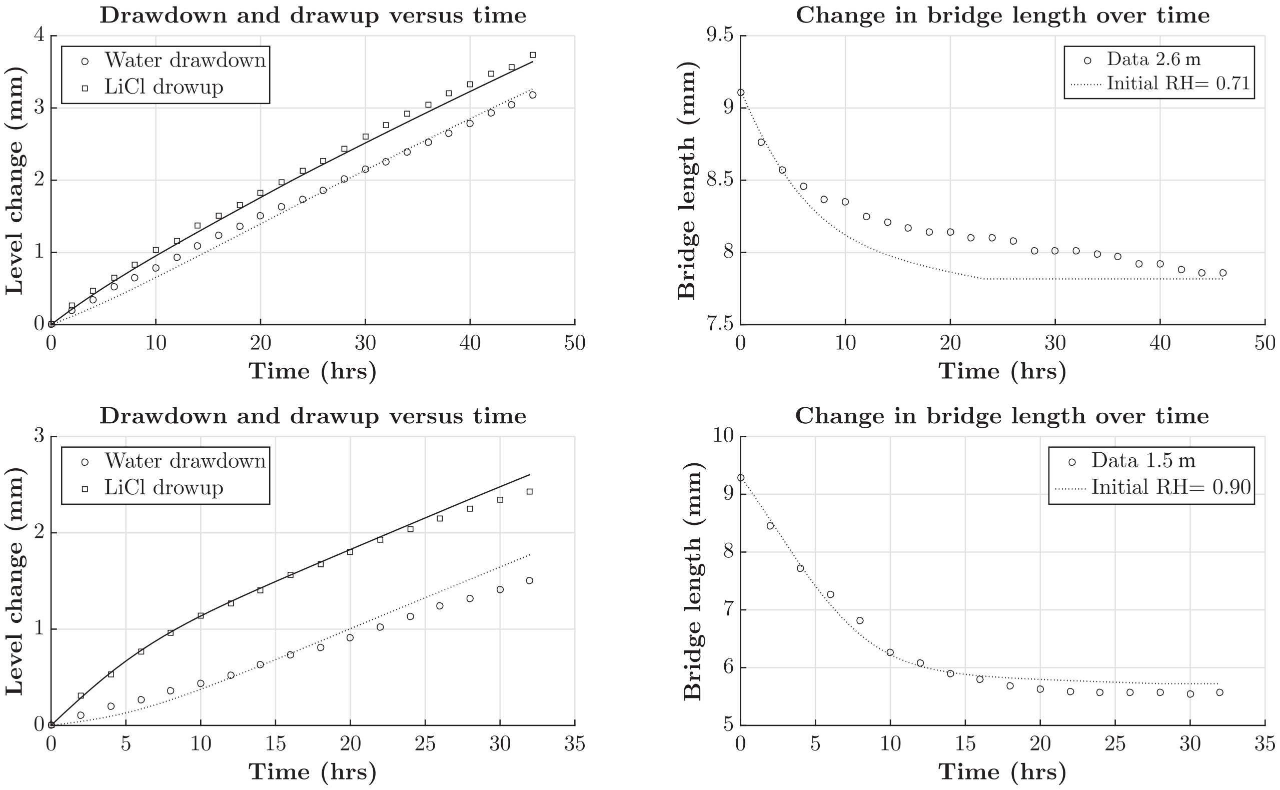

Figure 7. Numerical and *Silverman* [1999] data for drawdown, drawup, and change in 9.1 mm bridge length for two different bridge initial concentrations: 2.6 molality (top) and 1.5 molality (bottom).

$$\frac{\partial \bar{\phi}}{\partial t}=D^{g_v}\left(\frac{\partial^2 \bar{\phi}}{\partial x^2}+\frac{1}{A(x)}\frac{\partial \bar{\phi}}{\partial x}\frac{dA}{dx}\right), \tag{15}$$

$$\bar{\phi}(x=0,t)=1, \quad \bar{\phi}(x=L,t)=.11 \qquad t \geq 0, \tag{16}$$

$$\bar{\phi}(x,t=0)=\begin{cases} 1 & x=x_A \text{ (at reservoir interface Side A)} \\ \text{linear} & x \in \text{Side A} \\ 0.71 & x \text{ at bridge interface Side A} \\ 0.71 & x \text{ at bridge interface Side B} \\ \text{linear} & x \in \text{Side B)} \\ 0.11 & x=x_B \text{ (at reservoir interface Side B)} \end{cases}, \tag{17}$$

where “linear” refers to a linear interpolation in the region between the two interfaces.

The problem was solved as follows:

1. The change of the bridge volume is calculated using the difference in mass fluxes between side A and side B from the previous time step.
2. The new bridge concentration and resulting relative humidity of the bridge is calculated using the updated bridge volume.
3. The position of the liquid-gas interfaces are updated based on the mass flux of side A and side B from the previous time step.

The numerical result for the solution to (15)–(17) are presented in Figure 6 with ϕ_0=71%. Note that as the solution evaporates from the left the boundary at side A moves down (or left), and conversely on the right. Over time the bridge shortens.

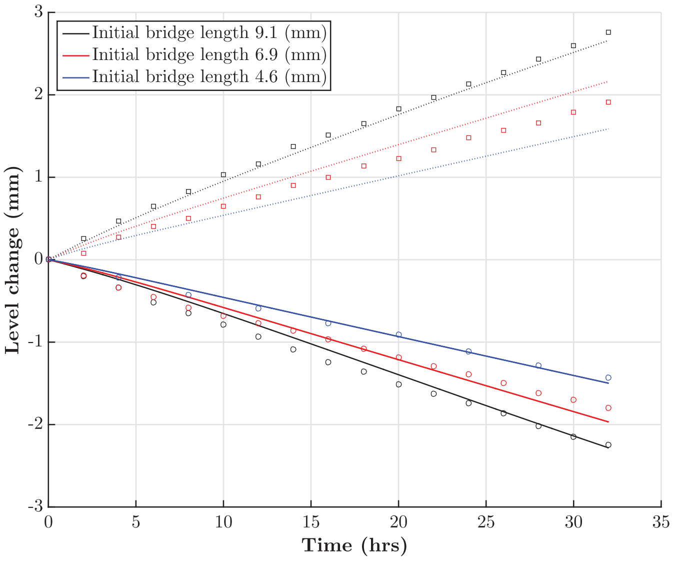

Figure 8. Numerical and *Silverman* [1999] experimental data for drawdown and drawup for three initial bridge lengths (no experimental data available for drawup of 4.6 mm length bridge).

Silverman [1999] performed the experiment with two different bridge concentrations, 2.6 molality and 1.5 molality, and the comparison with the numerical model is presented in Figure 7. Note that the lower concentration bridge (1.5 molality) which corresponds to a higher relative humidity at the bridge boundaries (90%) results in a faster change of bridge length and a shorter steady state bridge length at steady state as can be explained by the different rates of evaporation on side B due to the larger relative humidity gradient.

The comparison of experimental results with numerical results for three bridge lengths is presented in Figure 8. The initial bridge lengths were 9.1, 6.9, and 4.6 mm. We note that there is remarkable agreement given that there is no fitting parameter. The length measurements were made with a standard 12 inch ruler [*Silverman*, 1999], and as stated in *Silverman* [1999, p. 10] that "change in position of the meniscus in the projected image could be measured to within 0.5mm." So experimental and numerical differences of 0.4 mm would not be unexpected.

Lastly, we consider the enhancement factor. The enhancement factor was originally defined by *Philip and de Vries* [1957] in terms of a modified diffusion coefficient to explain the experimental speedup of diffusion in porous media where it was assumed that the enhanced diffusion was due to microscale thermal gradients and the presence of a liquid phase. It is defined as the rate of diffusion with a liquid *at steady state* divided by the rate of mass transfer without a liquid bridge at steady state. *Silverman* [1999] provides enhancement factors for varying bridge lengths and these values were used to help validate the model developed by *Shahraeeni and Or* [2010, 2012].

We emphasize that the enhancement factor is measured at steady state. *Silverman* [1999] assumed steady state was obtained when the bridge length appeared to stop changing. However we ran our numerical simulation for the case of an initial bridge length of 9.1 mm calculating the flux at each time step and the results are presented in Figure 9.

The top curve of Figure 9 represents the water flux on side B as measured in the rate of increase of height of side B reservoir (mm^3 per hour) and the bottom dashed curve represents the flux of water evaporating from side A. At first, because of the steeper gradient on the right side, the flux on the right is much greater than the flux on the left. Somewhere around 23 h, the bridge obtains maximum saturation (minimum humidity of about 51% at the boundaries) and the flux is limited by the flux on side B—the water able to evaporate from the right side of the bridge cannot cause the bridge concentration to drop below saturated conditions, so the amount evaporating can only be equal to the amount condensing on the left side of the bridge. Thus, once the bridge reaches saturated conditions, the bridge length can no longer change, but the rate of evaporation from side A has not reached steady state because as the water evaporates, the length between the interface at side A and the bridge increases, which ultimately decreases the flux rate. This would continue until all of the water in side A reservoir evaporates. Thus, we do not believe that a steady state was ever obtained in these experiments, making the reported enhancement factors unreliable.

However for comparison, we calculated the analytical enhancement factor under the following assumptions: (1) the height of the reservoir columns on sides A and B are both fixed at 7.5 mm, so that the distance between the reservoir and gas interfaces is 36 mm. (2) The bridge is assumed to have a $Ca(NO_3)_2$ concentration so that the boundary condition on either side of the bridge is a relative humidity of 55%, which gives equal flux on either side. These two assumptions provide a steady state within this system and these results are compared with those reported in *Silverman* [1999] as a function of bridge length. Note that the model gives a higher enhancement rate because the distance between the bridge and the water-gas interface at side A is shorter than that in the actual experiment, providing a larger flux of water vapor. This does give an idea of how the enhancement factor can change depending upon the location of the bridges (how far apart liquid water sources are from each other) and the length of bridges.

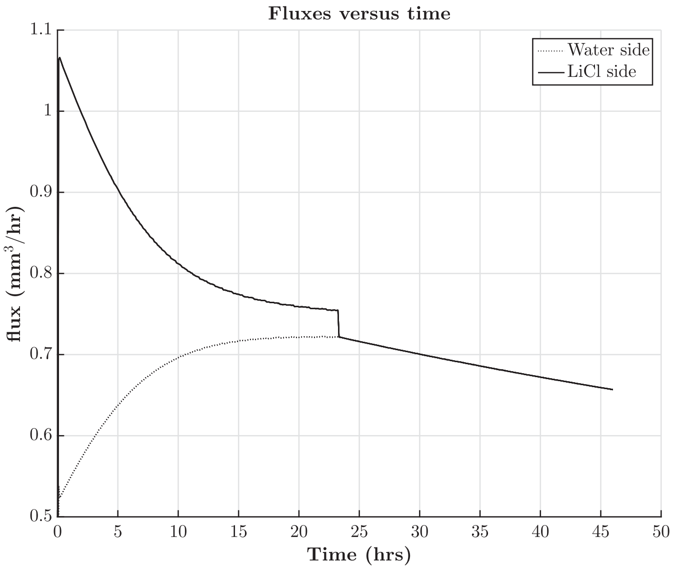

Figure 9. Numerical drawdown and drawup results for 9.1 mm bridge. The bridge reaches maximum concentration at approximates 23 h and after that the bridge length does not change.

4. Conclusion and Discussion

In this paper we took a first foray into using chemical potential to model vapor flow through partially saturated soils by demonstrating the conceptual advantage of using the chemical potential in modeling vapor transport at the pore scale. The governing equation, the Fick-Jacobs equation (13), is a one-dimensional equation for the area-averaged concentration (or relative humidity), assuming cylindrically symmetric geometry. This model is conceptually simple, requiring only the geometry and the relative humidity (or more generally the chemical potential) at the gas-liquid interfaces. The other known model used to capture this experiment was developed by *Shahraeeni and Or* [2010, 2012]. It incorporates temperature fluctuations via the heat equation, interfacial surface tension, contact angle, and rate of condensation and evaporation equations. Although much more complex, it does not require assuming constant temperature and diffusion-limited (not limited by phase-change) conditions for vapor transport.

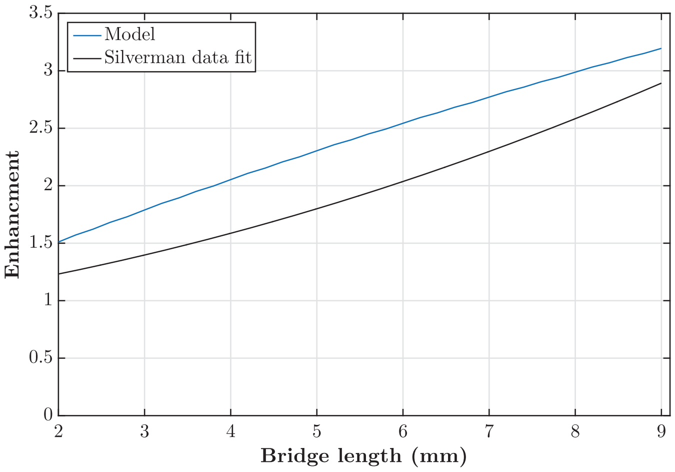

Figure 10. Enhancement calculated by *Silverman* [1999] using a data fit, and from numerical results for different length bridges. The difference is most likely due to the fact that the experimental system does not reach a steady state.

We emphasize that *there are no fitting parameters* used to compare the analytical and experimental results. The most sensitive parameter in this model is the initial relative humidity at the gas-liquid interface—a quantity directly measuring chemical potential under isothermal conditions, which is the energy required to remove a unit amount of water from the liquid phase. We were able to explain conceptually why the bridge lengthened and why the flux of water vapor was greater on one side than the other. We then discussed the enhancement factor explaining that the data given by *Silverman* [1999] were probably not at steady state conditions. We argued that a constant enhancement factor for this particular experimental setup does not exist because of the constantly changing distance between the bridge interfaces and the reservoir interfaces. However, we were able to numerically calculate an enhancement factor as a function of bridge length under the condition that the reservoir-gas interfaces did not move. These results are presented in Figure 10. In summary, we can state that the enhancement factor is a function of (at minimum) distance between liquid bridges, relative humidity boundary conditions at the bridge interfaces, and bridge lengths.

Because chemical potential is the most general potential for diffusive flow and phase transformation [*Castellan*, 1983; *Bennethum et al*., 1996, 2000], it provides a framework for generalizing to more complex vapor flow problems. Let us first consider the case where the surface is highly hydrophilic, creating a larger surface tension, higher radius of curvature, and a lower relative humidity at the interface. Although we might not know directly how the chemical potential changes as a function of the relative affinity of the liquid to the solid over gas, the relative humidity is directly measurable and gives an indication of its effect. Using the same geometry (e.g., capillary tube with fixed radius), and different materials making up the capillary tube, one could determine how the chemical potential changes by measuring the relative humidity at the liquid-gas interface. In fact, for the case of a capillary tube, the relationship between surface tension, γ, and relative humidity, ϕ, is already known by the Kelvin equation [*Haynes*, 1973; *Lu and Likos*, 2001]

$$\ln \phi = \frac{2\gamma V_m}{rRT}, \tag{18}$$

where V_m is the molar volume of the liquid, r is the radius of curvature of the interface from within the water phase (defined to be infinity if flat), and R is the universal gas constant. The Kelvin equation is the basis for determining pore size distribution using adsorption porosimetry [*Haynes*, 1973; *Wu et al*., 2014]. In the rare case that the radius of curvature is greater than zero (created by a nonwetting surface) then the relative humidity at the interface is greater than 1 and the gas phase is supersaturated with water vapor (although this condition would likely not last if the pore is connected to gas at atmospheric conditions or there were other places where the water vapor could condense at a lower relative humidity). When $\phi=1$ the gas phase is saturated and the radius of curvature is infinity, and as the radius of curvature increases in the negative direction (created by a hydrophilic surface), the relative humidity at the liquid-gas interface decreases, meaning that condensation occurs at low relative humidities (the water prefers the liquid phase over the gas phase more so than when the interface is flat). We note that an order-of-magnitude analysis indicates that a relative humidity of .999 at an interface with pure liquid water at equilibrium occurs at approximately $r=1$ mm. So neglecting curvature for capillary tubes of the size in the experiment modeled here in determining the relative humidity boundary conditions is justified.

Thermal gradients are of great importance in some applications such as soil borehole thermal energy storage (SBTES) systems [*Bear et al*., 1991; *Moradi et al*., 2015]. So consider a pore-scale experiment where we no longer have isothermal conditions. Using the principle that flow is determined by the gradient of chemical potential [*Castellan*, 1983], we would derive the governing equation beginning with equation (3). We can still use equation (9) for chemical potential, but in calculating the gradient of the chemical potential needed for (3) we would invoke the chain and product rules so that we have a sum of a term involving the gradient of relative humidity and a gradient of temperature.

And if rate of evaporation/condensation is not dominated by diffusion [e.g., *Bénet et al*., 2009], we would not be able to assume that the chemical potential of water at an interface is equal in the gas and liquid phases. However, fundamental physics dictates that the rate of evaporation is proportional to the difference of the chemical potentials in the two phases [*Bennethum et al*., 1996, 2000; *Bénet et al*., 2009; *Alexandersson et al*., 2016]. This is in fact a generalization of what is sometimes used: the rate of phase change is based on the difference between the gas vapor pressure and the equilibrium pressure at the water-gas interface [*Zhang and Datta*, 2004; *Smits et al*., 2011; *Moradi et al*., 2015]. Thus, using the chemical potential as a primary unknown could directly determine the rate of phase change [see, e.g., *Bénet et al*., 2009].

Whether chemical potential can be useful as a primary unknown for hydrological modeling at the macroscale is still unknown, but its potential benefits are clear, as indicated here and as suggested by its use in other fields. Further, we believe that understanding of the chemical potential could explain more clearly transport processes. Even under fully saturated conditions, flow is determined by the chemical potential (for a single component fluid, the chemical potential is the Gibbs potential, with pressure and temperature as the primary independent variables, leading to a generalized Darcy's law [*Bennethum and Cushman*, 2002; *Schreyer-Bennethum*, 2012].

Notation

Superscripts, Subscripts, and Others

$\overline{\cdot}$	area-averaged (see, e.g., equation (12)).
$\cdot^{g}$	gas phase.
$\cdot^{g_j}$	component *j* of the gas phase, $j=v$ for water vapor, and $j=a$ for dry air.
$\cdot^{g_j}_{*}$	pure component *j* in gas phase.
$\cdot^{g_v}_{sat}$	value of water vapor at saturated conditions.

Latin Symbols

$A(x)$	cross-sectional area as a function of position *x* [length^2].
C^{g_j}	mass fraction of component *j* in gas phase, ρ^{g_j}/ρ^{g}.
D	diffusion coefficient for Fick's law (see equation (2)) [length^2/time].
$D^{g_j}_{\mu}$	diffusion coefficient for generalized Fick's law (see equation (3)) [length^2/time].
M^{g_j}	molecular mass of component *j* in the gas phase [mass/mole].
p^{g}, p^{g}_{j}	pressure of gas phase mixture, partial pressure of component *j* in gas phase [force/area].
R	universal gas constant [energy/(mole-temperature)].
R^{g_j}	specific gas constant for component *j*, $R^{g_j}=R/M^{g_j}$ [energy/(mass-temp)].
T	absolute temperature [temperature].
$\mathbf{v}^{g}$, $\mathbf{v}^{g_j}$	velocity of the gas phase or component *j* of the gas phase, $\rho^{g}\mathbf{v}^{g}=\rho^{g_j}\mathbf{v}^{g_j}+\rho^{g_a}\mathbf{v}^{g_a}$ [length/time].
$\mathbf{v}^{g_j,g}$	diffusive velocity, $\mathbf{v}^{g_j}-\mathbf{v}^{g}$.

Greek Symbols

μ^{g_j}	mass-weighted chemical potential of component *j* in gas phase [energy/mass].
ρ^{g}, ρ^{g_j}	mass density of gas phase [mass of *g* per volume of *g*] mass density of component *j* in the gas phase [mass of g_j per volume of *g*].
ϕ	relative humidity (see equation (7)).

Acknowledgments
Thanks to INGENIØR CAND POLYT ERIK HEGENHOFTS LEGAT for supporting Addassi's visit to the Department of Mathematical and Statistical Sciences at the University of Colorado Denver, without which this research would not have been possible. Experimental data obtained for this article are published in Table 1. Code developed to solve numerically the governing equations presented in this manuscript can be obtained by e-mailing Mouadh Addassi at addassimouadh@gmail.com.

References

Alexandersson, M., H. Askfelt, and M. Ristinmaa (2016), Triphasic model of heat and moisture transport with internal mass exchange in paperboard, *Transp. Porous Media*, *112*(2), 381–408, doi:10.1007/s11242-016-0651-9.

Arfvidsson, J., and J. Claesson (2000), Isothermal moisture flow in building materials: Modelling, measurements and calculations based on Kirchhoff's potential, *Building Environ.*, *35*, 519–536.

Assouline, S., S. W. Tyler, J. S. Selker, I. Lunati, C. W. Higgins, and M. B. Parlange (2013), Evaporation from a shallow water table: Diurnal dynamics of water and heat at the surface of drying sand, *Water Resour. Res.*, *49*, 4022–4034, doi:10.1002/wrcr.20293.

Bazant, Z. P., and Y. Xi (1993), Stochastic drying and creep effects in concrete structures, *J. Struct. Eng. ASCE*, *119*(1), 301–322.

Bear, J. (1972), *Dynamics of Fluids in Porous Media*, Dover, N. Y.

Bear, J., J. Bensabat, and A. Nir (1991), Heat and mass transfer in unsaturated porous media at a hot boundary: I. One-dimensional analytic model, *Transp. Porous Media*, *6*(3), 281–298.

Bénet, J.-C., A.-L. Lozano, F. Cherblanc, and B. Cousin (2009), Phase change of water in a hygroscopic porous medium. Phenomenological relation and experimental analysis for water in soil, *J. Non-Equilibrium Thermodyn.*, *34*(2), 133–153.

Bennethum, L. S., and J. H. Cushman (2002), Multicomponent, multiphase thermodynamics of swelling porous media with electroquasi-statics: II. Constitutive theory, *Transp. Porous Media*, *47*(3), 337–362.

Bennethum, L. S., M. A. Murad, and J. H. Cushman (1996), Clarifying hybrid mixture theory and the macroscale chemical potential for porous media, *Int. J. Eng. Sci.*, *34*(2), 125–145.

Bennethum, L. S., M. A. Murad, and J. H. Cushman (2000), Macroscale thermodynamics and the chemical potential for swelling porous media, *Transp. Porous Media*, *39*(2), 187–225.

Bird, R. B., W. E. Stewart, and E. N. Lightfoot (2007), *Transport Phenomena*, John Wiley, N. Y.

Burch, D. M., and J. Chi (1997), MOIST: A PC program for predicting heat and moisture transfer in building envelopes: Release 3.0, *Tech. Rep. Spec. Publ. 917*, Dep. of Commer., Natl. Inst. of Stand. and Technol., Gaithersburg, Md.

Cahill, A. T., and M. B. Parlange (1998), On water vapor transport in field soils, *Water Resour. Res.*, *34*(4), 731–739.

Cary, J. W. (1963), Onsager's relation and the non-isothermal diffusion of water vapor, *J. Phys. Chem.*, *67*, 126–129.

Cary, J. W. (1966), Soil moisture transport due to thermal gradients: Practical aspects, *Soil Sci. Soc. Am. Proc.*, *30*(4), 428–433.

Cass, A., G. Campbell, and T. Jones (1984), Enhancement of thermal water vapor diffusion in soils, *Soil Sci. Soc. Am. J.*, *48*(1), 25–32, doi:10.2136/sssaj1984.03615995001800040001x.

Castellan, G. W. (1983), *Physical Chemistry*, The Benjamin/Cummings Publ. Co, Menlo Park, Calif.

Delgado, J. M. P. Q., E. Barreira, N. M. M. Ramos, and V. P. de Freitas (2013), *Hydrothermal Numerical Simulation Tools Applied to Building Physics*, Springer, N. Y.

Gonzalez, R. G., A. Verhoef, P. L. Vidale, and I. Braud (2012), Incorporation of water vapor transfer in the JULES land surface model: Implications for key soil variables and land surface fluxes, *Water Resour. Res.*, *48*, W05538, doi:10.1029/2011WR011811.

Grasley, Z., D. Lange, and M. D'Ambrosia (2006), Internal relative humidity and drying stress gradients in concrete, *Mater. Struct.*, *39*, 901–909.

Gray, W. G., and C. Miller (2014), *Introduction to the Thermodynamically Constrained Averaging Theory for Porous Medium Systems*, Springer, Berlin.

Gurr, C., T. Marshall, and J. Hutton (1952), Movement of water in soil due to a temperature gradient, *Soil Sci.*, *74*(5), 335–346.

Haynes, J. (1973), Pore size analysis according to the Kelvin equation, *Mater. Construct.*, *6*(3), 209–213.

Huang, Q., Z. Jiang, X. Gu, W. Zhang, and B. Guo (2015), Numerical simulation of moisture transport in concrete based on a pore size distribution model, *Cement Concrete Res.*, *67*, 31–43.

Jackson, R. D., R. J. Reginato, B. A. Kimball, and F. S. Nakayama (1974), Diurnal soil-water evaporation: Comparison of measured and calculated soil-water fluxes, *Soils Sci. Soc. Am. Proc.*, *38*(6), 861–866.

Jacobs, M. H. (1967), *Diffusion Processes*, Springer, N. Y.

Janssen, H. (2014), Simulation efficiency and accuracy of different moisture transfer potentials, *J. Building Performance Simul.*, *7*(5), 379–389.

Johannesson, B., and U. Nyman (2010), A numerical approach for non-linear moisture flow in porous materials with account to sorption hysteresis, *Transp. Porous Media*, *84*(3), 735–754.

Kalinay, P., and J. K. Percus (2005), Extended Fick-Jacobs equation: Variational approach, *Phys. Rev. E*, *72*, 061203, doi:10.1103/PhysRevE.72.061203.

Kalinay, P., and J. K. Percus (2006), Exact dimensional reduction of linear dynamics: Application to confined diffusion, *J. Stat. Phys.*, *123*(5), 1059–1069.

Kunzel, H. (1995), Simultaneous heat and moisture transport in building components: One- and two-dimensional calculations using simple parameters, PhD thesis, Fraunhofer Inst. of Building Phys., Stuttgart, Germany.

Lu, N., and W. J. Likos (2001), *Unsaturated Soil Mechanics*, John Wiley, N. Y.

Marshall, T., J. Holmes, and C. Rose (2006), *Soil Physics*, Cambridge Univ. Press, Cambridge, U. K.

Moradi, A., K. M. Smits, J. Massey, A. Cihan, and J. McCartney (2015), Impact of coupled heat transfer and water flow on soil borehole thermal energy storage (SBTES) systems: Experimental and modeling investigation, *Geothermics*, *57*, 56–72.

Patlak, C. K. (1973), An approximation diffusion equation for a long narrow channel with varying cross-sectional area, *Bull. Math. Biol.*, *35*, 81–86.

Pedersen, C. R. (1992), Prediction of moisture transfer in building constructions, *Building Environ.*, *27*(3), 387–397.

Philip, J. R. (1964), Kinetics of capillary condensation in wedge-shaped pores, *J. Chem. Phys.*, *41*(4), 911–916.

Philip, J. R., and D. A. de Vries (1957), Moisture movement in porous materials under temperature gradients, *Trans. AGU*, *38*(2), 222–232.

Raats, P. (1975), Transformations of fluxes and forces describing the simultaneous transport of water and heat in unsaturated porous media, *Water Resour. Res.*, *11*(6), 938–942.

Saito, H., J. Simunek, and B. Mohanty (2006), Numerical analysis of coupled water, vapor, and heat transport in the vadose zone, *Vadose Zone J.*, *5*(2), 784–800, doi:10.2136/vzj2006.0007.

Sakai, H., N. Toride, and J. Simunek (2009), Water and vapor movement with condensation and evaporation in a sandy column, *Soil Sci. Soc. Am. J.*, *73*(3), 707–717, doi:10.2136/sssaj2008.0094.

Schreyer-Bennethum, L. S. (2012), Macroscopic flow potentials in swelling porous media, *Transp. Porous Media*, *94*, 47–68.

Shahraeeni, E., and D. Or (2010), Pore-scale analysis of evaporation and condensation dynamics in porous media, *Langmuir*, *26*(17), 13,924–13,936.

Shahraeeni, E., and D. Or (2012), Pore scale mechanisms for enhanced vapor transport through partially saturated porous media, *Water Resour. Res.*, *48*, W05511, doi:10.1029/2011WR011036.

Shokri, N., P. Lehmann, and D. Or (2009), Critical evaluation of enhancement factors for vapor transport through unsaturated porous media, *Water Resour. Res.*, *45*, W10433, doi:10.1029/2009WR007769.

Siau, J. F. (1983), Chemical potential as a driving force for nonisothermal moisture movement in wood, *Wood Sci. Technol.*, *17*, 101–105.

Silverman, T. S. (1999), A pore-scale experiment to evaluate enhanced vapor diffusion in porous media, MS thesis, 126 pp., Purdue Univ., Socorro, N. M.

Smits, K., A. Cihan, T. Sakaki, and T. Illangasekare (2011), Evaporation from soils under thermal boundary conditions: Experimental and modeling investigation to compare equilibrium and nonequilibrium-based approaches, *Water Resour. Res.*, *47*, W05540, doi:10.1029/2010WR009533.

Taylor, S., and L. Cavazza (1954), The movement of soil moisture in response to temperature gradients, *Soil Sci. Soc. Am. J.*, *18*(4), 351–358, doi:10.2136/sssaj1954.03615995001800040001x.

van Schijndel, A. (2011), Multiphysics modeling of building physical constructions, *Building Simul.*, *4*, 49–60.

Wang, J., and I. Catton (2001), Enhanced evaporation heat transfer in triangular grooves covered with a thin fine porous layer, *Appl. Therm. Eng.*, *21*, 1721–1737.

Whitaker, S. (1991), Role of the species momentum equation in the Stefan diffusion tube, *Ind. Eng. Chem. Res.*, *30*, 978–983.

Wildenschild, D., and J. Roberts (2001), Experimental tests of enhancement of vapor diffusion in topopah spring tuff, *J. Porous Media*, *4*(1), 1–13, doi:10.1615/JPorMedia.v4.i1.10.

Wu, M., B. Johannesson, and M. Geiker (2014), Application of water vapor sorption measurements for porosity characterization of hardened cement pastes, *Construct. Building Mater.*, *66*, 621–633.

Zhang, J., and A. K. Datta (2004), Some considerations in modeling of moisture transport in heating of hygroscopic materials, *Drying Technol.*, *22*(8), 1983–2008.

Zwanzig, R. (1992), Diffusion past an entropy barrier, *J. Phys. Chem.*, *96*(10), 3926–3930.

WATER RESOURCES RESEARCH

Supporting Information for"Pore-Scale Modeling of Vapor Transport in Partially Saturated Capillary Tube with Variable Area Using Chemical Potential"

Mouadh Addassi,[1] Lynn Schreyer,[1]

Björn Johannesson,[1] and Hai Lin[1]

Contents of this file

1. Details of Experimental Apparatus Geometry
2. The Fick-Jacobs Equation - Derivation and Numerical Validation

Introduction Here we provide supplemental information related to the geometry of the experimental apparatus used to generate the experimental results by *Silverman* [1999] and a derivation of the Fick-Jacobs Equation along with a numerical validation.

Corresponding author: L. Schreyer, Department of Mathematics and Statistics, Washington State University, 103 Neill Hall, Pullman, WA 99164, USA. (Lynn.Schreyer@wsu.edu)

[1]Technical University of Denmark

[2]Washington State University

[3]Linnaeus University

[4]University of Colorado Denver

Details of Experimental Apparatus Geometry

The geometry (blueprint) of the experimental apparatus provided in *Silverman* [1999] is reproduced in Figure 1.

The Fick-Jacobs Equation

Here we upscale the diffusion equation

$$\frac{\partial \phi}{\partial t} = D^{g_v} \boldsymbol{\nabla} \cdot \left(\boldsymbol{\nabla} \phi \right), \tag{1}$$

by using Leibniz rule, and then discuss the assumptions necessary to recover the Fick-Jacobs equation, the one-dimensional version of the diffusion equation. We then numerically compare the solutions of the three-dimensional version of the diffusion equation with the one-dimensional solution to the Fick-Jacobs equation to demonstrate that the Fick-Jacobs equation is a reasonable approximation to the 3-dimensional diffusion equation. Please see the Appendix of the main article for definition of all variables.

We begin with the a three-dimensional diffusion equation at the microscale:

$$\frac{\partial \phi}{\partial t} + \boldsymbol{\nabla} \cdot \mathbf{J} = \mathbf{o} \tag{2}$$

where $\mathbf{J} = -D^{g_v} \boldsymbol{\nabla} \phi$ is the mass flux (up to a constant) in terms of relative humidity. We wish to upscale by averaging over the cross-sectional area, $A(x)$, which can change along the longitudinal direction, x, and write the result in terms of an averaged value of ϕ. Assuming axisymmetric geometry, we integrating (2) over $A(x)$ and considering each derivative in turn. Thus we begin with the time-derivative term:

$$\int_{A(x)} \frac{\partial \phi(x,y,z,t)}{\partial t} dy\, dz = \frac{\partial}{\partial t} \int_{A(x)} \phi(x,y,z,t) dy\, dz = \frac{\partial}{\partial t} \left[\overline{\phi}(x,t) A(x) \right], \tag{3}$$

where

$$\overline{\phi}(x) = \frac{1}{A(x)} \int_{A(x)} \phi(x,y,z,t)dy\ dz. \tag{4}$$

To tackle the integral of the divergence term of (2) we begin by writing the divergence in cylindrical coordinates:

$$\int_{A(x)} \boldsymbol{\nabla} \cdot \mathbf{J}\ dy\ dz = \int_0^{2\pi} \int_0^{R(x)} \left[\frac{1}{r}\frac{\partial}{\partial r}(rJ_r^j) + \frac{1}{r}\frac{\partial J_\theta^j}{\partial \theta} + \frac{\partial J_x^j}{\partial x} \right] r\ dr\ d\theta. \tag{5}$$

We consider each term independently, assuming that the flux is radially symmetric. Beginning with the first term on the right side, we use the fundamental theorem of calculus to obtain:

$$\int_0^{2\pi} \int_{r=0}^{r=R(x)} \frac{\partial}{\partial r}(rJ_r^j(x,r))dr\ d\theta = 2\pi R(x) J_r^j(x, R(x)) = 0 \tag{6}$$

since the flux in the radial direction at the capillary tube surface is zero.

The second term, involving $\frac{\partial J_\theta^j}{\partial \theta}$, is zero because the problem is assumed to be axial symmetric so that no component of $\mathbf{J}$ is a function of the angle, θ.

For the third term, we use Leibniz rule, which is stated here for convenience. If $f(x,t)$ is a continuous function which has a partial derivative with respect to x that is well-defined then

$$\frac{d}{dx}\left(\int_{a(x)}^{b(x)} f(x,s)ds \right) = \int_{a(x)}^{b(x)} \frac{\partial f(x,s)}{\partial x} ds + f(x,b(x))b'(x) - f(x,a(x))a'(x). \tag{7}$$

Using Leibniz rule, we have

$$\begin{aligned} &\int_{\theta=0}^{2\pi} \int_{r=0}^{R(x)} \frac{\partial J_x^j(x,r)}{\partial x} r\ dr\ d\theta \\ &\quad = \int_{\theta=0}^{2\pi} \left[\frac{\partial}{\partial x} \int_{r=0}^{R(x)} J_x^j(x,r) r\ dr - J_x^j(x,R(x)) R \frac{dR}{dx} \right] d\theta. \\ &\quad = \frac{d}{dx} \int_{\theta=0}^{2\pi} \int_{r=0}^{R(x)} J_x^j(x,r)\ r dr d\theta - 2\pi J_x^j(x,R(x)) R \frac{dR}{dx} \end{aligned}$$

$$= \frac{d}{dx}\int_{A(x)} J^j_x(x,r)dA - 2\pi J^j_x(x,R(x))R\frac{dR}{dx}$$
$$= \frac{d}{dx}\left(A(x)\overline{J}^j_x(x)\right) - J^j_x(x,R(x))A'(x), \tag{8}$$

where $A = \pi R^2$ so that $A'(x) = 2\pi R(x)R'(x)$, and $\overline{J}^j_x(x) = \frac{1}{A(x)}\int_{A(x)} J^j_x(x,y,z)\, dy\, dz$.

Substituting the appropriate expressions from equations (6-7) into (5) gives us

$$\int_{A(x)} \nabla\cdot\mathbf{J}\, dy\, dz = \frac{d}{dx}\left[A(x)\overline{J}^j_x(x)\right] - J^j_x(x,R(x))A'(x) \tag{9}$$

Using (3) and (9) in the integrated form of equation (2) we get

$$A(x)\frac{\partial\overline{\phi}(x,t)}{\partial t} = -A(x)\frac{d\overline{J}^j_x(x)}{dx} - \overline{J}^j_x(x)A'(x) + J^j_x(x,R(x))A'(x). \tag{10}$$

At this point we note that there are two sets of assumptions that get us to Fick-Jacobs equation:

$$\frac{\partial\overline{\phi}}{\partial t} = D^{g_v}\left(\frac{\partial^2\overline{\phi}}{\partial x^2} + \frac{1}{A(x)}\frac{\partial\overline{\phi}}{\partial x}\frac{dA}{dx}\right). \tag{11}$$

Assumption Set 1

The assumptions essentially used by *Jacobs* [1967] and also by *Patlak* [1973] who both used a linearization type argument through a trunkated Taylor series, are that (1) the upscaled flux is given by Fick's law and (2) that fluxes at $r = R$ can be neglected. This latter assumption implies in particular that the flux in the x direction at the boundary ($r = R$) is much smaller than the averaged flux, i.e.

$$|J^j_x(x,R(x))| << |\overline{J}^j_x(x)| \tag{12}$$

so that (10) becomes

$$A(x)\frac{\partial\overline{\phi}(x,t)}{\partial t} = -A(x)\frac{d\overline{J}^j_x(x)}{dx} - \overline{J}^j_x(x)A'(x). \tag{13}$$

Now assuming that Fick's law holds at the averaged scale so that:

$$\overline{J}^j_x(x) = -D^{g_v}\frac{d\overline{\phi}}{dx} \tag{14}$$

we can eliminate the averaged flux and (10) gives us the Fick-Jacobs equation (11).

Assumption Set 2

Here we continue using Leibniz rule for determining the upscaled flux in the x-direction to get:

$$\begin{aligned} A(x)\overline{J}^j_x(x) &= -D^{g_v}\int_{A(x)}\frac{\partial\phi}{\partial x}dA \\ &= -D^{g_v}\frac{\partial}{\partial x}\left[\overline{\phi}(x,t)A(x)\right] + D^{g_v}\phi(x,R(x),t)A'(x). \end{aligned} \tag{15}$$

Substituting into (10) we obtain:

$$\begin{aligned} A(x)\frac{\partial\overline{\phi}(x,t)}{\partial t} &= -\frac{\partial}{\partial x}\left[A(x)\overline{J}^j_x(x,t)\right] + J^j_x(x,R(x),t)A'(x) \\ &= \left.\frac{\partial}{\partial x}\right|_t \left[D^{g_j}\frac{\partial}{\partial x}[\overline{\phi}(x,t)A(x)] - D^{g_j}\phi(x,R(x),t)A'(x)\right] \\ &\qquad -D^{g_j}\left.\frac{\partial\phi(x,R(x),t)}{\partial x}\right|_{r,t} A'(x) \\ &= D^{g_j}\frac{\partial^2}{\partial x^2}\left[\overline{\phi}(x,t)A(x)\right] \\ &\quad -D^{g_j}\left[\left.\frac{\partial\phi}{\partial x}\right|_{r,t}(x,R(x),t)A'(x) + \left.\frac{\partial\phi}{\partial r}\right|_{x,t}(x,R(x),t)R'(x)A'(x)\right. \\ &\qquad \left. +\phi(x,R(x),t)A''(x) + \left.\frac{\partial\phi}{\partial x}\right|_{r,t}(x,R(x),t)A'(x)\right] \end{aligned} \tag{16}$$

Now we assume that terms with $A''(x)$ are small relative to the others, and that at the solid surface of the capillary tube the mass flux is zero in the radial direction so that $\left.\frac{\partial\phi}{\partial r}\right|_{x,t}(x,R(x),t) = 0$. Then equation (15) simplifies to

$$A(x)\frac{\partial\overline{\phi}(x,t)}{\partial t} = D^{g_j}\left[\frac{\partial^2\overline{\phi}}{\partial x^2}A(x) + 2\frac{\partial\overline{\phi}}{\partial x}A'(x) - 2\left.\frac{\partial\phi}{\partial x}\right|_{r,t}(x,R(x),t)A'(x)\right] \tag{17}$$

If we further assume that $\frac{\partial\overline{\phi}}{\partial x} \approx 2\left.\frac{\partial\phi}{\partial x}\right|_{r,t}(x,R(x),t)$ then we recover the Fick-Jacobs equation (11).

Next we provide numerical evidence that the one-dimensional Fick-Jacobs equation, (11), is a reasonable approximation of the three-dimensional equation, (1). This was done by comparing the solutions to these equations over a small section of a hypothetical capillary tube where the inner radius decreases linearly from 2 mm to 0.5 mm, a left-side boundary condition of a uniform relative humidity of 1, and a right-side boundary condition of uniform relative humidity of 0. The one-dimensional equation was solved using a MATLAB code (used for other numerical results presented in this paper), and the three-dimensional equation was solved using COMSOL. The average relative humidity from the three-dimensional simulation was calculated via:

$$\mathrm{RH}_{\mathrm{avg}} = \frac{1}{A(x)} \int_0^R \phi(x,r)\, 2\pi r \, dr.$$

Figures 2 and 3 are the results of the comparison at steady-state, and in time, respectively. The ℓ_2 measure of the difference between the 26 points given in Figure 2 was calculated to be 0.006. The one and three-dimensional results are remarkably similar given the assumptions needed to arrive at the Fick-Jacobs equation (1).

References

Jacobs, M. H. (1967), *Diffusion Processes*, Springer-Verlag, New York.

Patlak, C. K. (1973), An approximation diffusion equation for a long narrow channel with varying cross-sectional area, *Bulletin of Mathematical Biology*, *35*, 81–86.

Silverman, T. S. (1999), A pore-scale experiment to evaluate enhanced vapor diffusion in porous media, Master's thesis, Purdue University, Socorro, New Mexico, advisor: John Wilson, 126pp.

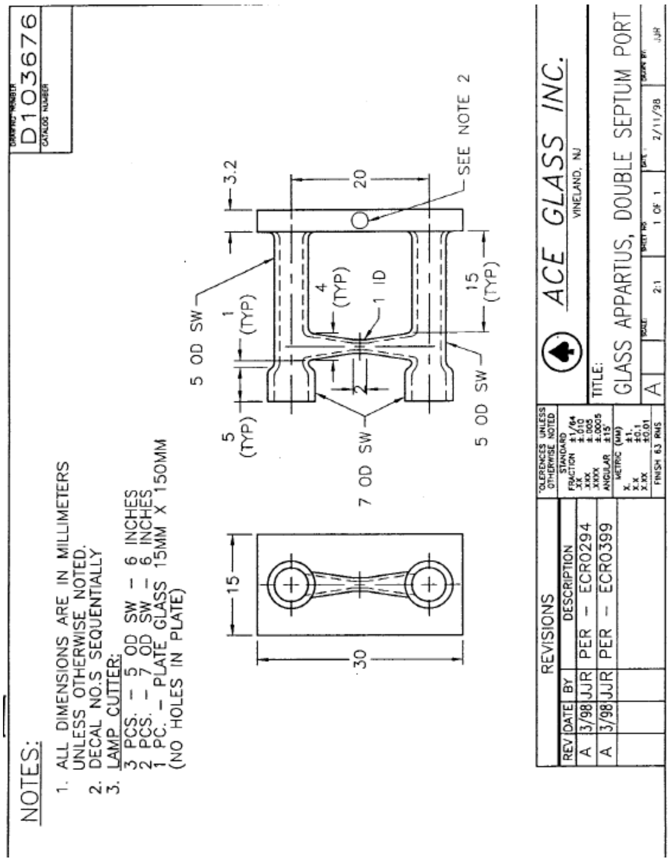

Figure 1. Detailed geometry for experimental setup as given in *Silverman* [1999].

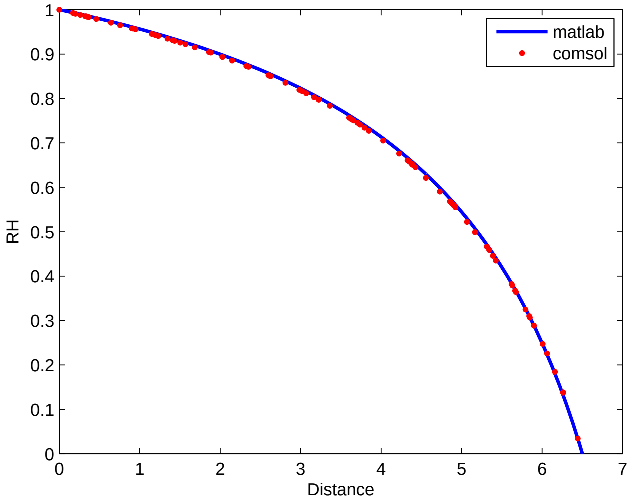

Figure 2. Steady-state numerical comparison between solutions of Fick-Jacobs equation in blue, and three-dimensional diffusion equation, averaged, in red.

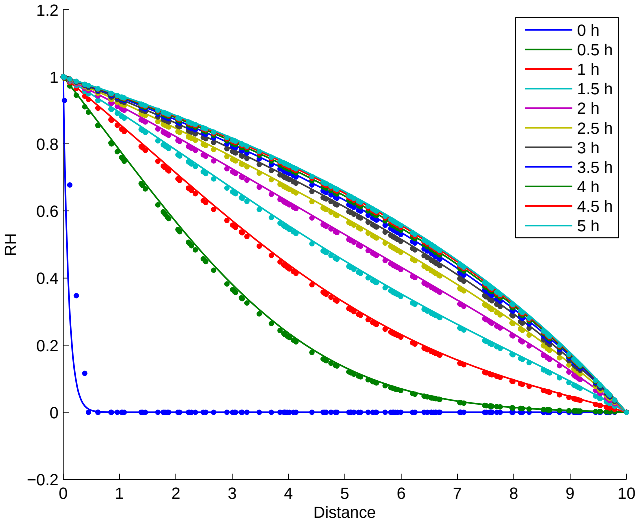

Figure 3. Dynamic numerical comparison between solutions of Fick-Jacobs equation denoted by solid lines, and three-dimensional diffusion equation, averaged, denoted by dots.

Paper II

"Inverse analyses of effective diffusion parameters relevant for a two-phase moisture model of cementitious materials"

M. Addassi & B. Johannesson & L. Wadsö

Published in: *Cement and Concrete Research, 2018*

Cement and Concrete Research 106 (2018) 117–129

Contents lists available at ScienceDirect

Cement and Concrete Research

journal homepage: www.elsevier.com/locate/cemconres

Inverse analyses of effective diffusion parameters relevant for a two-phase moisture model of cementitious materials

Mouadh Addassi[a,*], Björn Johannesson[b], Lars Wadsö[c]

[a] Department of Civil Engineering, Technical University of Denmark, Lyngby, Denmark
[b] Department of Building Technology, Linnaeus University, Växjö, Sweden
[c] Division of Building Materials, Lund University, Lund, Sweden

ARTICLE INFO

Keywords:
Moisture transport (C)
Inverse analyses (B)
Effective diffusion parameters (C)
Cementitious materials (E)
Durability (C)

ABSTRACT

Here we present an inverse analyses approach to determining the two-phase moisture transport properties relevant to concrete durability modeling. The purposed moisture transport model was based on a continuum approach with two truly separate equations for the liquid and gas phase being connected by the sorption kinetics. The moisture properties of ten binder-systems containing fly ash, calcined clay, burnt shale and gray micro-filler, were investigated experimentally. The experiments used were, (i) sorption test (moisture fixation), (ii) cup test in two different relative humidity intervals, (iii) drying test, and, (iv) capillary suction test. Mass change over time, as obtained from the drying test, the two different cup test intervals and the capillary suction test, was used to obtain the effective diffusion parameters using the proposed inverse analyses approach. The moisture properties obtained with the proposed inverse analyses method provide a good description of the test period for the ten different binder-systems.

1. Introduction

Concern about the environmental impact of cement and concrete production has motivated many studies on new cement-based binder-systems with increased use of different combinations of Supplementary Cementitious Materials (SCMs), [1–6]. Such cement-based binder-systems will be referred to as binder-systems in the following. The use of this kind of binder-system can lead to a reduction of CO_2 emission from cement and concrete production. The use of SCMs based on industrial waste and by-products also benefits the environment. However, blending Portland cement with different SCMs leads to binder-systems with more complicated hydration products, which affect the pore structure and thereby the durability of the final concrete product [1]. It is therefore important to evaluate various durability aspects of new binder-systems.

The use of theoretically sound multi-phase reactive mass transport models to estimate the long term durability of cement and concrete has gained more acceptance in recent years, e.g. [7–10]. The reference [9] presented a general framework for durability estimation using a multi-species reactive mass transport model with the focus on application for cement binder-systems. The model in [11] can simulate long term conditions for different service environments by solving a modified version of the Poisson-Nernst-Plank (PNP) system of equations developed using hybrid mixture theory in [12–14]. It includes ionic transport in the liquid phase, chemical interaction and mass exchange between the phases, electro-migration of the ionic species and two-phase moisture transport including sorption hysteresis effects, allowing the investigation of binder-system undersaturated and unsaturated conditions. Reference [15] demonstrated this model's ability to reproduce chloride ingress profiles from experimental measurements by adjusting the tortuosity factor τ. However, proper input data to the moisture transport part of the model will increase the performance and accuracy of the model. Moisture input data especially are needed to evaluate the performance of new binder-systems.

A well described moisture transport model is important since most deterioration processes in cementitious binder-systems are related to moisture transport [16]. Moisture transport models can in general be divided into single phase and two-phase models. Both types of models are commonly found in the concrete literature. The one-phase models, using a single driving potential, describes coupled liquid water and water vapor transport using a single diffusion coefficient, e.g. see [17–21]. This coefficient, sometimes referred to as the apparent diffusion coefficient, [22], is often assumed to be a function of the saturation degree (the fraction of the pore system that is filled with liquid). The single phase models are in general described using Fick's first law when assuming steady state flow and Fick's second law for non-

---

[*] Corresponding author at: Brovej 119, Kgs. Lyngby 2800, Denmark.
E-mail address: moadda@byg.dtu.dk (M. Addassi).

https://doi.org/10.1016/j.cemconres.2018.01.011
Received 24 July 2017; Received in revised form 11 January 2018; Accepted 11 January 2018

steady state flow, as described in e.g. [21,22]. This simple description makes it possible to directly identify the apparent diffusion coefficient using various types of diffusion experiments, for example cup test [21] and drying test [23]. The use of an apparent moisture diffusion coefficient is in general a good assumption, but some of the more detailed models that include ionic diffusion require a separate description of liquid water flow and water vapor flow in order to take the ionic convection correctly into account. In a two-phase moisture model the diffusion of water liquid phase and the water vapor phase are treated separately, using different diffusion parameters for each phase. Furthermore, the sorption kinetics are influenced by mass exchange between the vapor and liquid phase.

In [11] moisture transport was described using a two-phase approach suggested by [24]. This approach was adopted due to its modeling advantages when using a multi-phase reactive transport framework including ionic convection. The importance of using a two-phase moisture approach for multi-phase reactive transport models is emphasized in e.g. [25]. Reactive mass transport models like the one presented in [11], have the advantage of being capable of modeling a wide range of concrete durability effects for different service environments. This comes at the cost of the need for a detailed description of the separate phases in the system, that is, a description of the effective diffusion in the liquid phase and in the gas phase. Reactive mass transport models facilitate the study of different phenomena, e.g. ionic transport and chemical interaction in the liquid water phase and carbon dioxide diffusion in the gas phase and its chemical interaction with the liquid phase.

When treating the sorption hysteresis effect, it is well documented that cement-based materials, in common with many other porous materials, show a strong effect of the wetting and drying cycle history on the equilibrium water-vapor ratio at a given relative humidity (RH), see e.g. [26–29]. In some cases, the exposure of cement-based materials to naturally occurring wetting and drying is considered to be the most severe case, since it accelerates degradation processes such as chloride penetration [30]. It is important to know the moisture state in the material at any time and to account for the sorption hysteresis behavior of the binder-system as described in, e.g. [24,25,31]. Dynamic Vapor Sorption (DVS) measurement was used in this study to measure the drying and wetting boundary sorption isotherms of the binder-systems. These boundary sorption isotherms were used to relate the RH and saturation degree in the numerical model.

In this study, moisture transport properties relevant for a two-phase model were investigated using an inverse analysis approach. The main challenge with two-phase moisture transport models is to identify a separate description of the effective diffusion in the liquid phase and in the vapor phase as a function of the saturation degree. This is mainly due to the coupled nature of liquid water and water vapor transport. This challenge was addressed in the present study by proposing a stringent approach to "back calculate" the required effective diffusion parameters for a two-phase moisture flow through experiments and numerical modeling. The idea was to conduct a set of diffusion experiments both in drying and wetting conditions, covering different RH intervals and then use a two-phase moisture transport model and optimization tools to "back calculate" the targeted effective diffusion of the two phases. This type of inverse analyses was recently used in [32] and [33], in which simple drying experiments were used. In the present study four different experiments were used for the inverse analyses in order to increase the reliability results of the analysis: 1. Sorption isotherms in drying and wetting conditions. 2. A drying test with a low RH boundary condition, 33% RH, similar to [32,33]. 3. Cup measurements in relatively high RH intervals (75–85 % RH and 95–85 % RH). 4. A capillary suction test to evaluate moisture transport behavior above 95% RH. Paste samples were used in Experiment 1, while mortar samples where used in Experiments 2–4. The cup-test is a method where disc shaped samples are exposed to different RH conditions on the two sides, in order to establish an average steady-state diffusion coefficient for the selected RH interval, e.g. see [21]. The one dimensional drying test is similar to the cup-test, but simpler in that only one surface of the sample disc is exposed. Drying tests are typically used to evaluate the transient diffusion rate e.g. see [23]. The drying test was selected with a low RH target to cover a wide range of RH when evaluating the diffusion parameters in the numerical model. In the capillary suction test cylindrical samples were pre-dried to a given RH and then placed in contact with water to measure the rate of water uptake, e.g. see [34]. In this study, the initial conditions and mass change results from the drying test, the two intervals of cup test and capillary suction test, from the time of exposure to the established equilibrium or end of experiment, were used to represent the whole process for each one of the tests separately using the proposed two-phase moisture transport model. An optimization scheme was developed where in each iteration, one simulation for each of the diffusion experiments was made in sequence, using the same set of two-phase diffusion parameters. At the end of each iteration the difference between the simulation output and the experimental results, was used as a base for updating the diffusion parameters. The diffusion parameters were updated in each iteration until the simulation results gave a good fit for all experimental results, see Fig. 1.

Nine different binder-systems were made with different SCMs and a new rapidly hardening cement clinker with high C_3A and C_3S content that should provide improved binding capacity for the SCMs. As a reference a standard rapidly hardening, often used in aggressive service environments, was used. The SCMs included in the studied binder-systems are fly ash, calcined clay, burnt shale and gray micro-filler.

The intention was to use the proposed optimization scheme to find a set of optimal diffusion parameters for each of the ten binder-systems included in this study.

2. Methods

2.1. Experimental investigations on ten binder-systems

In this section the methods used in the experimental investigations are described. The section contains description of the materials used in the ten different binder-systems that were considered, the preparation and curing of the samples and a description of the different experiments that were performed.

2.1.1. Materials

Two slightly different clinkers were used in this study; an ordinary rapidly hardening cement klinker (K1), used as a reference, and a new rapidly hardening cement clinker with high C_3A and C_3S content (K2), was used in combination with the SCMs to form nine different binder-systems with cement replacement levels of up to 40 wt%. The oxide composition of the two clinkers are given in Table 1. The K2 clinker is very similar to the K1 clinker, but it has a slightly better binding capacity in SCMs due to its higher C_3A and C_3S content. C_3A is 10% for the K2 clinker compared to 8% for the K1, and C_3S is 72% for the K2 compared to 68% for the K1. The SCMs used in the binder-systems investigated in this study were siliceous Fly Ash (FA), Gray micro-filler (GMF), a limestone dust collected as a by-product in cement production kiln, from two different batches with different chloride content (GMF 1 Cl = 0.48% and GMF 2 Cl = 0.14%), Burnt Shale (BS) and Calcined bentonitic Clay (CC). The oxide composition of the SCMs used are listed in Table 1. The sand used was a standard sand with a maximum particle size of 2 mm, according to the standard EN 196-1.

The binder composition of the ten different binders investigated in the present study are given in Table 2. Rapidly hardening cement containing 83.3 wt% K1 clinker and 16.7 wt% FA, often used in aggressive service environment, was used as a reference binder (R1) in this study. The binder-system B1 composed of the K2 clinker has the same clinker replacement level as the reference binder R1 to evaluate the effect of the clinker type on the binder-system performance. The

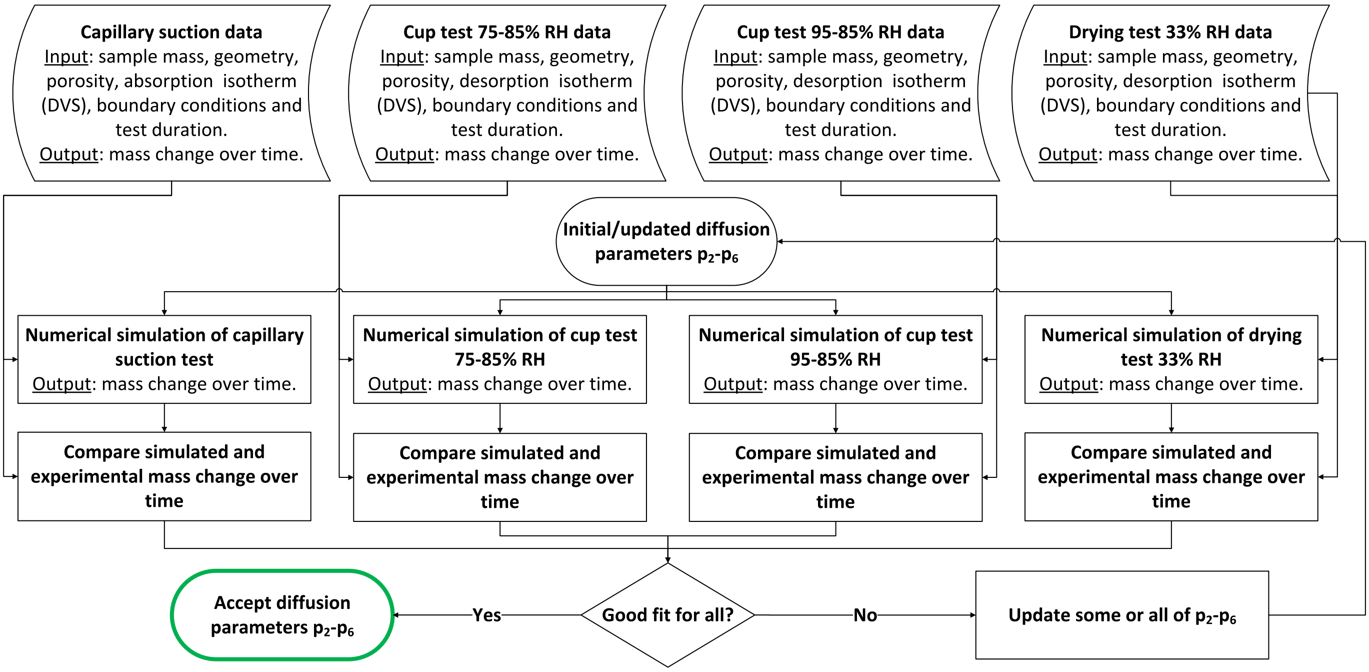

Fig. 1. Schematic representation of the inverse analysis procedure.

binder-systems B2–B8 all have a clinker replacement level of 35 wt % according to EN 197-1 and the binder-system B9 has a clinker replacement level of 40 wt % according to EN 197-1. In binder-systems B2 and B3 20 wt % of the clinker is replaced by limestone from the two different batches of GMF 1. FA is used to reach 35 wt % total clinker replacement for B2 and B3. The binder-systems B4 and B5 are with 20 wt % clinker replacement with BS, with an internal mass ratio between the BS and GMF 1 of 0.5 and 0.75, respectively (mass ratio = $m_{BS}/(m_{BS} + m_{GMF})$). FA is used to reach 35% total clinker replacement for B4 and B5. In binder-system B6 35 wt % of the clinker is replaced with GMF 2 without any FA. The binder-systems B7, B8 and B9 are with 35 wt % clinker replacement with CC, and no FA for B7 and B8, with an internal mass ratio between the CC and GMF 1 of 0.5 for B9, 0.75 for B7 and 1 for B8 (mass ratio = $m_{CC}/(m_{CC} + m_{GMF})$). FA was added to B9 to reach a total clinker replacement of 40 wt %. The SO_3 content of all binders was kept constant by adding gypsum.

2.1.2. Preparation and curing

An initial curing period of 90 days was selected for all mortar and paste samples to minimize the effect of any different reactivity of the SCMs. In order to compare the durability performance of the ten binder-systems, a preliminary study was made to normalize the strength of all binder-systems after 90 days to the compressive strength of R1 after 90 days by adjusting the w/b ratio (where c is the binder including SCMs) . A preliminary study calibrating all the mixes to give the same 90 days compressive strength resulted in the mix design shown in Table 3.

The mortar flow properties of **B2–B9** was adjusted to achieve

Table 2
Binder compositions of the ten binder-systems.

	K1	K2	FA	GMF 1	GMF 2	CC	BS	Gypsum
R1	83.33		16.67					
B1		76.53	16.67	4.00				2.81
B2		63.66	18.22		15.79			2.34
B3		63.66	18.22	15.79				2.34
B4		63.66	18.98	7.92			7.92	1.54
B5		63.66	19.35	3.96			11.89	1.14
B6		63.66			34.01			2.34
B7		63.66		8.50		25.51		2.34
B8		63.66				34.01		2.34
B9		58.89	7.49	15.73		15.73		2.16

Table 3
Mix design of the mortars.

Binder name	Binder (g)	Distilled water (g)	Sand (g)	Glenium sky 631 (g)	w/b
R1	450.0	225.0	1350		0.50
B1	452.6	224.5	1350		0.50
B2	464.2	216.3	1350	1.02	0.47
B3	456.8	219.2	1350	0.59	0.48
B4	448.8	222.0	1350	0.83	0.50
B5	451.7	220.7	1350	1.35	0.49
B6	482.9	213.3	1350	1.79	0.44
B7	416.7	233.1	1350	0.45	0.56
B8	434.2	224.2	1350	2.37	0.52
B9	433.6	226.2	1350	0.38	0.52

Table 1
The oxide composition of the K1 and the K2 cement clinkers, and the SCMs used in this study.

	CaO	SiO_2	Al_2O_3	Fe_2O_3	SO_3	MgO	K_2O	Na_2O	TiO_2	P_2O_5	Cr_2O_3	Cl	LOI	Total (%)
K1 clinker	65.39	20.17	5.52	3.97	1.55	0.8	0.54	0.21	0.28	0.26	0.01	0.24	0.03	98.97
K2 clinker	65.98	19.55	6.05	3.32	1.57	0.92	0.52	0.25	0.32	0.33	0.01	0.47	0.00	99.29
Siliceous fly-ash (FA)	0.82	62.51	16.64	9.38	0.37	2.95	2.82	1.95	0.93	0.15	0.02	2.39	0.03	100.96
Gray micro-filler (GMF 1)	44.03	12.7	3.57	1.85	0.44	0.6	0.58	0.23	0.24	0.2	0.01	35.00	0.21	99.66
Burnt shale (BS)	30.13	34.24	8.25	4.81	5.56	5.59	4.38	0.11	0.48	0.15	0.02	4.55	0.29	98.56
Calcined clay (CC)	4.48	55.04	19.92	5.53	0.38	1.81	2.16	1.12	0.9	0.53	0.02	3.2	0.00	95.09

similar flow properties as **R1** and **B1** (20 stroke flow) by adding different amounts of a superplasticizer, Glenium sky 631. All mortar samples were cast according to EN 196-1 standard with a *w/b* ratio according to Table 3 and a binder-to-sand ratio of 1/3. One batch of paste samples and two different batches of mortar samples were cast as follows:

- Paste samples of all ten binders, consisting of only water and binder (without superplasticizer), where cast in small plastic containers with *w/b* ratios according to Table 3. The samples were stored in closed plastic containers with 100% RH for 90 days in a temperature controlled room at 20 °C. The paste samples where used for the sorption isotherm measurements and the vacuum porosity measurement.
- Mortar Batch 1: 8 samples of each of the ten binders were cast in small closeable cylindrical plastic bottles with a diameter of 48 mm. The samples were stored in their closed containers in a temperature controlled room at 20 °C. A small amount water was added to the plastic containers to maintain 100% RH. Samples from this batch where used for the capillary suction test, drying test and to obtain the vacuum porosity of the mortars of all ten binders. Unfortunately, the flow properties of B7–B9 samples from Batch 1 were observed to be different from the rest of the binders in Batch 1. The difference in flow properties was not observed with Batch 2, indicating an error in the mixing of B7–B9 samples from Batch 1.
- Mortar Batch 2: One sample of each of the ten binders were cast in a cylindrical steel mold with inner diameter of 100 mm and height of 200 mm. The samples were de-molded after a week wrapped in a wet cloth inside closed plastic bags to maintain RH close to 100% and stored for 90 days in a temperature controlled room at 20 °C. After curing a cylindrical core with a diameter of 64 mm were drilled out of the 100 mm samples. Discs 12 mm in thickness where sliced from the 64 mm diameter core and used for the cup measurements and vacuum porosity measurements.

2.1.3. Vacuum porosity and density

The porosity and density of the paste and mortar samples were evaluated after about 90 days of curing, using vacuum porosity. Two to three samples of each binder-system from each Batch were saturated using distilled water in desiccators in a vacuum environment for 2–5 days. After saturation, the samples were dried in an oven at 105 °C until steady dry weight was obtained. The saturated samples' masses under water was measured to estimate the volumes.

2.1.4. Sorption isotherm measurements

The sorption isotherms of all ten binder-systems were measured using a DVS advantage sorption balance as detailed in [35] and [5]. Paste samples were tested after about 90 days of curing in a humid environment. Before testing the paste samples were crushed into powder from which small samples, around 20 mg in mass, were extracted for the DVS tests. The following RH-cycle was used for all samples: 95-85-75-55-35-10-35-55-75-85-95-0% RH. The RH-schedule continued to the next level when the mass change was close to zero (the following criterion was used: $dm/dt < 0.0002\%/\text{min}$; minimum 200 min; maximum 1000 min), which resulted in step sizes from 200 to 1000 min. The repeatability of the DVS results was tested on three of the binders-systems, R1, B5 and B7.

2.1.5. Capillary suction test

The rate of water uptake of mortars made with the ten binder-systems was tested using a one dimensional capillary suction method according to ASTM standard C1585-13 [36] with modification concerning the sample size and changes to the conditioning of the samples. Three mortar samples of each binder-system produced from mortar Batch 1 were used to perform the test. After about 90 days of curing, the samples were removed from the plastic containers, and cut with a diamond saw to discs 30 ± 3 mm in height and 48 ± 0.5 mm in diameter. The samples were dried in an oven at 50 ± 5 °C in sealed metal containers until a steady weight had been reached for all samples (took about 60 days) . The RH inside the metal containers was measured by the end of the drying period to be around 10% RH. The samples were coated with epoxy coating, leaving one open end for exposure to a free water surface. During the capillary suction test, the initial mass of each sealed sample was measured. The sample was then placed in contact with a free water surface and the mass change over a few days was measured at intervals, in according to ASTM C1585-13 [36].

2.1.6. Cup test

In a cup test, a discs shaped sample is sealed on the side and placed as a lid on a cup containing a saturated salt solution with a known RH providing the samples exposure to fixed internal RH. The cups are placed in a salt box with another RH providing a different RH environment for the outer surface of the disc. The mass change of the sample is measured over time to evaluate the vapor diffusion rate in the selected RH intervals.

In the present study, two sets of cup test with two RH intervals were carried out using an improved technique presented in [21]. Three saturated mortar discs from Batch 2 were used for each of the two selected RH intervals after a curing period of 90 days. The internal RH exposure condition was 75% for one set and 95% for the other set. The external exposure condition for all samples was 85% RH. The saturated salt solutions used were NaCl (75% RH), KCl (85% RH) and KNO_3 (95% RH). The mass change of the samples was measured over time until steady rate of mass change was observed.

2.1.7. Drying test

The drying test is similar to the cup test, but with only one surface exposed to a fixed RH condition. Three saturated disc samples of each binder-system from mortar Batch 1 were used for the drying tests. After 90 days of curing the samples were removed from the plastic containers, then discs 15 ± 2 mm in length were cut with a diamond saw. The diameter of the samples was not changed compared to the mold size and had a diameter of 48 ± 0.5 mm. The discs were then saturated using distilled water in desiccators under vacuum for 2–5 days. After this, the discs were sealed using aluminum tape leaving only one exposed surface. The sealed samples were then placed in a salt box with a saturated $MgCl_2$ solution providing 33% RH. The mass change of the samples was measured over three months.

2.2. Numerical model

This section describes the numerical approach used to establish effective diffusion parameters on the basis of the experimental results. First the governing equations for the two-phase moisture transport are presented. Secondly the inverse analysis procedure to obtain the effective diffusion parameters is explained.

2.2.1. Two-phase moisture transport model

Moisture transport was treated as a continuum two-phase flow in the model: a liquid water phase, and a water vapor phase. The liquid and vapor phase were linked with exchange terms. This follows the framework detailed in [11]. The liquid water flow was expressed using a generalized version of Darcy's law where instead of the pressure gradient the volume fraction of an incompressible liquid is used as driving potential for the liquid flow as derived in [37,38] and modified in [39], as follows:

$$\rho_w \frac{\partial \varepsilon^l}{\partial t} = \nabla\cdot(D_{\varepsilon^l}\nabla\varepsilon^l) + \widehat{m}_l \tag{1}$$

where ρ_w is the water density, treated as a constant in the model, ε^l is the volume fraction of the liquid phase relative to the pore space. ε^l is the main unknown in Eq. (1). $D_{\varepsilon^l} = D_{\varepsilon^l}(\varepsilon^l)$ is the effective diffusion function for the liquid phase. D_{ε^l} is one of the two main targets of the inverse analysis procedure. $\widehat{m}_l$ is the mass exchange term of the liquid phase, which accounts for the mass exchange between the liquid and vapor phase.

An expression similar to Eq. (1) is used for the water vapor flow [40], that is

$$\rho_{vs}(\varepsilon_p - \varepsilon^l)\frac{\partial \phi_v}{\partial t} - \rho_{vs}\phi_v\frac{\partial \varepsilon^l}{\partial t} = \nabla\cdot(D_\phi \nabla \phi_v) + \widehat{m}_v \tag{2}$$

where ρ_{vs} is the vapor saturation density, treated as a constant assuming isothermal conditions, ε_p is the total porosity which is assumed to be constant. ϕ_v is the relative humidity, the main unknown in Eq. (2). $D_\phi = D_\phi(\varepsilon^l)$ is the effective diffusion function for the vapor phase, the other main target of the inverse analysis procedure besides D_{ε^l}. $\widehat{m}_v$ is the mass exchange term of vapor phase, which is equal to $-\widehat{m}_l$. The mass exchange terms of the liquid and vapor phases, $\widehat{m}_l$ and $\widehat{m}_v$, are functions depending on the relative humidity, ϕ_v, saturation degree, ε^l, and the liquid-equilibrium functions, $\varepsilon^{l,eq,*}$ [11,25,40], expressed as follows:

$$\widehat{m}_l = -\widehat{m}_v \tag{3}$$

$$\widehat{m}_l = R(\varepsilon^{l,eq,*}(\phi_v) - \varepsilon^l) \tag{4}$$

where R is a rate constant for the local mass exchange of water between the liquid and vapor phase. The liquid-equilibrium functions $\varepsilon^{l,eq,*}$ are defined as the best fit of a third order polynomial to the measured sorption isotherms.

The mass exchange terms $\widehat{m}_l$ and $\widehat{m}_v$ in Eqs. (1) and (2) accounts for the difference between ε^l and $\varepsilon^{l,eq,*}(\phi_v)$ which can be different in the case of non equilibrium sorption, that is when the moisture state is not located at the sorption isotherm. In traditional models where local equilibrium between the RH and saturation degree is assumed, Eqs. (1) and (2) are usually combined to one equation. However, in this model we do not assume local equilibrium. The model allows for non-equilibrium conditions in the sorption process. This means that there is no direct relation between the vapor and liquid water concentration through the equilibrium sorption isotherm. Instead an assumption is made that the sorption equilibrium is reached at a certain rate determined by the material constant R. When the numerical value of R is chosen to be sufficient high it works as a penalty number. That is, when R is a sufficiently high value, the sorption phenomenon follows the equilibrium sorption isotherm curve without any kinetic sorption effects involved. Allowing for kinetic sorption effects, as described above, it is not possible to eliminate one of the transport equations from the system instead they need to be solved as a truly coupled system of equations.

The effective diffusion functions chosen in this study were

$$D_{\varepsilon^l}(\varepsilon^l) = p_1 + p_2{\varepsilon^l}^{p_3} \tag{5}$$

$$D_\phi(\varepsilon^l) = p_4 + p_5{\varepsilon^l}^{p_6} \tag{6}$$

where $p_1,\ldots, p_6$ are the parameters used to optimize the effective diffusion functions. The parameter p_1 is a constant introduced to avoid numerical instability. A value of $p_1 = 10^{-12}$ was used throughout this study.

Two different states of the liquid-equilibrium function $\varepsilon^{l,eq,*}$ are considered, a wetting state, referred to as the lower sorption curve *lb* and a drying state, referred to as the upper sorption curve *ub*. That is, the liquid-equilibrium functions $\varepsilon^{l,eq,ub}$ and $\varepsilon^{l,eq,lb}$ are defined as

$$\varepsilon^{l,eq,ub}(\phi_v) = h_1^{ub}\phi_v + h_2^{ub}\phi_v^2 + h_3^{ub}\phi_v^3 \tag{7}$$

$$\varepsilon^{l,eq,lb}(\phi_v) = h_1^{lb}\phi_v + h_2^{lb}\phi_v^2 + h_3^{lb}\phi_v^3 \tag{8}$$

where $\{h_1^{ub}, h_2^{ub}, h_3^{ub}\}$, and $\{h_1^{lb}, h_2^{lb}, h_3^{lb}\}$ are constant coefficients established by fitting measured sorption isotherm data expressed in terms of RH using Eqs. (7) and (8), respectively.

The overall and more general two-phase moisture transport model can take the effect of the change in the sorption direction by the use of sorption scanning curves between the upper and lower boundary, as described in [40,41]. This was not used in the present study since the experiments performed were either in drying or wetting conditions, with no change in sorption direction during an experiment.

An implicit transient finite element method was used to solve the model equations in a fully coupled system. A modified Newton-Raphson iteration scheme was used to account for the non-linearity of the model. Details of the numerical approach are available in [9].

2.2.2. Inverse analysis of the effective diffusion parameters

Fig. 1 shows a schematic representation of the inverse analyses procedure used to obtain an optimal set of water and vapor effective diffusion parameters $p_2,\ldots,p_6$ for each binder-system. The proposed two phase moisture transport model was used to simulate the samples mass change over time from the following four experiments:

1. The drying experiment with 33% RH.
2. Cup measurement with the interval 75–85 % RH.
3. Cup measurement with the interval 95–85 % RH.
4. The capillary suction test.

In each optimization iteration, four simulations were made in sequence, one for each of Experiments 1–4, using an initial set of parameters $p_2,\ldots,p_6$. At the end of each iteration the error, that is the difference between the mass change simulated by the model and the experimentally measured mass change, was used as a basis for updating the parameters $p_2,\ldots,p_6$. A combination of manual selection and the use of a Maximum Likelihood Estimation technique [42] was used to select the updated parameters $p_2,\ldots,p_6$. The updated parameters were then used in the next iteration run. The iteration continued until a good fit for all four experimental results was reached. In this process, information from each of the four experiments, in terms of the boundary conditions, the duration, the porosity, the initial mass and the dimensions of the samples, was used as input to the model. The upper and lower sorption boundary coefficients $\{h_1^{ub}, h_2^{ub}, h_3^{ub}\}$, and $\{h_1^{lb}, h_2^{lb}, h_3^{lb}\}$ were established by fitting measured sorption isotherm data from DVS measurements. The measured porosity of the paste was used to express the DVS results in term of saturation degree.

It should be noted that the number of iterations needed to find the optimized parameters $p_2,\ldots,p_6$ greatly depends on the initial guess. The following steps were carried out for the binder-systems where the initial guesses were not within the targeted order of magnitude:

1. Manually updating the liquid water diffusion parameters p_2 and p_3 only on the basis of the capillary suction test, keeping p_4, p_5 and p_6 fixed. This required more than 20 iterations to reach simulation results within he same order of magnitude as the experimental results. It should be noted, that the parameters p_2 and p_3 also affects the simulation results of the cup tests and to a lesser extend the drying test, which is why getting results within the same order of magnitude is sufficient at this step. Experience with the model, where all four experiments were used as illustrated in Fig. 1, later led to the selection of a fixed value for the exponential coefficient $p_3 = 50$, which was found to give reasonable results for all experiments of all the binder-systems included. The selected value, $p_3 = 50$, is not unique in it self, but the coefficient p_3 needed to be have a high value to account for the rapid increase of water uptake at RH = 100%. Fixing p_3 in practice reduced the number of variable liquid water diffusion parameters to one parameter, that is p_2. This simplified this step and reduced the number of iterations needed.
2. Manually updating the water vapor diffusion parameters p_4, p_5 and p_6 on the basis of the drying test only, keeping p_2 and p_3 fixed. This initially required more than 50 iterations due to the countless possible combinations of the three parameters. The number of iterations was significantly reduced for the rest of the analyzed binder-system

when this initial set of parameters p_4, p_5 and p_6 was obtained. Since the drying test condition was at a low RH value, of 33%, it was less sensitive to the liquid water diffusion parameters p_2 and p_3 which were more sensitive to the high RH domain.

3. Finally, the parameters p_2, p_4,…,p_6 were fine tuned by running all four simulations corresponding to the four experiments as illustrated in Fig. 1. This was the most crucial step where a lot of fine tuning was needed in order to fit all four experimental results at the same time. It was especially challenging to fit the 95–85 % RH cup measurements since it was more sensitive to all four parameters p_3, …,p_6.
4. Once steps 1, 2 and 3 have been performed, a Maximum Likelihood Estimation technique [42] can be used to further optimize the parameters p_2,p_4,…,p_6.

3. Results

The experimental test results for all ten binder-systems are presented in the first part of this section. Based on the experimental results, numerical examples of the optimization procedure of the effective diffusion parameters are given in the second part.

3.1. Experimental results

The measured vacuum porosity and dry density of the paste and the two mortar batches are given in Table 4. A theoretical approximation of capillary porosity obtained using Powers formula is also shown in Table 4. A rough estimation of the degree of hydration was calculated from the w/b ratio and the measured total porosity using the Power's formula. In a second step, the estimated degree of hydration was used to calculate the capillary porosity.

The presented porosity and density values of mortar Batch 2 are average values with a maximum standard deviation less than 0.01. As expected, there was no significant difference in porosity or density between mortar samples from Batch 1 and Batch 2 other than for binder B6. (see 2.1.2)

Subplot (a) in Figs. 2–6 compares the sorption isotherm results of all the binder-systems, with RH in percentage along the x-axis, and moisture content in gram water per gram dry sample along the y-axis. The displayed sorption isotherms of R1, which are given in all plots, are average values of two replicates with their standard deviation indicated with the error bars. Subplot (b) in Figs. 2–6 compares capillary suction results with the square root of time along the x-axis, and mass change in gram per gram initial sample mass along the y-axis. Subplots(c), (d) and (e) in Figs. 2–6 compare cup test results with the interval 75–85 % RH, cup test results with the interval 95–85 % RH and the drying test results, respectively, with time in days along the x-axis, and mass change in gram per gram initial sample mass along the y-axis. All the results in subfigure (b–e) in Figs. 2–6 are average values of three replicates with their standard deviation indicated with the error bars. Fig. 2 compares all the experimental results between R1 and B1 to study the difference between the K1 and K2 clinkers. Fig. 3, compares R1 to B2 and B3 to compare the effect of the two different limestone fillers, GMF 2 and GMF 1, which were used in B2 and B3, respectively. All three binder-systems R1, B2 and B3, contain fly ash. Fig. 4 compares R1 to B6 with K2 and GMF 1 without FA. Fig. 5 compares R1 to B4 and B5 with BS and GMF 1 with an internal mass ratio of 0.50 and 0.75, respectively. Fig. 6 compares R1 to B7, B8 and B9 with CC and GMF 1 with an internal mass ratio of 0.50 for B9, 0.75 for B7 and 1 for B8.

Table 4
Porosity and dry density of the past and the two mortar batches for all ten binder-systems.

	Paste			Mortar 1		Mortar 2	
	Por.	Dry den.	Cap. por.	Por.	Dry den.	Por.	Dry den.
R1	0.44	1.40	0.32	0.19	2.15	0.18	2.13
B1	0.45	1.40	0.32	0.18	2.14	0.18	2.12
B2	0.43	1.41	0.31	0.19	2.11	0.18	2.12
B3	0.44	1.37	0.31	0.18	2.13	0.18	2.13
B4	0.44	1.40	0.31	0.2	2.11	0.18	2.13
B5	0.45	1.38	0.32	0.2	2.09	0.20	2.12
B6	0.43	1.47	0.29	0.28	2.11	0.17	2.15
B7	0.48	1.30	0.36	0.19	1.92	0.20	2.08
B8	0.45	1.34	0.33	0.21	2.06	0.19	2.07
B9	0.48	1.30	0.35	0.22	1.98	0.20	2.06

3.2. Numerical simulation

The results of the proposed inverse analyses are displayed in Figs. 7, 8 and 9.

Subplot (a) in Figs. 7, 8 and 9 shows the sorption isotherms data recalculated in terms of saturation degree along the y-axis, together with the best fit to the data with the liquid-equilibrium functions in Eqs. (7) and (8). The liquid-equilibrium curves in subplot (a) in Figs. 7, 8 and 9 were forced to go through point (0,0) and (1,1) to ensure model stability. Eqs. (7) and (8) for the ten binder-systems are listed in Table 5. Note that these coefficients are sensitive to changes even in the fourth decimal position. Subplot (b) in Figs. 7, 8 and 9 shows the optimized diffusion curves used to generate the model results which are shown together with the corresponding experimental data in subplots (c–f) in Figs. 7, 8 and 9. The obtained diffusion parameters p_2,…,p_6 of the ten binder-systems are listed in Table 6. Fig. 10 shows an example of how the simulated relative humidity and saturation degree profiles develop over time for the capillary suction test, the drying test and the two intervals of the cup test.

4. Discussion

In the first part of this section the experimental results of the ten binder-systems are briefly discussed with the focus on comparing the new binder-systems B1–B9 to the reference binder-system R1 in terms of moisture transport characteristics. A number of analyses could be carried out on the data collected in this study, for example, the DVS data could be used to evaluate the specific surface area and pore size distribution of the ten binder systems as described in, e.g. [5,43]. These kinds of analyses are important in order to get a better understanding of effects like pore-size distribution on the moisture transport properties. However, they were not included in the present paper in order to keep the focus on the proposed inverse analysis method for determining two-phase diffusion parameters. A discussion of the proposed method is given in the second part of this section.

4.1. The experimental part

In the lower curves of Fig. 2 (a) the lower boundary sorption isotherms of the two binder-systems R1 and B1 are shown. The two curves overlap in the low and medium RH range but they differ slightly in the higher RH range, with B1 having a slightly lower moisture content at high RH. The capillary suction results shown in Fig. 2 (b) show no clear difference between B1 and R1. The results from the capillary suction test can be related to the lower boundary sorption isotherms since the samples were dried before exposure to water, and the results from the drying test and cup test can be related to the upper boundary sorption isotherms as the samples were saturated and then exposed to lower RH during these tests. The upper curves in Fig. 2 (a) show a difference in the upper boundary sorption isotherm of R1 and B1 in the mid range RH interval. This is consistent with the results from the drying test in Fig. 2 (e) in which the mass reduction of B1 is slightly less than that of R1. The effect of the difference in upper boundary sorption isotherms between R1 and B1 was not captured by the cup test results in Fig. 2 (c) and (d), where no significant difference between R1 and B1 was observed. In general, no significant difference in moisture sorption and

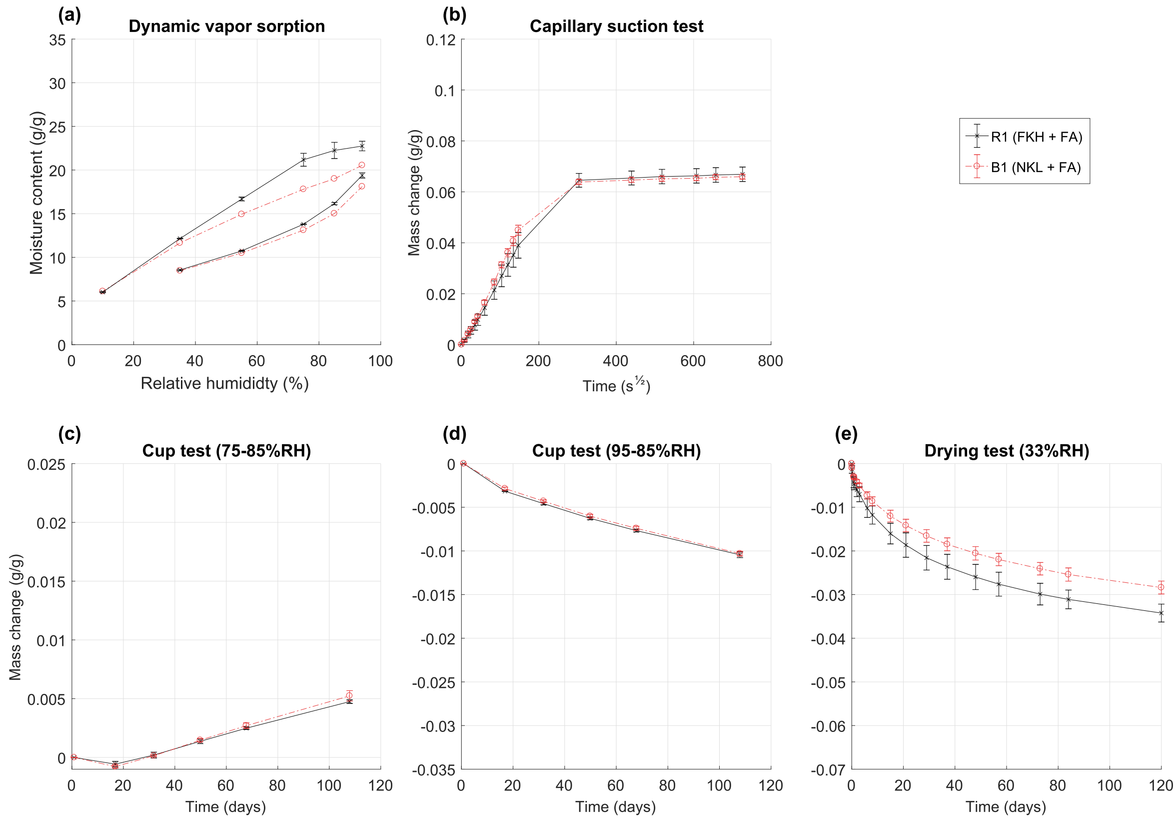

Fig. 2. Comparing the experimental results for the K2 clinker and the K1 clinker.

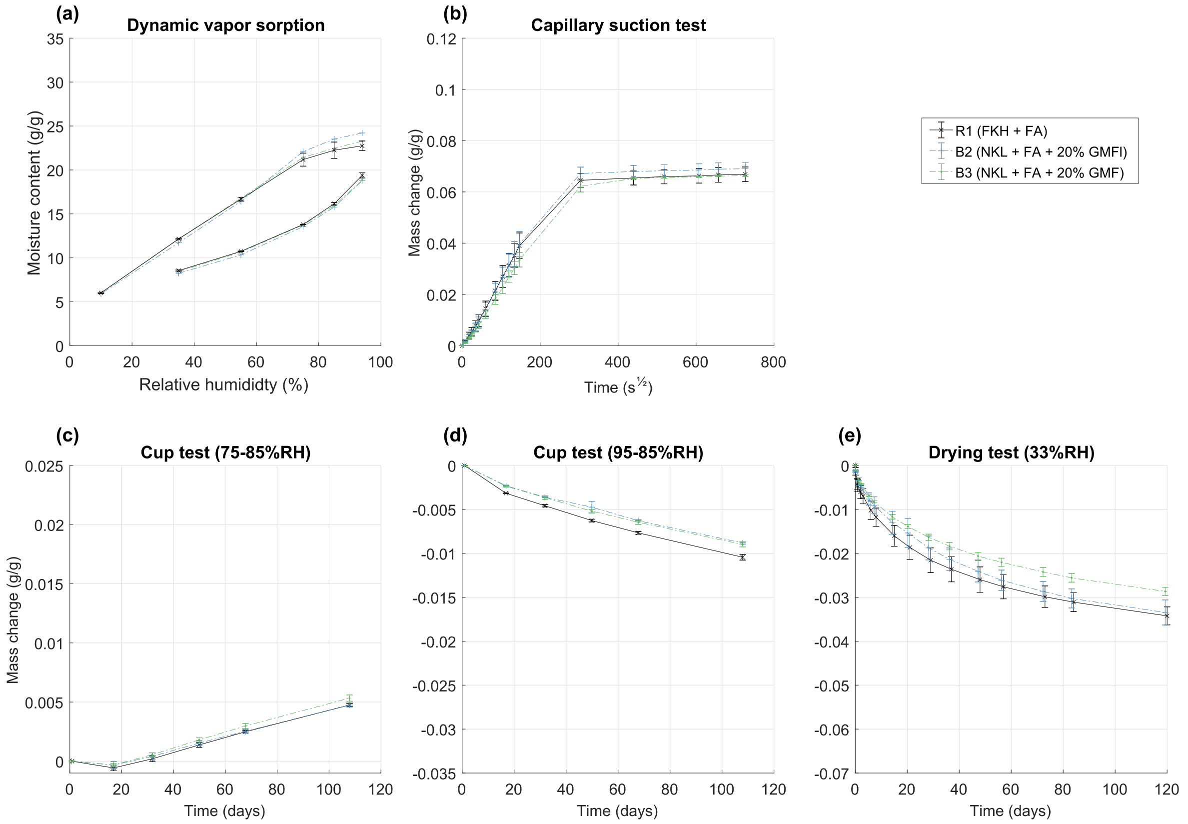

Fig. 3. Comparing the experimental results of R1 and B2–B3 containing K2 + GMF 1 + FA.

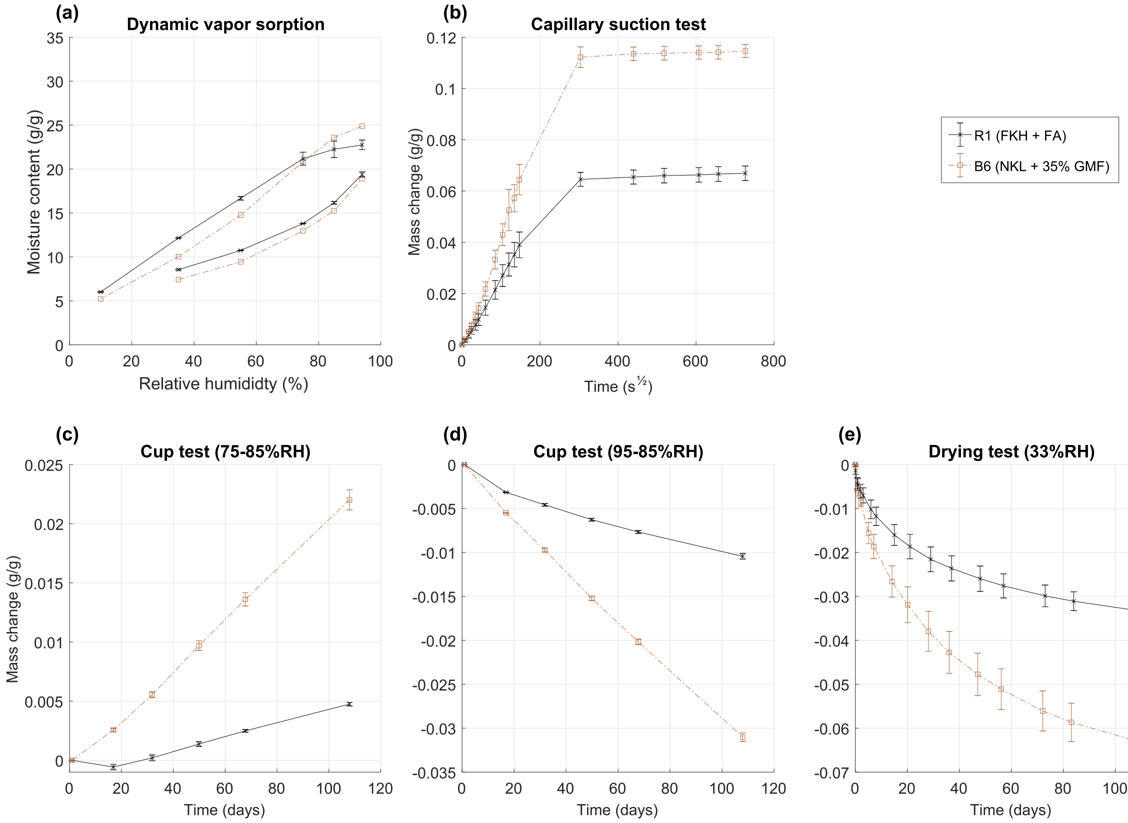

Fig. 4. Comparing the experimental results of R1 and B6 containing K2 + GMF 1.

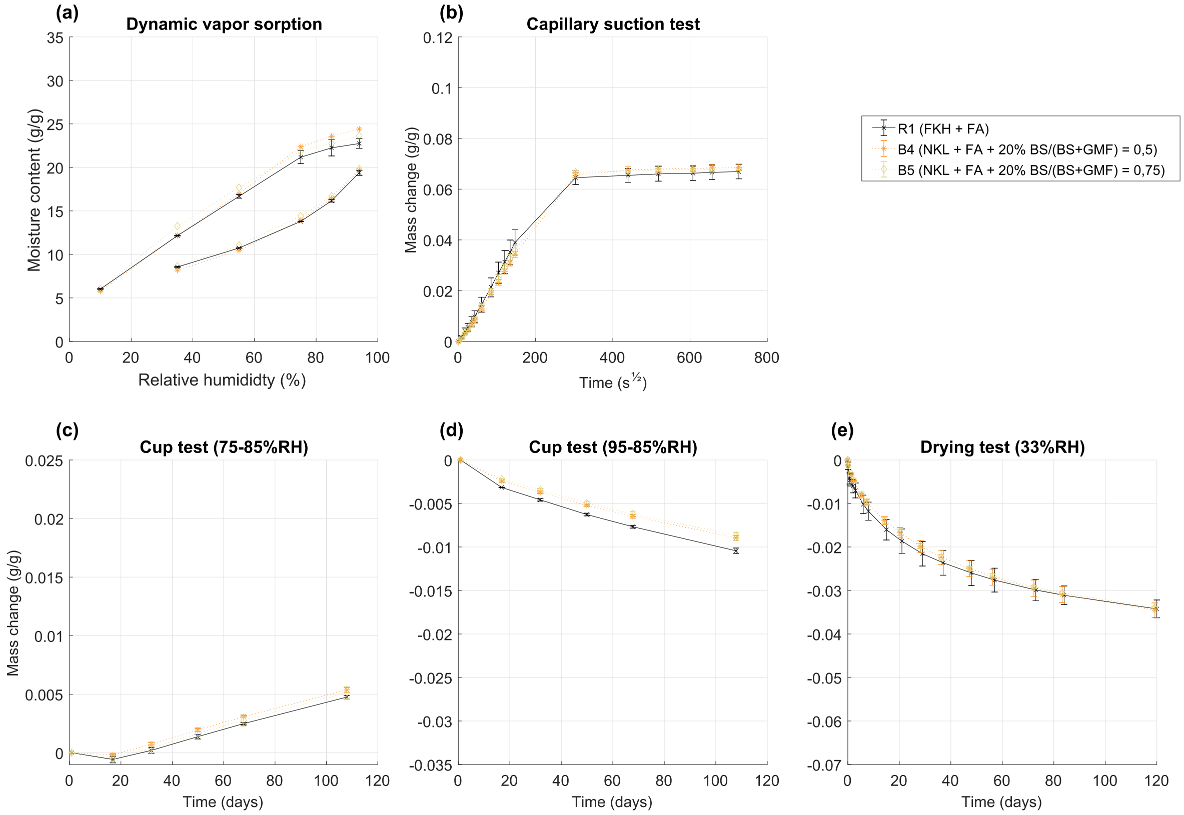

Fig. 5. Comparing the experimental results of R1 and B4–B5 containing K2 + BS + FA.

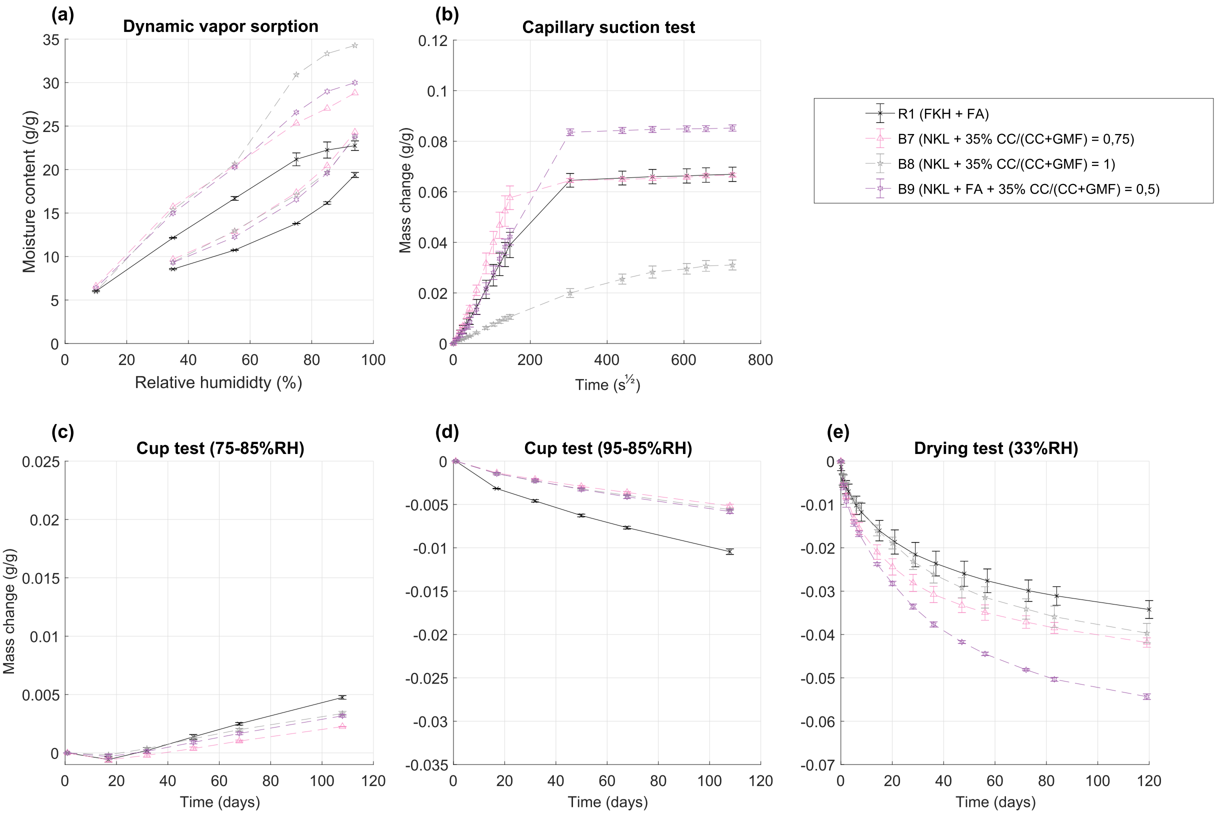

Fig. 6. Comparing the experimental results of R1 and B7–B9 containing K2 + CC + GMF 1 + FA.

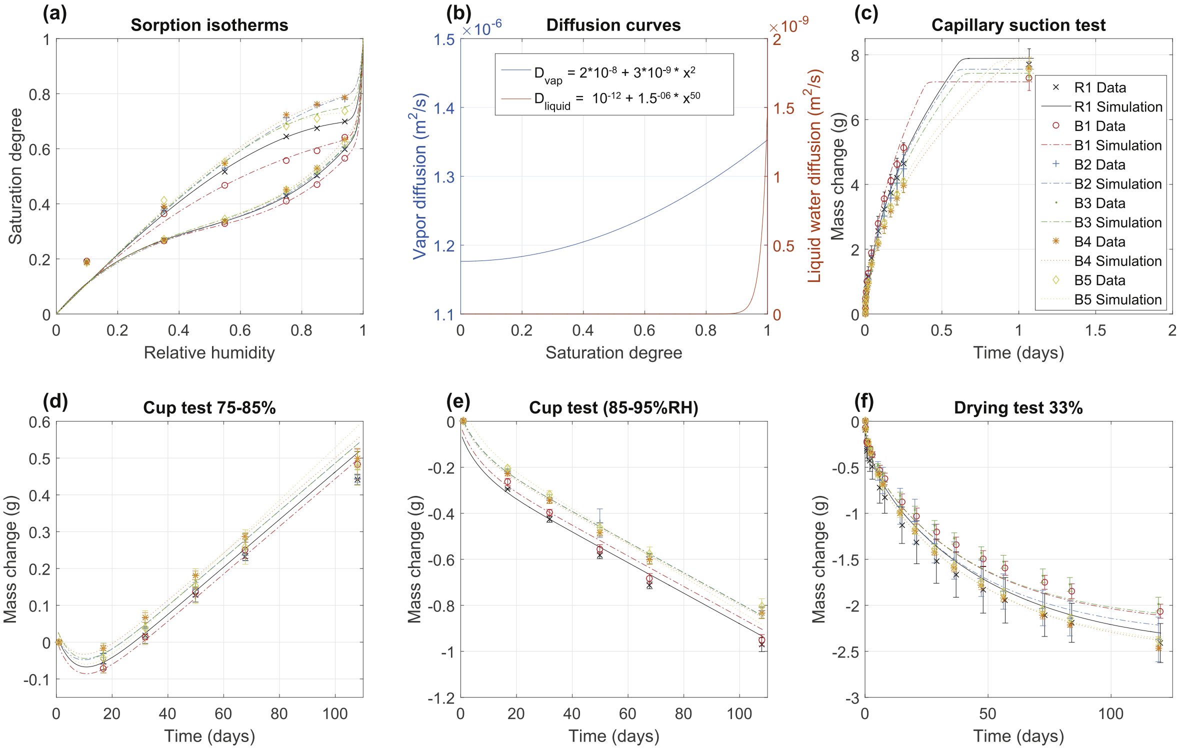

Fig. 7. A good fit of the numerical simulations to experimental results for R1, B1,…,B5 using the same set of diffusion parameters for all.

transport properties between B1 and R1 was observed. This is consistent with the fact that the K1 and K2 clinkers used in R1 and B1 respectively, are similar, as shown in Table 1.

Figs. 3 and 5 show no significant difference between binder-systems R1, B2 and B3 and binder-system R1, B4 and B5. Fig. 3 indicates that the difference between GMF 2 and GMF 1, used in B2 and B3, respectively, has no significant effect on the overall moisture properties. The higher chloride content in GMF 1 can however have an effect on the

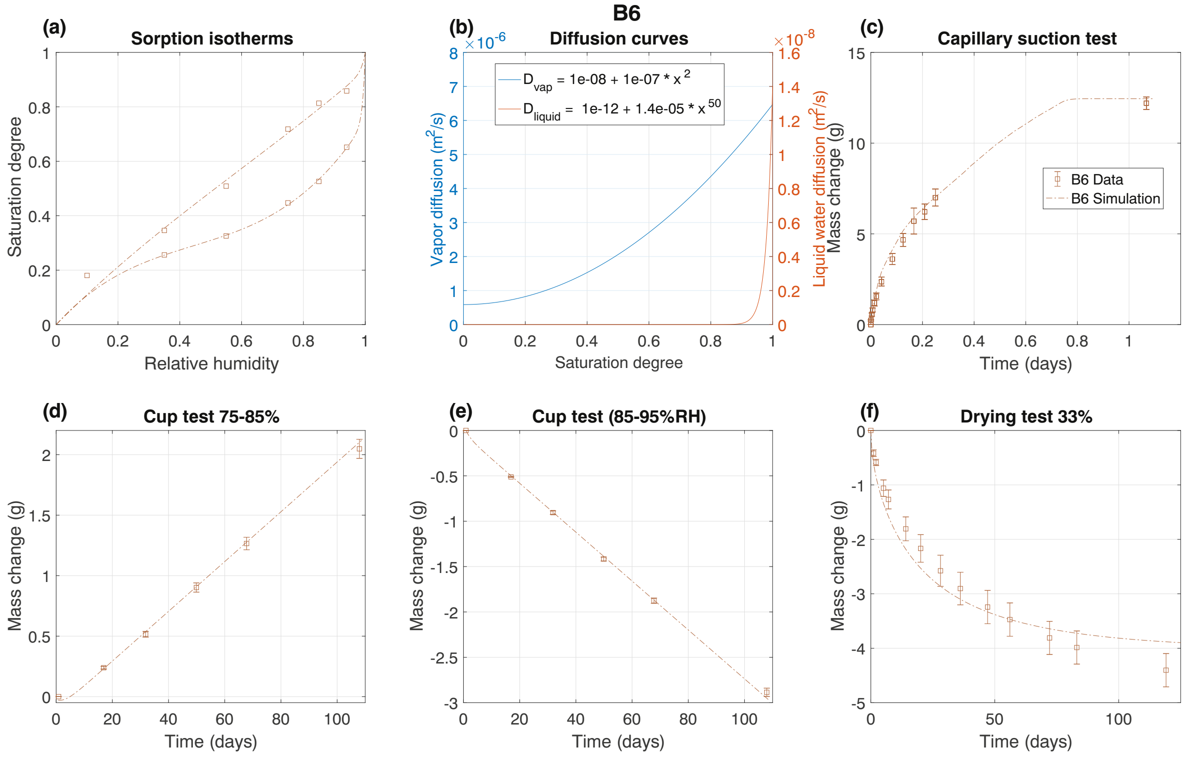

Fig. 8. A good fit of the numerical simulations to experimental results for binder-system B6.

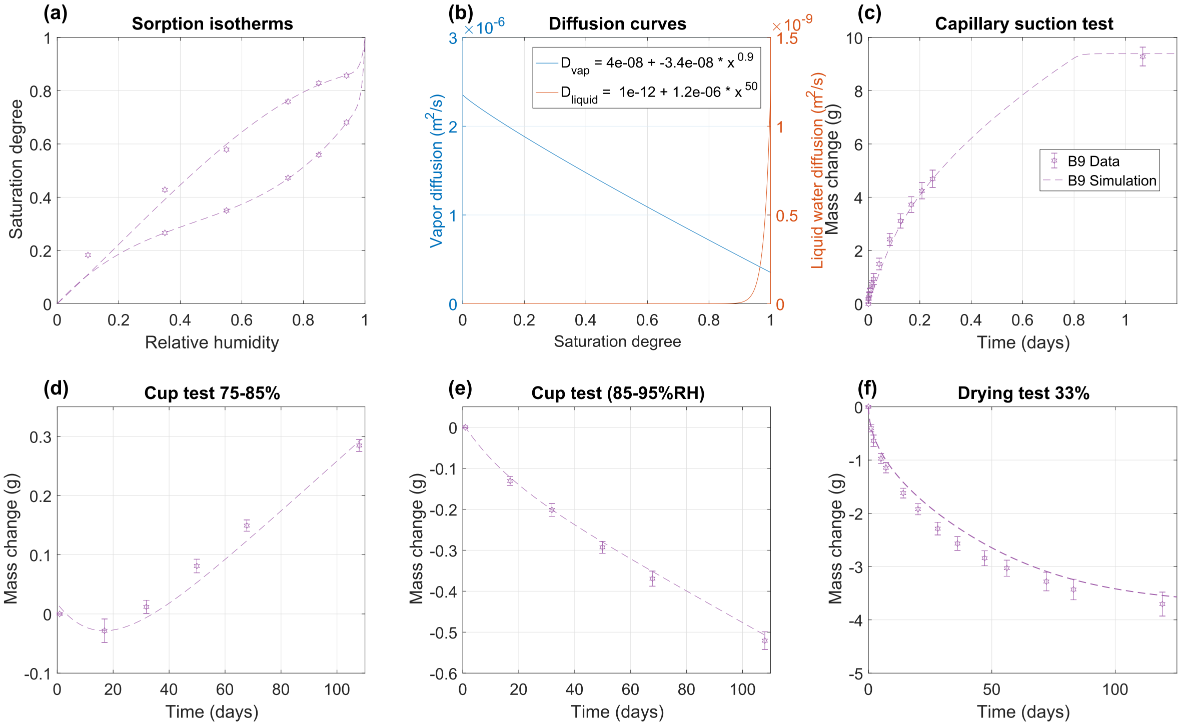

Fig. 9. A good fit of the numerical simulations to experimental results for binder-system B9.

durability.

Fig. 4 shows that binder-system B6, which contains 35% GMF 1 and no FA, has much higher moisture transport rates than R1. B6 is in fact the worst performing binder-system in this study in terms of durability. The results clearly indicate that part of the limestone filler did not react, resulting in a reduction of the hydrated phases and increase in the connectivity of the pore space, allowing faster transfer of moisture.

Fig. 6 shows how binder-systems B7–B9 tends to have a lower diffusion rate for the cup test results compared to R1, and higher overall mass change for the drying test. Unfortunately, the capillary suction and drying test results of B7–B9 cannot be trusted due to the error explained in the method section. However, this indicates that the presence of the calcined clay led to a refinement of the pore sizes as reviewed in, e.g., [44,45].

Table 5
The liquid-equilibrium functions coefficients $\{h_1^{ub}, h_2^{ub}, h_3^{ub}\}$, and $\{h_1^{lb}, h_2^{lb}, h_3^{lb}\}$ in Eqs. (7) and (8) giving the best fit to the sorption isotherms for the ten binder-systems

	h_1^{ub}	h_2^{ub}	h_3^{ub}	h_1^{lb}	h_2^{lb}	h_3^{lb}
R1	1.1165	−0.1370	−0.2795	1.3089	−2.0424	1.4119
B1	1.1617	−0.6286	0.1139	1.3246	−2.1139	1.4275
B2	0.1074	−0.0486	−0.2510	1.3080	−2.0400	1.4119
B3	1.0987	0.0531	−0.3977	1.3080	−2.0400	1.4119
B4	1.0942	0.0971	−0.3902	1.2950	−2.0000	1.2000
B5	1.0879	0.1752	−0.5394	1.2970	−2.0000	1.2000
B6	1.1443	−0.4685	0.2584	1.2560	−2.0397	1.5301
B7	1.0839	0.2114	−0.5066	1.1988	−1.6718	1.2346
B8	1.0814	0.2182	−0.3259	1.2166	−1.6093	1.1682
B9	1.0746	0.3046	− 0.5078	1.2554	− 1.9127	1.4312

Table 6
The optimized diffusion parameters $p_2,\ldots, p_6$ of the ten binder-systems in accordance with Eqs. (5) and (6).

	p_2	p_3	p_4	p_5	p_6
R1–B5	$1.5 \cdot 10^{-6}$	50	$2 \cdot 10^{-8}$	$3 \cdot 10^{-9}$	2
B6	$1.4 \cdot 10^{-5}$	50	$1 \cdot 10^{-8}$	$1 \cdot 10^{-7}$	2
B7	$1.2 \cdot 10^{-6}$	50	$4.5 \cdot 10^{-9}$	$- 4 \cdot 10^{-8}$	0.8
B8	$5 \cdot 10^{-7}$	50	$4 \cdot 10^{-8}$	$- 4 \cdot 10^{-8}$	1.5
B9	$1 \cdot 2^{-6}$	50	$4 \cdot 10^{-8}$	$- 3.4 \cdot 10^{-8}$	0.9

4.2. Numerical optimization model

As shown in Figs. 7, 8 and 9 the proposed two phase model with the optimized diffusion parameters, listed in Table 6, gives a good fit for all four experiments on the different binder-systems.

Fig. 7 shows that it was possible to get a good fit to R1 and B1-B5 using the same set of effective diffusion parameters $p_1,\ldots,p_6$ for all six binder-systems, but with different coefficients, $\{h_1^{ub}, h_2^{ub}, h_3^{ub}\}$ and $\{h_1^{lb}, h_2^{lb}, h_3^{lb}\}$, for liquid-equilibrium functions, shown in Table 5. This agrees with the observation from the experimental results that no significant difference was noted between R1 and B1–B5. It can be seen in Fig. 8 and Table 6 that the effective diffusion parameters obtained in order to fit the experimental results of B6 were almost one order of magnitude higher than that of R1. The optimization results for binder-systems B7–B9 are listed in Table 6 and also presented in Fig. 9 for the case of B9. These results were included despite the earlier discussed experimental issues with the capillary suction and drying test samples. Getting a good fit for B7–B9 required effective vapor diffusion functions which decrease with increased saturation degree. This illustrates the flexibility and generality of the proposed inverse method.

In the following, a discussion of the proposed diffusion functions is given, followed by a discussion of the sorption equilibrium functions.

4.2.1. The shape of the suggested diffusion functions

Eqs. (5) and (6) were used as empirical relations to describe the effective diffusion function of the liquid and vapor phase for the two-phase moisture transport model given by Eqs. (1) and (2). Note that the term effective diffusion in Eqs. (1) and (2) includes geometry effects and capillary effects. The study in [32] used a similar inverse analysis approach to determine effective diffusion functions based on one drying experiment. They compared four different effective diffusion functions of the two-phase models suggested in [46–49] and a single phase model, see Table 1 in [32]. All four two-phase models gave a better fit to drying data compared to the single phase model. The functions for liquid water effective diffusion used in all four two-phase models in [32] were described using different forms of exponential functions depending on the RH and/or degree of saturation while the effective diffusion function for vapor was described using a single constant value. Initial inverse analyses were carried out in this study to fit the experimental data using a function for the liquid phase and a constant value for the gas phase, as was also done in [46–49]. It was possible to obtain acceptable fits between the model and either the drying experiment, cup test or capillary suction test, one at a time using different sets of diffusion parameter to fit each experiment. However, it was not possible to fit all four experiments using the same set of parameters when assuming that vapor diffusion is constant. Fitting one diffusion

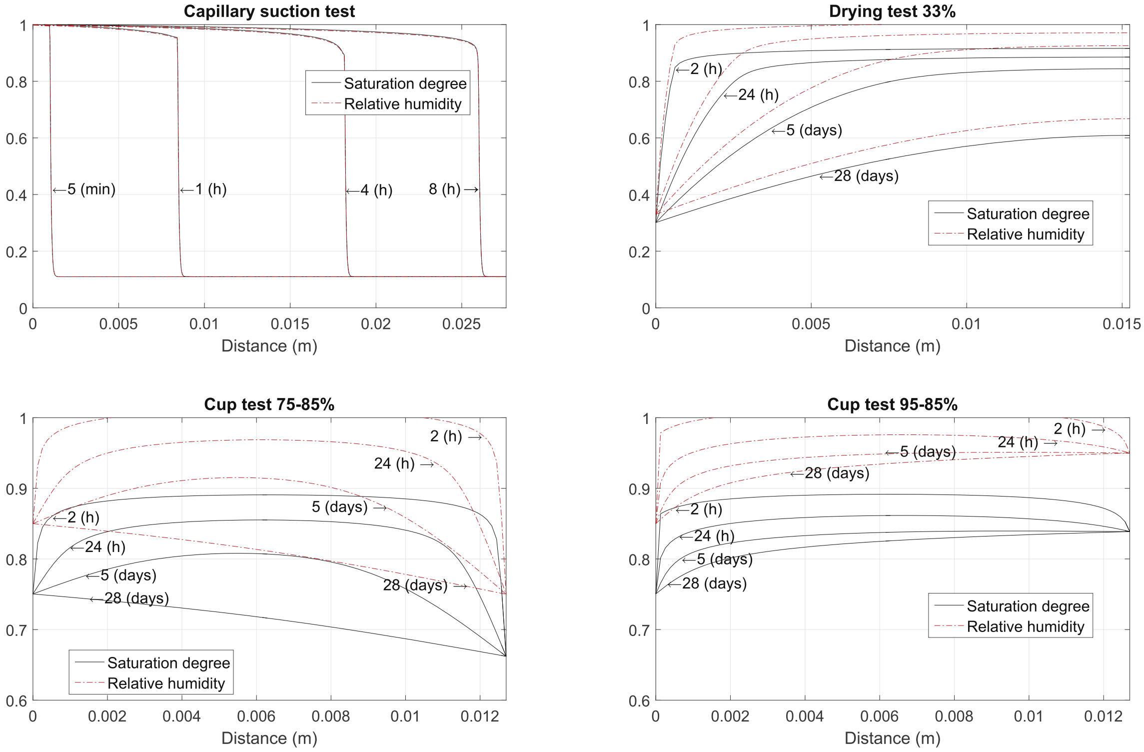

Fig. 10. The development of the relative humidity and saturation degree over time for the four diffusion experiments.

experiment at a time, for example, the drying experiment, was fairly straightforward but, fitting all four diffusion experiment using the same set of parameters was not possible unless vapor diffusion parameters were included as adjustable parameters. The study in [24] suggested using a linearly decreasing function of saturation degree to describe effective vapor diffusion by assuming vapor transport would be blocked by the presence of liquid water in the pore system. Using this assumption, it was possible to fit the experimental results for binder-systems B7–B9 using almost linearly decreasing effective vapor diffusion functions, see Table 6 and Fig. 9 for B9. It was not possible to fit binder systems R1 and B1–B6 using decreasing effective vapor diffusion functions.

It was shown in [50] that vapor diffusion in the presence of ‘ trapped’ liquid in a single capillary pore can be modeled if the RH of the pore liquid and the RH on both sides of the liquid is known. It was confirmed that vapor transport is enhanced by the presence of liquid in a capillary pore, since the vapor diffusion can occur on both sides of the ‘ trapped’ liquid, so the effective diffusion rate of vapor should increase with increased water saturation, because the trapped liquid shortens the apparent distance the vapor need to travel through a capillary pore. The coupled nature of moisture transport and the complexity of the pore structure of cement binder-systems, with a wide range of sizes, shapes and connectivity of pores makes it very difficult to accurately describe the geometry of the pore structure and the position and RH boundary conditions at each liquid water meniscus in the pore system. Moreover, the RH of the trapped liquid is dependent on the chemistry of the liquid and the pore size [51,52].

The use of vapor effective diffusion functions that increase with increased saturation was tested in the present study and it proved to give a good fit between the model and the results of all experiments for binder-systems R1 and B1–B6, as shown in Figs. 7 and 8 and listed in Table 6. For binder-systems B7–B9 the suspected pore size refinement induced by the calcined clay reduces the presence of capillary pores and thus reduces the effect of enhanced vapor transport through capillary pores.

The suggested shape and format of Eqs. (5) and (6) were selected on the basis of the writers' experience with the optimization model. It was challenging to find an optimal set of diffusion parameters to fit all experiments, especially since the effect of capillary suction required a very strong increase of water transport at high RH [53]. This, in combination with the fitting of the two intervals of the cup test results, required fine tuning of the diffusion parameters where the coupled nature of vapor and water transport was clear. As seen in Figs. 7 and 8 vapor diffusion seems to be the dominant factor at low RH ranges up to approximately 80% RH, after which water transport becomes more and more important. This is in agreement with findings in e.g. [21,54]. It is, however, worth noting that the proposed diffusion functions and parameters, listed in Table 6, do not have a direct physical meaning and should only be considered as functions giving the best match of the experimental results. A deeper understanding of the effect of the shape and form of these functions and their dependency on the micro-structure is the target for future studies. Models like, e.g. [54] who suggested relating the dependency of moisture diffusion to pore size distribution represented by a Multi-Rayleigh-Ritz model, and [33] who discussed the use of relative permeability and Knudsen diffusion, are examples of the kind of analysis required. Furthermore, there is a need for models that can recalculate the obtained transport properties measured using mortar and paste samples to transport properties of concrete. The two-phase moisture transport model used in the present study is a continuum approach with two truly separate equations for the liquid and gas phase which are coupled through their kinetic sorption behavior. This approach makes it more challenging to relate the diffusion functions to the micro-structure since the model does not allow for the calculation of a combined diffusivity, as suggested in e.g. [33,54].

4.2.2. *The sorption isotherms*

The sorption isotherm boundary functions shown in Figs. 7 and 8 were established by fitting the sorption isotherms from DVS measurement data using Eqs. (7) and (8). In the proposed model the measured moisture content in gram water per gram dry sample must be converted to a dimensionless saturation degree between 0–1 in order to use Eqs. (7) and (8). We attempted to use vacuum porosity measurements on paste to scale the moisture content and obtain the saturation degree. This was based on the rough assumption that the maximum saturation degree corresponds to the total porosity measured by vacuum porosity. This resulted in relatively low saturation degrees close to RH 95%, e.g., for binder-system B1 the saturation degree is about 0.45 at 95% RH, which seemed very low. The total porosity measured with vacuum porosity was concluded to be a poor measure of the maximum saturation degree. This is mainly due to the harsh drying at 105 °C which changes the pore structure and most likely dries out some of the non-evaporable water, as reported in e.g. [55]. As an alternative method, capillary porosity was assumed to correspond to the maximum saturation degree. Theoretical capillary porosity for the ten binder-systems was estimated using Powers' porosity formulas. This is a very rough estimation especially since Powers' porosity formula does not include the effects caused by the presence of SCMs. Nevertheless, this was the method used in this study due to the absence of any better estimation. Future studies should include a better measurement of the water content of the samples at saturation. Measuring techniques such as pressure plates or equivalent methods could be considered.

5. Conclusions

The moisture transport properties of different binder-systems relevant for a continuum two-phase moisture transport model were established in this study. Two truly separate set of ‘ optimized’ effective diffusion parameters for the liquid and gas phase were established, using four different sets of diffusion experiments and the inverse analysis approach suggested in this paper. A good fit between the two-phase moisture transport model and the results of all four diffusion experiments was obtained. It was concluded that vapor diffusion was dominant at low RH and up to approximately 80% RH. It was necessary to use increasing vapor diffusion functions with increased RH to fit all four experiments for binder-systems R1 and B1-B6 and a decreasing vapor diffusion functions to fit binder-systems B7–B9. It was concluded that liquid water transport was dominant at high RH. It was found to be important to have a steep increase of the function describing liquid water flow at RH close to 1 in order to fit the experimental capillary suction test results.

The moisture properties used in the model simulations provide a good description of the tested period for all four experiments. The measured properties provide a good description of the initial conditions for durability modeling of the binder-systems increasing the accuracy of the durability model performance.

This investigation does not explicitly include the effect of pore structural change over time as a result of, for example, hydration and leaching. This should be a subject for future studies.

Acknowledgments

Thanks to the Danish Innovation Fund (1382-00054B) (InnovationsFonden) for the financial support to this work as a part of the “Green transition of cement and concrete production” (“Grøn Beton II”) project. Without their financial support and the contribution from the project partners, this research would not have been possible.

References

[1] B. Lothenbach, K. Scrivener, R.D. Hooton, Supplementary cementitious materials, Cem. Concr. Res. 41 (2011) 1244–1256.

[2] K. De Weerdt, M.B. Haha, G. Le Saout, K.O. Kjellsen, H. Justnes, B. Lothenbach, Hydration mechanisms of ternary Portland cements containing limestone powder and fly ash, Cem. Concr. Res. 41 (2011) 279–291.

[3] Y. Hosokawa, K. Yamada, B. Johannesson, L.-O. Nilsson, Development of a multi-species mass transport model for concrete with account to thermodynamic phase equilibriums, Mater. Struct. 44 (2011) 1577–1592.

[4] K.L. Scrivener, B. Lothenbach, N. De Belie, E. Gruyaert, J. Skibsted, R. Snellings, A. Vollpracht, TC 238-SCM: hydration and microstructure of concrete with SCMs, Mater. Struct. 48 (2015) 835–862.

[5] M. Saeidpour, L. Wadsö, Moisture equilibrium of cement based materials containing slag or silica fume and exposed to repeated sorption cycles, Cem. Concr. Res. 69 (2015) 88–95.

[6] Z. Shi, B. Lothenbach, M.R. Geiker, J. Kaufmann, A. Leemann, S. Ferreiro, J. Skibsted, Experimental studies and thermodynamic modeling of the carbonation of Portland cement, metakaolin and limestone mortars, Cem. Concr. Res. 88 (2016) 60–72.

[7] T.Q. Nguyen, V. Baroghel-Bouny, P. Dangla, Prediction of chloride ingress into saturated concrete on the basis of a multi-species model by numerical calculations, Comput. Concr. 3 (2006) 401–421.

[8] E. Samson, J. Marchand, Modeling the transport of ions in unsaturated cement-based materials, Comput. Struct. 85 (2007) 1740–1756.

[9] M. Jensen, B. Johannesson, M. Geiker, Framework for reactive mass transport: phase change modeling of concrete by a coupled mass transport and chemical equilibrium model, Comput. Mater. Sci. 92 (2014) 213–223.

[10] Q.-F. Liu, J. Yang, J. Xia, D. Easterbrook, L.-Y. Li, X.-Y. Lu, A numerical study on chloride migration in cracked concrete using multi-component ionic transport models, Comput. Mater. Sci. 99 (2015) 396–416.

[11] M.M. Jensen, B. Johannesson, M.R. Geiker, Framework for reactive mass transport: phase change modeling of concrete by a coupled mass transport and chemical equilibrium model, Comput. Mater. Sci. 92 (2014) 213–223.

[12] L. Bennethum, J. Cushman, Multicomponent, multiphase thermodynamics of swelling porous media with electroquasistatics: I. Macroscale field equations, Transp. Porous Media 47 (2002) 309–336.

[13] L. Bennethum, J. Cushman, Multicomponent, multiphase thermodynamics of swelling porous media with electroquasistatics: II. Constitutive theory, Transp. Porous Media 47 (2002) 337–362.

[14] B. Johannesson, Development of a generalized version of the Poisson-Nernst-Planck equations using the hybrid mixture theory: presentation of 2D numerical examples, Transp. Porous Media 85 (2010) 565–592.

[15] M.M. Jensen, K. De Weerdt, B. Johannesson, M.R. Geiker, Use of a multi-species reactive transport model to simulate chloride ingress in mortar exposed to NaCl solution or sea-water, Comput. Mater. Sci. 105 (2015) 75–82.

[16] L. Nilsson, On the role of moisture in degradation of concrete structures, Repair and renovation of concrete structures: proceedings of the International Conference held at the University of Dundee, Scotland, UK, Thomas Telford Publishing, 2005, pp. 15–24.

[17] O.M. Jensen, P.F. Hansen, Autogenous relative humidity change in silica fume-modified cement paste, Adv. Cem. Res. 7 (1995) 33–38.

[18] S. Roy, K. Poh, D. Northwood, Durability of concrete-accelerated carbonation and weathering studies, Build. Environ. 34 (1999) 597–606.

[19] B. Persson, Consequence of cement constituents, mix composition and curing conditions for self-desiccation in concrete, Mater. Struct. 33 (2000) 352–362.

[20] M. Thiery, V. Baroghel-Bouny, G. Villain, P. Dangla, Numerical modeling of concrete carbonation based on durability indicators, Spec. Publ. 234 (2006) 765–780.

[21] M. Saeidpour, L. Wadsö, Moisture diffusion coefficients of mortars in absorption and desorption, Cem. Concr. Res. 83 (2016) 179–187.

[22] V. Baroghel-Bouny, Water vapour sorption experiments on hardened cementitious materials. Part II: essential tool for assessment of transport properties and for durability prediction, Cem. Concr. Res. 37 (2007) 438–454.

[23] K. Sakata, A study on moisture diffusion in drying and drying shrinkage of concrete, Cem. Concr. Res. 13 (1983) 216–224.

[24] B. Johannesson, U. Nyman, A numerical approach for non-linear moisture flow in porous materials with account to sorption hysteresis, Transp. Porous Media 84 (2010) 735–754.

[25] U. Nyman, P. Gustafsson, B. Johannesson, R. Hägglund, A numerical method for the evaluation of non-linear transient moisture flow in cellulosic materials, Int. J. Numer. Methods Eng. 66 (2006) 1859–1883.

[26] R.M. Espinosa, L. Franke, Inkbottle pore-method: prediction of hygroscopic water content in hardened cement paste at variable climatic conditions, Cem. Concr. Res. 36 (2006) 1954–1968.

[27] R.M. Espinosa, L. Franke, Influence of the age and drying process on pore structure and sorption isotherms of hardened cement paste, Cem. Concr. Res. 36 (2006) 1969–1984.

[28] V. Baroghel-Bouny, Water vapour sorption experiments on hardened cementitious materials. Part I: essential tool for analysis of hygral behaviour and its relation to pore structure, Cem. Concr. Res. 37 (2007) 414–437.

[29] N.D. Belie, J. Kratky, S.V. Vlierberghe, Influence of pozzolans and slag on the microstructure of partially carbonated cement paste by means of water vapour and nitrogen sorption experiments and BET calculations, Cem. Concr. Res. 40 (2010) 1723–1733.

[30] K. Hong, R.D. Hooton, Effects of cyclic chloride exposure on penetration of concrete cover, Cem. Concr. Res. 29 (1999) 1379–1386.

[31] Z. Zhang, M. Thiery, V. Baroghel-Bouny, Numerical modelling of moisture transfers with hysteresis within cementitious materials: verification and investigation of the effects of repeated wetting-drying boundary conditions, Cem. Concr. Res. 68 (2015) 10–23.

[32] B. Villmann, V. Slowik, F.H. Wittmann, P. Vontobel, J. Hovind, Time-dependent moisture distribution in drying cement mortars: results of neutron radiography and inverse analysis of drying tests, Restoration of buildings and monuments 20 (2014) 49–62.

[33] Z. Zhang, M. Thiery, V. Baroghel-bouny, Cement and concrete research investigation of moisture transport properties of cementitious materials, Cem. Concr. Res. 89 (2016) 257–268.

[34] N.S. Martys, C.F. Ferraris, Capillary transport in mortars and concrete, Cem. Concr. Res. 27 (1997) 747–760.

[35] D. Williams, The Characterisation of Powders by Gravimetric Water Vapour Sorption, 40 (1995), pp. 40–43.

[36] A. Standard, C1585-13, Standard Test Method for Measurement of Rate of Absorption of Water by Hydraulic-Cement Concretes, ASTM International, West Conshohocken, PA, 2012.

[37] L.S. Bennethum, J.H. Cushman, Multicomponent, multiphase thermodynamics of swelling porous media with electroquasistatics: I. Macroscale field equations, Transp. Porous Media 47 (2002) 309–336.

[38] L. Bennethum, J. Cushman, Multiscale, hybrid mixture theory for swelling systems-I: balance laws, Int. J. Eng. Sci. 34 (1996) 125–145.

[39] M.M. Jensen, B. Johannesson, M.R. Geiker, A numerical comparison of ionic multi-species diffusion with and without sorption hysteresis for cement-based materials, Transp. Porous Media 107 (2015) 27–47.

[40] B. Johannesson, U. Nyman, A numerical approach for non-linear moisture flow in porous materials with account to sorption hysteresis, Transp. Porous Media 84 (2010) 735–754.

[41] U. Nyman, P.J. Gustafsson, B. Johannesson, R. Hagglund, A numerical method for the evaluation of non-linear transient moisture flow in cellulosic materials, Int. J. Numer. Methods Eng. 66 (2006) 1859–1883.

[42] G. Sin, K.V. Gernaey, A.E. Lantz, Good modelling practice (GMoP) for PAT applications: propagation of input uncertainty and sensitivity analysis, Biotechnol. Prog. 25 (2009) 1043–1053.

[43] M. Wu, B. Johannesson, M. Geiker, Application of water vapor sorption measurements for porosity characterization of hardened cement pastes, Constr. Build. Mater. 66 (2014) 621–633.

[44] J. Kostuch, V. Walters, T. Jones, High performance concretes incorporating metakaolin: a review, Concrete 2 (2000) 1799–1811.

[45] B. Sabir, S. Wild, J. Bai, Metakaolin and calcined clays as pozzolans for concrete: a review, Cem. Concr. Compos. 23 (2001) 441–454.

[46] M. Krus, Feuchtetransport-und Speicherkoeffizienten poroeser mineralischer Baustoffe: theoretische Grundlagen und neue Messtechniken, na, 1995.

[47] P. Häupl, H. Stopp, Feuchtetransport in Baustoffen und Bauwerksteilen, (1987).

[48] P. Häupl, H. Fechner, Hygric material properties of porous building materials, J. Therm. Envel. Build. Sci. 26 (2003) 259–284.

[49] J. Carmeliet, H. Hens, S. Roels, O. Adan, H. Brocken, R. Cerny, Z. Pavlik, C. Hall, K. Kumaran, L. Pel, Determination of the liquid water diffusivity from transient moisture transfer experiments, J. Therm. Envel. Build. Sci. 27 (2004) 277–305.

[50] M. Addassi, L. Schreyer, B. Johannesson, H. Lin, Pore-scale modeling of vapor transport in partially saturated capillary tube with variable area using chemical potential, Water Resour. Res. 52 (2016) 7023–7035.

[51] C. Villani, R. Spragg, M. Pour-Ghaz, W. Jason Weiss, The role of deicing salts on the non-linear moisture diffusion coefficient of cementitious materials during drying, Brittle Matrix Composites 10 (2012) 101–114.

[52] C. Villani, R. Spragg, M. Pour-Ghaz, W. Jason Weiss, The influence of pore solutions properties on drying in cementitious materials, J. Am. Ceram. Soc. 97 (2014) 386–393.

[53] E. Samson, K. Maleki, J. Marchand, T. Zhang, Determination of the water diffusivity of concrete using drying/absorption test results, J. ASTM Int. 5 (2008) 1–12.

[54] Q. Huang, Z. Jiang, X. Gu, W. Zhang, B. Guo, Numerical simulation of moisture transport in concrete based on a pore size distribution model, Cem. Concr. Res. 67 (2015) 31–43.

[55] C. Gallé, Effect of drying on cement-based materials pore structure as identified by mercury intrusion porosimetry, Cem. Concr. Res. 31 (2001) 1467–1477.

Paper III

"Numerical framework for reactive mass transport in concrete including for gaseous constituents"

M. Addassi & B. Johannesson & M. M. Jensen

under review *Cement and Concrete Research, 2018*

Numerical framework for reactive mass transport in concrete including for gaseous constituents

Mouadh Addassi[a,*], Björn Johannesson[b], Mads M. Jensen

[a]Department of Civil Engineering, Technical University of Denmark, Lyngby, Denmark
[b]Department of Building Technology, Linnaeus University, Växjö, Sweden

---

Abstract

This article presents a numerical framework for multi-phase reactive mass transport modeling for durability estimation of cement-based materials. The governing system of equations includes a modified version of the Poisson-Nernst-Planck system of equations including gaseous transport in the air-filled space, ionic transport in the liquid phase, electro-migration of ionic species, a two-phase moisture transport model, and sorption. The addition of the gas phase to the framework enables the user of the model to investigate individual and combined effects of different degradation processes in unsaturated systems. Three numerical examples were studied, to show the simulation results from the model, and to illustrate some of the model's capabilities. The numerical examples studied the altering of hydrated cement under three different environments representing an accelerated carbonation environment, a submerged marine environment and a cyclic drying-wetting zone in a marine environment.

Keywords: Modeling (E), Durability (C), Degradation (C), Transport Properties (C), Carbonation (C)

---

1. Introduction

Reinforced concrete structures are often expected to be durable for at least a 100 years. The durability of concrete structures mainly depends on the properties of the cement-based binder-system and on the service environment. In general, the end of service life of reinforced concrete structures is evaluated based on the initiation of corrosion of the reinforcing steel. At the beginning of the reinforced concrete service life, the high pH of concrete pore fluid (typically a pH above 13) protects the reinforcing steel from corrosion. Depending on the service environment, e.g., chloride ingress, carbonation or sulfate attack, the pore structure and pore fluid are changed. Especially leaching and carbonation result in a drop in the pH level allowing the reinforcing steel to start corroding

---

[*] Mouadh Addassi, Brovej 119, 2800 Kgs. Lyngby, Denmark
Email address: `moadda@byg.dtu.dk` (Mouadh Addassi)

Preprint submitted to Cement and Concrete Research *February 10, 2018*

and expanding, creating cracks in the concrete structure, eventually leading to the end of service life of the structure [1]. The combination of a drop in pH and a high chloride concentration is also a common cause for steel corrosion in for example marine concrete.

The environmental awareness and increased concrete demand have motivated significant research effort to reduce CO_2 emission from cement production, for example by increasing the use of supplementary cementitious materials (SCMs) to form new cement-based binder-systems. The presence of SCM's can both increase and decrease the durability performance of concrete structures depending on the changes in the hydration mechanisms, e.g., [2–5], and changes to the microstructure and its effect on, e.g., moisture transport properties [6, 7], carbonation resistance [8–11] or chloride ingress [12–14].

The durability performance of new more environmentally friendly binder-systems, need to be investigated thoroughly using a combination of experimental investigations and physically sound numerical models. Short-term experimental investigations are needed for verification of the models. The isolated use of accelerated test does not always represent the true progress of degradation processes, especially in the presence of SCM's with different hydration and reaction kinetics compared to the well investigated Portland cement, see e.g. [8, 15].

Most of the existing concrete durability models focus on investigating one of the major degradation processes, for example, chloride ingress [12, 16–18] or carbonation [19–25]. The use of multi-phase reactive transport models, enable the investigation of the individual and combined effect of the different degradation processes [26–29]. This type of models combines mass transport models with chemical equilibrium models.

By adding the gas phase to the framework presented in [30] the overall durability can be accessed in a more consistent and accurate way. Adding the gas phase expands the model capabilities and allows investigating durability effects due to the presence and transport of gases like CO_2 and O_2. The transport part of the durability model described in [30] solves an extended version of the Poisson–Nernst–Planck (PNP) system of equations. In [28, 31–33], the transport part includes ionic transport in the liquid phase, vapor and liquid water transport with sorption kinetics and hysteresis, electro-migration of the ionic species present in the liquid water phase.

The main aim of this paper is to add the gas reactions and gas transport into the system of equations, see Figure 1 for a schematic illustration. The chemical part now includes equilibrium between the gas phase and the liquid phase, aqueous reactions in the liquid phase, and interaction between the liquid phase and solid phases introduced as equilibrium phases, solid solutions or using surface complexation models accounting for the electrical double layers, see Figure 1. The transport is solved using a non-linear finite element approach coupled with chemical equilibrium modeling using PHREEQC, a geochemical solver.

In addition, findings from[34] are incorporated in [30] to describe moisture transport in the model more accurately.

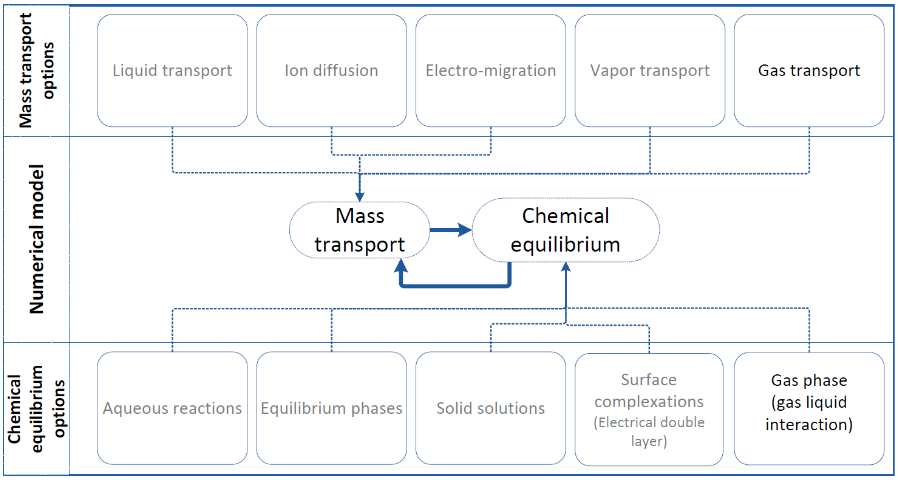

Figure 1: Schematic illustration of the different options of the framework, where the volume fractions of the solid, liquid and gas phase are indicated.

2. Methods

This section provides a description of the numerical model and methods used in this framework, including the governing system of equations, the numerical solution methods for the mass transport and the chemical equilibrium solution methods with the focus on the added gas phase, and a description of how to apply the framework.

2.1. Governing system of transport equations

The governing system of transport equations is based on a modified version of the Poisson-Nernst-Planck (PNP) system of equations including gaseous transport in the air-filled space, ionic transport in the liquid phase, electro-migration of ionic species, a two-phase water vapor and liquid water transport, and sorption.

2.1.1. Volume fraction of the phases

The transport of ions in the liquid phase and gases in the air filled space of the porosity are dependent on the total porosity of the system, ε_p. The sum of the porosity and the solid phase volume fraction ε^s is restricted by the following

$$\varepsilon_p + \varepsilon^s = 1. \tag{1}$$

The solid phase volume fraction ε^s is allowed to change in the model based on the chemical changes in the solid phase composition. This change is restricted only by the changes in the solid phase and the densities of the phases present.

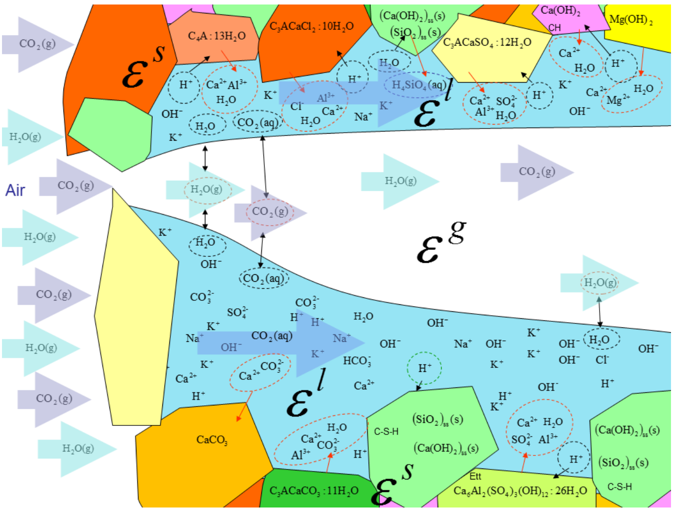

Figure 2: Schematic illustration of the model.

Within the pore space, the volume fraction of the liquid phase relative to the pore space ε^l(the superscript l denote the liquid phase), and the volume fraction of the gas phase ε^g (the superscript g denote the gas phase) being the non-water filled pore space, must satisfy the following

$$\varepsilon_p = \varepsilon^l + \varepsilon^g. \tag{2}$$

A schematic illustration representing the different phases in the model can be seen in Figure 2.

2.1.2. Transport within the liquid phase

Two types of transport within the liquid phase are considered, that is, the liquid water transport itself and the reactive transport of species in the liquid phase governed by the PNP equations. The liquid water transport is expressed using a generalized version of a Darcy's law type of equation derived in [31, 35, 36], where the liquid volume fraction ε^l is used as the driving potential for the liquid flow for incompressible fluids in a porous material. The liquid water transport is expressed as

$$\rho_w \frac{\partial \varepsilon^l}{\partial t} = \nabla \cdot \left(D_{\varepsilon^l} \nabla \varepsilon^l\right) + \hat{m}_l \tag{3}$$

where ρ_w is the water density, $D_{\varepsilon^l} = D_{\varepsilon^l}(\varepsilon^l)$ is the effective diffusion for the liquid phase which is a function of the liquid volume fraction ε^l. $\hat{m}_l$ is the mass exchange between the liquid water phase and the water vapor phase due to sorption.

The form of the PNP equation derived from hybrid mixture theory [31–33] used in the model is as follows

$$\begin{aligned}\varepsilon^l \frac{\partial c_i^l}{\partial t} + c_i^l \frac{\partial \varepsilon^l}{\partial t} &= \nabla \cdot \left(D_i^l \varepsilon^l \nabla c_i^l + D_i^l c_i^l \nabla \varepsilon^l - A_i^l z_i \varepsilon^l c_i^l \nabla \Phi \right) + \\ & \quad \mathbf{v}^{l,s} \cdot \varepsilon^l \nabla c_i^l + \mathbf{v}^{l,s} \cdot c_i^l \nabla \varepsilon^l + q_i^l; \quad i = 1, 2.., N\end{aligned} \tag{4}$$

where c_i^l is the concentration of species i in the liquid phase, D_i^l is the effective diffusion coefficient of species i in liquid phase, A_i^l is the ionic mobility of species i in liquid phase, z_i is the valance of species i, Φ is the electrical potential, $\mathbf{v}^{l,s}$ is the liquid velocity relative to the solid, q_i^l is the mass exchange term for chemical interactions between the species and N is the total number of constituent in the liquid phase. The equation states that the mass concentration of each constituent in the liquid phase over time is dependent on the liquid volume fraction and its changes. The equation accounts for the diffusion driven transport expressed by the first term on the right hand side of the equation, the motion of the liquid phase relative to the solid phase expressed in the second and third term on the right hand side, and the mass exchange between the constituents due to chemical interaction as expressed by the last term of Equation (4).
Besides the liquid water fraction ε^l and its changes, equation (4) needs a relation for the electrical potential Φ in order to obtain a closed system of equations. The relation for Φ is based on Gauss' law which in this case represents the Poisson equation which has the following form

$$\xi_d \xi_0 \nabla^2 \Phi = F \sum_{i=1}^{N} c_i^l z_i \tag{5}$$

where ξ_d is the relative dielectricity coefficient, ξ_0 is the dielectricity coefficient of vacuum and F is the Faraday's constant and z_i is valance for ion i.

2.1.3. Transport within the gas phase

Two forms of transport are considered in the non-water filled pore space ε^g, that is, water vapor transport and transport of other gaseous species. The equation for the water vapor is expressed in terms of the relative humidity ϕ_v in the following manner [36]

$$\rho_{vs}(\varepsilon_p - \varepsilon^l) \frac{\partial \phi_v}{\partial t} - \rho_{vs} \phi_v \frac{\partial \varepsilon^l}{\partial t} = \nabla \cdot (D_\phi \nabla \phi_v) - \hat{m}_l \tag{6}$$

where ρ_{vs} is the vapor saturation density, $D_\phi = D_\phi(\varepsilon^l)$ is the effective diffusion coefficient for the vapor phase which is a function of the volume fraction of the liquid water.
The transport of gaseous species j in spatial the domain occupied by the gas phase ε^g is described by an equation of similar structure as used for the ionic transport in the liquid phase, Equation (4), that is

$$\begin{aligned}(\varepsilon_p - \varepsilon^l) \frac{\partial c_j^g}{\partial t} - c_j^g \frac{\partial \varepsilon^l}{\partial t} &= \nabla \cdot \left(D_j^g (\varepsilon_p - \varepsilon^l) \nabla c_j^g - D_j^g c_j^g \nabla \varepsilon^l \right) \\ & \quad + q_j^g; \quad j = 1, 2.., M\end{aligned} \tag{7}$$

where c_j^g is the concentration of gas species j in the phase and is defined as a density fraction of the total density of the gas phase ρ^g, D_j^g is diffusion coefficient for gas j, q_j^g is the rate of mass exchange term for chemical interactions of the gaseous species and M denotes the number of gas species building up the gas phase. However, under the assumption that the rate of gas absorption by the liquid phase is much faster than the rate of gas transport, the overall effect is that the gas diffusion in the air filled space of the porosity becomes very slow. This approach is widely accepted for modelingCO_2 gas diffusion in connection to carbonation problems in concrete [25, 37]. Using this workaround, we are able to model gas transport in the air-filled pore space alongside with liquid transport. The suggested approach is as follows:

1. The volume of the gas phase for each element, the gas-filled pore space, is calculated from the porosity and saturation degree.
2. The rate of diffusion of a specific gas constituent is approximated using the calculated results from the proposed model.
3. The accumulated volume of the gas during a selected time increment is calculated and used as input for the gas phase when calculating the gas-liquid equilibrium in the IPHREEQC program.

For example, if an element has a gas-filled pore volume of 1L, a diffusion rate of 1L/min then the accumulation of gas in one volume element in a time step of 10h is 600L.

2.1.4. Rate of sorption and sorption hysteresis

The rate of mass exchange between the liquid water and water vapor is expressed as a function of the relative humidity and saturation degree [36, 38, 39], that is

$$\hat{m}_l = R_c(\varepsilon^{l,eq*}(\phi_v) - \varepsilon^l) \tag{8}$$

where R_c is a rate constant for mass exchange between liquid and vapor and $\varepsilon^{l,eq*}$ is the equilibrium sorption hysteresis function. In the case in which the moisture state is not located at the sorption isotherm, the rate constant R_c is used to account for the non-equilibrium kinetic conditions in the sorption process.

As described in [36, 39], the equilibrium sorption hysteresis function is history dependent and in this case based on a third order polynomials established between a set of adsorption and desorption boundary isotherms. Figure 3 illustrates an example of upper and lower boundary sorption isotherms.

2.1.5. Effective moisture diffusion functions

The effective diffusion functions for the liquid phase and the vapor phase, in Equation (3) and (6), respectively, are defined as in [34]

$$D_{\varepsilon^l}(\varepsilon^l) = k_1 + k_2 \varepsilon^{l\,k_3} \tag{9}$$

$$D_{\phi}(\varepsilon^l) = k_4 + k_5 \varepsilon^{l\,k_6} \tag{10}$$

where $k_1 - k_6$ are moisture diffusion parameters inversely determined from moisture diffusion experiments [34]. Figure 3 shows an example of calculated effective moisture diffusion curves for a specific material.

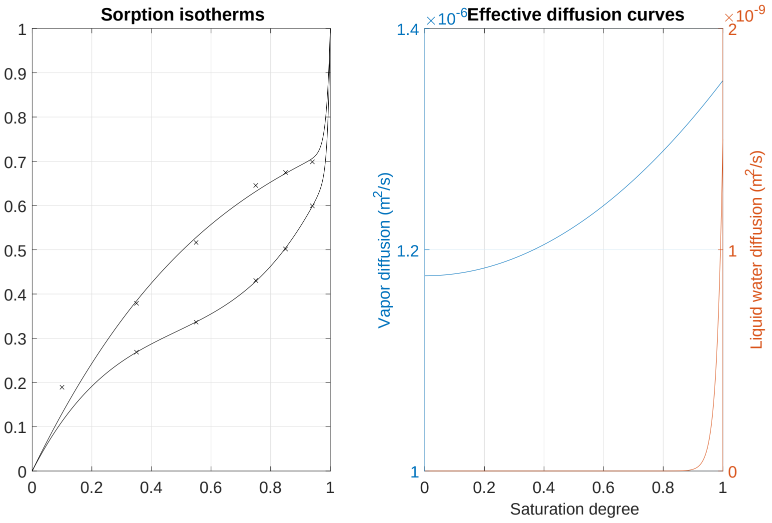

Figure 3: Example of upper and lower boundary sorption isotherms and effective moisture diffusion curves for water vapor and liquid water.

2.2. Numerical methods

The overall system including mass transport and chemical equilibrium is solved using an operator splitting approach, adapted to enable the use of two separate solvers, one for the mass transport and the other for the chemical equilibrium. The mass transport part of the model is solved numerically using a finite element approach, where the Green-Gauss theorem [40, 41] was used to obtain the weak form of the governing equations. The Galerkin's method was used to discretize the one-dimensional spatial scheme using linear spatial elements. A single parameter implicit time integration scheme was used for time discretization. A modified Newton-Raphson scheme [42] was used to account for non-linearity in the model. A more detailed description of the adopted finite element approach can be found in [29].

The mass exchange term q_i^l in Equation (4) and q_j^g in Equation (7) accounting for the chemical interactions between the liquid-gas and solid phase are solved using the geochemical program IPHREEQC [43, 44]. This program establishes chemical equilibrium by solving thermodynamically derived mass action laws, element balance and charge balance. The IPHREEQC program can solve for chemical equilibrium for aqueous reactions in the liquid phase, the interaction between the gas phase and the liquid phase, and the interaction between the liquid phase and solid phase using mineral phase reactions and solid solution reactions [29]. A review of the mass action laws presented in [43] relevant for the aqueous reactions and liquid-solid interaction used in this model, including mineral solid solution equilibrium, was presented in [29]. A description of the gas phase and its mass exchange with the liquid phase, and the mass action laws governing the gas-liquid equilibrium is given next.

2.3. Gas phase equilibrium

The IPHREEQC code models the interaction between a liquid phase and a single or multi-constituent gas phase. The model uses mass action equations in terms of the partial pressure and an additional equation for total pressure, under the condition that the total pressure in the gas phase is assumed constant. All gases in the gas phase are assumed to behave as ideal gases and as a result the mixture of gases within the same gas phase is assumed to behave ideally as well. At equilibrium between two-phases, e.g., the liquid phase and the gas phase, the chemical potential of any constituent coexisting in both phases is equal at equilibrium [45] and the rate of change before equilibrium is reached is proportional to the difference between the two constituents chemical potentials [46, 47]. The equilibrium condition for the partial gases in the gas mixture phase in equilibrium with the aqueous species is expressed as

$$\mathbf{V}_g^{*\mathrm{T}}\widetilde{\boldsymbol{\mu}}^{aq} - \widetilde{\boldsymbol{\mu}}^{g} = \mathbf{0} \tag{11}$$

where $\widetilde{\boldsymbol{\mu}}^{aq}$ is a vector containing the chemical potential of the aqueous species, and $\widetilde{\boldsymbol{\mu}}^{g}$ is a vector containing the chemical potential of the gas constituents of the gas mixture. The matrix $\mathbf{V}_g^{*\mathrm{T}}$ is the right-hand side of the stoichiometric coefficients of the reactions and the gas constituent reacting with the aqueous species are left alone on the left-hand side of the reactions in this case. The ideal gas law of a gas constituent j in terms of the concentration of the gas c_j^g is

$$p_j^g = RTc_j^g \tag{12}$$

where p_j^g is the pressure of the gas constituent j in the gas phase, R is the gas constant and T is the absolute temperature. The ideal condition of a gas constituent leads to the following assumption for a partial gas chemical potential [45]

$$\widetilde{\mu}_j^g = \widetilde{\mu}_j^{g,\ominus} + RT\ln(c_j^g) \tag{13}$$

where $\widetilde{\mu}_j^{g,\ominus}$ is the reference chemical potential. At constant temperature one have

$$\widetilde{\mu}_j^g = \widetilde{\mu}_j^{g,\ominus} + \ln p_j^g \tag{14}$$

The reference chemical potential $\widetilde{\mu}_j^{g,\ominus}$ is in this setting the same as Henry's law constant K_j for a gas species j in the air filled gas mixture in equilibrium with the aqueous species participating in the specific dissolution reaction involving the constituent j, that is

$$\widetilde{\mu}_j^{g,\ominus} = K_j \tag{15}$$

Using Equation (11), (14) and (15), the partial pressures $\mathbf{p}^g$ of all the gasses in the gas phase becomes

$$\mathbf{p}^g = \mathbf{K}\mathbf{V}_g^{*\mathrm{T}}\widetilde{\boldsymbol{\mu}}^{aq} \tag{16}$$

where $\mathbf{K}$ is a diagonal matrix including the inverse values of Henry's law constants K_j for the different gas dissolution reactions included in the model. Following the terminology normally used in chemical equilibrium descriptions, the partial pressure of each gas p_j^g can alternatively be expressed in terms of aqueous phase activities instead of concentration, as

$$p_j^g = \frac{1}{K_j} \prod_i a_i^{b_{j_i}} \tag{17}$$

where a_i is the activity of the master aqueous species i, and b_{j_i} is the stoichiometric coefficient of aqueous master species i. The activity a_i is given by the activity coefficient γ_i as: $a_i = \gamma_i c_i$. Equation (17) is an extension of (16) and (13) in the sense that the activity is accounted for and not only the concentration of the gaseous species alone. A master species in the terminology used in [43] are pure chemical elements, e.g. Cl^- or pure chemical elements at different valance state, e.g. Fe^{2+} and Fe^{3+}. All chemical equations are written in terms of master species in IPHREEQC.

The IPHREEQC program has the option of specifying a constant total pressure p. In this case, the following restriction will be added to the system of equations

$$\mathbf{p}^g \cdot \mathbf{n}_u^g - p = 0 \tag{18}$$

where the unity vector $\mathbf{n}_u^g$ have the same dimension as the partial pressure vector $\mathbf{p}^g$.

Gas-liquid equilibrium can be calculated using three different assumptions in IPHREEQC [43]:

1. Assuming fixed partial pressure of a gas (infinite access of the gas to keep a fixed partial pressure): With this assumptions, it is possible to add a gas to the system as an equilibrium phase using the EQUILIBRIUM_PHASES data block [29, 43], where the input is the logarithm of the partial pressure of the gas with the possibility of adding a targeted saturation degree.
2. Assuming fixed total volume of the gas phase: The GAS_PHASE data block using a fixed volume is needed for this case. The system is solved using Equation (16) where the input is the total volume of the gas phase in a specific spatial element and at a specific time step of the calculation and the initial partial pressure of the individual gases included in the gas phase.
3. Assuming fixed total pressure of the gas phase: The GAS_PHASE data block using fixed pressure is needed for this case, where the input is the total pressure and the initial partial pressures of the individual gases included in the gas phase. The system is solved using Equations (16) and (18). It is also possible to specify the volume of the gas phase, but the initial moles of any gas is calculated using the ideal gas equation, where the given volume may be adjusted to satisfy the total fixed pressure assumption.

In this work, the above option 2, the fixed total volume assumption was selected to model the overall gas transport in the gas phase. As mention in Section 2.1.3, the approximated accumulative volume of the gas phase after a transport calculation step is used as input of the volume of the gas phase in IPHREEQC. The ideal gas law equation is used to convert the gas concentration to the partial pressure of each gas in case where multiple gases are present.

2.4. Model framework

It is possible to use the presented framework to study different degradation phenomena by combining a system with the needed mass transport options and the relevant chemical equilibrium options, as illustrated in Figure 1. Note that mass transport options and chemical equilibrium options refer to parts of the model framework that can be included or excluded. For example, in [34] only the moisture transport option was used to inversely calculate moisture transport properties, and in [29] a numerical example was given comparing two chemical models for C-S-H using solid solutions description of the C-S-H base on the CEMDATA07 database [48–52] in one case, and the surface complexation model proposed in [53] in the other.

In general, the modeling approach using this framework can be divided into the following steps:

1. Identify and select the relevant mass transport options and chemical equilibrium options, see Figure 1. For example, if the system of interest, is a case in which the sample is saturated and submerged throughout the service life cycle then there is no need to include gas transport in that system.
2. Identify and select input parameters and databases. The number of input parameters needed in the framework can be extensive depending on the selected options in step 1. The input parameters can be categorized as:
    (a) Model discretization parameters, e.g., element length, number of elements, time step size, and total time of the simulation.
    (b) Material parameters, which can be divided into two major groups:
        i. Parameters related to the transport part. This includes geometry parameters, diffusion parameters of the ions, gases, and moisture transport and sorption properties.
        ii. Parameters related to the chemical part. This includes initiation of the calculation in terms of defining the oxide composition of the cement and the schemes of the chemical reactions and their related parameters. It can be challenging to identify the representitative thermodynamical model for the chemical system of interest and select all the ions, gases, solid phases, and solid solutions that are formed initially or that can be formed during the durability study.
3. Define the boundary conditions of the system, e.g., the relative humidity at the boundary. The framework allows for both fixed and variable boundary conditions.

When the model input parameters and boundary conditions are defined the model first solves the initial value problem, where the clinker composition is calculated using a modied Bouge equation [29] which are then used as input in IPHREEQC to calculate the initial equilibrium system including initial ionic concentration in the aqueous pore solution and initial amounts of solid phases. Secondly, the coupled transport part of the model is solved in the following described order:

1. The transport equations, for the specific selected system, are solved to establish the new concentrations of all ions and gases after a given time step.
2. The new concentrations of species calculated in step 1 is used as input to the geochemical model to calculate the new chemical equilibrium conditions.
3. The output of the geochemical model from step 2 is used as a result of the current step, and as new input to the next transport step.

The above steps are repeated until the required predefined total time of simulation is reached.

3. Numerical examples

Three numerical examples representing three different exposure environments in which the same cement-based material were used for all three cases.

1. Accelerated carbonation: The first example aims to demonstrate possible applications of the implemented gas phase by studying altering of hydrated cement due to accelerated carbonation. The simulation was compared to experimental results for samples exposed to 1% CO_2 and 80% relative humidity. After 56 days of exposure, carbonation depth of 5mm was measured using phenolphthalein pH-indicator. This experimental result was used as a benchmark for the numerical simulation of this specific case.
2. Cyclic drying-wetting: The second example consider the altering of hydrated cement in a cyclic drying-wetting zone exposed to a marine environment. This example was constructed to demonstrate the capability of the model to study combined effects of different degradation processes involving both ionic and gaseous reactive transport. To simulate the cyclic drying-wetting zone case, a periodic boundary condition was used with intervals of 60 hours. During the drying period the boundary conditions were set to 80% relative humidity and the CO_2 gas and O_2 gas concentration in air were set to 20 and 0.04, respectively, see Table A.4. The chemical composition of sea-water was used as boundary conditions during the wetting period.
3. Constantly submerged: This example simulate the altering of hydrated cement in a submerged marine environment. One of the main purposes of this calculation was to compare it to the cyclic drying-wetting example.

Table 1: The oxide composition of the cement used in all three examples.

	CaO	SiO_2	Al_2O_3	Fe_2O_3	SO_3	MgO	K_2O	Na_2O
Mass%	63.20	19.38	5.41	3.78	3.41	0.94	0.34	0.26

Table 2: Input parameters used for all three numerical simulations.

	parameters
w/c ratio	0.5
Initial porosity	0.2
Degree of hydration	1
Initial relative humidity	0.8
System temperature (°C)	20
System pressure (bar)	1
Liquid water density, ρ_w (kg/m^3)	1000
Vapor saturation density, ρ_{vs} (kg/m^3)	0.017
Ideal gas constant (L bar/(K mol))	0.082
Faraday's constant	96490
Ioninc tortuosity factor τ	0.008
Gas tortuosity factor τ_g	10^{-6}

The material was assumed to be exposed to seawater at the boundary throughout the simulation time. The chemical composition of sea-water used tin this example and the cyclic drying-wetting example was the same, see Table A.4.

The oxide composition of the cement presented in Table 1 was used in all three examples, the other material parameters common for all three examples are shown in Table 2. The model discretization parameters of the three different examples are listed in Table 3. The diffusion properties of all the included ionic and gaseous species are presented in Table A.4. The reactions schemes of the specific chemical equilibrium model used are presented in Table B.5. The aqueous complexation reactions are the standard ones defined in IPHREEQC. In the examples including gas transport, that is, examples 1 and 2, the following transport and chemical equilibrium options were used:

- Transport: Liquid water transport, ionic transport in the liquid phase

Table 3: Model discretization parameters.

	Carbonation example	Marine environment examples
Total spatial distance (m)	0.02	0.1
Number of spatial elements	400	400
Total time	56 (days)	3 (years)
Time step, Δt (h)	4	12

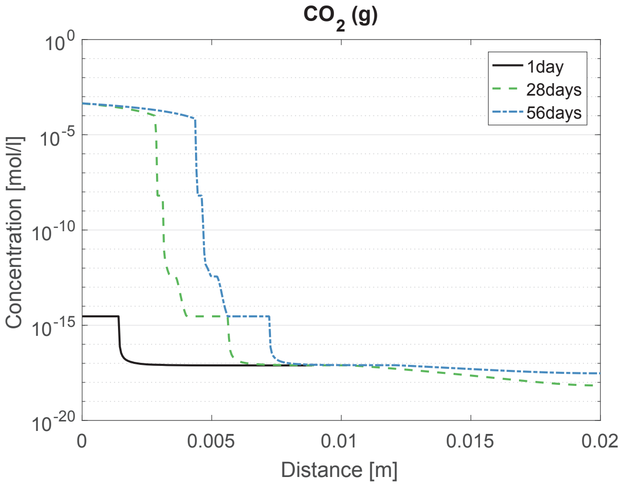

Figure 4: CO_2 gas concentration profiles in the air filled space of the porosity from example 1.

including electro-migration, water vapor transport, and gas transport in the gas phase.

- Chemical equilibrium: Aqueous reactions in the liquid phase, the interaction between the liquid and solid phase using equilibrium phases and solid solutions, and the interaction between the gas phase and liquid phase using the constant volume gas phase option in IPHREEQC.

Gas phase transport and chemical equilibrium involving gas-liquid interaction were not needed for example 3.
The following assumptions and simplifications were made for all three examples:

- The initial relative humidity and initial saturation degree throughout the sample were set to a given value.
- As a simplification, only CO_2 was included in the gas phase in example 1. In example 2, the only gas constituents of air included were CO_2 and O_2.
- The effect of solid phase changes on porosity and transport properties, such as resulting changes of the tortuosity of ionic and gaseous species was not accounted for.

3.1. Results

3.1.1. Example 1

Selected simulation results from the accelerated carbonation simulation after 1, 28 and 56 days are shown in Figures 4, 5 and 6. Figure 4 shows the concentration profiles of CO_2 gas in the gas phase. It can be seen that CO_2

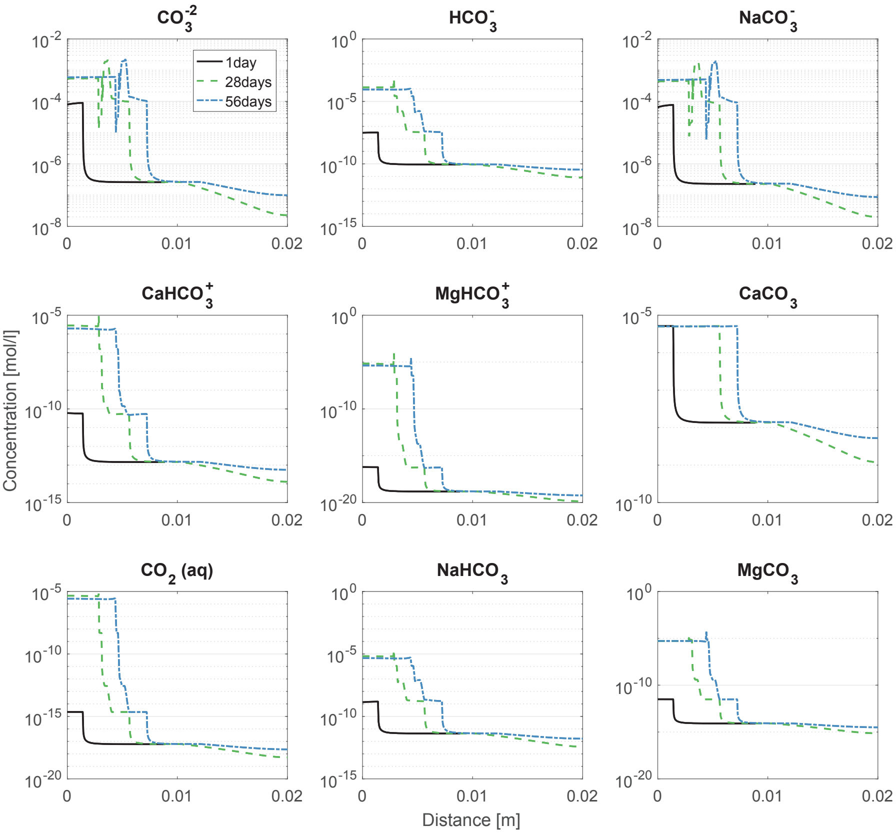

Figure 5: Ionic concentration profiles of ions containing carbon in the aqueous solution for example 1.

gas concentration profiles in the gas phase are low after 1 day, black line, even close to the exposed boundary since most of the gas is assumed to dissolve immediately and the liquid phase was therefore not yet saturated. The CO_2 gas profile after 28 and 56 days, green and blue lines in Figure 4, respectively, shows that part of the liquid phase close to the boundary was saturated allowing the concentration of CO_2 in the gas phase to increase corresponding to the concentration at the boundary. Figure 5 show ionic concentration profiles of all ions containing carbon in the aqueous solution. A clear connection can be seen between the development of the carbon-containing ions shown in Figure 5 and the CO_2 gas front in Figure 4. Figure 6 shows the initial chemical composition of the solid phases and the resulting changes due to carbonation. For simplicity, all the end members of the C-S-H, AFm and AFt solid solutions were grouped together in Figure 6. It can be seen in Figure 6 that the presence of CO_2 gas first leads to the formation of monocarboaluminate, followed by the dissolution of the portlandite phase and formation of calcium carbonate (calcite)

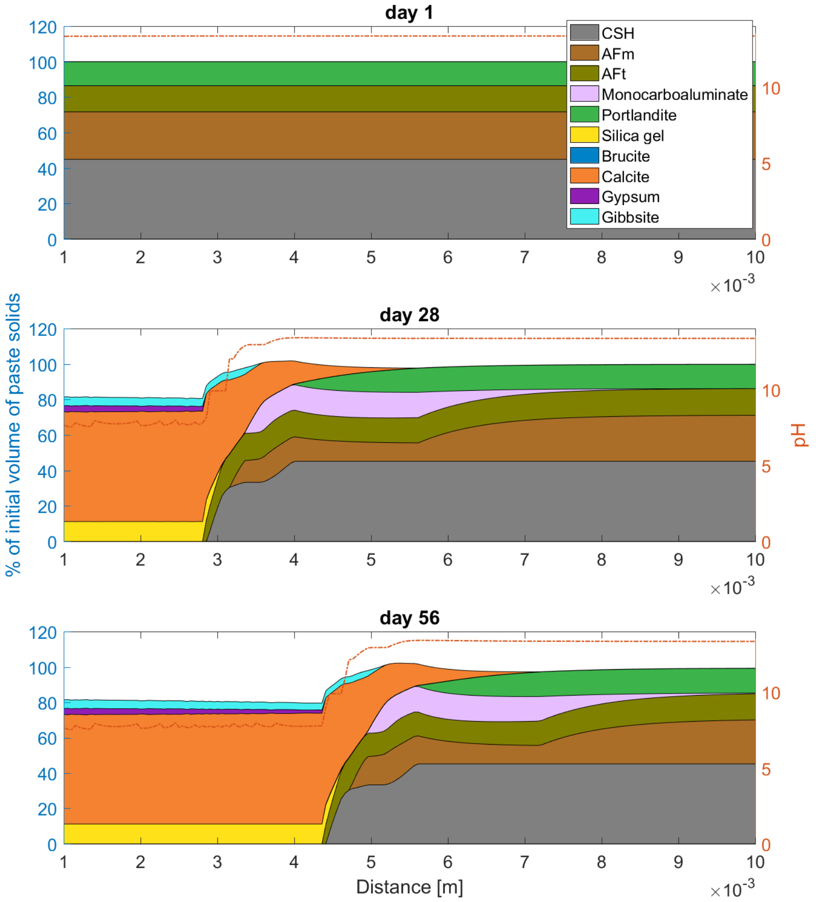

Figure 6: Change in solid composition for example 1, after 1, 28 and 56 days of exposure to 1% CO_2.

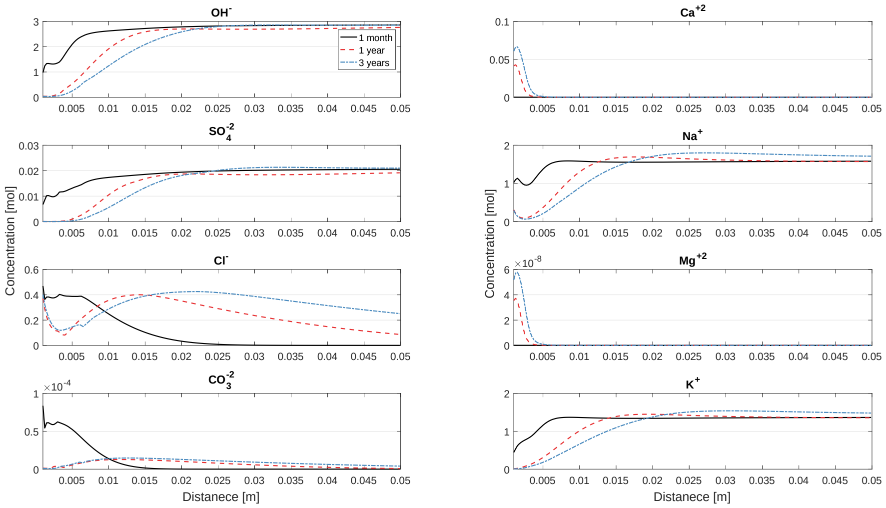

Figure 7: Ionic concentration profiles for selected ions of example 2 after 1 month, 1 year and 3 years of exposure to seawater.

in an expected manner. After the portlandite phase was fully replaced by calcite, the dissolution of C-S-H gradually leading to a drop in pH as indicated by the right-hand side y-axes in Figure 6.

3.1.2. Results from example 2 and 3

Selected simulation results from the simulation of marine environments in example 2, the cyclic drying-wetting condition, and example 3, the submerged condition, are shown in Figure 7 and 8.

Figure 7 shows the development of the ionic concentration in the aqueous phase of the selected ionic species from example 3. Figure 7 demonstrates how the concentration profiles differ as a result of different transport properties and chemical interactions. Figure 8 compares the changes in the solid phases between example 2 and 3 . The end members of the C-S-H, AFm and AFt solid solutions were grouped together in Figure 8, similar to how the results is presented in Figure 6. The phase change results indicates that the cyclic drying-wetting condition might led to accelerated degradation of the hydrated cement minerals and solid solutions.

4. Discussion

4.1. Numerical examples

For any complex coupled model it is important to mention that presented results in terms of examples and results in a way are constructed and may only represent a real life concrete structure to a certain degree. In the current state of the development of the framework the results should therefore be interpreted as

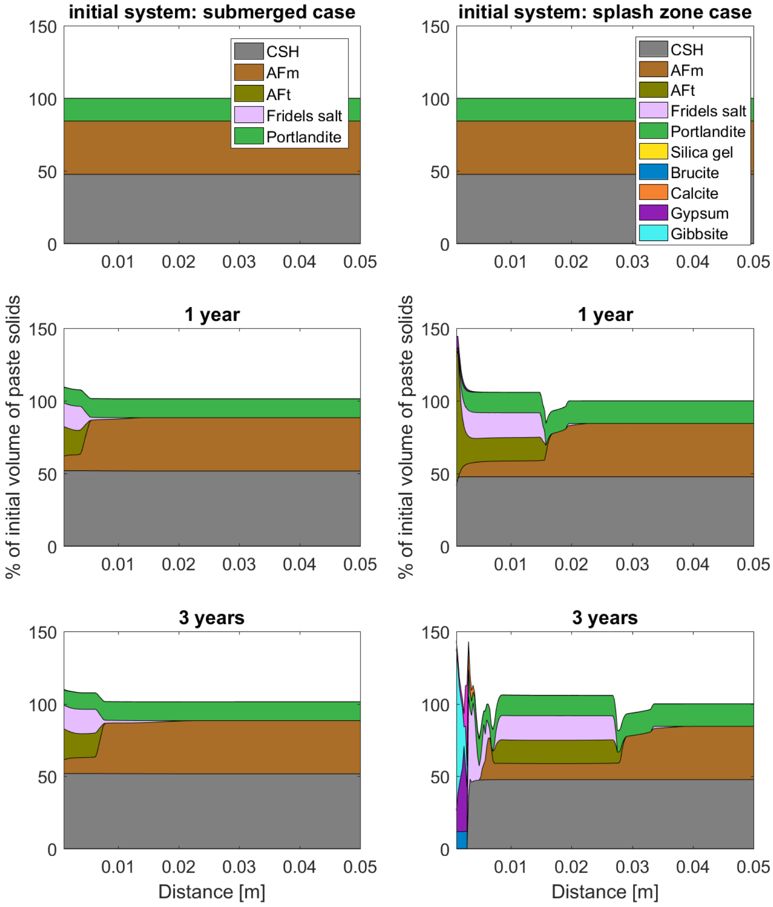

Figure 8: Comparing initial solid composition to the change in solid composition for example 2 and 3 cases after 1 and 3 years.

trends, rather than exact conclusions. The main trends observed in the results were, however, concluded to be in line with what can be found in the literature for corresponding cases. For example, the increased total volume in vicinity of the carbonation front followed by the decrease in total porosity after full carbonation, which results is presented in Figure 6, was reported in, e.g., [54–57]. After full carbonation, the remaining solid phases for this system were calcite, silica gel, gibbsite and gypsum. These results are also consistent with the solid phases reported in, e.g, [11]. Another important trend is the accelerated degradation of the hydrated cement due to the cyclic drying-wetting condition. This result was illustrated with the difference in solid phases composition between example 2 and 3 as shown in Figure 8. This behavior was reported in, e.g., [58] for cyclic chloride exposure, and in [59, 60] for cyclic sulfate attack.

4.2. Gas phase transport

The description of the gas phase transport adopted in this framework is different from what is commonly used, where a single reaction usually is used to describe an isolated mechanism, e.g., carbonation. The use of an accumulative volume for the gas phase described in section 2.1.3 enables modeling the transport in the gas phase alongside the transport in the liquid phase using the same framework. This allows for more detailed analysis where multiple constituents in the gas and liquid phase interact governed by mass action laws. However, one drawback of this kind of complex coupled models is the fact that it can be challenging to estimate a representative volume for the gas phase, especially after changes in hydration products.

The effect of the changes in the solid phase assemblage as a result of the altering of hydrated cement can easily be translated to changes in the porosity using the densities of the solid phases. In general, the changes in porosity in a porous media can be related to changes in pore connectivity through relations like the Carman-Koseny relation [61]. However, for cement-based materials, other types of changes to the microstructure can have a larger impact than the porosity itself, e.,g, formation or redistribution of gel pores and formation of coarser or finer capillary pores. Understanding the effect of altering the hydrated cement mineral composition on the changes in the microstructure and how to the transport properties are change in a multi-phase framework is of course rather challenging. In for example [57], the effects of accelerated carbonation on moisture transport properties were studied. The results in [57] highlight two effects contradicting each other at the carbonation front, that is, porosity clogging decreasing transport and microcracking increasing transport. The measurements in [55] revealed that carbonation of blended paste with high substitution ratio of SCMs and a high water to cement ratio leads to increased drying rates despite the decrease in porosity, at the carbonation front. This effect was attributed to the development of coarser capillary pores which result in extensive drying. In this context it can also be mentioned that the work presented in [62] highlighted how vapor transport through a single capillary pore can be accelerated as a result of increased saturation. It was beyond the scope of this work to identify and implement models that can account for the different effect of the change in microstructure on the different transport properties. To try to link changes in microstructure and transport properties is, however, a natural course of future development for the presented framework.

5. Conclusion

The addition of the gas phase to the multi-phase reactive mass transport framework for durability estimation of cement-based materials presented in earlier works, e.g., [29] was described and numerical examples demonstrating applications of the added options were presented. It is concluded that the addition of the gas phase contributes to a better understanding of the 'true' mechanisms responsible for the altering of hydrated cement-based materials in unsaturated moisture conditions as well as cyclic drying-wetting conditions. This is due to the fact that gas-liquid interaction between the different gases present in the gas phase and the ionic constitutes in the liquid phase is controlled by mass action laws including all the constituents in the gas and liquid phase.

Three numerical simulation examples using different exposure conditions were conducted in which the same cement-based material was investigated.

The first example simulated the results from an accelerated carbonation experiment over 56 days. Examples of the model output were presented including the concentrations profiles of CO_2 gas concentration profiles in the gas phase, concentration profiles of all ions containing carbon in the aqueous phase, and the change in the composition of the solid phases. It is concluded that the simulation was able to reproduce the carbonation progress observed in the experiment by adjusting the tortuosity factors for ionic and gaseous transport alone. Furthermore, it is concluded that the general trends observed in the results, e.g., increased porosity after full carbonation and pH drop during the dissolution of C-S-H, were in agreement with comparable observations reported in the literature.

The second and third example of this work simulated the altering of hydrated cement in a cyclic drying-wetting marine environment compared to a constantly submerged zone in the same marine environment. From the comparison of the two cases it is concluded that combined effect of multiple degradation processes is crucial, hence, simple models do not apply and cannot be used to adequately model all three example cases included in this work. It should be noted that the comparison between the second and third examples was purely a result of using the described initial conditions and boundary condition together with the constitutive relations for the chemical equilibrium part and the transport part and the results should be treated as general trends that can help improve the understanding of the underlying processes. Experimental results needs to confirm the simulation results. For example, effects like the change in porosity and microstructure and its effects on the transport processes needs to be investigated further in the purpose of continuously improve the constitutive assumptions of the developed framework.

The future work should mainly focus on including the effects of the transient changes in the microstructure on the transport properties. This will improve the model's predictive capabilities of the developed model and reduce the need for indirect fitting approaches typically used in models dedicated to one single durability mechanism.

Acknowledgments

Thanks to the Danish Innovation Fond (Innovations Fonden) for the financial support to this work as a part of the "Green transition of cement and concrete production" (Grøn Beton II) project, grant number 1382-00054B. Without their financial support and the contribution from the project partners, this research would not have been possible. Special thanks to the Danish Technological Institute for providing the experimental results of the accelerated carbonation test.

AppendixA. Diffusion properties and boundary values

The diffusion properties for gaseous and ionic constituents together with the boundary conditions are given in Table A.4.

AppendixB. Thermodynamic database

The thermodynamic database used is presented in Table B.5. The thermodynamical database is based on the CEMDATA07 database [48–52] and the mineral densities are from Balonis [65].

---

[1] K. Tuutti, Corrosion of steel in concrete, Tech. Rep., 1982.

[2] B. Lothenbach, K. Scrivener, R. D. Hooton, Supplementary cementitious materials, Cement and Concrete Research 41 (2011) 1244–1256.

[3] K. De Weerdt, M. B. Haha, G. Le Saout, K. O. Kjellsen, H. Justnes, B. Lothenbach, Hydration mechanisms of ternary Portland cements containing limestone powder and fly ash, Cement and Concrete Research 41 (2011) 279–291.

[4] R. D. Moser, A. R. Jayapalan, V. Y. Garas, K. E. Kurtis, Assessment of binary and ternary blends of metakaolin and Class C fly ash for alkali-silica reaction mitigation in concrete, Cement and Concrete Research 40 (2010) 1664–1672.

Table A.4: Diffusion properties for gaseous and ionic constituents and boundary conditions.

Gaseous species	$D_j^g \cdot 10^{-5}$		Ex. 1 boundary mol/l	Ex. 2 drying boundary mol/l	Sea water boundary mol/l
O_2	2.00^c		-	0.008	-
CO_2	1.60^c		0.0004	$1.635 \cdot 10^{-5}$	-
Ionic species	$D_i^l \cdot 10^{-9}$	$A_i^l \cdot 10^{-7}$	z_i	δ_i	
OH^-	5.300^a	2.253	-1	1.0^a	$1.621 \cdot 10^{-7}$
H^+	9.311^c	3.958	1	1.0^b	$1.327 \cdot 10^{-7}$
$Al(OH)_4^-$	5.040^a	2.142	-1	1.0^a	-
$Al(OH)_3$	5.040^b	-	-	1.0^b	-
$Al(OH)_2^-$	5.040^b	0.442	1	1.0^b	-
$AlOH^{+2}$	5.040^b	0.442	2	1.0^b	-
Al^{+3}	0.541^c	0.230	3	1.0^b	-
$AlSO_4^+$	5.040^b	0.442	1	1.0^b	-
$Al(SO_4)_2^-$	5.040^b	0.442	-1	1.0^b	-
Ca^{+2}	0.792^a	0.337	2	0.2^a	$9.879 \cdot 10^{-3}$
$CaOH^+$	0.792^a	0.337	1	0.2^a	$5.330 \cdot 10^{-9}$
$CaSO_4$	0.471^a	-	-	1.0^a	$1.196 \cdot 10^{-3}$
$CaHSO_4^+$	0.471^b	0.200	1	1.0^b	$1.099 \cdot 10^{-9}$
SO_4^{-2}	1.070^a	0.455	-2	1.0^a	$1.609 \cdot 10^{-2}$
HSO_4^-	1.385^c	0.589	-1	1.0^b	-
$H_2SiO_4^{-2}$	1.100^a	0.468	-2	0.02^a	-
$H_3SiO_4^-$	1.107^d	0.468	-1	1.0^b	-
H_4SiO_4	1.107^d	-	-	1.0^b	-
Cl^-	2.030^a	0.863	-1	1.0^a	$6.183 \cdot 10^{-1}$
Na^+	1.330^a	0.565	1	0.02^a	$4.898 \cdot 10^{-1}$
$NaOH$	1.330^b	-	-	1.0^b	$1.902 \cdot 10^{-8}$
$NaSO_4^-$	0.618^a	0.263	-1	1.0^a	$6.625 \cdot 10^{-3}$
$CaCO_3$	0.446^a	-	-	1.0^a	$1.368 \cdot 10^{-6}$
CO_3^{-2}	0.955^a	0.406	-2	1.0^a	$1.903 \cdot 10^{-6}$
HCO_3^-	1.180^a	0.502	-1	1.0^a	-
$CaHCO_3^+$	0.471^b	0.200	1	1.0^b	$3.880 \cdot 10^{-5}$
$H_3CaSiO_4^+$	0.471^b	0.200	1	1.0^b	-
$MgOH^+$	0.705^a	0.299	1	1.0^a	$6.656 \cdot 10^{-7}$
Mg^{+2}	0.705^a	0.299	2	1.0^a	$4.861 \cdot 10^{-2}$
$MgHCO_3^+$	0.705^b	0.299	1	1.0^b	$1.819 \cdot 10^{-4}$
CO_2	1.91^d	-	-	1.0^b	$1.618 \cdot 10^{-4}$
$NaHCO_3$	0.133^b	-	-	1.0^b	$1.373 \cdot 10^{-4}$
$MgCO_3$	0.705^b	-	-	1.0^b	$4.436 \cdot 10^{-6}$
$NaCO_3^-$	0.0585^a	0.405	-1	1.0^a	$3.345 \cdot 10^{-6}$
K^+	1.957^a	0.405	1	0.02^a	$9.911 \cdot 10^{-3}$
KSO_4^-	1.070^a	0.454	-1	1.0^a	$1.648 \cdot 10^{-4}$
KOH	1.960^a	-	-	1.0^a	$1.771 \cdot 10^{-10}$
$MgSO_4$	0.705^b	-	-	1.0^b	$8.019 \cdot 10^{-3}$
$Fe(OH)_4^-$	0.719^b	0.299	-1	1.0^b	-
$Fe(OH)_3$	0.719^b	0.299	0	1.0^b	-
$Fe(OH)_2^+$	0.719^b	0.299	1	1.0^b	-
$FeOH^{+2}$	0.719^b	0.299	2	1.0^b	-

[a] Data from Hosokawa et al. [28]

[b] Data estimated in Jensen et al. [29]

[c] Data from Lide and Haynes [63]

[d] Data from Shen et al. [64]

Table B.5: Thermodynamic data and densities.

	Reactions		
Equilibrium phases		log K	Density
Portlandite	$Ca(OH)_2 + 2H^+ \leftrightarrow Ca^{2+} + 2H_2O$	22.80	32.78
Silica gel	$SiO_2 + +2H_2O \leftrightarrow H_4SiO_4$	−2.71	22.75
Calcite	$CaCO_3 \leftrightarrow Ca^{2+} + CO_3^{2-}$	1.85	37.00
Brucite	$Mg(OH)_2 + 2H^+ \leftrightarrow Mg^{2+} + 2H_2O$	16.84	25.00
Gypsum	$CaSO_4 : 2H_2O \leftrightarrow Ca^{2+} + SO_4^{2-} + 2H_2O$	−4.58	74.50
Monocarboaluminate	$(CaO)_3Al_2O_3(CaCO_3) : 11H_2O \leftrightarrow 4Ca^{2+} + 2Al(OH)_4^- + CO_3^{2-} + 4OH^- + 5H_2O$	31.47	242.89
Gibbsite	$Al(OH)_3 \leftrightarrow Al(OH)4^- - OH^-$	0.24	32.22
Solid solution			
	C-S-H (ss)		
TobH	$(CaO)_{0.66}(SiO_2)(H_2O)_{1.5} + 1.32H^+ \leftrightarrow 0.66Ca^{2+} + H_4SiO_4 + 0.16H_2O$	8.27	75.63
TobD	$(CaO)_{0.83}(SiO_2)_{0.66}(H_2O)_{1.83} + 1.66H^+ \leftrightarrow 0.83Ca^{2+} + 0.66H_4SiO_4 + 1.34H_2O$	13.62	82.59
JenH	$(CaO)_{1.33}(SiO_2)(H_2O)_{2.16} + 2.66H^+ \leftrightarrow 1.33Ca^{2+} + H_4SiO_4 + 1.49H_2O$	22.17	47.95
JenD	$(CaO)_{1.5}(SiO_2)_{0.66}(H_2O)_{2.5} + 3H^+ \leftrightarrow 0.66Ca^{2+} + H_4SiO_4 + 0.16H_2O$	28.71	55.30
	AFm (1) (ss)		
C_2AH_8	$Ca_4Al_2(OH)_{10} : 3H_2O \leftrightarrow 2Ca^{2+} + 2Al(OH)_4^- + 2OH^- + 3H_2O$	−13.56	183.71
C_2FH_8	$Ca_4AFe_2(OH)_{10} : 3H_2O \leftrightarrow 2Ca^{2+} + 2Fe(OH)_4^- + 2OH^- + 3H_2O$	−17.60	194.00
	AFm (2) (ss)		
C_2AH_{13}	$Ca_4Al_2(OH)_{14} : 6H_2O \leftrightarrow 4Ca^{2+} + 2Al(OH)_4^- + 6OH^- + 6H_2O$	−25.40	274.20
C_2FH_{13}	$Ca_4AFe_2(OH)_{14} : 6H_2O \leftrightarrow 4Ca^{2+} + 2Fe(OH)_4^- + 6OH^- + 6H_2O$	−29.40	285.93
	AFm (3) (ss)		
C_4AH_{13}	$Ca_4Al_2(OH)_{14} : 6H_2O \leftrightarrow 4Ca^{2+} + 2Al(OH)_4^- + 6OH^- + 6H_2O$	−25.40	274.20
Monosulfoaluminate	$Ca_4Al_2SO_4(OH)_{12} : 4H_2O \leftrightarrow 4Ca^{2+} + 2Al(OH)_4^- + 4OH^- + SO_4^{2-} + 4H_2O$	−29.26	308.94
	AFm (4) (ss)		
C_4AH_{13}	$Ca_4Al_2(OH)_{14} : 6H_2O \leftrightarrow 4Ca^{2+} + 2Al(OH)_4^- + 6OH^- + 6H_2O$	−25.40	274.20
Friedels salt	$Ca_4Al_2Cl_2(OH)_{12} : 4H_2O \leftrightarrow 4Ca^{2+} + 2Al(OH)_4^- + 4OH^- + 2Cl^- + 4H_2O$	−27.3	271.97
	AFt (ss)		
Fe- Ettringite	$Ca_6Fe_2(SO_4)_2(OH)_{12} : 26H_2O \leftrightarrow 6Ca^{2+} + 2Fe(OH)_4^- + 3SO_4^{2-} + 4OH^- + 26H_2O$	−44.01	717.40
Al-Ettringite	$Ca_6Al_2(SO_4)_2(OH)_{12} : 26H_2O \leftrightarrow 6Ca^{2+} + 2Al(OH)_4^- + 3SO_4^{2-} + 4OH^- + 26H_2O$	−44.91	705.91

[5] K. L. Scrivener, B. Lothenbach, N. De Belie, E. Gruyaert, J. Skibsted, R. Snellings, A. Vollpracht, TC 238-SCM: hydration and microstructure of concrete with SCMs, Materials and Structures 48 (2015) 835–862.

[6] M. Saeidpour, L. Wadsö, Moisture equilibrium of cement based materials containing slag or silica fume and exposed to repeated sorption cycles, Cement and Concrete Research 69 (2015) 88–95.

[7] M. Saeidpour, L. Wadsö, Moisture diffusion coefficients of mortars in absorption and desorption, Cement and Concrete Research 83 (2016) 179–187.

[8] P. Van Den Heede, N. De Belie, A service life based global warming potential for high-volume fly ash concrete exposed to carbonation, Construction and Building Materials 55 (2014) 183–193.

[9] B. Dong, Q. Qiu, Z. Gu, J. Xiang, C. Huang, Y. Fang, F. Xing, W. Liu, Characterization of carbonation behavior of fly ash blended cement materials by the electrochemical impedance spectroscopy method, Cement and Concrete Composites 65 (2016) 118–127.

[10] L. Mo, F. Zhang, M. Deng, D. K. Panesar, Effectiveness of using CO2 pressure to enhance the carbonation of Portland cement-fly ash-MgO mortars, Cement and Concrete Composites 70 (2016) 78–85.

[11] Z. Shi, B. Lothenbach, M. R. Geiker, J. Kaufmann, A. Leemann, S. Ferreiro, J. Skibsted, Experimental studies and thermodynamic modeling of the carbonation of Portland cement, metakaolin and limestone mortars, Cement and Concrete Research 88 (2016) 60–72.

[12] M. D. Thomas, P. B. Bamforth, Modelling chloride diffusion in concrete: effect of fly ash and slag, Cement and Concrete Research 29 (1999) 487–495.

[13] M. Maes, E. Gruyaert, N. De Belie, Resistance of concrete with blast-furnace slag against chlorides, investigated by comparing chloride profiles after migration and diffusion, Materials and Structures 46 (2012) 89–103.

[14] Z. Zhang, M. T. andV. Baroghel-Bouny, Chloride penetration in concrete exposed to cyclic drying-wetting and carbonation, Construction and Building Materials 112 (2016) 457–463.

[15] E. Gruyaert, P. Van Den Heede, N. De Belie, Carbonation of slag concrete: Effect of the cement replacement level and curing on the carbonation coefficient - Effect of carbonation on the pore structure, Cement and Concrete Composites 35 (2013) 39–48.

[16] O. Francy, R. François, Measuring chloride diffusion coefficients from non-steady state diffusion tests, Cement and concrete research 28 (1998) 947–953.

[17] T. Luping, Concentration dependence of diffusion and migration of chloride ions: Part 1. Theoretical considerations, Cement and concrete research 29 (1999) 1463–1468.

[18] Q. Yuan, C. Shi, G. De Schutter, D. Deng, F. He, Numerical model for chloride penetration into saturated concrete, Journal of Materials in Civil Engineering 23 (2010) 305–311.

[19] C. G. V. Vagelis G. Papadakis, M. N. Fardis, Fundamental Modeling and Experimental Investigation of Concrete Carbonation, ACI Materials Journal 88 (4) (1991) 186–196.

[20] A. V. Saetta, B. A. Schrefler, R. V. Vitaliani, The carbonation of concrete and the mechanism of moisture,heat and carbon dioxide flow through porous materials., Cement and Concrete Composites 23 (1993) 761–772.

[21] A. Steffens, D. Dinkler, H. Ahrens, Modeling carbonation for corrosion risk prediction of concrete structures, Cement and Concrete Research 32 (2002) 935–941.

[22] A. V. Saetta, R. V. Vitaliani, Experimental investigation and numerical modeling of carbonation process in reinforced concrete structures: Part II. Practical applications, Cement and Concrete Research 35 (2005) 958–967.

[23] G. Villain, M. Thiery, G. Platret, Measurement methods of carbonation profiles in concrete: Thermogravimetry, chemical analysis and gammadensimetry, Cement and Concrete Research 37 (2007) 1182–1192.

[24] S. Kashef-Haghighi, Y. Shao, S. Ghoshal, Mathematical modeling of CO2 uptake by concrete during accelerated carbonation curing, Cement and Concrete Research 67 (2015) 1–10.

[25] Q. T. Phung, N. Maes, D. Jacques, G. De Schutter, G. Ye, J. Perko, Modelling the carbonation of cement pastes under a CO2 pressure gradient considering both diffusive and convective transport, Construction and Building Materials 114 (2016) 333–351.

[26] V. Baroghel-Bouny, T. Nguyen, P. Dangla, Assessment and prediction of RC structure service life by means of durability indicators and physical/chemical models, Cement and Concrete Composites 31 (2009) 522–534.

[27] J. Marchand, E. Samson, Predicting the service-life of concrete structures–limitations of simplified models, Cement and Concrete Composites 31 (2009) 515–521.

[28] Y. Hosokawa, K. Yamada, B. Johannesson, L.-O. Nilsson, Development of a multi-species mass transport model for concrete with account to thermodynamic phase equilibriums, Materials and Structures 44 (2011) 1577–1592.

[29] M. Jensen, B. Johannesson, M. Geiker, Framework for reactive mass transport: Phase change modeling of concrete by a coupled mass transport and chemical equilibrium model, Computational Materials Science 92 (2014) 213–223.

[30] M. M. Jensen, A Coupled Transport and Chemical Model for Durability Predictions of Cement Based Materials, Ph.D. thesis, Department of Civil Engineering Technical University of Denmark, 2014.

[31] L. Bennethum, J. Cushman, Multicomponent, multiphase thermodynamics of swelling porous media with electroquasistatics: I. Macroscale field equations, Transport in Porous Media 47 (2002) 309–336.

[32] L. Bennethum, J. Cushman, Multicomponent, multiphase thermodynamics of swelling porous media with electroquasistatics: II. Constitutive theory, Transport in Porous Media 47 (2002) 337–362.

[33] B. Johannesson, Development of a Generalized Version of the Poisson-Nernst-Planck Equations Using the Hybrid Mixture Theory: Presentation of 2D Numerical Examples, Transport in Porous Media 85 (2010) 565–592.

[34] M. Addassi, B. Johannesson, L. Wadsö, Inverse analyses of effective diffusion parameters relevant for a two-phase moisture model of cementitious materials, Cement and Concrete Research 00 (2018) 00–0.

[35] L. Bennethum, J. Cushman, Multiscale, hybrid mixture theory for swelling systems–I: balance laws, International Journal of Engineering Science 34 (1996) 125–145.

[36] B. Johannesson, U. Nyman, A Numerical Approach for Non-Linear Moisture Flow in Porous Materials with Account to Sorption Hysteresis, Transport in Porous Media 84 (2010) 735–754.

[37] J. K. Stolaroff, D. W. Keith, G. V. Lowry, Carbon Dioxide Capture from Atmospheric Air Using Sodium Hydroxide Spray, Environmental Science & Technology 42 (8) (2008) 2728–2735.

[38] U. Nyman, P. Gustafsson, B. Johannesson, R. Hägglund, A numerical method for the evaluation of non-linear transient moisture flow in cellulosic materials, International journal for numerical methods in engineering 66 (2006) 1859–1883.

[39] M. M. Jensen, B. Johannesson, M. R. Geiker, A Numerical Comparison of Ionic Multi-Species Diffusion with and without Sorption Hysteresis for Cement-Based Materials, Transport in Porous Media 107 (2015) 27–47.

[40] N. Ottosen, H. Petersson, Introduction to the finite element method, Prentice Hall International, 1992.

[41] O. Zienkiewicz, R. Taylor, J. Zhu, The finite element method: its basis and fundamentals, vol. 1, Butterworth-Heinemann, 2005.

[42] N. Ottosen, M. Ristinmaa, Mechanics of Constitutive Modeling, Elsevier, 2005.

[43] D. Parkhurst, C. Appelo, User's Guide to PHREEQC (Version 2): a Computer Program for Speciation, Batch-reaction, One-dimensional Transport, and Inverse Geochemical Calculations, U.S. Geological Survey Water-Resources Investigations, 1999.

[44] S. R. Charlton, D. L. Parkhurst, Modules based on the geochemical model {PHREEQC} for use in scripting and programming languages, Computers & Geosciences 37 (2011) 1653 – 1663.

[45] G. W. Castellan, Physical Chemistry, The Benjamin/Cummings Publ. Co, 1983.

[46] L. Bennethum, J. Cushman, M. Murad, Clarifying mixture theory and the macroscale chemical potential for porous media, International Journal of Engineering Science 34 (1996) 1611–1621.

[47] L. S. Bennethum, M. A. Murad, J. H. Cushman, Macroscale Thermodynamics and the Chemical Potential for Swelling Porous Media, Transport in Porous Media 39 (2000) 187–225.

[48] G. Möschner, B. Lothenbach, J. Rose, A. Ulrich, R. Figi, R. Kretzschmar, Solubility of Fe–ettringite ($Ca_6[Fe(OH)_6]_2(SO_4)_3 \cdot 26H_2O$), Geochimica et Cosmochimica Acta 72 (2008) 1–18.

[49] G. Möschner, B. Lothenbach, F. Winnefeld, A. Ulrich, R. Figi, R. Kretzschmar, Solid solution between Al-ettringite and Fe-ettringite (Ca 6 [Al 1- x Fe x (OH) 6] 2 (SO 4) 3· 26H 2 O), Cement and Concrete Research 39 (2009) 482–489.

[50] T. Schmidt, B. Lothenbach, M. Romer, K. Scrivener, D. Rentsch, R. Figi, A thermodynamic and experimental study of the conditions of thaumasite formation, Cement and Concrete Research 38 (2008) 337–349.

[51] B. Lothenbach, F. Winnefeld, Thermodynamic modelling of the hydration of Portland cement, Cement and Concrete Research 36 (2006) 209–226.

[52] B. Lothenbach, T. Matschei, G. Möschner, F. P. Glasser, Thermodynamic modelling of the effect of temperature on the hydration and porosity of Portland cement, Cement and Concrete Research 38 (2008) 1–18.

[53] D. Kulik, Improving the structural consistency of C-S-H solid solution thermodynamic models, Cement and Concrete Research 41 (2011) 477–495.

[54] A. Morandeau, M. Thiéry, P. Dangla, Investigation of the carbonation mechanism of CH and C-S-H in terms of kinetics, microstructure changes and moisture properties, Cement and Concrete Research 56 (2014) 153 – 170.

[55] A. Morandeau, M. Thiéry, P. Dangla, Impact of accelerated carbonation on OPC cement paste blended with fly ash, Cement and Concrete Research 67 (2015) 226 – 236.

[56] A. Leemann, P. Nygaard, J. Kaufmann, R. Loser, Relation between carbonation resistance, mix design and exposure of mortar and concrete, Cement and Concrete Composites 62 (2015) 33–43.

[57] M. Auroy, S. Poyet, P. L. Bescop, J. Torrenti, T. Charpentier, M. Moskura, X. Bourbon, Impact of carbonation on unsaturated water transport properties of cement-based materials, Cement and Concrete Research 74 (2015) 44 – 58.

[58] K. Hong, R. D. Hooton, Effects of cyclic chloride exposure on penetration of concrete cover, Cement and Concrete Research 29 (1999) 1379–1386.

[59] M. Bassuoni, M. Nehdi, Durability of self-consolidating concrete to sulfate attack under combined cyclic environments and flexural loading, Cement and Concrete Research 39 (3) (2009) 206 – 226.

[60] J. Gao, Z. Yu, L. Song, T. Wang, S. Wei, Durability of concrete exposed to sulfate attack under flexural loading and drying–wetting cycles, Construction and Building Materials 39 (2013) 33–38.

[61] J. Bear, Dynamics of fluids in porous media, p. 764, Dover Publications, 1972.

[62] M. Addassi, L. Schreyer, B. Johannesson, H. Lin, Pore-scale modeling of vapor transport in partially saturated capillary tube with variable area using chemical potential, Water Resources Research 52 (2016) 7023–7035.

[63] D. R. e. Lide, W. M. e. Haynes, CRC handbook of chemistry and physics: a ready-reference book of chemical and physical data, CRC Press, 91. ed. edn., ISBN 1439820775, 9781439820773, 2010.

[64] J. Shen, P. Dangla, M. Thiery, Reactive Transport Modeling of CO_2 Through Cementitious Materials Under Supercritical Boundary Conditions, Geomechanics in CO Storage Facilities (2013) 181–208.

[65] M. Balonis, The Influence of Inorganic Chemical Accelerators and Corrosion Inhibitors on the Mineralogy of Hydrated Portland Cement Systems, ISBN 2005019283, 2010.

Towards a better understanding of long-term durability aspects of new CO2-reduced cements with special focus on moisture and gas transport processes. The research findings include a conceptually simple model enhancing the understanding of important vapor transport mechanisms in unsaturated systems; a novel inverse analyses approach for determining a separate description of the diffusion in the liquid phase and in the vapor phase; and the addition of the gas phase to a multi-phase reactive mass transport framework for durability estimation of cement-based

DTU Civil Engingeering
Technical University of Denmark

Brovej, Bygning 118
2800 Kongens Lyngby

www.byg.dtu.dk

ISBN 9788778774897
ISSN 1601-2917